Optical fluctuations on the transmission and reflection of mesoscopic systems

Johannes F. de Boer

Ph.D. Thesis, Sept. 1995, Amsterdam.

promotor:	Prof. Dr. A. Lagendijk
commissie:	Dr. M.P. van Albada Prof. Dr. C.W.J. Beenakker Prof. Dr. J.C. Dainty Dr. L.G. Suttorp Prof. Dr. J.T.M. Walraven
paranimfen:	Elisabeth de Boer en Pier Philipsen

The work described in this thesis was part of the research program
of the 'Stichting voor Fundamenteel Onderzoek der Materie (FOM)',
which is financially supported by the
'Nederlandse Organisatie voor Wetenschappelijk Onderzoek (NWO)',
and carried out at the

Van der Waals-Zeeman Laboratorium
Universiteit van Amsterdam
Valckenierstraat 65-67
1018 XE Amsterdam
The Netherlands

where a number of copies of this thesis are available.

Optical fluctuations on the transmission and reflection of mesoscopic systems

ACADEMISCH PROEFSCHRIFT

ter verkrijging van de graad van doctor
aan de universiteit van Amsterdam,
op gezag van de Rector Magnificus
prof. dr. P.W.M. de Meijer
ten overstaan van een door het college van dekanen
ingestelde commissie in het openbaar te verdedigen
in de Aula der Universiteit
op woensdag 20 september 1995 te 13.30 uur
door Johannes Fitzgerald de Boer
geboren te Amsterdam

Dankwoord

Ik wil een aantal mensen bedanken, zonder wiens inspiratie en aanwezigheid dit proefschrift niet tot stand zou zijn gekomen.

Allereerst wil ik mijn promotor Ad Lagendijk bedanken. Grote bewondering heb ik voor je brede kennis van en je inspirerende enthousiasme voor de fysica. Menigmaal heb je me op het juiste spoor gezet met een artikel of een boek over een probleem of heb je mijn inzicht verdiept in discussies. Ik ben je ook dankbaar voor de vrijheid die ik heb genoten gedurende het tweede deel van mijn promotie.

De tweede persoon die ik erg graag wil bedanken is Meint van Albada. Je bent mijn leermeester geweest in de experimentele fysica. De JBF methode heeft dank zij jou een geuzennaam verworven. Ik ben trots op de experimentele resultaten die we samen behaald hebben.

Theo Nieuwenhuizen wil ik bedanken voor zijn college over veelvuldige verstrooiing, waar ik veel aan gehad heb. Verder ben ik hem en Mark van Rossum erkentelijk voor de vruchtbare samenwerking die geleid heeft tot de twee artikelen over de derde cumulant.

For the fruitful cooperation on the non-linear speckle work I would like to thank Shechao Feng, en Rudolf Sprik, die daarnaast als vraagbaak een grote ondersteuning was.

Van de werkplaats wil ik vooral Ad Wijkstra en Flip de Leeuw bedanken voor het bouwen van mechanische respectievelijk electronische apparatuur. Voor de ondersteuning op computergebied ben ik Paul Langemeijer, Jaap Berkhout en Ton Jongeneelen erkentelijk en voor de kleine maar o zo belangrijke mechanische haastklusjes Wim Koops.

Na de mensen die hebben bijgedragen aan publicaties wil ik vooral mijn collega's bedanken voor de (wetenschappelijke) discussies en de gezelligheid die het leven voor deze promovendus dragelijk hebben gemaakt. Als eerste mijn kamergenoot Rik, en verder de (ex)-collega's Peter, Marcus, Mark K., Willem, Irwan, Jom, Tom, Boris, Rogier, Ron, Hilde, Monique, Suzan, Tycho, Merrit, Bert, Peter M., Maurice, Pedro, Martin, Raymond, Mick, Jaap, Pepijn, Allard, Mischa, Frank, Jook en Gerard, buiten onze groep Barbara, Joost en Arnout, van het Amolf Diederik, Marco en Eloy, en mijn goede vrienden in voor- en tegenspoed, Marcus, Pier en Ronald.

Als laatste wil ik mijn moeder, mijn vader en mijn zus bedanken voor hun niet aflatende steun en belangstelling.

Johannes de Boer
Amsterdam, augustus 1995

List of publications

M. P. van Albada, J. F. de Boer, and A. Lagendijk. Observation of long-range intensity correlation in the transport of coherent ligth through a random medium. *Phys. Rev. Lett.*, **64**, 2787, (1990).

M. P. van Albada, J. F. de Boer, A. Lagendijk, B. A. van Tiggelen, and A. Tip. Recent results in the field of light localisation. Inst. Phys. Conf. 108, 99-110 (1991).

J. F. de Boer, M. P. van Albada, and A. Lagendijk. Intensity and field correlation's in multiple scattered light. *Physica B*, **175**, 17, (1991).

J. F. de Boer, M. P. van Albada, and A. Lagendijk. Intensity and field correlation's in multiple scattered light. In W. van Haeringen, and D. Lenstra, editors, *Analogies in Optics and Micro-Electronics*, Proceedings of the International symposium on the Analogies in Optics and Micro-Electronics, Eindhoven, The Netherlands, 1-3 May 1991, reprinted from *Physica B*, **175**, 17, (1991).

J. F. de Boer, M. P. van Albada, and A. Lagendijk. Transmission and intensity correlation's in wave propagation through random media. *Phys. Rev. B*, **45**, 658, (1992).

J. F. de Boer, R. Sprik, A. Lagendijk, and S. Feng. Preliminary experiments on the transmission of light through non-linear disordered media. in: Photonic Band Gaps and Localization, edited by C.M. Soukoulis, Plenum, New York, 165-169, (1993).

J. F. de Boer, A. Lagendijk, R. Sprik, and S. Feng. Transmission and Reflection Correlation's of Second Harmonic Waves in Non-linear Random Media. *Phys. Rev. Lett.*, **71**, 3947, (1993).

J. F. de Boer, and A. Lagendijk. Mesoscopische fysica met licht (Mesoscopic physics with light). Ned. Tijdschrift voor Natuurkunde, **60**, 199-202, (1994).

J. F. de Boer, M. C. W. van Rossum, M. P. van Albada, Th. M. Nieuwenhuizen, and A. Lagendijk. Probability distribution of multiple scattered light measured in total transmission. *Phys. Rev. Lett.*, **73**, 2567, (1994).

M. C. W. van Rossum, J. F. de Boer, and Th. M. Nieuwenhuizen. Third cumulant of the total transmission of diffuse waves. (1995). To be published in *Phys. Rev. E.*

Contents

Chapter 1

Introduction

1.1 History

This thesis deals with the transport of waves through disordered media. Interference of waves plays an important role in the (static) fluctuations on transport properties and makes the transport properties of waves different from "classical" transport of particles. The interest in the transport properties of disordered media received new impetus in the early eighties with the discovery of Universal Conductance Fluctuations (UCF) in disordered conductors cooled below 1 Kelvin[1, 2] and the discovery of enhanced backscattering of light from a disordered dielectric sample[3, 4]. The fluctuations on the conductance turned out to be independent of sample parameters such as the conductance itself, the size of the sample, or the mean free path of the electrons in the sample, hence the name UCF. For the observation of UCF the conductors needed to be several mean free paths thick and in the mesoscopic regime, i.e. the mean free path ℓ is smaller than the dephasing length ℓ_ϕ or equivalently the inelastic scattering length ℓ_{in}; $\ell \ll \ell_\phi, \ell_{in}$. It was soon discovered that interference of electron wave functions plays a crucial role in the explanation of the phenomenon. Enhanced backscattering of light is the effect that light scattered from a disordered dielectric sample shows an enhanced intensity in the exact backscatter direction (for the copolarized intensity). The intensity in the exact backscatter direction is twice as high as expected from a "classical" description, the effect is caused by light that interferes with light that has travelled along a time reversed path through the disordered sample. Both discoveries were the start of a new discipline in physics, known as Mesoscopic Physics[5, 6].

In 1958 P. W. Anderson showed that electrons can become localized when subject to a spatially random potential; Electron transport undergoes a drastic change from a finite conductance to zero conductance at a critical disorder, known as Anderson localization[7]. It is believed that interference plays an important role in this process.

The analogy between electrons and light (i.e. their wave character) has led to a vivid search for Anderson localization of light. Although Anderson localization of light has not been observed yet, the pursuit of this goal has led to many interesting discoveries on the propagation of light in disordered structures and the role of interference.This thesis deals for a large part with experiments on the precursors of the optical analogue of the Universal Conductance Fluctuations and with the distribution of the fluctuations. The last part of this thesis addresses interference in a disordered structure with non-linear susceptibility. Interference of both fundamental and second harmonic generated light is described.

1.2 Outline of this thesis

In **chapter 2** an introduction into multiple scattering theory is given. First a particle diffusion model is presented. Then the wave equation with a random potential is introduced along with useful concepts such as the optical theorem. The difference between multiple scattering on the amplitude level and on the intensity level is explained. It is shown that diffusion of light is derived on the intensity level. The diffusion constant and speed of propagation are derived from a microscopic picture. Finally these results as derived for an infinite disordered medium are applied to a slab geometry, where the appropriate boundary conditions are found from transport theory. The last part explains how the incoming and outgoing intensities are coupled to the intensity propagators inside the slab and gives simple expressions for the coupling that will be used throughout this thesis.

In **chapter 3** we go beyond the diffusion approach and calculate higher moments of the intensity. In chapter 2 we were interested in the average intensity, a quantity in which the wave character was not manifest. In the results of chapter 3 however, interference of waves plays a major role. The distribution of the fluctuations in laser speckle is discussed shortly, as is the number of independent speckles in reflection and transmission of a disordered slab. The model of a wave guide with disorder is introduced, and employing this model it is shown that correlation exists on the fluctuations in transmission. As shown in an article by Feng *et al.*[8] three types of correlation can be distinguished. The first type is known as the short-range correlation. The second type of correlation (the long range correlation) will be the subject of extensive theoretical discussion, both here and in Appendix A. (An experimental study will be discussed in chapter 4.) The third type of correlation is the optical analogue of the UCF. We start with the calculation of the short-range correlation. The results of this calculation are then used to obtain the long range correlation in a Langevin approach. At the end of chapter 3 a physical interpretation of the origin of the long range correlation is given. In Appendix A a diagrammatic calculation of the long range correlation is presented. The results of the diagrammatic calculation agree completely with the results of the Langevin approach in this chapter.

In **chapter 4** the measurements on the long range correlation are presented. The experimental set-up is described, and the precautions taken to ensure that the measured fluctuations result from interference effects inside the disordered sample only are discussed. We present measurements of the short-range correlation, and deduce the diffusion constant of the light from them. It is shown that the finite wavelength range over which the fluctuations could be measured in the long range correlation experiment influences the results. It is explained how the data were analysed to get past this problem. Finally the long-range correlation functions as measured for several different samples and experimental parameters are presented and compared with the theory of chapter 3. The reader, discouraged by the tedious calculations in chapter 3, is amply rewarded for his or her effort by the beautiful agreement between experiment and theory. The experimental results even allow for an evaluation of the energy transport velocity, and constitute an independent confirmation of its drastic reduction compared to the vacuum velocity, that was found earlier by van Albada *et al.*[9].

In **chapter 5** we study the distribution of the fluctuations on the total transmission. The interest in this distribution was raised through an article by Kogan *et al.*[10], who derived theoretically that the speckle statistics in transmission through a disordered medium crosses over from a Rayleigh distribution to a stretched exponential, as was earlier found experimentally by Genack and Garcia[11]. For the total transmission Kogan *et al.* found to lowest order in the conductance a Gaussian distribution of the fluctuations. The distribution of the electronic conductance fluctuations was first calculated by Altshuler, Kravtsov and Lerner[12]. They showed that the distribution of the conductance changes from Gaussian to log-normal as one approaches the Anderson transition. Based on the analogy between de Broglie waves and light waves[13], this raised the question whether a deviation from a Gaussian distribution was present in our experimental results on the total transmission. In chapter 5 the experimental distribution of the total transmission is presented. It is shown that indeed a third cumulant is present in the distribution (i.e. a deviation from a Gaussian distribution). Heuristic arguments predict a quadratic relation between the second and the third cumulant, and this is indeed found in the experiment. Careful statistical analysis of the data even gives the prefactor of the quadratic relation, which is in agreement with a theoretical calculation. In Appendix B the quadratic relation between the second and third cumulant is proven by a diagrammatic calculation, which also gives the prefactor.

In **chapter 6** the interference of second harmonic light generated by a non-linear susceptibility of a disordered medium is studied. Agranovich and Kravtsov [14] and Kravtsov, Agranovich and Grigorishin[15] showed that enhanced backscatter should occur in the second harmonic light generated in a non-linear disordered medium. The effect, however, is small. Much larger effects are expected for the short-range correlation in transmission and reflection of the second harmonic speckle. In chapter 6 these correlations are studied, and compared to their linear counterparts. The experimental set-up and the sample preparation are described. The measurements of the fundamental and second harmonic correlation functions are presented, and compared with theory. As most striking result it is found that the correlation function of the second harmonic light in reflection scales with the sample thickness, whereas the linear correlation function in reflection scales essentially with the mean free path.

Chapter 2

Diffusion of light

In this chapter an introduction to the multiple scattering theory is given. We begin with the diffusion of particles through a disordered medium, known as classical diffusion since interference plays no role. After this short introduction of diffusion we turn to the equation of motion of waves. The basic principles of the scattering of waves are introduced. First the scattering of waves by a single particle is treated, then by a collection of scatterers. It will be shown that on the amplitude level, there is no diffusion. A propagator for the intensity is constructed, and this propagator will satisfy a diffusion equation. Since the experiments are always done on finite disordered structures, we will explore the boundary conditions of a finite disordered medium on multiple scattered (diffuse) light. To this end, results from transport theory are introduced. From these boundary conditions an intensity propagator for the slab geometry is derived. This is the main result of this chapter. The last part deals with the total amount of light that is reflected from and transmitted through a disordered slab. Part of the theory in this chapter is based on Ishimaru[16], Frisch[17], van der Mark *et al.*[18], van Tiggelen *et al.*[19] and Kirkpatrick[20].

2.1 Classical diffusion

Let us assume that light diffuses as particles do through a random structure. In one dimension the equation of motion is

$$\frac{\partial n(x,t)}{\partial t} = D\frac{\partial^2 n(x,t)}{\partial x^2}, \tag{2.1}$$

with $n(x,t)$ the one particle probability density and D the diffusion constant. At $t=0$ the boundary condition $n(x,0)=\delta(x)$ is imposed. The solution to Eq. (2.1) can be found by substituting the Fourier transform of $n(x,t)$,

$$n(x,t) = \frac{1}{2\pi}\int n(k,t)e^{-ikx}\mathrm{d}k, \tag{2.2}$$

into the equation of motion. The substitution yields

$$\frac{\partial n(k,t)}{\partial t} = -Dk^2 n(k,t), \tag{2.3}$$

with the solution,

$$n(k,t) = n(k,0)e^{-Dk^2 t}, \tag{2.4}$$

and boundary condition $n(k,0) = 1$. Transforming this solution to real space gives the solution to the equation of motion,

$$n(x,t) = \frac{1}{\sqrt{4\pi Dt}} e^{-x^2/4Dt}. \tag{2.5}$$

In three dimensions the solution is

$$n(\mathbf{r},t) = \frac{1}{(4\pi Dt)^{3/2}} e^{-\mathbf{r}^2/4Dt}. \tag{2.6}$$

Eq. (2.6) describes the one particle probability density at arbitrary time t and position $\mathbf{r}$ due to an initial delta distribution.

2.1.1 Specific intensity

The one particle probability density can be converted to the specific intensity, commonly used in transport theory of light[21]. The specific intensity is defined as the average power flux density within a unit frequency band centred at frequency ν within a unit solid angle in the direction defined by the unit vector $\hat{\mathbf{s}}$,

$$I(\mathbf{r},\hat{\mathbf{s}}) = \left[\frac{\text{Joule}}{dSd\Omega d\nu dt}\right], \tag{2.7}$$

with dS, $d\Omega$, $d\nu$ and dt respectively the unit area, solid angle, frequency and time. In this thesis the unit energy is implicitly assumed, and the frequency is integrated over in the specific intensity. The unit of the specific intensity becomes per meter squared per second per steradian. With the specific intensity we can define the average intensity and the energy density respectively as,

$$I(\mathbf{r}) \equiv \frac{1}{4\pi}\int_{4\pi} I(\mathbf{r},\hat{\mathbf{s}})\mathrm{d}\Omega, \tag{2.8}$$

and

$$u(\mathbf{r}) \equiv \frac{1}{v}\int_{4\pi} I(\mathbf{r},\hat{\mathbf{s}})\mathrm{d}\Omega, \tag{2.9}$$

with v the speed of light in the medium. Later we will use v_E, the energy transfer velocity, for the speed of light in the medium. Since the energy density $u(\mathbf{r})$ is analogous to the particle density $n(\mathbf{r},t)$, the following intensity distribution is found from Eqs. (2.6, 2.8, 2.9),

$$I(\mathbf{r},t)=\frac{v}{4\pi}\frac{1}{(4\pi Dt)^{3/2}}e^{-\mathbf{r}^2/4Dt}, \tag{2.10}$$

with as isotropic source,

$$I(\mathbf{r},t=0)=\frac{v}{4\pi}\delta(\mathbf{r}). \tag{2.11}$$

2.2 The wave equation with disorder

In the previous section Eq. (2.10) describes classical diffusion of light, based on a particle picture. We will turn to the wave picture of light and derive light diffusion from a wave equation with disorder. In this section we will introduce the scattering of waves by a single particle, and derive an important conservation law, the optical theorem. The light waves will be treated as scalar waves. The scalar wave equation is

$$\nabla^2\Psi(\mathbf{r},t)-\frac{\varepsilon(\mathbf{r})}{c^2}\frac{\partial^2}{\partial t^2}\Psi(\mathbf{r},t)=0, \tag{2.12}$$

with c the speed of light in the vacuum and $\varepsilon(\mathbf{r})$ the dielectric constant. The dielectric constant is a function of the disorder in the medium. The dielectric constant can be split into two parts, a constant part, and a part that depends on the disorder, $\varepsilon(\mathbf{r})\equiv\varepsilon+(\varepsilon(\mathbf{r})-\varepsilon)$ where ε is the dielectric constant outside the scatterer. For simplicity we assume the dielectric constant outside the scatterer to be unity. The classical wave equation can be made time independent by taking monochromatic waves, $\Psi(\mathbf{r},t)=\mathrm{Re}\Psi(\mathbf{r})e^{iEt}$, where E stands for the internal frequency of the waves. The wave equation becomes,

$$-\nabla^2\Psi(\mathbf{r})-\frac{E^2}{c^2}\Psi(\mathbf{r})=V(\mathbf{r})\Psi(\mathbf{r}), \tag{2.13}$$

with $V(\mathbf{r})=\frac{E^2}{c^2}(\varepsilon(\mathbf{r})-1)$. Note that the potential $V(\mathbf{r})$ depends on the frequency of the wave. This is an important difference from the scattering of electron waves, since for electrons the potential does not depend on the frequency of the waves.

2.2.1 Fields, intensity and units

The energy density and the current density associated with the scalar wave equation Eq. (2.13) in homogeneous media are respectively[22],

$$W=\frac{\varepsilon\varepsilon_0}{2}\left|\frac{\partial\Psi}{\partial t}\right|^2+\frac{1}{2\mu_0}\left|\nabla\Psi\right|^2; \qquad \mathbf{J}=\frac{1}{\mu_0}\mathrm{Im}\left[\left(\frac{\partial\Psi}{\partial t}\right)^*\nabla\Psi\right]. \tag{2.14}$$

One can make the identification with the electromagnetic fields,

$$\left|\vec{E}\right|=\frac{\partial\Psi}{\partial t}; \qquad \vec{B}=\nabla\Psi, \tag{2.15}$$

where the field Ψ has units volts second per meter Applying the slowly varying wave approximation and cycle averaging, the current density, which is the specific intensity, becomes,

$$I(\mathbf{r},\hat{\mathbf{s}}) = \eta\Psi(\mathbf{r})\Psi^*(\mathbf{r}) \quad \left[\frac{J}{m^2 s}\right]; \qquad \eta = \frac{\varepsilon_0 c^2 E^2}{2v_\phi} \quad \left[\frac{J}{V^2 s^3}\right], \qquad \hat{\mathbf{s}} = \frac{\mathbf{k}}{|\mathbf{k}|}, \tag{2.16}$$

with E the internal frequency of the waves, $\mathbf{k}$ the wave vector of the waves, c/v_ϕ the refractive index, and v_ϕ the phase velocity. For convenience the units volt second of the scalar waves are omitted throughout this thesis. This gives us the following units,

$$\Psi = \left[\frac{1}{m}\right] \qquad \eta = \left[\frac{J}{s}\right] \qquad \epsilon = [s] \qquad \eta\epsilon = [J], \tag{2.17}$$

where ϵ is a unit time that we will use later. The unit power is η and the unit energy is $\eta\epsilon$. The intensity is thus simply expressed as,

$$I = \Psi\Psi^* \quad \text{in units } \eta. \tag{2.18}$$

2.2.2 Free space propagator

The free space propagator $g(\mathbf{r})$ is the solution of the wave equation in the absence of scatterers,

$$-\nabla^2 g(\mathbf{r}) - \frac{E^2}{c^2} g(\mathbf{r}) = \delta(\mathbf{r}). \tag{2.19}$$

The solution is found by a Fourier transform of the above equation,

$$\int e^{i\mathbf{pr}} \left(\nabla^2 g(\mathbf{r}) - \frac{E^2}{c^2} g(\mathbf{r}) - \delta(\mathbf{r})\right) \mathrm{d}\mathbf{r} = 0, \tag{2.20}$$

resulting in,

$$(\mathbf{p}^2 - \frac{E^2}{c^2}) \int \mathrm{d}\mathbf{r} g(\mathbf{r}) e^{i\mathbf{pr}} = 1, \quad \Rightarrow \quad g(\mathbf{p}) = \frac{1}{\mathbf{p}^2 - E^2/c^2}, \tag{2.21}$$

and after transforming to real space,

$$g(\mathbf{r}) = \frac{e^{iE|\mathbf{r}|/c}}{4\pi|\mathbf{r}|}. \tag{2.22}$$

2.2.3 The t-matrix

With the help of the green's function in Eq. (2.22) we can write an iterating solution for the wave function in the presence of one scatterer,

$$\Psi(\mathbf{r}) = \Psi_0(\mathbf{r}) + \int \mathrm{d}\mathbf{r}' g(\mathbf{r}-\mathbf{r}') V_\alpha(\mathbf{r}') \Psi(\mathbf{r}'), \tag{2.23}$$

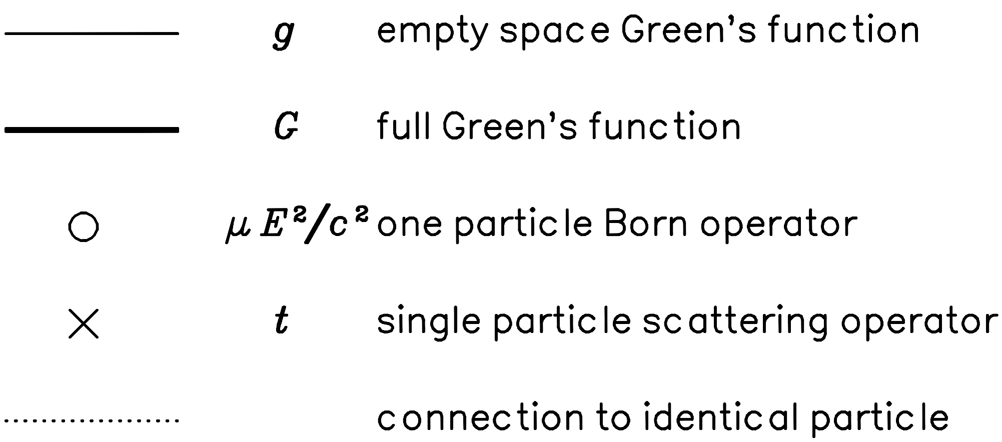

Figure 2.1: *Symbols in figures*

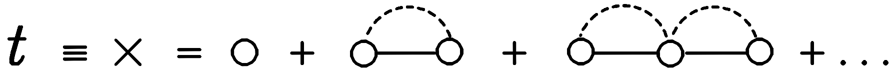

Figure 2.2: *Series of recurrent scattering from the same scatterer.*

where $\Psi_0(\mathbf{r})$ is a homogeneous solution of the differential equation Eq. (2.13), and $V_\alpha(\mathbf{r})$ is the potential of the scatterer with index α. Iteration of Eq. (2.23) gives an explicit sum of scattering events, each term in the series represents a higher order scattering contribution of the same scatterer. The solution can be written as,

$$\Psi(\mathbf{r}) = \Psi_0(\mathbf{r}) + \int g(\mathbf{r},\mathbf{r}_1)t_\alpha(\mathbf{r}_1,\mathbf{r}_2,E)\Psi_0(\mathbf{r}_2)\mathrm{d}\mathbf{r}_1\mathrm{d}\mathbf{r}_2, \tag{2.24}$$

with the scattering matrix $t_\alpha(\mathbf{r}_1,\mathbf{r}_2,E)$ representing the series,

$$\begin{aligned} t_\alpha(\mathbf{r}_1,\mathbf{r}_2,E) &= V_\alpha(\mathbf{r}_1)\delta(\mathbf{r}_1-\mathbf{r}_2) + V_\alpha(\mathbf{r}_1)g(\mathbf{r}_1,\mathbf{r}_2)V_\alpha(\mathbf{r}_2) + \\ &\int V_\alpha(\mathbf{r}_1)g(\mathbf{r}_1,\mathbf{r}')V_\alpha(\mathbf{r}')g(\mathbf{r}',\mathbf{r}_2)V_\alpha(\mathbf{r}_2)\mathrm{d}\mathbf{r}' + \cdots, \end{aligned} \tag{2.25}$$

known as the Born series. The dependence on the frequency of the t-matrix comes about through the dependence of the potential V on E. In Fig. (2.1) the graphical definition of symbols used in drawing diagrams is given. The series Eq. (2.25) is graphically depicted in Fig. (2.2). The Fourier transform of Eq. (2.24) is given by,

$$\Psi(\mathbf{p}) = \Psi_0(\mathbf{p}) + \frac{1}{(2\pi)^6}\int g(\mathbf{p},\mathbf{p}_2)t_\alpha(\mathbf{p}_2,\mathbf{p}_1,E)\Psi_0(\mathbf{p}_1)\mathrm{d}\mathbf{p}_2\mathrm{d}\mathbf{p}_1, \tag{2.26}$$

with

$$g(\mathbf{p},\mathbf{p}') = \frac{\delta(\mathbf{p}-\mathbf{p}')}{\mathbf{p}^2 - E^2/c^2}; \qquad t_\alpha(\mathbf{p},\mathbf{p}',E) = \int t_\alpha(\mathbf{r},\mathbf{r}',E)e^{-i\mathbf{pr}}e^{i\mathbf{p}'\mathbf{r}'}\mathrm{d}\mathbf{r}\mathrm{d}\mathbf{r}'. \tag{2.27}$$

A closer look at Eqs.(2.26) and (2.27) reveals the physical meaning of $t(\mathbf{p},\mathbf{p}',E)$. Suppose as the homogeneous solution $\Psi_0(\mathbf{r}) = e^{-iE\hat{\mathbf{s}}\mathbf{r}/c}$ with $\hat{\mathbf{s}}$ a unit vector in the direction of the travelling wave, then $\Psi_0(\mathbf{p}') = (2\pi)^3\delta(\mathbf{p}' - E\hat{\mathbf{s}}/c)$. The scattering matrix $t(\mathbf{p}'', \mathbf{p}', E)$ in Eq. (2.26) gives the transfer of incoming wave vector $\mathbf{p}'$ to the outgoing wave vector $\mathbf{p}''$ by a single particle. The Green's function $g(\mathbf{p}, \mathbf{p}'')$ describes the propagation of this outgoing wave. The Green's function peaks around the value $|\mathbf{p}| = |\mathbf{p}'| = E/c$. The resulting solution $\Psi(\mathbf{p})$ is a function of $\mathbf{p}$ with a contribution from the unscattered wave (a delta function) and a contribution from the scattered wave that peaks around the value $|\mathbf{p}| = E/c$. In general $t(\mathbf{p}, \mathbf{p}', E)$ is a complicated function of the shape and size of the scattering particle. In 1908 Mie found the solution of the t-matrix for a spherical particle and for vector waves *half on-shell*, i.e. $|\mathbf{p}_{in}| = E/c$. The solution of the on-shell part of the t-matrix for s-wave scattering (i.e. isotropic scattering) of a particle with radius a is given by[23],

$$t(|\mathbf{p}_{out}| = \frac{E}{c}, |\mathbf{p}_{in}| = \frac{E}{c}, E) = \left(\frac{4\pi c e^{-2iaE/c}}{mE\cot(maE/c) - iE} - \frac{4\pi c e^{-iaE/c}\sin(aE/c)}{E} \right), \tag{2.28}$$

where m is the ratio between the refractive index inside and outside the sphere. The on-shell t-matrix of the spherical particle has a resonance when the cotangent approaches zero[24]. The first resonance appears at the internal frequency $E_{res} = \frac{\pi c}{2ma}$. However the full t-matrix of a finite size particle is not available and we restrict ourself to point scatterers, and develop a multiple scattering theory based on the t-matrix of the point scatterer.

For point scatterers the fluctuating part of the dielectric constant is given by,

$$\varepsilon(\mathbf{r}) - 1 = \sum_\alpha \delta(\mathbf{r} - \mathbf{R}_\alpha)\mu, \tag{2.29}$$

with μ a constant of dimension volume. For a single point scatterer this leads to $V_\alpha(\mathbf{r}) = V\delta(\mathbf{r} - \mathbf{R}_\alpha)$, with $\mathbf{R}_\alpha$ the position of the scatterer and $V \equiv \frac{\mu E^2}{c^2}$. The Born series Eq. (2.25) reduces to,

$$\begin{aligned} t_\alpha(\mathbf{r}_1, \mathbf{r}_2, E) &= \delta(r_1 - \mathbf{R}_\alpha)\delta(\mathbf{r}_2 - \mathbf{R}_\alpha) \times \\ &[V + Vg(\mathbf{R}_\alpha, \mathbf{R}_\alpha)V + Vg(\mathbf{R}_\alpha, \mathbf{R}_\alpha)Vg(\mathbf{R}_\alpha, \mathbf{R}_\alpha)V + \cdots]. \end{aligned} \tag{2.30}$$

The closed form expression for the Born series in Eq. (2.30) is,

$$t_\alpha(\mathbf{r}_1, \mathbf{r}_2, E) = \delta(r_1 - \mathbf{R}_\alpha)\delta(\mathbf{r}_2 - \mathbf{R}_\alpha)\frac{V}{1 - Vg(\mathbf{R}_\alpha, \mathbf{R}_\alpha)}. \tag{2.31}$$

In the remainder of this section the index α is dropped.

2.2.4 Second order Born approximation to a point scatterer

There exist a problem with the Born series. The Green's function $g(\mathbf{r}, \mathbf{r}')$ goes to infinity in the limit $\mathbf{r}' \to \mathbf{r}$, and the series for $t(\mathbf{r}_1, \mathbf{r}_2, E)$ in Eq. (2.30) goes to infinity, while the closed form expression in Eq. (2.31) goes to zero. This makes the Born series useless. An often used approximation is to retain only the first two terms of the Born series, and to neglect the infinite real part of the expansion of $g(\mathbf{r}, \mathbf{r}')$ around $\mathbf{r} = \mathbf{r}'$,

$$\lim_{\mathbf{r}\to 0} g(\mathbf{r}) = \lim_{\mathbf{r}\to 0} \frac{1}{4\pi|\mathbf{r}|} + \frac{iE}{4\pi c} \quad \Rightarrow \quad \frac{iE}{4\pi c}, \tag{2.32}$$

$$\begin{aligned} t(\mathbf{r}_1, \mathbf{r}_2, E) &\approx \delta(r_1 - \mathbf{R})\delta(\mathbf{r}_2 - \mathbf{R}) \left(V + iV^2 \mathrm{Im}(g(\mathbf{R}, \mathbf{R}))\right) \\ &\approx \delta(r_1 - \mathbf{R})\delta(\mathbf{r}_2 - \mathbf{R}) \left(V + V^2 \frac{iE}{4\pi c}\right). \end{aligned} \tag{2.33}$$

This is known as the second order Born approximation. One also can sum the series in Eq. (2.30) neglecting the real part of Eq. (2.32), giving the closed form for the scattering matrix t (known as the Fermi-Wu Approximation),

$$t(\mathbf{r}_1, \mathbf{r}_2, E) = \delta(r_1 - \mathbf{R})\delta(\mathbf{r}_2 - \mathbf{R}) t(E) \quad \text{with} \quad t(E) = \frac{V}{1 - \frac{iVE}{4\pi c}}. \tag{2.34}$$

As will be shown in the next section the last expression obeys the optical theorem for all orders in V, while Eq. (2.33) obeys the optical theorem only to second order in V. The closed form of the t-matrix in the Fourier representation is,

$$t(\mathbf{p}, \mathbf{p}', E) = e^{i\mathbf{R}(\mathbf{p}' - \mathbf{p})} t(E) \quad \text{with} \quad t(E) = \frac{V}{1 - \frac{iVE}{4\pi c}}. \tag{2.35}$$

The price we have paid for restricting ourselves to point scatterers is the absence of resonances in the t-matrix. In section 2.5 it will be shown that resonances in the t-matrix can strongly influence energy transport of light. Nieuwenhuizen *et al.*[25] have shown that the first resonance of the on-shell t-matrix in Eq. (2.28) can be build into the t-matrix of the point scatterer. We will not go into details, but only give this t-matrix for didactic purposes.

$$t(\mathbf{r}_1, \mathbf{r}_2, E) = \delta(r_1 - \mathbf{R})\delta(\mathbf{r}_2 - \mathbf{R}) \left(\frac{V_{eff}}{1 - V_{eff} \frac{iE}{4\pi c}} \right), \quad \text{with} \quad V_{eff} = \frac{V}{1 - E^2/E_{res}^2}. \tag{2.36}$$

2.2.5 Optical theorem

In this section the cross sections of a single scatterer and the connection with the t-matrix is derived. A conservation law (the amount of light scattered out of a beam by a lossless scatterer is equal to the amount of scattered light) leads to a relation between the square of the absolute value of the t-matrix and the complex part of the t-matrix, the optical theorem. The scattering cross section σ_{sc} and the extinction cross section σ_{ex} are defined in Eq. (2.39) and Eq. (2.42) [26, 16]. The scattering cross section σ_{sc} can be interpreted as the area perpendicular to the incoming flux through which the same intensity flows as scattered intensity flows through a sphere around the scatterer. The radius of the sphere is assumed to be much larger than the wavelength (far-field approximation) and the scattering is assumed to be isotropic (the scattered amplitude is independent of the direction). The total amplitude is given by Eq. (2.24) ($\Psi_{inc} = \Psi_0$),

$$\Psi(\mathbf{r}) = \Psi_{inc}(z) + \Psi_{sc}(\mathbf{r}), \tag{2.37}$$

with $\Psi_{inc}(\mathbf{r}) = e^{iEz/c}$ and $\Psi_{sc}(\mathbf{r})$ the wave scattered by the scatterer (assuming the scatterer in the origin),

$$\Psi_{sc}(\mathbf{r}) = \frac{e^{iEr/c}}{4\pi r} t(E) \quad \text{far-field approximation } r \gg \lambda. \tag{2.38}$$

The incoming amplitude Ψ_{inc} does not give a contribution to the flux through the sphere, so the scattering cross section is given by,

$$\sigma_{sc} \equiv \int_{4\pi} \Psi^*_{sc}(r)\Psi_{sc}(r) r^2 \mathrm{d}\Omega = \int_{4\pi} r^2 \frac{t(E)t^*(E)}{(4\pi r)^2} \mathrm{d}\Omega = \frac{t(E)t^*(E)}{4\pi}. \tag{2.39}$$

The extinction cross section σ_{ex} describes the amount of intensity that has disappeared from the incoming plane wave incident from $z = -\infty$. The intensity through a plane of area A perpendicular to the z-axis far away from the position of the scatterer is integrated and compared to the flux in the absence of the scatterer. The difference gives the extinction cross section. Far away from the origin and in the neighbourhood of the z-axis $\mathbf{r}$ can be approximated, $\mathbf{r} \approx z + (x^2 + y^2)/2z$, and the amplitude is,

$$\Psi(\mathbf{r}) \approx e^{iEz/c} + t(E)\frac{e^{iEz/c}}{4\pi z} e^{iE(x^2+y^2)/2zc}. \tag{2.40}$$

The intensity for large z is,

$$\Psi^*(\mathbf{r})\Psi(\mathbf{r}) \approx 1 + \mathrm{Re}\left(\frac{t(E)}{2\pi z} e^{iE(x^2+y^2)/2zc}\right), \tag{2.41}$$

where the term that decays with z^{-2} has been neglected. The extinction cross section is,

$$\sigma_{ex} \equiv \int_A -\mathrm{Re}\left(\frac{t(E)}{2\pi z} e^{iE(x^2+y^2)/2zc}\right) \mathrm{d}x\mathrm{d}y = \frac{c\,\mathrm{Im}\,t(E)}{E}. \tag{2.42}$$

The extinction cross section is the area over which the incoming intensity has to be integrated to remove the same amount of intensity out of the incident wave as in the presence of the scatterer. The albedo a is defined as the ratio of the scattered intensity and the removed intensity,

$$a = \frac{\sigma_{sc}}{\sigma_{ex}}. \tag{2.43}$$

If there is no absorption (albedo $a = 1$) the scattered intensity and the removed intensity should be equal, so $\sigma_{sc} = \sigma_{ex}$. This is called the optical theorem, and leads with Eqs. 2.39 and 2.42 to the equality

$$\frac{t(E)t^*(E)}{4\pi} = \frac{c\,\mathrm{Im}\,t(E)}{E}. \tag{2.44}$$

It can easily be verified that the closed form of the t-matrix (Eq. (2.34)) obeys the optical theorem to all orders in V. In the case of absorption ($a < 1$) the absorption cross section can be defined as,

$$\sigma_{abs} \equiv \sigma_{ex} - \sigma_{sc}, \tag{2.45}$$

and gives the area over which to integrate the incoming intensity to get the absorbed intensity. The optical theorem does not hold anymore and one finds instead of Eq. (2.44),

$$\frac{t(E)t^*(E)}{4\pi} = \frac{ac\,\mathrm{Im}\,t(E)}{E}. \tag{2.46}$$

2.3 Waves in the multiple scattering regime

In the previous sections the free space propagator and the scattering properties of a single point scatterer were derived. In this section we extend the theory to the multiple scattering regime. The full Green's function, that describes the propagation in the presence of many scatterers, is derived, and the recurrent scattering from the same particle is discussed. At the end a relation between the mean free path ℓ and the t-matrix is found in the lowest order in the density.

2.3.1 The full Green's function

First the propagator in the presence of many scatterers is sought. The full Green's function is the solution of the following equation,

$$-\nabla^2 G(\mathbf{r},\mathbf{r}') - [\frac{E^2}{c^2} + \sum_\alpha V_\alpha(\mathbf{r})]G(\mathbf{r},\mathbf{r}') = \delta(\mathbf{r}-\mathbf{r}'). \tag{2.47}$$

The scattering properties of a single particle are known. The solution to the above equation can be written as a series of scattering from the particles in the volume,

$$\begin{aligned} G(\mathbf{r},\mathbf{r}') = g(\mathbf{r},\mathbf{r}') + \sum_\alpha \int g(\mathbf{r},\mathbf{r}_1)t_\alpha(\mathbf{r}_1,\mathbf{r}_2)g(\mathbf{r}_2,\mathbf{r}')\mathrm{d}\mathbf{r}_1\mathrm{d}\mathbf{r}_2 + \\ \sum_{\alpha\neq\beta} \int g(\mathbf{r},\mathbf{r}_1)t_\alpha(\mathbf{r}_1,\mathbf{r}_2)g(\mathbf{r}_2,\mathbf{r}_3)t_\beta(\mathbf{r}_3,\mathbf{r}_4)g(\mathbf{r}_4,\mathbf{r}')\mathrm{d}\mathbf{r}_1\mathrm{d}\mathbf{r}_2\mathrm{d}\mathbf{r}_3\mathrm{d}\mathbf{r}_4 + \cdots. \end{aligned} \tag{2.48}$$

where the greek indices label different particles. The series is graphically depicted in Fig. (2.3).

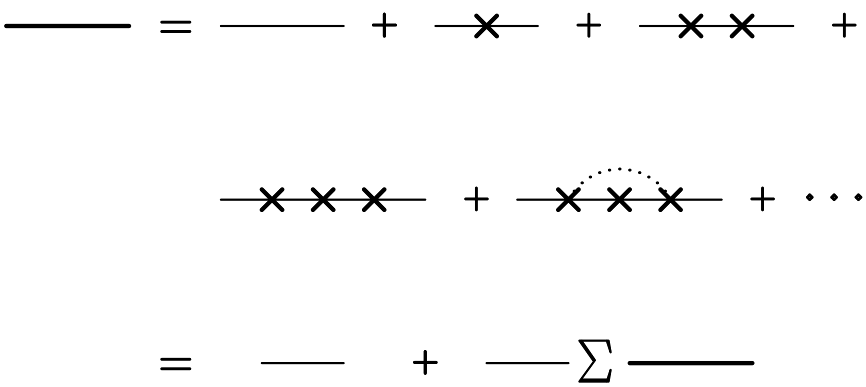

Figure 2.3: *Series for the full Green's function*

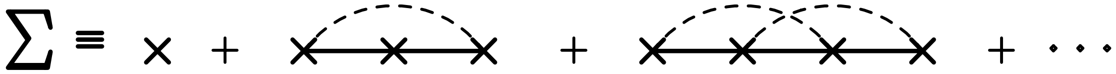

Figure 2.4: *Series of the mass operator* Σ

2.3.2 The mass operator

Introducing the mass or self energy operator, $\Sigma(\mathbf{r},\mathbf{r}')$, Eq. (2.48) can be written as an iterating equation,

$$G(\mathbf{r},\mathbf{r}') = g(\mathbf{r},\mathbf{r}') + \int g(\mathbf{r},\mathbf{r}_1)\Sigma(\mathbf{r}_1,\mathbf{r}_2)G(\mathbf{r}_2,\mathbf{r}')\mathrm{d}\mathbf{r}_1 d\mathbf{r}_2, \tag{2.49}$$

with the mass operator defined as,

$$\Sigma(\mathbf{r},\mathbf{r}') = \sum_{\alpha} t_\alpha(\mathbf{r},\mathbf{r}') + \\ \int \sum_{\alpha\neq\beta} t_\alpha(\mathbf{r},\mathbf{r}_1)g(\mathbf{r}_1,\mathbf{r}_2)t_\beta(\mathbf{r}_2,\mathbf{r}_3)g(\mathbf{r}_3,\mathbf{r}_4)t_\alpha(\mathbf{r}_4,\mathbf{r}')\mathrm{d}\mathbf{r}_1\mathrm{d}\mathbf{r}_2\mathrm{d}\mathbf{r}_3\mathrm{d}\mathbf{r}_4 \ + \ \cdots. \tag{2.50}$$

The mass operator can be interpreted as the interaction part of a Hamiltonian. Fig. (2.4) gives the different contributions the mass operator, irreducible parts that can be written fully in terms of t-matrices. The average Green's function is now given by,

$$\langle G(\mathbf{r},\mathbf{r}')\rangle = \langle g(\mathbf{r},\mathbf{r}')\rangle + \int \langle g(\mathbf{r},\mathbf{r}_1)\rangle\langle\Sigma(\mathbf{r}_1,\mathbf{r}_2)\rangle\langle G(\mathbf{r}_2,\mathbf{r}')\rangle\mathrm{d}\mathbf{r}_1\mathrm{d}\mathbf{r}_2, \tag{2.51}$$

Angular brackets denote averaging over the disorder. Averaging is done by integrating over the positions of all scatterers and dividing by the volume to the power of the number of scatterers. Since the averaged Green's functions and the mass operator have to be translationally invariant, they can be defined as,

$$\langle g(\mathbf{r},\mathbf{r}')\rangle \equiv g(\mathbf{r}-\mathbf{r}'); \qquad \langle G(\mathbf{r},\mathbf{r}')\rangle \equiv G(\mathbf{r}-\mathbf{r}'); \quad \langle \Sigma(\mathbf{r},\mathbf{r}')\rangle \equiv \Sigma(\mathbf{r}-\mathbf{r}'). \tag{2.52}$$

and in the Fourier domain the integral equation Eq. (2.51) is given by,

$$G(\mathbf{p}) = g(\mathbf{p}) + g(\mathbf{p})\Sigma(\mathbf{p})G(\mathbf{p}), \tag{2.53}$$

which leads to the result,

$$G(\mathbf{p}) = [g(\mathbf{p})^{-1} - \Sigma(\mathbf{p})]^{-1} = [\mathbf{p}^2 - E^2/c^2 - \Sigma(\mathbf{p})]^{-1}. \tag{2.54}$$

2.3.3 The full Green's function in real space

The full Green's function describes the propagation of the amplitude in the medium. The pole of the full Green's function in Eq. (2.54) has shifted with respect to the pole of the free space propagator (Eq. (2.21)). The real part of the mass operator shifts the pole to a larger wave vector, i.e. to smaller wavelengths, due to the average refractive index of the medium. The imaginary part of the mass operator leads to an exponential decay of the full Green's function in real space caused by the scattering of the amplitude out of the propagation direction. To show this explicitly first an approximate expression for the averaged mass operator is derived,

$$\langle\Sigma(\mathbf{r},\mathbf{r}')\rangle = \int_V \prod_\alpha \frac{\mathrm{d}\mathbf{R}_\alpha}{V}\Big(\sum_\alpha t_\alpha(\mathbf{r},\mathbf{r}') +$$
$$\sum_{\alpha\neq\beta}\int t_\alpha(\mathbf{r},\mathbf{r}_1)g(\mathbf{r}_1,\mathbf{r}_2)t_\beta(\mathbf{r}_2,\mathbf{r}_3)g(\mathbf{r}_3,\mathbf{r}_4)t_\alpha(\mathbf{r}_4,\mathbf{r}')\mathrm{d}\mathbf{r}_1\mathrm{d}\mathbf{r}_2\mathrm{d}\mathbf{r}_3\mathrm{d}\mathbf{r}_4 + \cdots\Big). \tag{2.55}$$

with V the volume that is integrated over, the summation is over the particles in the volume and $\mathbf{R}_\alpha$ is the position of particle α. Included in the definition of the mass operator are all scattering events, including these events where the wave is scattered from one particle to another and back, i.e. recurrent scattering from the same particle. The recurrent scattering contributions are of higher order in the density, and their inclusion in the mass operator leads to more and complex diagrams in the intensity propagator[27]. We restrict ourselves to a mass operator up to linear order in the density, and derive the intensity propagator based on this mass operator in section 2.4. The mass operator is approximated by the first term in Eq. (2.55),

$$\langle\Sigma(\mathbf{r},\mathbf{r}',E)\rangle \approx \int \prod_\alpha \frac{\mathrm{d}\mathbf{R}_\alpha}{V}\Big(\sum_\alpha t(E)\delta(\mathbf{r}-\mathbf{R}_\alpha)\delta(\mathbf{r}'-\mathbf{R}_\alpha)\Big) = nt(E)\delta(\mathbf{r}-\mathbf{r}'), \tag{2.56}$$

with n the density of the scatterers. The explicit expression of the mass operator in Eq. (2.56) in the Fourier domain does not depend on $\mathbf{p}$,

$$\Sigma(\mathbf{p}) = nt(E). \tag{2.57}$$

The real space full Green's function, as derived from Eq. (2.54), is,

$$G(\mathbf{r}) = \frac{e^{iK|r|}}{4\pi|r|}, \tag{2.58}$$

with

$$K \equiv \sqrt{E^2/c^2 + \Sigma(E)} = \sqrt{E^2/c^2 + nt(E)} \equiv k + \frac{i}{2\ell}, \tag{2.59}$$

with ℓ the mean free path in the medium. To linear order in the density k and ℓ are found by expanding the square root in the above equation,

$$k = \frac{E}{c}\left(1 + \frac{nc^2 \mathrm{Re}\, t(E)}{2E^2}\right); \qquad \ell = \frac{E}{nc\,\mathrm{Im}\, t(E)} = \frac{1}{n\sigma_{ex}}. \tag{2.60}$$

The real part of the average refractive index leads to a new wave vector k in the medium, due to the real part of the t-matrix. The imaginary part of the t-matrix is connected with the mean free path in the medium. The mean free path, and thus the imaginary part of the t-matrix, describes the exponential decay of the propagating wave by scattering out of its propagation direction. The amplitude propagator decays exponentially, i.e. has a short range, and does not lead to long range diffusion. Using Eq. (2.42) the mean free path in Eq. (2.60) is expressed in the density and the extinction cross section. Finally the optical theorem Eq. (2.46) and Eq. (2.60) are used to find a very useful relation between the density times the square of the absolute value of the t-matrix and the mean free path,

$$nt(E)t^*(E) = \frac{4\pi a}{\ell}. \tag{2.61}$$

2.3.4 Coherent intensity

To show that the results for the wave propagation in the disordered regime do *not* lead to diffusion of the intensity, we will apply the results of the previous section to a plane wave falling on a semi-infinite disordered medium in the half space $z > 0$. Using the full Green's function the average amplitude in a semi-infinite medium originating from a plane wave coming from $z = -\infty$, $\Psi_{inc}(\mathbf{r}) = e^{iEz/c}$ is,

$$\langle \Psi(\mathbf{r}) \rangle = \Psi_{inc}(\mathbf{r}) + \int_{z \geq 0} G(\mathbf{r}, \mathbf{r}') nt(E) \Psi_{inc}(\mathbf{r}') \mathrm{d}\mathbf{r}'. \tag{2.62}$$

Since the problem is translationally invariant in the x and y direction, these coordinates can be integrated out of the Green's function.

$$G(z, z') = \int_{-\infty}^{\infty} \mathrm{d}x \mathrm{d}y \frac{e^{iK(x^2+y^2+(z-z')^2)^{1/2}}}{4\pi(x^2+y^2+(z-z')^2)^{1/2}} = \frac{i}{2K} e^{iK|z-z'|}. \tag{2.63}$$

For the average amplitude at depth z we find,

$$\langle \Psi(z) \rangle = e^{iEz/c} + \int_{z' \geq 0} \mathrm{d}z' \frac{ie^{iK|z-z'|}}{2K} nt(E) e^{iEz'/c} = \frac{E/c + K}{2K} e^{iKz}. \tag{2.64}$$

To first order in the density the amplitude of the transmitted wave at $z = 0$ in Eq. (2.64) is equal to the fresnel coefficient[28]. The average amplitude leads to the average coherent intensity at depth z, $I_{coh}(z)$,

$$I_{coh}(z) \equiv \langle \Psi(z) \rangle \langle \Psi^*(z) \rangle = \frac{(E/c + K)(E/c + K^*)}{4KK^*} e^{iz(K-K^*)} \approx e^{-z/\ell}. \tag{2.65}$$

The above intensity does not describe the diffusion of the light, nor does it describe the diffuse intensity. It gives the exponential decay of the impinging coherent intensity, known as Lambert-Beer's law. Apparently to find diffusion we cannot start from the average amplitude in the medium. To describe the diffuse intensity we have to develop a multiple scattering theory on the intensity level, which shall first be done for the infinite medium. In section 2.6 we return to the semi-infinite medium .

2.4 Intensity in the multiple scattering regime

From the previous section it is clear that a multiple scattering theory on the amplitude level does not describe the diffuse intensity, nor does it lead to diffusion of the light. Multiple scattered amplitudes having travelled along different paths do not give a net contribution to the averaged intensity, since their phases are random because of different path lengths. To obtain the diffuse intensity, one has to calculate the product of the amplitude and its complex conjugate and then average over the disorder $\langle \Psi(\mathbf{r})\Psi^*(\mathbf{r})\rangle$. In this section the intensity propagator in the stationary case is derived. Diagrams are constructed of paired amplitudes, that in lowest order in the density lead to the so called "Ladder vertex", describing the diffuse propagation[17]

2.4.1 Intensity propagator

We introduce the intensity propagator R, which is the product of two full Green's functions before averaging over the disorder,

$$\langle R(\mathbf{r}_1,\mathbf{r}_2;\mathbf{r}_3,\mathbf{r}_4)\rangle \equiv \langle G(\mathbf{r}_1,\mathbf{r}_2)\times G^*(\mathbf{r}_3,\mathbf{r}_4)\rangle. \tag{2.66}$$

The intensity propagator R is given by the following expansion using the series of Eq. (2.48) for $G(\mathbf{r},\mathbf{r}')$ and the t-matrix in Eq. (2.34),

$$\begin{gathered}\langle R(\mathbf{r}_1,\mathbf{r}_2;\mathbf{r}_3,\mathbf{r}_4)\rangle = \\ \int\Big(g(\mathbf{r}_1,\mathbf{r}_2)+\sum_\alpha\Big(g(\mathbf{r}_1,\mathbf{R}_\alpha)t_\alpha(E)g(\mathbf{R}_\alpha,\mathbf{r}_2)\Big)+\cdots\Big)\times \\ \Big(g(\mathbf{r}_3,\mathbf{r}_4)+\sum_\beta\Big(g(\mathbf{r}_3,\mathbf{R}_\beta)t_\beta(E)g(\mathbf{R}_\beta,\mathbf{r}_4)\Big)+\cdots\Big)\prod_\alpha\frac{\mathrm{d}\mathbf{R}_\alpha}{V}.\end{gathered} \tag{2.67}$$

The integration over the positions of the scatterers $\mathbf{R}_\alpha$ gives the average intensity propagator. Some contributions to the series are given in Fig. (2.5). The two amplitudes can visit the same scatterer, where the dashed line identifies the same scatterers. The averaging over the position of the scatterers is after the identification of the same particles in the sequence each amplitude scatters off. The leading contributions to the series in Fig. (2.5) are given by those diagrams where the amplitude and the complex conjugate travel along the same sequence of scatterers because then their phase factors cancel exactly. The diagrams where the amplitudes

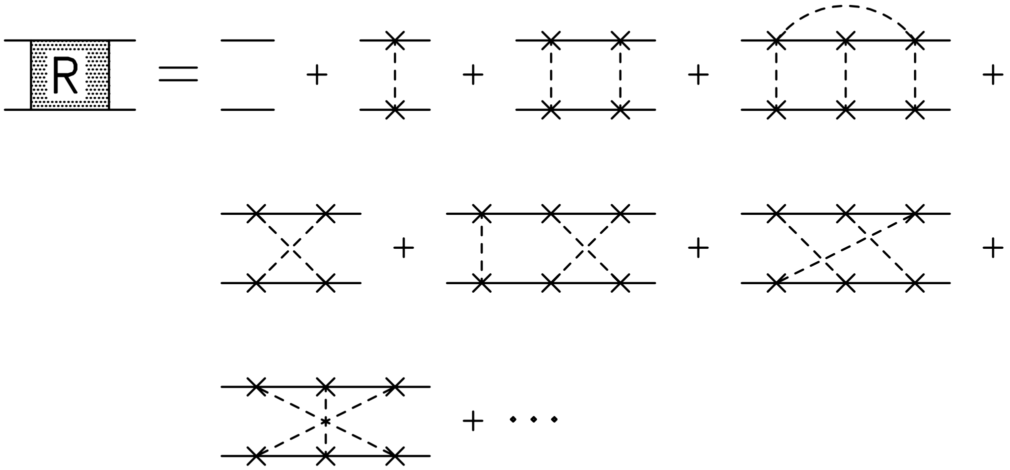

Figure 2.5: *Some contributions to the reducible series of the amplitude and its complex conjugate.*

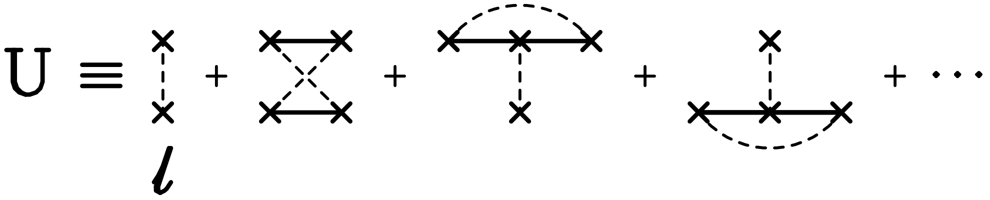

Figure 2.6: *Lowest order contributions to the irreducible vertex U.*

return to a scatterer that was already visited are of higher order in the density. The "backbone" of the series in Fig. (2.5) is given by the diagrams in Fig. (2.6). These are the "irreducible" parts U of the series in Fig. (2.5). By irreducible is meant that one cannot disentangle the diagrams by cutting across two propagators, without cutting also a dashed line. The vertex $\langle R\rangle$ can now be written as an expansion in irreducible parts,

$$\langle R\rangle = \langle G\rangle \times \langle G^*\rangle + (\langle G\rangle \times \langle G^*\rangle)\langle U\rangle\langle R\rangle. \tag{2.68}$$

2.4.2 The Ladder vertex

The manipulations in section 2.4.1 are still formal, the actual form of U is too complex and contains too many terms to do calculations with[27]. The full form of U is approximated by the first irreducible diagram in Fig. (2.6) (i.e. to lowest order in the density), denoted by $\langle l\rangle$, where $\langle l\rangle$ is given by,

$$\langle l\rangle = nt(E)t^*(E) = \frac{4\pi a}{\ell}. \tag{2.69}$$

Thus the intensity inside the disordered medium will be calculated in lowest order in the density, all diagrams where the phase factors of the Green's functions do not

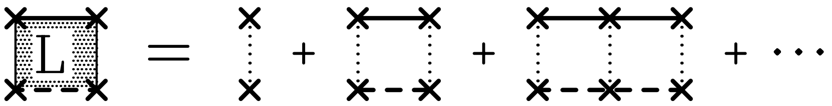

Figure 2.7: *The vertex L, an infinite sum of ladder terms (see Eq. (2.70)). The vertex L starts and ends on a scatterer.*

exactly cancel will be neglected. Among the neglected diagrams are the localization corrections to the diffuse propagation of the light[20, 29, 30, 31] The important class of diagrams known as the most crossed diagrams, responsible for the enhanced backscatter, are neglected also. For a comprehensive treatment of the most crossed diagrams, see van der Mark, van Albada and Lagendijk[18] and Ref. [32]. As is clear from the Fig. (2.5) and Eq. (2.67) the vertex $\langle R\rangle$ contains incoming and outgoing amplitude propagators. The skeleton of $\langle R\rangle$, $\langle L\rangle$ is defined as the diagrams without the incoming and outgoing amplitude propagators. The Bethe-Salpeter like equation[33] for $\langle L\rangle$ is given by,

$$\langle L\rangle = \langle \ell\rangle + \langle \ell\rangle(\langle G\rangle \times \langle G^*\rangle)\langle L\rangle. \tag{2.70}$$

The Ladder vertex $\langle L\rangle$ is graphically depicted in Fig. (2.7). In real space Eq. (2.70) is given by,

$$L(\mathbf{r}) = \frac{4\pi a}{\ell}\delta(\mathbf{r}) + \frac{4\pi a}{\ell}\int \frac{e^{-|\mathbf{r}'|/\ell}}{(4\pi\mathbf{r}')^2}L(\mathbf{r}-\mathbf{r}')\mathrm{d}\mathbf{r}'. \tag{2.71}$$

The convolution in $\mathbf{r}$-space is most easily solved by transforming to the $\mathbf{p}$-space, which results in,

$$L(\mathbf{p}) = \frac{4\pi a}{\ell} + \frac{4\pi a}{\ell} \times \frac{1}{4\pi|\mathbf{p}|}\arctan(|\mathbf{p}|\ell)L(\mathbf{p}). \tag{2.72}$$

Since we are interested in the long range behaviour, i.e. the regime where $|\mathbf{p}|\ell$ is small, the $\arctan(|\mathbf{p}|\ell)$ can be approximated by[34],

$$\arctan(x) = \frac{x}{1+\frac{1}{3}x^2}, \qquad |x| \leq 1. \tag{2.73}$$

For $L(\mathbf{p})$ this results in,

$$L(\mathbf{p}) = \frac{4\pi a}{\ell}\left(1 + \frac{3a}{3(1-a)+\mathbf{p}^2\ell^2}\right). \tag{2.74}$$

Transforming back to real space gives,

$$L(\mathbf{r}) = \frac{4\pi a}{\ell}\delta(\mathbf{r}) + \frac{3a^2\ e^{-|\mathbf{r}|/\ell_{abs}}}{\ell^3|\mathbf{r}|}, \tag{2.75}$$

with the absorption length ℓ_{abs} defined as $\ell_{abs} \equiv \ell/\sqrt{3(1-a)}$. The first term in Eq. (2.75) is the contribution from the vertex $\langle l\rangle$, the second term is the linear decay of the multiple scattered intensity inside the disordered medium. The absorption gives an exponential decay for lengths longer than the absorption length ℓ_{abs}. As can be seen in Fig. (2.7) the Ladder vertex L starts *and* ends on a scatterer. With Eq. (2.75) we have found diffusion of light in the stationary case!

2.5 The time-dependent Ladder vertex

The previous section gave the stationary state propagator of the diffuse intensity in a disordered medium. We will now introduce time in the intensity propagator. Thus we will be able to find the distribution in time and space of the diffuse intensity in response to e.g. a short pulse. Also the time dependent propagator will give us the distribution of path lengths (the time it takes) to go from point $\mathbf{r}_1$ to $\mathbf{r}_2$. In this section the time dependent full Green's function is discussed, and microscopic expressions for the phase and group velocity are derived. At the end of this section we will recover Eq. (2.10), but microscopic expressions are found for the velocity in the medium, the diffusion constant, and the absorption length. The theory in this section is based on work by van Tiggelen *et al.*[19, 31] and Kirkpatrick[20].

2.5.1 Time-dependent Bethe-Salpeter equation

To get the time dependent intensity propagator $L(\mathbf{r}, t)$, time is introduced into the Bethe-Salpeter like equation Eq. (2.70). Since time dependence is more easily handled in the frequency domain, Eq. (2.70) is Fourier transformed with ω conjugate to the time t (for the moment the explicit space dependence is suppressed),

$$L(\omega) = \langle \ell \rangle + \langle \ell \rangle [\langle G \rangle * \langle G^* \rangle](\omega) L(\omega), \tag{2.76}$$

with $[\langle G \rangle * \langle G^* \rangle](\omega)$ the convolution in the frequency domain. Since we are interested in the long time behaviour (i.e. small ω) throughout this section the frequency dependence is calculated to linear order in ω. The convolution in the frequency domain $[\langle G \rangle * \langle G^* \rangle]$ is given by,

$$\begin{aligned} [\langle G \rangle * \langle G^* \rangle](\mathbf{r}, \omega) &= \int_0^\infty e^{i(\omega + i0)t} G(\mathbf{r}, t) G^*(\mathbf{r}, t) \mathrm{d}t \\ &= \int_0^\infty \mathrm{d}t_1 \mathrm{d}t_2 \int_{-\infty}^\infty \frac{dE}{2\pi} e^{iE(t_1 - t_2)} G(\mathbf{r}, t_1) G^*(\mathbf{r}, t_2) e^{\frac{1}{2} i(w + i0)(t_1 + t_2)} \\ &= \int_{-\infty}^\infty \frac{\mathrm{d}E}{2\pi} G(\mathbf{r}, E^+) G^*(\mathbf{r}, E^-), \end{aligned} \tag{2.77}$$

where E^+ and E^- denote respectively $E + \omega/2 + i0$ and $E - \omega/2 - i0$.

2.5.2 Wave packet

First it will be shown that by introducing a source with internal frequency Ω the integration over E in Eq. (2.77) can be performed, and E is identified with the internal frequency Ω of the propagating waves. As a source a Gaussian wave packet is considered, with the source of the waves defines as,

$$S_\Psi(\mathbf{r},t) \equiv 2\,(2\pi)^{1/4}\, e^{-t^2/\epsilon^2+i\Omega t}\ \delta(\mathbf{r}); \qquad S^*_\Psi(\mathbf{r},t) \equiv 2\,(2\pi)^{1/4}\, e^{-t^2/\epsilon^2-i\Omega t}\ \delta(\mathbf{r}), \tag{2.78}$$

where Ω is the internal frequency of the waves, and ϵ is the unit time. The total energy emitted by the source is,

$$\eta \int S_\Psi(\mathbf{r},t) S^*_\Psi(\mathbf{r}',t)\mathrm{d}\mathbf{r}\mathrm{d}\mathbf{r}'\mathrm{d}t = 4\pi\eta\epsilon, \tag{2.79}$$

with η unit power and $\eta\epsilon$ unit energy. Fourier transforming the source of the waves gives,

$$\begin{aligned} S_\Psi(\mathbf{r},E) &= \int S_\Psi(\mathbf{r},t)e^{-iEt}\mathrm{d}t = 2\left(2\pi^3\right)^{1/4} \epsilon\ e^{-\epsilon^2(E-\Omega)^2/4}\ \delta(\mathbf{r}) \\ S^*_\Psi(\mathbf{r},E) &= S_\Psi(E,\mathbf{r}). \end{aligned} \tag{2.80}$$

The unscattered wave at time t (in the frequency domain) is given by,

$$\langle\Psi(\mathbf{r},\omega)\rangle = \int S_\Psi(\mathbf{r}',\omega)G(\mathbf{r}',\mathbf{r};\omega)\mathrm{d}\mathbf{r}'. \tag{2.81}$$

In analogy with Eq. (2.77) we find,

$$[\langle\Psi\rangle * \langle\Psi^*\rangle](\mathbf{r},\omega) = \int_{-\infty}^{\infty} \frac{\mathrm{d}E}{2\pi} S_\Psi(E^+)S^*_\Psi(E^-)G(\mathbf{r},E^+)G^*(\mathbf{r},E^-), \tag{2.82}$$

where the space coordinates of the sources have been integrated out. Eq. (2.82) gives the unscattered waves in the direction $\hat{\mathbf{r}}$ originating from the source. The explicit form of the source in Eq. (2.82) is,

$$S_\Psi(E^+)S^*_\Psi(E^-) = 4\left(2\pi^3\right)^{1/2} \epsilon^2\, e^{-\epsilon^2(E-\Omega)^2/2}\, e^{-\epsilon^2\omega^2/8}. \tag{2.83}$$

For sufficiently large ϵ (i.e. a broad wave packet), the source peaks strongly around the internal frequency Ω of the waves while the product of the Green's functions in Eq. (2.82) varies slowly. Thus the source can be replaced by a δ-function,

$$S_\Psi(E^+)S^*_\Psi(E^-) = 8\pi^2\epsilon\ \delta(E-\Omega)e^{-\epsilon^2\omega^2/8}. \tag{2.84}$$

Provided that $1/\omega \gg \epsilon$, i.e. time scales much longer than the duration of the source, the exponent in Eq. (2.84) is unity to linear order in ω. The condition $1/\omega \gg \epsilon$ means that only the valid time behaviour of $[\langle\Psi * \Psi^*\rangle](\mathbf{r},\omega)$ is found for times much larger than the width of the wave package. Let us calculate the total flux through a sphere of radius $\mathbf{r}$ due to the source defined in Eq. (2.78) in vacuum. The specific intensity at $\mathbf{r}$ in the direction $\hat{\mathbf{r}}$ integrated over time (i.e. $\lim \omega \to 0$) is given by,

$$\begin{aligned} \int I(\mathbf{r},\hat{\mathbf{r}})\mathrm{d}t &= \eta \lim_{\omega\to 0}[\langle\Psi\rangle * \langle\Psi^*\rangle](\mathbf{r},\omega) \\ &= \eta \lim_{\omega\to 0}\int_{-\infty}^{\infty} \frac{\mathrm{d}E}{2\pi} S_\Psi(E^+)S^*_\Psi(E^-)g(\mathbf{r},E^+)g^*(\mathbf{r},E^-) = \frac{\eta\epsilon}{4\pi\mathbf{r}^2}. \end{aligned} \tag{2.85}$$

The total flux through a sphere of radius $\mathbf{r}$ is unity in units $\eta\epsilon$. One important remark needs to be made here. In general $\eta[\langle\Psi\rangle * \langle\Psi^*\rangle](\mathbf{r},t)$ does not give the specific intensity, since the specific intensity has a direction (see Eq. (2.16)). In the above example we know where the intensity was coming from (the origin) and the interpretation as a specific intensity is justified. As the direction where the intensity is coming from is known, $\eta[\langle\Psi\rangle * \langle\Psi^*\rangle](\mathbf{r},t)$ can be interpreted as a specific intensity. In all other cases, care has to be taken. The conclusion of this subsection is that the introduction of a source with internal frequency Ω eliminates the integral over E in Eq. (2.77) and E is identified with the internal frequency Ω of the source. The Bethe-Salpeter equation Eq. (2.76) for a broad light pulse centred at internal frequency $\Omega = E$ becomes,

$$L(E,\omega,\mathbf{p}) = nt(E^+)t^*(E^-) + nt(E^+)t^*(E^-)[\langle G\rangle * \langle G^*\rangle](E,\omega,\mathbf{p})L(E,\omega,\mathbf{p}), \tag{2.86}$$

with

$$[\langle G\rangle * \langle G^*\rangle](E,\omega,\mathbf{p}) = \frac{1}{(2\pi)^3}\int G(E^+,\mathbf{p}')G^*(E^-,\mathbf{p}'-\mathbf{p})\mathrm{d}\mathbf{p}' \tag{2.87}$$

For $\langle\ell\rangle$ the time dependence implies that the t-matrices have to be evaluated at the appropriate internal frequencies $E^\pm = E \pm \omega/2$, and the following substitution was made in Eq. (2.86),

$$\langle\ell\rangle \Rightarrow nt(E^+)t^*(E^-). \tag{2.88}$$

2.5.3 Time dependent Green's function

Before solving the Bethe-Salpeter like equation (Eq. (2.86)) for the intensity propagator, we will first use the time dependent full Green's function to derive the phase and group velocity of the amplitude. The ω-dependent Green's functions are found by substituting respectively E^+ and E^- into Eq. (2.54),

$$G(E^+,\mathbf{p}) = \frac{1}{\mathbf{p}^2 - (E^+/c)^2 - nt(E^+)}; \quad G^*(E^-,\mathbf{p}) = \frac{1}{\mathbf{p}^2 - (E^-/c)^2 - nt^*(E^-)}. \tag{2.89}$$

The two poles of each Green's function are evaluated to first order in ω. The pole of the first Green's function is calculated in detail. The two poles are given by $|\mathbf{p}| = K$ with,

$$K^\pm(\omega) = \pm\left(k^2 + \frac{\omega E}{c^2} + \frac{\omega n}{2}\mathrm{Re}\frac{\partial t(E)}{\partial E} + in\mathrm{Im}\,t(E) + \frac{i\omega n}{2}\mathrm{Im}\frac{\partial t(E)}{\partial E}\right)^{1/2}, \tag{2.90}$$

where the expression for k in Eq. (2.60) was used. The square root is approximated by extracting k^2 out of the square root and using $\sqrt{1+x} \approx 1 + x/2$ for $x \ll 1$,

$$K^\pm(\omega) = \pm\left(k + \frac{\omega E}{2c^2k} + \frac{\omega n}{4k}\mathrm{Re}\frac{\partial t(E)}{\partial E} + \frac{in\,\mathrm{Im}\,t(E)}{2k} + \frac{i\omega n}{4k}\mathrm{Im}\frac{\partial t(E)}{\partial E}\right). \tag{2.91}$$

From this expression for K the phase and group velocity of the waves can be derived,

$$v_\phi = \left[\mathrm{Re}\frac{K(\omega)}{E}\right]^{-1} = \frac{E}{k} \approx c\left(1 - \frac{n\,\mathrm{Re}t(E)}{2k_0^2}\right), \tag{2.92}$$

$$v_{gr} = \left[\mathrm{Re}\frac{\partial K(\omega)}{\partial(w/2)}\right]^{-1} = \left[\frac{E}{c^2k} + \frac{n}{2k}\mathrm{Re}\frac{\partial t(E)}{\partial E}\right]^{-1} \approx \frac{c^2}{v_\phi}\left(1 - \frac{cv_\phi n}{2E}\mathrm{Re}\frac{\partial t(E)}{\partial E}\right), \tag{2.93}$$

where the approximation is made to linear order in the density. Note that since the expansion of the Green's function was made in $\omega/2$ the derivative in Eq. (2.93) is taken with respect to $\omega/2$. The pole of the complex conjugate Green's function in Eq. (2.89) is given by,

$$\overline{K}^{\pm}(\omega) = \pm\left(k - \frac{\omega E}{2c^2k} - \frac{\omega n}{4k}\mathrm{Re}\frac{\partial t(E)}{\partial E} - \frac{in\,\mathrm{Im}\,t(E)}{2k} + \frac{i\omega n}{4k}\mathrm{Im}\frac{\partial t(E)}{\partial E}\right). \tag{2.94}$$

The real space Green's functions are found by contour integration around the poles given in Eqs. (2.91) and (2.94),

$$G(E^+,\mathbf{r}) = \frac{1}{(2\pi)^3}\int \frac{e^{i\mathbf{pr}}}{\mathbf{p}^2 - (E^+/c)^2 - nt(E^+)}\mathrm{d}\mathbf{p} = \frac{e^{iK^+|\mathbf{r}|}}{4\pi|\mathbf{r}|}, \tag{2.95}$$

$$G^*(E^-,\mathbf{r}) = \frac{1}{(2\pi)^3}\int \frac{e^{-i\mathbf{pr}}}{\mathbf{p}^2 - (E^-/c)^2 - nt^*(E^-)}\mathrm{d}\mathbf{p} = \frac{e^{i\overline{K}^-|\mathbf{r}|}}{4\pi|\mathbf{r}|}. \tag{2.96}$$

2.5.4 Solving the Bethe-Salpeter equation

The time dependent vertex $L(E,\omega,\mathbf{p})$ is found by solving the frequency dependent version of the Bethe-Salpeter equation Eq. (2.86),

$$\begin{aligned} L(E,\omega,\mathbf{p}) &= nt(E^+)t^*(E^-) + \\ &\frac{nt(E^+)t^*(E^-)}{(2\pi)^3}L(E,\omega,\mathbf{p})\int G(E^+,\mathbf{p}')G^*(E^-,\mathbf{p}'{-}\mathbf{p})\mathrm{d}\mathbf{p}'. \end{aligned} \tag{2.97}$$

The solution is,

$$L(E,\omega,\mathbf{p}) = \frac{nt(E^+)t^*(E^-)}{1 - M(E,\omega,\mathbf{p})}, \tag{2.98}$$

with

$$M(E,\omega,\mathbf{p}) = \frac{nt(E^+)t^*(E^-)}{(2\pi)^3}\int G(E^+,\mathbf{p}')G^*(E^-,\mathbf{p}'{-}\mathbf{p})\mathrm{d}\mathbf{p}'. \tag{2.99}$$

To find the linear dependence on ω of $L(E,\omega,\mathbf{p})$ it is sufficient to evaluate the dependence of $M(E,\omega,\mathbf{p})$ linear in ω. The linear expansion in ω of $nt(E^+)t^*(E^-)$ gives,

$$nt(E^+)t^*(E^-) = \frac{4\pi a}{\ell}\left(1 + i\omega\mathrm{Im}\left(\frac{\partial\log t(E)}{\partial E}\right)\right), \tag{2.100}$$

where Eq. (2.61) was used. The integral in Eq. (2.99) can be evaluated in real space, since

$$\int G(E^+,\mathbf{p}')G^*(E^-,\mathbf{p}'-\mathbf{p})\mathrm{d}\mathbf{p}' = (2\pi)^3\int G(E^+,\mathbf{r})G^*(E^-,\mathbf{r})e^{i\mathbf{p}\mathbf{r}}\mathrm{d}\mathbf{r}. \tag{2.101}$$

For the kernel $M(E,\omega,\mathbf{p})$ of the time-dependent Ladder equation this leads to

$$M(E,\omega,\mathbf{p}) = \frac{\frac{a}{\ell}\left(1+i\omega\mathrm{Im}\frac{\partial\log t(E)}{\partial E}\right)}{\frac{1}{\ell}-i\omega\left(\frac{E}{c^2k}+\frac{cn}{2E}\mathrm{Re}\frac{\partial t(E)}{\partial E}\right)+\frac{1}{3}\mathbf{p}^2\ell}, \tag{2.102}$$

where $i(K^+ + \overline{K}^-)$ is used, given by,

$$i(K^+ + \overline{K}^-) = -\frac{n\mathrm{Im}\,t(E)}{k}+\frac{i\omega E}{c^2k}+\frac{i\omega n}{2k}\mathrm{Re}\frac{\partial t(E)}{\partial E} \approx \frac{-1}{\ell}+i\omega\left(\frac{E}{c^2k}+\frac{cn}{2E}\mathrm{Re}\frac{\partial t(E)}{\partial E}\right). \tag{2.103}$$

The approximation is again to linear order in the density, and the expression for ℓ in Eq. (2.60) was used. Substituting the kernel $M(E,\omega,\mathbf{p})$ in Eq. (2.98) for the Ladder this leads to,

$$L(E,\omega,\mathbf{p}) = \frac{4\pi a}{\ell}+\frac{4\pi a^2 v_E/\ell^2}{-i\omega+v_E(1-a)/\ell+\frac{1}{3}\mathbf{p}^2 v_E\ell}, \tag{2.104}$$

with the energy transport velocity v_E defined as,

$$v_E \equiv \frac{c^2}{v_\phi}\left(1-\frac{cv_\phi n}{2E}\mathrm{Re}\frac{\partial t(E)}{\partial E}-\frac{av_\phi}{\ell}\mathrm{Im}\frac{\partial\log t(E)}{\partial E}\right), \tag{2.105}$$

where the expression for the energy transport velocity was evaluated to linear order in the density. Transforming to real space and time gives the final result,

$$L(\mathbf{r},t) = \frac{4\pi a}{\ell}\delta(t)\delta(\mathbf{r})+\frac{4\pi a^2 v_E}{\ell^2(4\pi Dt)^{3/2}}e^{-t/\tau_a}e^{-\mathbf{r}^2/(4Dt)}\Theta(t), \tag{2.106}$$

with $\Theta(t)$ the Heaviside step function and with the microscopic expressions for the diffusion constant D and the absorption time τ_a,

$$D \equiv \frac{v_E\ell}{3}; \qquad \tau_a \equiv \frac{\ell}{v_E(1-a)}. \tag{2.107}$$

To summarize, we have derived the time dependent Ladder vertex Eq. (2.106) by evaluating the propagation of a wave packet with a finite spectral content. It turns out that the speed of propagation that appears in the diffusion constant is neither the group velocity nor the phase velocity, but a velocity named the energy transport velocity v_E that is a function of the wave energy dependence of the scattering properties of the scatterer. For the t-matrix in Eq. (2.33) or Eq. (2.34) the energy transport velocity reduces to the group velocity, but when the t-matrix with

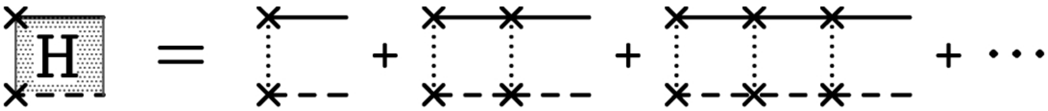

Figure 2.8: *The vertex H, on one end open (ending on Green's functions), on the other end closed (ending on a scatterer).*

an internal resonance is used (e.g. Eq. (2.36)) the energy transport velocity differs (strongly) from the phase or group velocity near the resonance of the scatterer[19]. For light a dielectric sphere can have strong resonances, and experimentally a reduction of the energy transport velocity by a factor of six compared to the vacuum velocity has been reported[9] and will be found also experimentally in chapter 4. Since the determination of the mean free path was often done by measuring the diffusion constant, a large and unexpected reduction of the speed that appears in the diffusion constant has great impact. For scatterers without a resonance (e.g. in electron scattering) the two derivatives in Eq. (2.105) cancel.

2.5.5 Intensity distribution

We have found the time-dependent propagator $L(\mathbf{r}, t)$ in a disordered medium. To obtain the intensity inside the medium a source *and* full Green's functions have to be connected to the Ladder propagator L in Eq. (2.106). The propagator L starts and ends on a scatterer (see Fig. (2.7)). Since we will make extensive use of the propagator that is closed on one end (i.e. beginning on a scatterer) and open on the other end (i.e. ending in two full Green's functions), it is introduced as $H(\mathbf{r}, t)$ (see Fig. (2.8). Attaching amplitude propagators to the "bare" vertex $L(\mathbf{r}, t)$ gives,

$$\begin{aligned} H(\mathbf{r},t) &\equiv \frac{1}{4\pi}\int \mathrm{d}t'\mathrm{d}\mathbf{r}' L(\mathbf{r}',t')G(\mathbf{r}-\mathbf{r}',t-t')G^*(\mathbf{r}-\mathbf{r}',t-t') \\ &= \frac{v_E a}{4\pi\ell(4\pi Dt)^{3/2}} e^{-t/\tau_a} e^{-\mathbf{r}^2/(4Dt)}. \end{aligned} \tag{2.108}$$

Note the factor of $1/4\pi$ before the integral. The end of the vertex L can be interpreted as the source of the intensity at $\mathbf{r}'$ that is propagated by the full Green's functions to $\mathbf{r}$. Since the position $\mathbf{r}'$ where the light is coming from is integrated over, information where the intensity was coming from is lost. It amounts to integrating the specific intensity over the full solid angle, which is equal to $4\pi I(\mathbf{r})$ (see Eq. (2.8) and the remark after Eq. (2.85)). Therefore the integral in Eq. (2.108) is divided by 4π. The propagator H converts specific intensity into isotropic (diffuse) intensity. To find the diffuse intensity inside the disordered medium the specific intensity originating from a source has to be attached to the diffuse intensity propagator H. The specific intensity with unit flux through a sphere around the origin is given in Eq. (2.82) with Eq. (2.84) as the source that radiates isotropic in all directions. The time-dependent intensity (in the frequency domain) is given by solving,

$$I(E,\omega,\mathbf{p}) = \eta[\langle\Psi\rangle * \langle\Psi\rangle](E,\omega,\mathbf{p})H(E,\omega,\mathbf{p}) = \frac{4\pi\eta\epsilon M(E,\omega,\mathbf{p})}{nt(E^+)t(E^-)(1-M(E,\omega,\mathbf{p}))}. \tag{2.109}$$

The calculation yields,

$$I(E,\omega,\mathbf{p}) = \frac{\eta\epsilon v_E}{-i\omega + v_E(1-a)/\ell + \frac{1}{3}\mathbf{p}^2 v_E \ell}. \tag{2.110}$$

In real space and time the time dependent isotropic intensity distribution in the disordered medium due to a source in the origin radiating a pulse at time $t = 0$ with energy $4\pi\eta\epsilon$ is,

$$I(\mathbf{r},t) = \frac{\eta\epsilon v_E}{(4\pi D t)^{3/2}} e^{-t/\tau_a} e^{-\mathbf{r}^2/(4Dt)}. \tag{2.111}$$

One sees that the diagrammatic result for the diffuse intensity in the disordered medium gives rise to the result obtained from the particle diffusion picture in Eq. (2.10), only now microscopic expressions for the velocity in the medium Eq. (2.105), the diffusion constant and the absorption length Eq. (2.107) were found. The difference of a factor 4π comes from a different norm. Here the norm was a source with unit total flux integrated over time (Eq. (2.85)) with a total energy of $4\pi\eta\epsilon$ (Eq. (2.79)), in section 2.1 the norm was total density (energy). From now on the norm is unit total flux η and we drop the explicit dependence of the intensity on unit power η.

2.6 Diffuse intensity in a semi-infinite medium

We will try to find the diffuse intensity inside the medium occupying the half space $z > 0$ with an incident plane wave coming from $z = -\infty$. The coherent (unscattered) intensity inside the medium was given in subsection 2.3.4 by Eq. (2.65). Since the system is not translationally invariant in the z coordinate, the intensity propagator derived for an infinite disordered medium has to be modified to satisfy boundary conditions. Using transport theory a boundary condition for the diffuse intensity is derived. We apply this boundary condition to the intensity propagator that was derived in the diffusion approximation. The boundary condition for the diffuse intensity is that at the surface $z = 0$ there should be no diffuse intensity entering the medium from outside. This condition is first translated into a mixed Dirichlet-von Neumann condition on the average intensity at the boundary and then to a Dirichlet condition at an extrapolated distance from the boundary. A new propagator is constructed for a semi-infinite medium and for a slab geometry that satisfy the boundary conditions. With the new propagator the diffuse intensity inside the medium is calculated. To derive the boundary condition some results of transport theory are introduced[35], which we will use.

2.6.1 Transport theory

Transport theory is a macroscopic theory, where the diffuse intensity is assumed to be a slow varying function over length scales of the order of the mean free path ℓ. We consider the stationary case and will give a fenomenological derivation of the Master equation. The specific intensity is split into two parts, the isotropic intensity $I(\mathbf{r})$ (Eq. (2.8)) and the net flux $\mathbf{F}(\mathbf{r})$,

$$I(\mathbf{r},\hat{\mathbf{s}}) = I(\mathbf{r}) + \frac{3}{4\pi}\mathbf{F}(\mathbf{r})\cdot\hat{\mathbf{s}}; \qquad \text{with } \mathbf{F}(\mathbf{r}) \equiv \int_{4\pi} I(\mathbf{r},\hat{\mathbf{s}})\hat{\mathbf{s}}\mathrm{d}\Omega. \tag{2.112}$$

The specific intensity in the direction $\hat{\mathbf{s}}$ is written as an isotropic part, giving the same intensity in all directions, and the inner product of the net flux and the unit vector $\hat{\mathbf{s}}$ times the constant $\frac{3}{4\pi}$. The constant is found by substituting the expansion of $I(\mathbf{r},\hat{\mathbf{s}})$ into the definition of $\mathbf{F}(\mathbf{r})$ and using the identity $\int_{4\pi}(\mathbf{F}(\mathbf{r})\cdot\hat{\mathbf{s}})\hat{\mathbf{s}}\mathrm{d}\Omega = \frac{4\pi}{3}\mathbf{F}(\mathbf{r})$. The specific intensity at a small distance d$\mathbf{s}$ from $\mathbf{r}$ in the direction $\hat{\mathbf{s}}$, $I(\mathbf{r}+\mathrm{d}\mathbf{s},\hat{\mathbf{s}})$, is the specific intensity at $\mathbf{r}$ in the direction $\hat{\mathbf{s}}$, $I(\mathbf{r},\hat{\mathbf{s}})$, minus the intensity that is scattered out of the direction $\hat{\mathbf{s}}$ over the distance d$\mathbf{s}$, $\frac{\mathrm{d}\mathbf{s}}{\ell}I(\mathbf{r},\mathbf{s})$. The gain is the intensity coming from all directions that is scattered into the direction $\hat{\mathbf{s}}$ over the distance d$\mathbf{s}$. Assuming isotropic scattering the gain term is,

$$\frac{\mathrm{d}\mathbf{s}}{4\pi\ell}\int_{4\pi} I(\mathbf{r},\hat{\mathbf{s}}')\mathrm{d}\Omega' = \frac{\mathrm{d}\mathbf{s}}{\ell}I(\mathbf{r}). \tag{2.113}$$

Adding all contributions gives,

$$I(\mathbf{r}+\mathrm{d}\mathbf{s},\hat{\mathbf{s}}) = I(\mathbf{r},\hat{\mathbf{s}}) - \frac{\mathrm{d}\mathbf{s}}{\ell}I(\mathbf{r},\mathbf{s}) + \frac{\mathrm{d}\mathbf{s}}{\ell}I(\mathbf{r}), \tag{2.114}$$

the Master equation. Substituting Eq. (2.112) in the above equation and writing the variations over the distance d$\mathbf{s}$ as derivatives results in,

$$\hat{\mathbf{s}}\cdot\nabla I(\mathbf{r}) = \frac{-3}{4\pi\ell}\mathbf{F}(\mathbf{r})\cdot\hat{\mathbf{s}} - \frac{3}{4\pi}(\hat{\mathbf{s}}\cdot\nabla)(\mathbf{F}(\mathbf{r})\cdot\hat{\mathbf{s}}). \tag{2.115}$$

The last term can be neglected under the assumption that the diffuse intensity is a slow varying function of position. The specific intensity thus can be expressed in the isotropic intensity and the divergence of the isotropic intensity,

$$I(\mathbf{r},\hat{\mathbf{s}}) = I(\mathbf{r}) - \ell\nabla I(\mathbf{r})\cdot\hat{\mathbf{s}}. \tag{2.116}$$

2.6.2 Boundary condition

The boundary condition is that there should be no diffuse intensity entering the medium at the surface $\mathbf{r}_s$,

$$\int_{\hat{\mathbf{s}}'_z\geq 0} I(\mathbf{r}_s,\hat{\mathbf{s}}')(\hat{\mathbf{s}}'\cdot\hat{\mathbf{n}}_+)\mathrm{d}\Omega' = \mathbf{J}_{\hat{\mathbf{n}}_+}(\mathbf{r}_s) = 0, \tag{2.117}$$

with $\hat{\mathbf{n}}_+$ a unit vector perpendicular to the surface, pointing inwards, i.e. in the positive z direction, and $\mathbf{J}_{\hat{\mathbf{n}}_+}(\mathbf{r}_s)$ the diffuse flux on the surface propagating into the medium. Eq. (2.116) is substituted into the above equation, where the divergence of the isotropic intensity is decomposed into the part perpendicular to the surface and the part tangential to the surface,

$$\nabla I(\mathbf{r}) = (\nabla I(\mathbf{r}) \cdot \hat{\mathbf{n}}_+)\hat{\mathbf{n}}_+ + (\nabla I(\mathbf{r}) \cdot \hat{\mathbf{t}})\hat{\mathbf{t}}. \tag{2.118}$$

The boundary condition becomes,

$$\begin{aligned}\int_{\hat{\mathbf{s}}'_z \geq 0} I(\mathbf{r}_s, \hat{\mathbf{s}}')(\hat{\mathbf{s}}' \cdot \hat{\mathbf{n}}_+)\mathrm{d}\Omega' = \int_{\hat{\mathbf{s}}'_z \geq 0} I(\mathbf{r}_s)(\hat{\mathbf{s}}' \cdot \hat{\mathbf{n}}_+)\mathrm{d}\Omega' \; - \\ \ell \int_{\hat{\mathbf{s}}'_z \geq 0} (\nabla I(\mathbf{r}_s) \cdot \hat{\mathbf{n}}_+)(\hat{\mathbf{n}}_+ \cdot \hat{\mathbf{s}}')(\hat{\mathbf{s}}' \cdot \hat{\mathbf{n}}_+) + (\nabla I(\mathbf{r}_s) \cdot \hat{\mathbf{t}})(\hat{\mathbf{t}} \cdot \hat{\mathbf{s}}')(\hat{\mathbf{s}}' \cdot \hat{\mathbf{n}}_+)\mathrm{d}\Omega' = 0\end{aligned} \tag{2.119}$$

The part of the divergence of the isotropic intensity tangential to the surface does not contribute to the second integral in Eq. (2.119). Performing the integration gives,

$$\pi I(\mathbf{r}_s) - \ell \frac{2\pi}{3}(\nabla I(\mathbf{r}_s) \cdot \hat{\mathbf{n}}_+) = 0. \tag{2.120}$$

With

$$\nabla I(\mathbf{r}_s) \cdot \hat{\mathbf{n}}_+ = \frac{\partial I(\mathbf{r}_s)}{\partial z}, \tag{2.121}$$

the mixed boundary condition on the diffuse intensity is found,

$$I(\mathbf{r}_s) = \ell \frac{2}{3} \frac{\partial I(\mathbf{r}_s)}{\partial z}. \tag{2.122}$$

In line with transport theory the intensity close to the boundary is approximated by a first order polynomial, $I(z) = a + bz$, and the distance from the interface where the diffuse intensity extrapolates to zero can be found. Substituting $I(z) = a + bz$ into Eq. (2.122) leads to an extrapolation length $\tau_0 = 2\ell/3$ for which $I(-\tau_0) = 0$. It should be emphasized that the boundary condition is only approximate. The transport problem discussed in this section is well known as the Milne-problem[36, 37, 16], which can be solved exactly. The exact solution of the Milne-problem leads to an extrapolation length $\tau_0 = 0.7104\ \ell$ for the diffuse intensity. This is in the case of no absorption in the medium and the average refractive index inside the medium equal to the refractive index outside. Lagendijk, Vreeker and de Vries[38] and Zhu, Pine and Weitz[39] have shown that a mismatch in refractive index leads to reflections of the diffuse intensity at the interface, and accordingly to a different extrapolation length. From Eqs. (2.117,2.120,2.122) the diffuse flux $\mathbf{J}_{\hat{\mathbf{n}}_-}(\mathbf{r}_s)$ that is emerging from the surface can be determined,

$$\int_{\hat{\mathbf{s}}'_z \leq 0} I(\mathbf{r}_s, \hat{\mathbf{s}}')(\hat{\mathbf{s}}' \cdot \hat{\mathbf{n}}_-)\mathrm{d}\Omega' = \mathbf{J}_{\hat{\mathbf{n}}_-}(\mathbf{r}_s) = \frac{4\pi\ell}{3} \frac{\partial I(\mathbf{r}_s)}{\partial z}, \tag{2.123}$$

This equation holds only on the surface, since Eq. (2.120) was used that holds only on the surface. In connection with the flux on the surface it is interesting to repeat the definition of the diffuse "energy density" $u(\mathbf{r})$,

$$u(\mathbf{r}) = \frac{1}{v_E} \int_{4\pi} I(\mathbf{r}, \hat{\mathbf{s}}) \mathrm{d}\Omega. \tag{2.124}$$

For the diffuse flux a constitutive equation holds,

$$\mathbf{J}(\mathbf{r}) = -D\nabla u(\mathbf{r}); \qquad D = \frac{v_E \ell}{3}. \tag{2.125}$$

This equation results in the same flux as Eq. (2.123).

2.6.3 The intensity propagator for a semi-infinite medium

The boundary condition Eq. (2.117) or Eq. (2.122) was reformulated into a condition on the diffuse isotropic intensity $I(\mathbf{r})$, namely $I(-\tau_0) = 0$. With this new boundary condition the intensity propagator for the infinite medium $H(\mathbf{r}, t)$ is modified to the intensity propagator for the semi-infinite medium $H(\mathbf{r}, \mathbf{r}', t)$ that obeys the constraint that no intensity propagates to a trapping plane positioned at $z = -\tau_0$ parallel to the surface of the medium[40]. Note that the boundary condition can be imposed on H, since $H(\mathbf{r})$ gives the isotropic intensity in $\mathbf{r}$ due to the specific intensity in $\mathbf{r} = 0$, but not on L, since the quantity propagated to $\mathbf{r}$ by $L(\mathbf{r})$ is not an isotropic intensity. Later the propagator H will be used to find an approximate form of the propagator L for the semi-infinite medium and the slab geometry. The propagator H for a semi-infinite medium is found by subtracting from the intensity that propagates from $\mathbf{r}$ to $\mathbf{r}'$ the intensity that propagates from the point $\mathbf{r}$ mirrored in the trapping plane to $\mathbf{r}'$.

$$H(\mathbf{r}_\perp, z, \mathbf{r}'_\perp, z', t) = H(\mathbf{r}'_\perp - \mathbf{r}_\perp, z' - z, t) - H(\mathbf{r}'_\perp - \mathbf{r}_\perp, z' + (z + 2\tau_0), t). \tag{2.126}$$

In Fig. (2.9) the construction of $H(\mathbf{r}_\perp, z, \mathbf{r}'_\perp, z', t)$ is shown graphically. Using the expression Eq. (2.108) the following explicit expression for $H(\mathbf{r}_\perp, z, \mathbf{r}'_\perp, z', t)$ is found,

$$\begin{aligned} H(\mathbf{r}_\perp, z, \mathbf{r}'_\perp, z', t) &= \frac{v_E a}{4\pi\ell(4\pi D t)^{3/2}} e^{-t/\tau_a} \times \\ &\left(e^{-((\mathbf{r}_\perp - \mathbf{r}'_\perp)^2 + (z-z')^2)/(4Dt)} - e^{-((\mathbf{r}_\perp - \mathbf{r}'_\perp)^2 + (-z-z'-2\tau_0)^2)/(4Dt)} \right). \end{aligned} \tag{2.127}$$

The intensity propagator $H(\mathbf{r}_\perp, z, \mathbf{r}'_\perp, z', t)$ satisfies the condition that the intensity that propagates to the trapping plane is zero, $H(\mathbf{r}_\perp, z, \mathbf{r}'_\perp, -\tau_0, t) = 0$. We now have to define a source of diffuse intensity based on the coherent intensity given in Eq. (2.65). The coherent intensity inside the medium from an unit incident flux $\mathbf{J}_{coh}$ with direction $\hat{\mathbf{n}}_+$ is the specific intensity $I_{coh}(\mathbf{r}, \hat{\mathbf{s}})$,

$$I_{coh}(\mathbf{r}, \hat{\mathbf{s}}) = e^{-z/\ell}\, \delta(\hat{\mathbf{s}} - \hat{\mathbf{n}}_+) \Psi_{inc}(\mathbf{r}_\perp) \Psi^*_{inc}(\mathbf{r}_\perp), \tag{2.128}$$

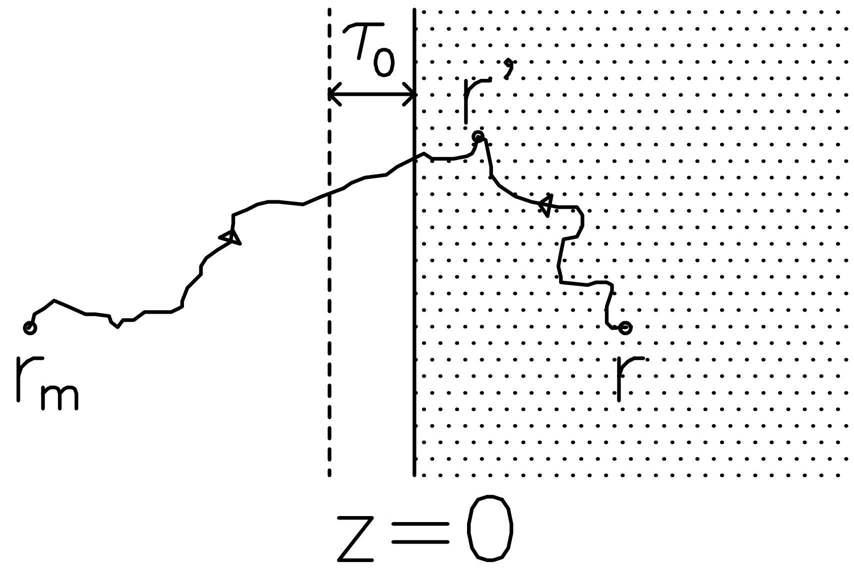

Figure 2.9: *The construction of the intensity propagator $H(\mathbf{r}, \mathbf{r}', t)$ for a semi-infinite slab. The slab boundary (the solid line) is at $z = 0$, the trapping or mirror plane (the dashed line) is at $z = -\tau_0$. The intensity propagates from $\mathbf{r}$ to $\mathbf{r}'$. The part that is subtracted is the part that travels from $\mathbf{r}_m$ to $\mathbf{r}'$, where $\mathbf{r}_m$ is the mirror point of $\mathbf{r}$ mirrored in the trapping plane. This construction ensures that no intensity propagates to the trapping plane.*

with $\Psi_{inc}(\mathbf{r}_\perp)\Psi^*_{inc}(\mathbf{r}_\perp)$ the flux distribution through a plane perpendicular to the beam (the beam profile) of the incoming light normalized to unity. The unit source of specific intensity is defined as,

$$S(\mathbf{r}) \equiv e^{-z/\ell}\ \Psi_{inc}(\mathbf{r}_\perp)\Psi^*_{inc}(\mathbf{r}_\perp). \tag{2.129}$$

In the special case that the absorption time τ_a goes to infinity the diffuse intensity in the semi-infinite medium from a perpendicular incoming unit plane wave becomes,

$$I(z) = \int d\mathbf{r}_\perp{}' \mathrm{d}\mathbf{r}_\perp \mathrm{d}z' \mathrm{d}t S(\mathbf{r}') H(\mathbf{r}_\perp{}', z', \mathbf{r}_\perp, z, t) = \frac{3}{4\pi}\left(1 + \frac{\tau_0}{\ell} - e^{-z/\ell}\right). \tag{2.130}$$

The flux leaving the semi-infinite medium is, according to Eq. (2.123), given by,

$$\mathbf{J}_{\hat{\mathbf{n}}_-}(z=0) = \frac{4\pi\ell}{3}\left.\frac{\partial I(z)}{\partial z}\right|_{z=0} = 1, \tag{2.131}$$

and the total flux is conserved.

2.7 Diffuse intensity in a slab

In the same manner as in the previous section one can find the diffuse intensity in a disordered slab of thickness L_{slab}. The physical slab boundaries are at $z = 0$ and

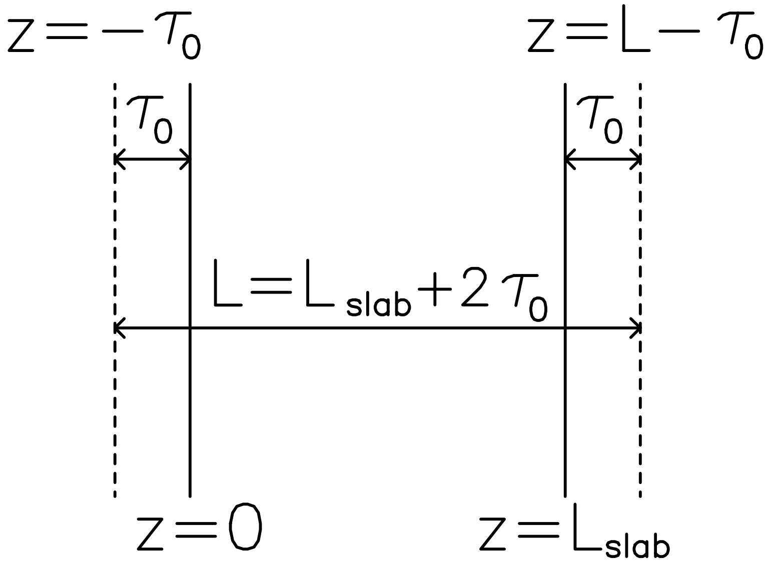

Figure 2.10: *The positions of the slab boundaries and the trapping planes with respect to the z-coordinate. The physical thickness of the slab is L_{slab}, the slab begins at $z = 0$ and ends at $z = L_{slab}$ (the solid lines). The positions of the trapping planes (the dashed lines) is at $z = -\tau_0$ and $z = L - \tau_0$. For later use the thickness L is defined as $L \equiv L_{slab} + 2\tau_0$.*

$z = L_{slab}$. The result for the diffuse intensity from the Milne-problem is extended to the interface at $z = L_{slab}$. The boundary conditions on the diffuse intensity become $I(-\tau_0) = I(L_{slab} + \tau_0) = 0$.

2.7.1 The intensity propagator for a slab

The intensity propagator H needs to be modified again, in such a manner that no intensity propagates to the trapping planes at $z = -\tau_0$ and $z = L_{slab} + \tau_0$. In Fig. (2.10) the positions of the slab boundaries and the trapping planes are shown with respect to the z-coordinate. The solution is found by multiple reflection of the diffuse intensity propagator in the trapping planes.

$$H(z_1, z_2, \mathbf{r}_\perp, t) = \frac{v_E e^{-t/\tau_0}}{4\pi\ell(4\pi D t)^{3/2}} \times$$
$$\sum_{n=-\infty}^{\infty} \{e^{-(\mathbf{r}_\perp^2 + [z_1 - z_2 + 2n(L_{slab} + 2\tau_0)]^2)/4Dt} - e^{-(\mathbf{r}_\perp^2 + [z_1 + z_2 + 2n(L_{slab} + 2\tau_0) + 2\tau_0]^2)/4Dt}\}. \quad (2.132)$$

This intensity propagator satisfies the boundary condition that no diffuse intensity propagates to the trapping planes. To get the intensity propagator in a more convenient form some mathematical manipulations follow. The thickness L is defined as $L \equiv L_{slab} + 2\tau_0$. With the help of the Poisson summation rule this equation can be rewritten as

$$H(z_1, z_2, \mathbf{r}_\perp, t) = \frac{v_E e^{-t/\tau_0}}{32\pi^2 \ell D t L} e^{-\mathbf{r}_\perp{}^2/(4Dt)} \times$$
$$\sum_{n=1}^{\infty} e^{-\pi^2 n^2 D t/L^2} 4 \sin[\pi n(z_1 + \tau_0)/L] \sin[\pi n(z_2 + \tau_0)/L]. \tag{2.133}$$

Fourier transforming the time and the perpendicular space coordinate to frequency ω and $\mathbf{p}_\perp$,

$$H(z_1, z_2, \mathbf{p}_\perp, \omega) = \int_0^\infty \mathrm{d}t \int_{-\infty}^{\infty} \mathrm{d}\mathbf{r}_\perp H(z_1, z_2, \mathbf{r}_\perp, t) e^{i\omega t} e^{i\mathbf{r}_\perp \cdot \mathbf{p}_\perp} =$$
$$\int_{-\infty}^{\infty} \mathrm{d}\mathbf{r}_\perp \left[\frac{v_E e^{i\mathbf{r}_\perp \cdot \mathbf{p}_\perp}}{8\pi^2 \ell D L} \sum_{n=1}^{\infty} \sin[\pi n(z_1 + \tau_0)/L] \sin[\pi n(z_2 + \tau_0)/L] \times \right.$$
$$\left. \int_0^\infty \mathrm{d}t \frac{e^{-t(1/\tau_0 - i\omega + \pi^2 n^2 D/L^2)}\, e^{-\mathbf{r}_\perp{}^2/(4Dt)}}{t} \right]. \tag{2.134}$$

Performing the time integral gives[41],

$$\int_0^\infty \mathrm{d}t \frac{e^{-t(1/\tau_0 - i\omega + \pi^2 n^2 D/L^2)}\, e^{-\mathbf{r}_\perp{}^2/(4Dt)}}{t} = 2\mathsf{K}_0 \left(|\mathbf{r}_\perp| \sqrt{\frac{1}{D\tau_a} - \frac{i\omega}{D} + \frac{\pi^2 n^2}{L^2}} \right). \tag{2.135}$$

with K_0 the zeroth order modified Bessel function of the second kind. Now the $\mathbf{r}_\perp$ integral can be done,

$$\int_{-\infty}^{\infty} \mathrm{d}\mathbf{r}_\perp \mathsf{K}_0 \left(|\mathbf{r}_\perp| \sqrt{\frac{1}{D\tau_a} - \frac{i\omega}{D} + \frac{\pi^2 n^2}{L^2}} \right) e^{i\mathbf{r}_\perp \cdot \mathbf{p}_\perp} =$$
$$\int_0^{2\pi} \int_0^\infty e^{i|\mathbf{p}_\perp| r_\perp \cos\theta} \mathsf{K}_0 \left(|r_\perp| \sqrt{\frac{1}{D\tau_a} - \frac{i\omega}{D} + \frac{\pi^2 n^2}{L^2}} \right) r_\perp \mathrm{d}r_\perp \mathrm{d}\theta. \tag{2.136}$$

First the integration over θ is done,

$$\int_0^{2\pi} e^{i|\mathbf{p}_\perp| r_\perp \cos\theta} \mathrm{d}\theta = 2\pi \mathsf{J}_0(|\mathbf{p}_\perp| r_\perp), \tag{2.137}$$

with J_0 the zeroth order Bessel function of the first kind. The result of the space integral is[42],

$$\int_0^\infty 2\pi r_\perp \mathsf{J}_0(|\mathbf{p}_\perp| r_\perp) \mathsf{K}_0 \left(r_\perp \sqrt{\frac{1}{D\tau_a} - \frac{i\omega}{D} + \frac{\pi^2 n^2}{L^2}} \right) \mathrm{d}r_\perp = \frac{2\pi}{\mathbf{p}_\perp{}^2 + \frac{1}{D\tau_a} - \frac{i\omega}{D} + \frac{\pi^2 n^2}{L^2}}. \tag{2.138}$$

The intermediate result is

$$H(z_1, z_2, \mathbf{p}_\perp, \omega) = \frac{v_E}{2\pi \ell D L} \sum_{n=1}^{\infty} \sin[\pi n(z_1 + \tau_0)/L] \times$$
$$\sin[\pi n(z_2 + \tau_0)/L] \frac{1}{\mathbf{p}_\perp{}^2 + \frac{1}{D\tau_a} - \frac{i\omega}{D} + \frac{\pi^2 n^2}{L^2}}. \tag{2.139}$$

The summation can be written in closed form[43], with as final result,

$$H(z_1, z_2, \mathbf{p}_\perp, \omega) = \frac{v_E}{4\pi\ell D\,\mathsf{Q}} \frac{\sinh\left[(z_< + \tau_0)\,\mathsf{Q}\right] \sinh\left[(L - z_> - \tau_0)\,\mathsf{Q}\right]}{\sinh\left[L\,\mathsf{Q}\right]}$$

$$\text{with } \mathsf{Q} = \left(\mathbf{p}_\perp{}^2 + \frac{1}{D\tau_a} - \frac{i\omega}{D}\right)^{1/2}, \qquad (2.140)$$

and $z_< \equiv min|z_1, z_2|$, $z_> \equiv max|z_1, z_2|$. Eq. (2.140) is an important formula, $H(z_1, z_2, \mathbf{p}_\perp, \omega)$ is the solution of (the Fourier transform of) the time and space dependent intensity propagator.

2.7.2 Diffuse intensity inside the slab

With the expression Eq. (2.140) for the intensity propagator inside the slab the time dependence and space dependence of the average intensity $I(\mathbf{r})$ can be calculated.

$$I(\mathbf{r}_\perp, z, t) = \frac{1}{(2\pi)^3} \times$$

$$\int S(\mathbf{r}_\perp{}', z', t') H(z', z, \mathbf{p}_\perp, \omega) e^{-i(\mathbf{r}_\perp - \mathbf{r}_\perp{}')\mathbf{p}_\perp} e^{-i\omega(t-t')} \mathrm{d}\omega \mathrm{d}\mathbf{p}_\perp \mathrm{d}\mathbf{r}_\perp{}' \mathrm{d}z' \mathrm{d}t'. \qquad (2.141)$$

Using the source in Eq. (2.129) and integrating out the time dependence and the dependence on the transversal coordinate $\mathbf{r}_\perp$, and $\tau_a \to \infty$ (i.e. in the absence of absorption) this results in the diffuse intensity inside the slab for an exponential decaying source,

$$I(z) \approx \frac{3}{4\pi\ell L}\left((\ell + \tau_0)(L - z - \tau_0) - \ell L e^{-z/\ell}\right). \qquad (2.142)$$

where a term of the order $e^{-L/\ell}$ was neglected.

2.7.3 Injection source

We will follow Akkermans *et al.*[44] to simplify future calculations and make the approximation that all diffuse intensity is generated at an injection depth z_i with respect to the physical boundary of the slab. The injection source $S_{inj}(\mathbf{r})$ is defined by the average and the weight of the source in Eq. (2.129), respectively,

$$\overline{S(\mathbf{r})} = \int_{z\geq 0} S(\mathbf{r})\mathrm{d}z = \ell \Psi_{inc}(\mathbf{r}_\perp)\Psi^*_{inc}(\mathbf{r}_\perp),$$

$$\overline{zS(\mathbf{r})} = \int_{z\geq 0} zS(\mathbf{r})\mathrm{d}\mathbf{r} = \ell^2 \Psi_{inc}(\mathbf{r}_\perp)\Psi^*_{inc}(\mathbf{r}_\perp). \qquad (2.143)$$

The source becomes,

$$S_{inj}(\mathbf{r}) \equiv \overline{S(\mathbf{r})}\delta(z - z_i) = \ell\delta(z - \ell)\Psi_{inc}(\mathbf{r}_\perp)\Psi^*_{inc}(\mathbf{r}_\perp) \quad \text{with } z_i = \frac{\overline{zS(\mathbf{r})}}{\overline{S(\mathbf{r})}} = \ell. \qquad (2.144)$$

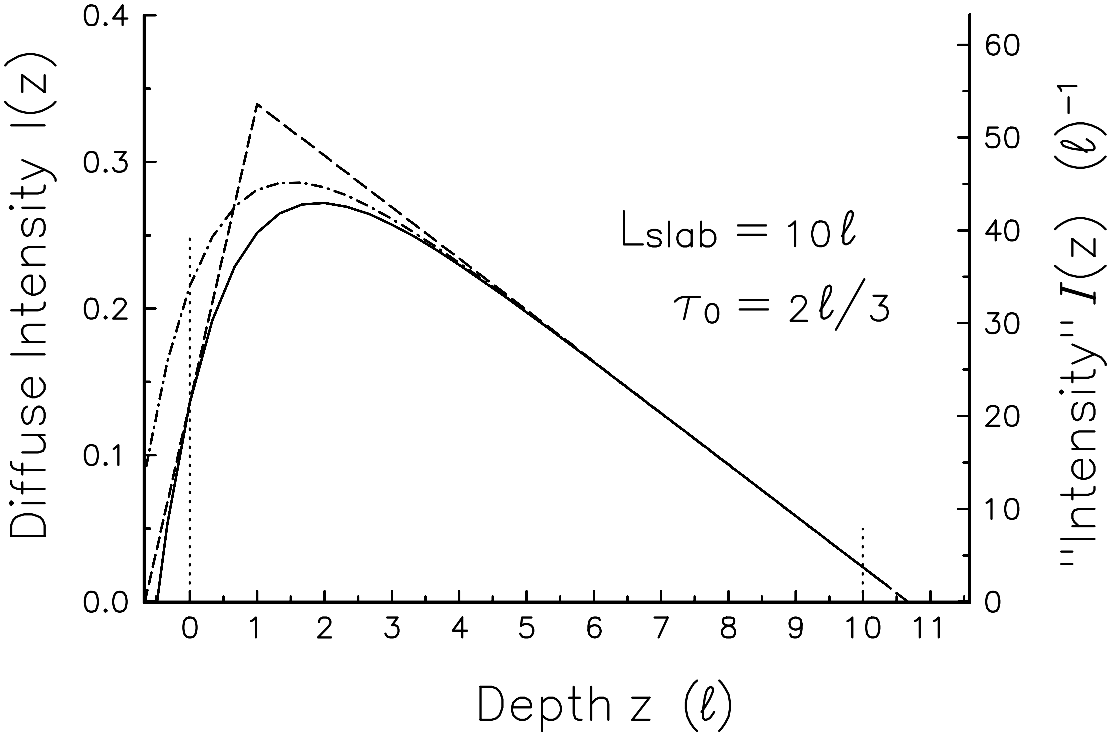

Figure 2.11: *The diffuse intensity $I(z)$ in a slab of ten mean free paths, $L_{slab} = 10\ell$, as a function of depth. The depth is expressed in mean free paths ℓ. The solid line is the intensity with an exponential decaying incoming beam in Eq. (2.142), the dashed line is the intensity with an injection of the incoming source at a mean free path in Eq. (2.145), both with respect to the left y-axis. The dashed-dotted line shows the intensity $\mathcal{I}(z)$ in Eq. (2.150) with respect to the right y-axis. The dotted vertical lines denote the physical slab boundaries.*

The injection depth z_i is equal to the average depth ℓ at which the diffuse intensity is generated. The injection source gives an exact result if the intensity propagator depends linearly on the z coordinate. The diffuse intensity $I_{inj}(z)$ for the source in Eq. (2.144) is,

$$I_{inj}(z) = \int S_{inj}(\mathbf{r}')H(\mathbf{r}_\perp{}', z', \mathbf{r}_\perp, z)\mathrm{d}\mathbf{r}'\mathrm{d}\mathbf{r}_\perp = \begin{cases} \dfrac{3}{4\pi\ell L}(z+\tau_0)(L-\ell-\tau_0) & z \le \ell \\ \dfrac{3}{4\pi\ell L}(\ell+\tau_0)(L-z-\tau_0) & z \ge \ell \end{cases} \tag{2.145}$$

Fig. (2.11) shows the intensity inside the slab for both sources. As can be seen from the figure the slope on the slab boundaries is equal for both sources. The total reflection and transmission are determined by using Eq. (2.123) on the transmission and reflection side,

$$R = \frac{4\pi\ell}{3}\left.\frac{\partial I(z)}{\partial z}\right|_{z=0} = 1 - \frac{\ell+\tau_0}{L}; \qquad T = -\frac{4\pi\ell}{3}\left.\frac{\partial I(z)}{\partial z}\right|_{z=L-2\tau_0} = \frac{\ell+\tau_0}{L}, \quad (2.146)$$

and the total flux is conserved. The same reflection and transmission are obtained by taking the isotropic intensity at an ejection depth z_e.

$$R = \pi I_{inj}(z_e) \quad (z_e = \frac{2}{3}\ell) \qquad T = \pi I_{inj}(z_e) \quad (z_e = L - 2\tau_0 - \frac{2}{3}\ell). \qquad (2.147)$$

2.8 Transmission and reflection using outgoing amplitude propagators

We want to derive a simpler formalism to calculate the transmission and reflection. In the previous section the reflection and transmission were derived by taking the derivative of the isotropic intensity at the boundary (Eq. (2.123)). Here we want to calculate the transmission and reflection by using propagators that propagate the intensity from within the medium to the outside. In principle the angular resolved transmission and reflection can be determined this way. Unfortunately, we cannot attach outgoing Green's functions to the propagator H, since it already ends on Green's functions (see Fig. (2.8)). Outward propagating amplitudes can be attached to the vertex L, since it starts and ends on a scatterer (see Fig. (2.7)). However the exact form of the vertex L for the semi-infinite medium or the slab geometry is not known, since the boundary condition Eq. (2.117) was derived for the diffuse intensity (i.e. a propagator ending on Green's functions) and thus applies only to H and not to L. An approximate form of the bare vertex L in the semi-infinite or the slab geometry can be inferred by noticing that for the infinite medium $L = \frac{16\pi^2}{\ell}H + \frac{4\pi}{\ell}\delta(\mathbf{r})$ (See Eq. (2.106) and Eq. (2.108), neglecting absorption and the time dependence). For the slab geometry we approximate the bare vertex L by multiplying the propagator H for the slab by $\frac{16\pi^2}{\ell}$ and adding the single scattering contribution $\frac{4\pi}{\ell}\delta(\mathbf{r})\delta(t)$,

$$L(\mathbf{r}_\perp, z, \mathbf{r}_\perp{}', z', t) \approx \frac{16\pi^2}{\ell} H(\mathbf{r}_\perp, z, \mathbf{r}_\perp{}', z', t) + \frac{4\pi}{\ell}\delta(\mathbf{r}-\mathbf{r}')\delta(t). \qquad (2.148)$$

2.8.1 The "intensity" $\mathcal{I}(\mathbf{r})$

We introduce the "intensity" $\mathcal{I}(\mathbf{r})$, which is defined as a source connected to L, i.e. the "intensity on a scatterer" with the dimensions of a source, unit power per volume.

$$\mathcal{I}(\mathbf{r}) = \int_0^L \langle\Psi_{inc}(\mathbf{r}')\rangle\langle\Psi^*_{inc}(\mathbf{r}')\rangle L(\mathbf{r}', \mathbf{r})\mathrm{d}\mathbf{r}'. \qquad (2.149)$$

Later the total transmission and reflection will be derived by connecting outgoing propagators to the source $\mathcal{I}(\mathbf{r})$. First the "intensity on a scatterer" $\mathcal{I}(\mathbf{r})$ is calculated.

With the incoming unit intensity $\langle\Psi_{inc}(\mathbf{r})\rangle\langle\Psi^*_{inc}(\mathbf{r})\rangle = e^{-z/\ell}\ \Psi_{inc}(\mathbf{r}_\perp)\Psi^*_{inc}(\mathbf{r}_\perp)$ from Eq. (2.65), the intensity $\mathcal{I}(z)$ in the slab geometry is given by,

$$\mathcal{I}(z) = \int \mathcal{I}(\mathbf{r})\mathrm{d}\mathbf{r}_\perp \approx \frac{12\pi}{\ell^2 L}(\ell + \tau_0)(L - z - \tau_0) - \frac{8\pi}{\ell}e^{-z/\ell}. \tag{2.150}$$

In the limit $L \to \infty$ Eq. (2.150) reduces to the intensity $\mathcal{I}(z)$ for a semi-infinite medium,

$$\mathcal{I}(z) \approx \frac{12\pi}{\ell^2}(\ell + \tau_0) - \frac{8\pi}{\ell}e^{-z/\ell}. \tag{2.151}$$

In Fig. (2.11), Eq. (2.150) is shown graphically in comparison with the intensities $I(z)$ in Eq. (2.142) and Eq. (2.145). The integral in Eq. (2.149) was taken from 0 to ∞, which for slabs thicker than five mean free paths gives a completely negligible extra contribution to Eq. (2.150). To transport the intensity outside the medium, outgoing propagators $G(\mathbf{r}, \mathbf{r}')$ are attached to the "intensity" $\mathcal{I}$. The outgoing propagator is defined by,

$$G_{out}(\mathbf{r}_\perp, z, \mathbf{r}_\perp{}', z') \equiv G_{out}(\mathbf{r}_\perp{}' - \mathbf{r}_\perp, z, z') = \frac{e^{-iKz/\cos\theta + ik_0 z'/\cos\theta}}{4\pi|\mathbf{r} - \mathbf{r}'|}, \tag{2.152}$$

with $\mathbf{r}$ inside $(z > 0)$ and $\mathbf{r}'$ outside $(z' < 0)$ the medium, θ the angle of the outgoing direction $\hat{\mathbf{s}}$ with the normal to the surface pointing outward, $\hat{\mathbf{n}}$, and k_0 the wave vector outside the medium, for convenience the vacuum, $k_0 = E/c$. The specific intensity through a plane at z' outside the medium, $I(z', \hat{\mathbf{s}})$ is,

$$I(z', \hat{\mathbf{s}}) = \int I(\mathbf{r}', \hat{\mathbf{s}})\mathrm{d}\mathbf{r}_\perp{}' = \int_{z \geq 0} \mathcal{I}(\mathbf{r})G_{out}(\mathbf{r}_\perp{}' - \mathbf{r}_\perp, z, z')G^*_{out}(\mathbf{r}_\perp{}' - \mathbf{r}_\perp, z, z')\mathrm{d}\mathbf{r}_\perp \mathrm{d}z. \tag{2.153}$$

The integration over $\mathbf{r}_\perp{}'$ in the last integral cancels against the condition that $\mathbf{r}' - \mathbf{r}$ is pointing in the direction $\hat{\mathbf{s}}$. The flux $\mathbf{J}(z')$ through a surface at z' far away from and parallel to the surface of the medium is,

$$\mathbf{J}(z') = \int_{\hat{\mathbf{s}}_z \leq 0} I(z', \hat{\mathbf{s}})(\hat{\mathbf{s}}\cdot\hat{\mathbf{n}})\mathrm{d}\Omega \qquad \text{with } (\hat{\mathbf{s}}\cdot\hat{\mathbf{n}}) = \cos\theta = \mu. \tag{2.154}$$

The fraction of the intensity $\mathcal{I}(z)$ at depth z contributing to the total flux in reflection is given by,

$$\begin{aligned} &\int G_{out}(\mathbf{r}_\perp{}' - \mathbf{r}_\perp, z, z')G^*_{out}(\mathbf{r}_\perp{}' - \mathbf{r}_\perp, z, z')\cos\theta \mathrm{d}(\mathbf{r}_\perp{}' - \mathbf{r}_\perp) = \\ &\int_\infty^\infty \frac{e^{z/(\ell\cos\theta)}\ \cos\theta}{(4\pi\mathbf{r})^2}\mathrm{d}\mathbf{r}_\perp = \frac{1}{8\pi}\int_0^1 e^{-z/(\ell\mu)}\mathrm{d}\mu = \frac{1}{8\pi}E_2(z/\ell), \end{aligned} \tag{2.155}$$

with $E_2(z)$ the exponential integral of second order. The same calculation can be done to find the total flux in transmission, resulting in a convolution of the intensity $\mathcal{I}(z)$ with $E_2((L - 2\tau_0 - z)/\ell)$. The total flux in reflection and transmission for the slab geometry, $\mathbf{J}_R$ and $\mathbf{J}_T$, are given by respectively,

$$\mathbf{J}_R = \frac{1}{8\pi}\int_0^\infty \mathcal{I}(z)E_2(z/\ell)\mathrm{d}z = \frac{3(\ell + \tau_0)(L - \tau_0 - \frac{2}{3}\ell)}{4\ell L} - (1 - \ln 2), \tag{2.156}$$

and

$$\mathbf{J}_T = \frac{1}{8\pi}\int_{-\infty}^{L-2\tau_0} \mathcal{I}(z)E_2((L-2\tau_0-z)/\ell)\mathrm{d}z = \frac{3(\ell+\tau_0)(\tau_0+\frac{2}{3}\ell)}{4\ell L}. \tag{2.157}$$

The sum of the reflection and transmission is,

$$\mathbf{J}_R + \mathbf{J}_T \approx 0.95 \tag{2.158}$$

Strictly speaking the integral boundaries for reflection and transmission in the slab geometry are at respectively $L-2\tau_0$ and 0, but for slabs thicker than five mean free paths the extension of the integral boundaries to infinity respectively minus infinity gives a contribution that is completely negligible. A more serious error is introduced by the approximate form of the bare vertex L in the semi-infinite or slab geometry. The total flux is not conserved. However the transmission is the same as derived in Eq. (2.146) for $\tau_0 = \frac{2}{3}\ell$. Clearly the reflection is underestimated, which means that the approximate form of the bare vertex L in Eq. (2.148) leads to an underestimating of the intensity $\mathcal{I}$ at the entrance interface. This is apparently the price we have to pay for an easier formalism.

2.8.2 Ejection drain

The convolution of the exponential integral of second order with the "intensity on a scatterer" $\mathcal{I}(\mathbf{r})$ is not yet a simple formalism. The last step is to assume that all ejected intensity comes from the same depth. In the same way as the injection source in Eq. (2.144) for the incoming intensity was defined, an ejection drain E_d is defined, based on the average and the weight of the ejection function in Eq. (2.155),

$$\overline{E} = \frac{1}{8\pi}\int_{z\geq 0} E_2(z/\ell)\mathrm{d}z = \frac{\ell}{16\pi}; \quad \overline{zE} = \frac{1}{8\pi}\int_{z\geq 0} zE_2(z/\ell)\mathrm{d}z = \frac{\ell^2}{24\pi}. \tag{2.159}$$

With this average and weight of the ejection function the ejection drain is defined as,

$$E_d(z) = \frac{\ell}{16\pi}\delta(z-z_e) \qquad z_e = \frac{2}{3}\ell. \tag{2.160}$$

The average ejection depth for diffuse light in reflection is $z_e = \frac{2}{3}\ell$. The analog argument for the transmission side of the slab leads to the ejection drain,

$$E_d(z) = \frac{\ell}{16\pi}\delta(z-z_e) \qquad z_e = L-2\tau_0-\frac{2}{3}\ell. \tag{2.161}$$

The average ejection depth for diffuse light in transmission is $z_e = L-2\tau_0-\frac{2}{3}\ell$. These ejection drains are exact for a linear intensity distribution $\mathcal{I}(\mathbf{r})$ near the slab boundaries. We make one more approximation to the Ladder vertex L by neglecting the single scattering term in Eq. (2.148),

$$L(\mathbf{r}_{\perp 1}, z_1, \mathbf{r}_{\perp 2}, z_2, t) \approx \frac{16\pi^2}{\ell} H(\mathbf{r}_{\perp 1}, z_1, \mathbf{r}_{\perp 2}, z_2, t). \tag{2.162}$$

We now have arrived at simple formulas to get the intensity $\mathcal{I}$ inside the slab, the total transmission and the total reflection. We use the injection source in Eq. (2.144) and the propagator in Eq. (2.162). The intensity $\mathcal{I}$ is then given by,

$$\mathcal{I}(z) = \ell \int L(\mathbf{r}_\perp{}', z_i, \mathbf{r}_\perp, z, t)\Psi_{inc}(\mathbf{r}_\perp{}')\Psi^*_{inc}(\mathbf{r}_\perp{}')\mathrm{d}\mathbf{r}_\perp{}'\mathrm{d}\mathbf{r}_\perp\mathrm{d}t$$

$$\mathcal{I}(z) = \begin{cases} \dfrac{12\pi}{\ell^2 L}(z+\tau_0)(L-\ell-\tau_0) & z \le \ell \\ \\ \dfrac{12\pi}{\ell^2 L}(\ell+\tau_0)(L-z-\tau_0) & z \ge \ell \end{cases} \tag{2.163}$$

With the ejection drains for reflection (Eq. (2.160)) and transmission (Eq. (2.161)) this leads to,

$$\mathbf{J}_R = \frac{L-\ell-\tau_0}{L} \qquad \mathbf{J}_T = \frac{\ell+\tau_0}{L}. \tag{2.164}$$

As could be expected the flux in transmission for the ejection drain is equal to the transmission found in Eq. (2.157), since the intensity $\mathcal{I}(\mathbf{r})$ near the transmission interface is a linear function. Compared to the exact reflection in Eq. (2.156) the ejection drain overestimates the reflection, effectively cancelling the error in the approximation made in the bare vertex L.

2.8.3 Conclusions

The injection source Eq. (2.144) and the ejection drains effectively are good approximations to find the reflection and transmission of disordered media from the intensity $\mathcal{I}(\mathbf{r})$. Recently Durian[45] found the transmission to be,

$$\mathbf{J}_T = \frac{\ell+\tau_0}{L_{slab}+2\tau_0} = \frac{\ell+\tau_0}{L}, \tag{2.165}$$

based on numerical simulations of diffusing particles, with a value of the trapping plane $\tau_0 \approx \frac{2}{3}\ell$. This numerical result is equal to the calculated total transmission in Eq. (2.146), Eq. (2.157) and Eq. (2.164). Since the approximations work extremely well, throughout this thesis we will use that all diffuse intensity is generated at an injection depth z_i with the source function in Eq. (2.144), and all reflected or transmitted intensity is emitted at an ejection depth z_e with the ejection drain of Eq. (2.160) or Eq. (2.161), and we use the bare vertex L for a slab in Eq. (2.162). One can include internal reflection at the slab boundaries because of a mismatch in refractive index by adapting the extrapolation length τ_0, as has been shown by Zhu, Pine and Weitz[39].

Chapter 3

Correlations on the transmission

In this chapter we will treat the theory that describes the experiments to be presented in chapter 4. We are interested in the fluctuations on the transmission and reflection of light multiply scattered by a disordered medium. In the previous chapter the average reflection and transmission were calculated. To describe the fluctuations we need to calculate higher moments of the intensity. For the higher moments interference plays an important role. The effects of interference will be calculated in the diagrammatic approach introduced in chapter 2. We will first describe the fluctuations of light reflected from a perfectly reflecting rough surface. We obtain the distribution of the fluctuations and the angular correlation in laser speckle. These results give us insight in the reflection and transmission of a waveguide with disorder, a concept that will prove to be very useful in the explanation of the fluctuations on the total transmission of light through a disordered medium. Then we come to the angular and frequency dependent short-range correlations in the fluctuations of the transmission. The theoretical results for the short-range correlation will be used in chapter 4 to determine the diffusion constant from the measured frequency dependent short-range correlation. In this chapter the theoretical short-range correlation is used to calculate the long-range correlation in the fluctuations of the total transmission as a function of angle and frequency in the Langevin approach. In chapter 4 the measurement of the long-range correlation will be presented, the first experimental confirmation of the full long-range correlation function on the total transmission. The theory will provide a very good description of the experimental results. In Appendix A it will be shown that the result of the Langevin approach coincides completely with the results of a full diagrammatic technique.

3.1 Laser speckle

A well known phenomenon in laser light is the strong angular fluctuation in light reflected from a rough, reflecting object[46]. It is caused by interference of the waves scattered from different points of the rough surface. For a continuous-wave laser beam and a quenched surface roughness the angular fluctuating pattern is

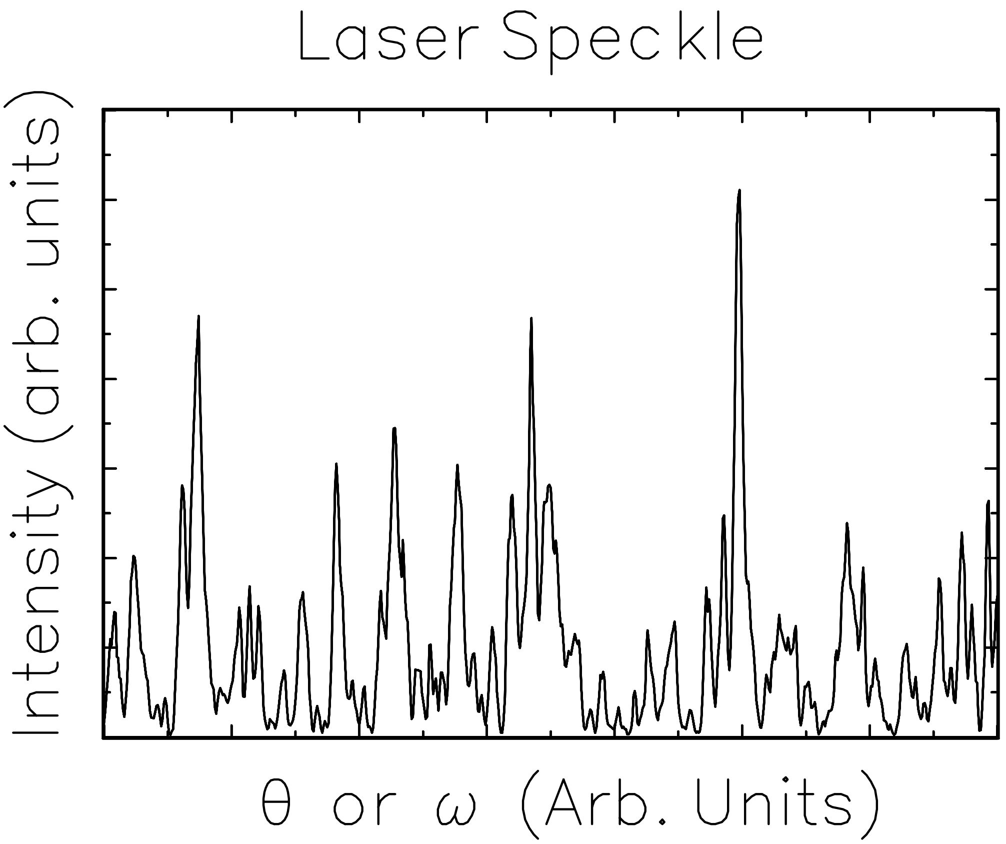

Figure 3.1: *Typical experimental speckle pattern of light multiple scattered by a disordered medium observed in transmission as a function of rotation angle of the sample or frequency (wavelength) of the light.*

static in time. In Fig. (3.1) a typical experimental speckle pattern is shown. In this section we will first calculate the distribution of the fluctuations in the intensity pattern of Fig. (3.1). Then we will calculate the angular correlation in the static speckle pattern. The result for the angular correlation in the speckle pattern from a perfectly reflecting rough surface is extended to the angular correlation in the speckle pattern in transmission and reflection generated by the scattered light from a disordered sample. The angular correlation in the laser speckle is used to define the number of modes N, in analogy with the number of modes supported by a waveguide.

3.1.1 Speckle distribution

The total amplitude in a point of observation far away from the surface is the vectorial sum of amplitudes coming from the whole rough surface, each with its own phase factor. It is assumed that the perfect reflection by the rough surface scrambles the phase and the direction of the reflected waves completely. The total amplitude for each polarization direction in a point of observation has a Gaussian distribution in a two dimensional complex plane. The total amplitude can be viewed as making a random walk in this complex plane as a function of the point of observation. The normalized probability distribution of the length of the total amplitude A is given by,

$$P(|A|) = \frac{2|A|}{\alpha} e^{-|A|^2/\alpha}, \tag{3.1}$$

with α an arbitrary constant describing the width of the distribution of the total amplitude. The average intensity for each polarization direction $\langle I \rangle$ that is observed in a certain direction is given by,

$$\langle I \rangle = \langle |A|^2 \rangle = \int_0^\infty \mathrm{d}A |A|^2 P(|A|) = \alpha. \tag{3.2}$$

Since we are interested in the intensity distribution, the amplitude distribution has to be rewritten in an intensity distribution, $P(I)$, with $I = |A|^2$.

$$P(I) = \int_0^\infty \mathrm{d}A \frac{2|A|}{\langle |A|^2 \rangle} e^{-|A|^2/\langle |A|^2 \rangle} \delta(|A|^2 - I). \tag{3.3}$$

The δ-function is rewritten as,

$$\delta(|A|^2 - I) = \frac{1}{2|A|} \delta(|A| - \sqrt{I}). \tag{3.4}$$

The probability distribution of the intensity in each of the two independent polarization directions becomes,

$$P(I) = \frac{1}{\langle I \rangle} e^{-I/\langle I \rangle}. \tag{3.5}$$

This is the well known Rayleigh distribution of laser speckle. It is a negative exponential distribution, implying the highest probability to measure zero intensity. The large fluctuations in the speckle are characterised by a variance equal to the mean squared,

$$\langle I^2 \rangle - \langle I \rangle^2 = \langle I \rangle^2. \tag{3.6}$$

In Fig. (3.2) the experimental distribution of the fluctuations in a speckle pattern is shown, together with the theory in Eq. (3.5), as measured in the short-range correlation measurements to be presented in chapter 4. The Rayleigh distribution describes the strong fluctuations in the laser speckle shown in Fig. (3.1).

3.1.2 Angular correlation in static laser speckle

We are interested in the angular correlation in the static laser speckle, i.e. over what solid angle is the scattered intensity in a certain direction correlated. This problem is closely related to the Van Cittert-Zernike theorem[28]. For a comprehensive treatment of the size of a speckle see also Goodman[47]. It will be shown that

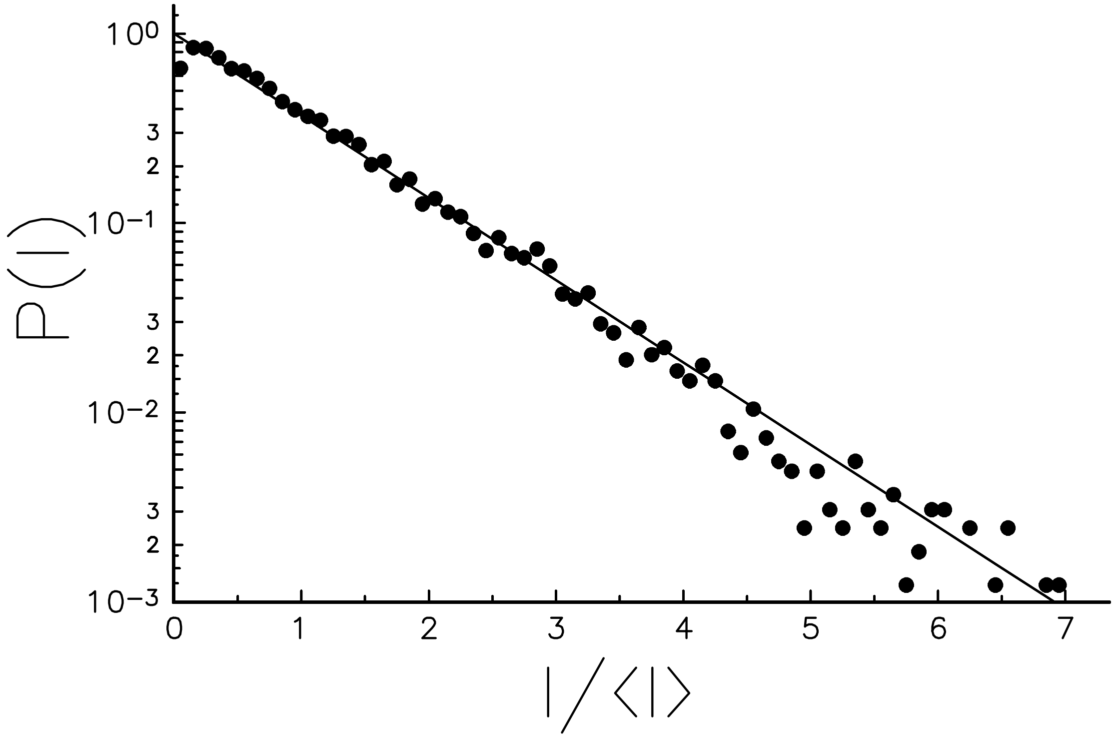

Figure 3.2: *Experimental intensity distribution of a typical speckle pattern. Typical data of the short-range correlation measurements in transmission through a disordered medium of chapter 4 was used. Dots: Experimental distribution. Solid line: Theoretical distribution as given in Eq. (3.5). The x-axis is scaled to the average intensity of the speckle pattern.*

the angular correlation in the speckle pattern is solely determined by the size and shape of the beam falling on the rough surface. We assume the observation of one polarization channel. The quantity $J_A(\hat{\mathbf{p}}_1, \hat{\mathbf{p}}_2)$ is defined as the amplitude per unit solid angle reflected in direction $\hat{\mathbf{p}}_1$ times the complex conjugate amplitude per unit solid angle reflected in direction $\hat{\mathbf{p}}_2$,

$$J_A(\hat{\mathbf{p}}_1, \hat{\mathbf{p}}_2) \equiv A(\hat{\mathbf{p}}_1)A^*(\hat{\mathbf{p}}_2), \tag{3.7}$$

with the length of the vector $|\hat{\mathbf{p}}| = k_0 = 2\pi/\lambda$. The angular speckle correlation function $C_S(\hat{\mathbf{p}}_1, \hat{\mathbf{p}}_2)$ is defined as,

$$C_S(\hat{\mathbf{p}}_1, \hat{\mathbf{p}}_2) \equiv \frac{\langle I(\hat{\mathbf{p}}_1)I(\hat{\mathbf{p}}_2)\rangle - \langle I(\hat{\mathbf{p}}_1)\rangle\langle I(\hat{\mathbf{p}}_2)\rangle}{\langle I(\hat{\mathbf{p}}_1)\rangle\langle I(\hat{\mathbf{p}}_2)\rangle} \approx \frac{|\langle J_A(\hat{\mathbf{p}}_1, \hat{\mathbf{p}}_2)\rangle|^2}{\langle I(\hat{\mathbf{p}}_1)\rangle\langle I(\hat{\mathbf{p}}_2)\rangle}, \tag{3.8}$$

where $I(\hat{\mathbf{p}})$ is the flux per unit solid angle in the direction $\hat{\mathbf{p}}$. For the last equation sign in Eq. (3.8) we have factorized the average of four amplitudes in the product of the average of two amplitudes,

$$\langle A(\hat{\mathbf{p}}_1)A^*(\hat{\mathbf{p}}_1)A(\hat{\mathbf{p}}_2)A^*(\hat{\mathbf{p}}_2)\rangle \approx$$
$$\langle A(\hat{\mathbf{p}}_1)A^*(\hat{\mathbf{p}}_1)\rangle\langle A(\hat{\mathbf{p}}_2)A^*(\hat{\mathbf{p}}_2)\rangle + \langle A(\hat{\mathbf{p}}_1)A^*(\hat{\mathbf{p}}_2)\rangle\langle A(\hat{\mathbf{p}}_2)A^*(\hat{\mathbf{p}}_1)\rangle. \tag{3.9}$$

The angular brackets denote averaging over different configurations of the surface roughness. The amplitude $A(\hat{\mathbf{p}})$ is given by,

$$A(\hat{\mathbf{p}}) = \int A(\mathbf{r}_\perp)e^{i\hat{\mathbf{p}}_\perp\cdot\mathbf{r}_\perp}\mathrm{d}\mathbf{r}_\perp, \tag{3.10}$$

with $A(\mathbf{r}_\perp)$ the amplitude and phase of the reflected wave on the rough surface (the "source" of the reflected waves). The field $A(\mathbf{r}_\perp)$ is split in an amplitude and a phase part, $A(\mathbf{r}_\perp) = |A(\mathbf{r}_\perp)|e^{i\phi(\mathbf{r}_\perp)}$. We assume that the phase is an extremely strong fluctuating function of position (i.e. the surface is extremely rough), such that $\phi(\mathbf{r}_\perp)$ has a white noise distribution,

$$\langle A(\mathbf{r}_{\perp 1})A(\mathbf{r}_{\perp 2})\rangle = \langle I(\mathbf{r}_{\perp 1})\rangle\delta(\mathbf{r}_{\perp 1}-\mathbf{r}_{\perp 2}) \tag{3.11}$$

With this assumption the quantity $\langle J_A(\hat{\mathbf{p}}_1,\hat{\mathbf{p}}_2)\rangle$ becomes,

$$\langle J_A(\hat{\mathbf{p}}_1,\hat{\mathbf{p}}_2)\rangle = \int\langle I(\mathbf{r}_\perp)\rangle e^{i\mathbf{r}_\perp(\hat{\mathbf{p}}_{\perp 1}-\hat{\mathbf{p}}_{\perp 2})}\mathrm{d}\mathbf{r}_\perp. \tag{3.12}$$

Introducing the difference between $\hat{\mathbf{p}}_1$ and $\hat{\mathbf{p}}_2$ as $\Delta\mathbf{p} = \hat{\mathbf{p}}_2 - \hat{\mathbf{p}}_1$ and substituting $\hat{\mathbf{p}}_1 \to \hat{\mathbf{p}}$, one obtains,

$$\langle J_A(\hat{\mathbf{p}},\hat{\mathbf{p}}+\Delta\mathbf{p})\rangle = \int\langle I(\mathbf{r}_\perp)\rangle e^{-i\Delta\mathbf{p}_\perp\mathbf{r}_\perp}\mathrm{d}\mathbf{r}_\perp; \qquad \langle I(\hat{\mathbf{p}})\rangle = J_A(\hat{\mathbf{p}},\hat{\mathbf{p}}). \tag{3.13}$$

From the above equation we see that the speckle correlation function Eq. (3.8) is determined by the Fourier transform of the spot on the rough surface,

$$C_S(\Delta\mathbf{p}_\perp) = \frac{\left|\int\langle I(\mathbf{r}_\perp)\rangle e^{-i\Delta\mathbf{p}_\perp\mathbf{r}_\perp}\mathrm{d}\mathbf{r}_\perp\right|^2}{\left|\int\langle I(\mathbf{r}_\perp)\rangle\mathrm{d}\mathbf{r}_\perp\right|^2}. \tag{3.14}$$

Eq. (3.14) describes over what angular direction the speckle is correlated, i.e. the average angular width of a speckle. The width of a speckle depends only on the size and shape of the source, which is determined by the incoming beam.

3.1.3 The number of independent speckle spots

We will determine the number of independent speckle spots in reflection. The speckle correlation function in Eq. (3.14) gives the angular size of a speckle. The area of one speckle spot in $\hat{\mathbf{p}}$-space is given by the integral over the speckle correlation function $C_S(\Delta\mathbf{p}_\perp)$,

$$\mathcal{S} = \int C_S(\Delta\mathbf{p}_\perp)\mathrm{d}\Delta\mathbf{p}_\perp. \tag{3.15}$$

The total available area in $\hat{\mathbf{p}}_\perp$-space (the area that is integrated over) is πk_0^2. The number of independent speckle spots N is the total area of the $\hat{\mathbf{p}}_\perp$-space divided by the area of one speckle spot $\mathcal{S}$. An extra factor of 2 is introduced to take the vector character of the light into account in this scalar theory. The vector character effectively doubles the number of independent speckle spots because of the two independent polarization directions.

$$N = \frac{2\pi k_0^2}{\mathcal{S}}. \tag{3.16}$$

As an example we will give the number of independent speckle spots for a Gaussian spot. For a Gaussian spot the amplitude is given by,

$$|A(\mathbf{r}_\perp)| = \frac{\sqrt{2}}{\rho_0\sqrt{\pi}} e^{\mathbf{r}_\perp{}^2/\rho_0^2}, \tag{3.17}$$

and the resulting number of independent speckle spots is given by,

$$N = \frac{2\pi^2\rho_0^2}{\lambda^2}. \tag{3.18}$$

We have obtained the intensity distribution and the angular correlation in the laser speckle reflected from a rough surface. The angular correlation was used to define the total number of independent speckle spots. The argument above is not completely correct. Energy conservation of the total reflected intensity correlates the intensity in independent speckle spots[48]. However we will use the above obtained results for a disordered slab, where energy conservation in the total reflection does not apply.

The number of independent speckle spots in transmission or reflection of laser light scattered by a disordered medium with $L \gg \ell$ can be calculated in a similar way. We saw that for the reflection from a rough surface the number of independent speckle spots depended only on the size and shape of the laser spot on the rough surface. We state that the size of the speckle spots generated by a disordered medium does only depend on the intensity distribution of the scattered light at the exit interface of the sample. In reality the light emerges from a layer of approximately a mean free path thick, but this is approximated by a plane at the ejection depth ($z = z_e$). Important difference with the rough surface is that in a disordered medium the incoming beam is broadened by diffuse propagation in the disordered medium[49]. The intensity distribution on the exit interface is calculated directly in $\mathbf{p}$-space, using the Ladder propagator of the previous chapter. $I_{in}(\mathbf{p}_\perp)$ is the Fourier transform of the incoming beam at the injection depth. $L(z_i, z_e, \mathbf{p}_\perp, \omega = 0)$ gives the diffuse broadening of the incoming beam. $\langle I_{out}(\mathbf{p}_\perp)\rangle$ is defined as the Fourier transform of the intensity profile on the exit interface at the ejection depth. The Fourier transform of the intensity profile on the exit interface $\langle I_{out}(\mathbf{p}_\perp)\rangle$ and the speckle correlation function $C_S(\Delta\mathbf{p}_\perp)$ are given by,

$$\langle I_{out}(\mathbf{p}_\perp)\rangle = \frac{\ell^2}{16\pi} I_{in}(\mathbf{p}_\perp) L(z_i, z_e, \mathbf{p}_\perp, \omega = 0); \qquad C_S(\Delta\mathbf{p}_\perp) = \frac{|\langle I_{out}(\Delta\mathbf{p}_\perp)\rangle|^2}{|\langle I_{out}(0)\rangle|^2}. \tag{3.19}$$

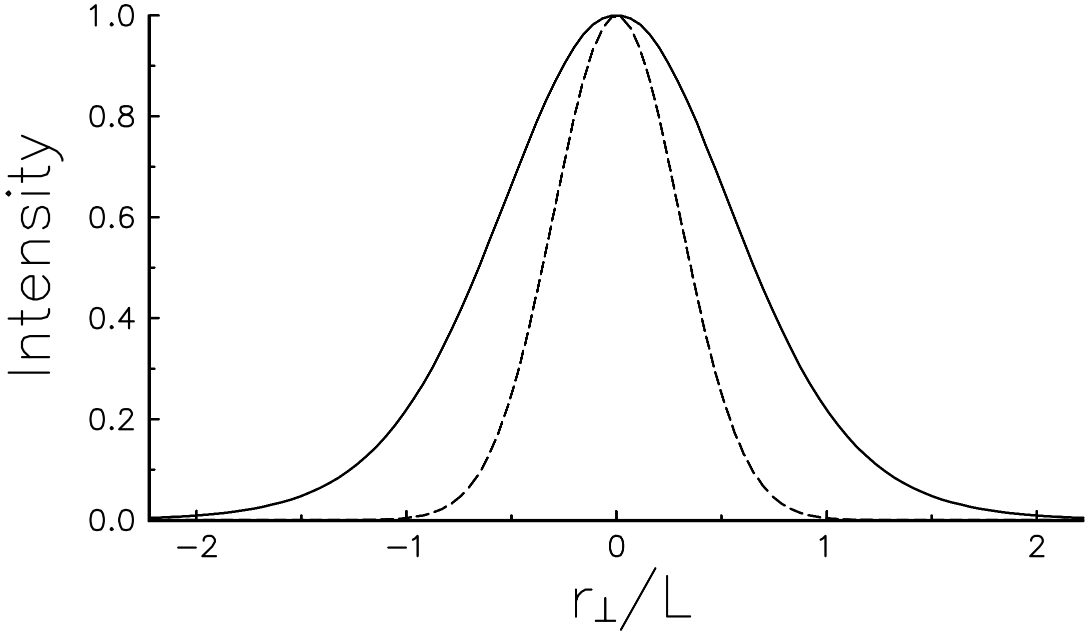

Figure 3.3: *The diffuse broadening of the incoming beam by the disordered medium in transmission. Dashed line: Gaussian intensity profile of the incoming beam Eq. (3.17) with $\rho_0 = 27\mu m$. Solid line: Calculated intensity profile at the exit interface ($z = z_e$) of a disordered sample of thickness $L = 45\mu m$, $\ell = 750nm$ and $\tau_0 = 2/3\ell$, by transforming $I_{out}(\mathbf{p}_\perp)$ in Eq. (3.19) to real space. The top of both curves is scaled to unity. The transverse coordinate $\mathbf{r}_\perp$ is scaled to the thickness L of the sample.*

For the Gaussian incoming beam in Eq. (3.17) the area in $\mathbf{p}_\perp$-space of one speckle spot in transmission ($z_e = L - 2\tau_0 - \frac{2}{3}\ell$) is,

$$\mathcal{S} = \int_0^\infty 2\pi p_\perp \left(\frac{L \sinh[(z_i + \tau_0)p_\perp] \sinh[(L - z_e - \tau_0)p_\perp]}{(z_i + \tau_0)(L - z_e - \tau_0)p_\perp \sinh[Lp_\perp]} \right)^2 e^{-p_\perp{}^2 \rho_0^2/4} \mathrm{d}p_\perp. \quad (3.20)$$

The number of independent speckle spots N in transmission is $N = 2\pi k_0^2/\mathcal{S}$. The number of independent speckle spots in reflection is found by taking $z_e = \frac{2}{3}\ell$, which for reasonable parameters ($\rho_0, L \gg \ell$) results in a number of modes slightly larger than for the random surface. The distribution of the intensity within one speckle spot and one polarisation direction is given by the Rayleigh distribution in Eq. (3.5). The number of independent speckle spots is an important parameter. In the next section we will discuss a waveguide with disorder. A discrete number of modes is supported by a waveguide. We will interpret the number of independent speckle spots as the number of modes supported by a waveguide.

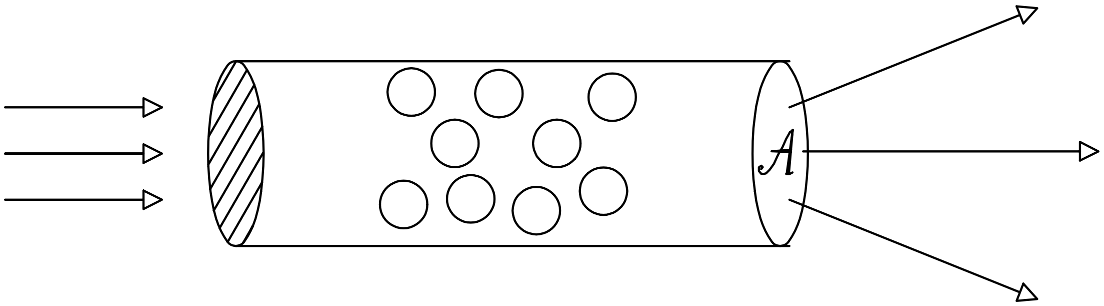

Figure 3.4: *Waveguide with disorder. The number of modes of the waveguide is* $N = \dfrac{2\pi\mathcal{A}}{\lambda^2}$.

3.2 Waveguide with disorder

We introduce a waveguide with disorder as a simple model to understand the multiple scattering regime. The waveguide is assumed to be ideal (i.e. perfectly reflecting walls), supporting discrete modes. In the middle the waveguide is filled with scatterers (see Fig. (3.4)). The disorder couples all ingoing modes to all outgoing modes in a random manner. Based on conservation of energy it will be shown that the modes in transmission and reflection have to be correlated. This argument was first used by Lee[50] to give a heuristic derivation of the Universal Conductance Fluctuations. The diameter of the waveguide determines the number of modes N that is supported,

$$N = \frac{2\pi\mathcal{A}}{\lambda^2}, \tag{3.21}$$

with λ the wavelength of the light and $\mathcal{A}$ the area of the cross section of the waveguide. The discrete modes can be labelled as $\mathbf{p}_{a\perp}$ and $\mathbf{p}_{b\perp}$ for respectively the incoming and outgoing mode, where $\mathbf{p}_\perp$ denotes the perpendicular component of the wave vector. The fraction of the intensity in incoming mode a that is coupled to outgoing mode b, T_{ab}, is determined by the realisation of the disorder. The average intensity that is scattered from mode a into mode b, $\langle T_{ab}\rangle$, is given by,

$$\langle T_{ab}\rangle \approx \frac{\ell}{NL}, \tag{3.22}$$

(See Eq. (2.146), Eq. (2.157) or Eq. (2.164) and divide by the number of modes). Although it will not be used in this section, we introduce the conductance g of the waveguide (or a disordered sample). The conductance is defined as the sum of the transmission coefficients over all incoming and all outgoing modes,

$$g \equiv \sum_{a,b}\langle T_{ab}\rangle \approx \frac{N\ell}{L}. \tag{3.23}$$

In analogy with the intensity distribution within one speckle spot, T_{ab} follows the Rayleigh distribution Eq. (3.5). The variance in the transmission is,

$$\langle \delta T_{ab}^2 \rangle = \langle (T_{ab} - \langle T_{ab} \rangle)^2 \rangle \approx \langle T_{ab} \rangle^2, \tag{3.24}$$

Assume for the time being that all outgoing modes are independent, then the total transmission $\langle T_a \rangle$ is the transmission $\langle T_{ab} \rangle$ summed over all outgoing modes,

$$\langle T_a \rangle = \sum_b \langle T_{ab} \rangle \approx \frac{\ell}{L}. \tag{3.25}$$

Using energy conservation $R_a + T_a = 1$ the average total reflection is (cf. Eq. (2.146)),

$$\langle R_a \rangle \approx \frac{L - \ell}{L}, \tag{3.26}$$

and the average reflection from mode a to mode a' is

$$\langle R_{aa'} \rangle \approx \frac{L - \ell}{NL}. \tag{3.27}$$

The coefficients $R_{aa'}$ follow also the Rayleigh distribution and the variance in the reflection is,

$$\langle \delta R_{aa'}^2 \rangle \approx \langle R_{aa'} \rangle^2 = \left(\frac{L - \ell}{NL} \right)^2. \tag{3.28}$$

Now it will be shown that the assumption of independent modes in transmission and reflection cannot be correct. Let us calculate the variance on the total transmission and the total reflection. For the variance on the total transmission we find,

$$\begin{gathered} \langle \delta T_a^2 \rangle = \langle T_a^2 \rangle - \langle T_a \rangle^2 = \langle \sum_b T_{ab} \sum_{b'} T_{ab'} \rangle - \langle \sum_b T_{ab} \rangle^2 = \\ N(N-1) \langle T_{ab} \rangle^2_{b \neq b'} + N \langle T_{ab}^2 \rangle_{b=b'} - N^2 \langle T_{ab} \rangle^2 = N \langle T_{ab} \rangle^2 = \frac{\ell^2}{NL^2}, \end{gathered} \tag{3.29}$$

where the assumption of independent modes is used. For the reflection we find,

$$\begin{gathered} \langle \delta R_a^2 \rangle = \langle R_a^2 \rangle - \langle R_a \rangle^2 = \langle \sum_{a'} R_{aa'} \sum_{a''} R_{aa''} \rangle - \langle \sum_{a'} R_{aa'} \rangle^2 = \\ N(N-1) \langle R_{aa'} \rangle^2_{a' \neq a''} + N \langle R_{aa'}^2 \rangle_{a'=a''} - N^2 \langle R_{aa'} \rangle^2 = \\ N \langle R_{aa'} \rangle^2 = \frac{(L-\ell)^2}{NL^2} \approx \frac{1}{N}. \end{gathered} \tag{3.30}$$

Energy conservation demands that the absolute fluctuations on the total transmission and total reflection are equal. As can be seen from Eqs. (3.29) and (3.30) this is not the case! The assumption of independent modes is not correct and somehow the transmission and the reflection coefficients become correlated. Measuring this correlation was the motivation for the experiments in chapter 4.

3.3 Correlation on the transmission

In this section we will start with an overview of the theory on correlations in the transmission of multiple scattered light by Shapiro[51], Stephen and Cwilich[52], Mello[53] and Feng *et al.*[8]. After this overview the theory of the short-range correlation and the long-range correlation are presented in detail. The subsection on the long-range correlation is the most important one. There we follow closely the article by Pnini and Shapiro[54], and extend their approach to incorporate experimental conditions that were crucial in the explanation of the experimental data to be presented in chapter 4. Finally, in appendix A, it is shown that a diagrammatic approach based on Nieuwenhuizen and van Rossum[55] gives a result that is exactly equal to the Langevin approach, introduced by Spivak and Zyuzin[56] and used by Pnini and Shapiro[54].

3.3.1 Three type of correlation on the transmission

As shown in section 3.2 the transmission coefficients of a waveguide with disorder or equivalently a disordered sample are correlated. Feng *et al.*[8] showed that one can distinguish three different type of correlations in the transmission,

$$C_{aba'b'} \equiv \langle \delta T_{ab} \delta T_{a'b'} \rangle = C_1 + C_2 + C_3, \tag{3.31}$$

each one of smaller magnitude. The first term, C_1, is of order unity. The second term, C_2, is of order g^{-1}, the last term, C_3, is of order g^{-2}, with g the conductance. The C_3 term is the optical analog of the Universal Conductance Fluctuations (UCF) observed in electronic systems[1, 2]. In the paper of Feng *et al.* the three type of angular correlations were defined as,

$$\begin{aligned} C^{(1)}_{aba'b'} &\equiv D_1 \langle T_{ab} \rangle \langle T_{a'b'} \rangle \delta_{\Delta \mathbf{p}_{\perp a}, \Delta \mathbf{p}_{\perp b}} F_1(\Delta \mathbf{p}_{\perp a} L), \\ C^{(2)}_{aba'b'} &\equiv D_2 g^{-1} \langle T_{ab} \rangle \langle T_{a'b'} \rangle [F_2(\Delta \mathbf{p}_{\perp a} L) + F_2(\Delta \mathbf{p}_{\perp b} L)], \\ C^{(3)}_{aba'b'} &\equiv D_3 g^{-2} \langle T_{ab} \rangle \langle T_{a/b'} \rangle, \end{aligned} \tag{3.32}$$

where the D's are constants of order unity and where F_1 and F_2 are form functions. The indices a and b label incoming respectively outgoing directions (modes) of the light with transverse wave vector $\mathbf{p}_{\perp a}$ and $\mathbf{p}_{\perp b}$ respectively. The C_1-part is of order 1 if $a = a'$ *and* $b = b'$, decays exponentially with increasing $\Delta \mathbf{p}_\perp \equiv \mathbf{p}_{\perp a} - \mathbf{p}_{\perp a'} = \mathbf{p}_{\perp b} - \mathbf{p}_{\perp b'}$ ("memory effect"), and is zero if $\Delta \mathbf{p}_{\perp a} \neq \Delta \mathbf{p}_{\perp b}$. The C_2-part is of the order g^{-1} if *either* $\Delta \mathbf{p}_{\perp a}$ *or* $\Delta \mathbf{p}_{\perp b} = 0$, and shows power-law decay with increasing $\Delta \mathbf{p}_\perp$. Finally the C_3-part is of the order g^{-2} and does not depend on either $\Delta \mathbf{p}_{\perp a}$ or $\Delta \mathbf{p}_{\perp b}$.

Each correlation function requires its own experimental set-up to be measured. The three experimental set-up's are shown in Fig. (3.5). The short-range correlation C_1 is measured in a one-mode-in-one-mode-out configuration. A laser beam falls on the sample. In transmission the detector is at a fixed position. The fluctuations are

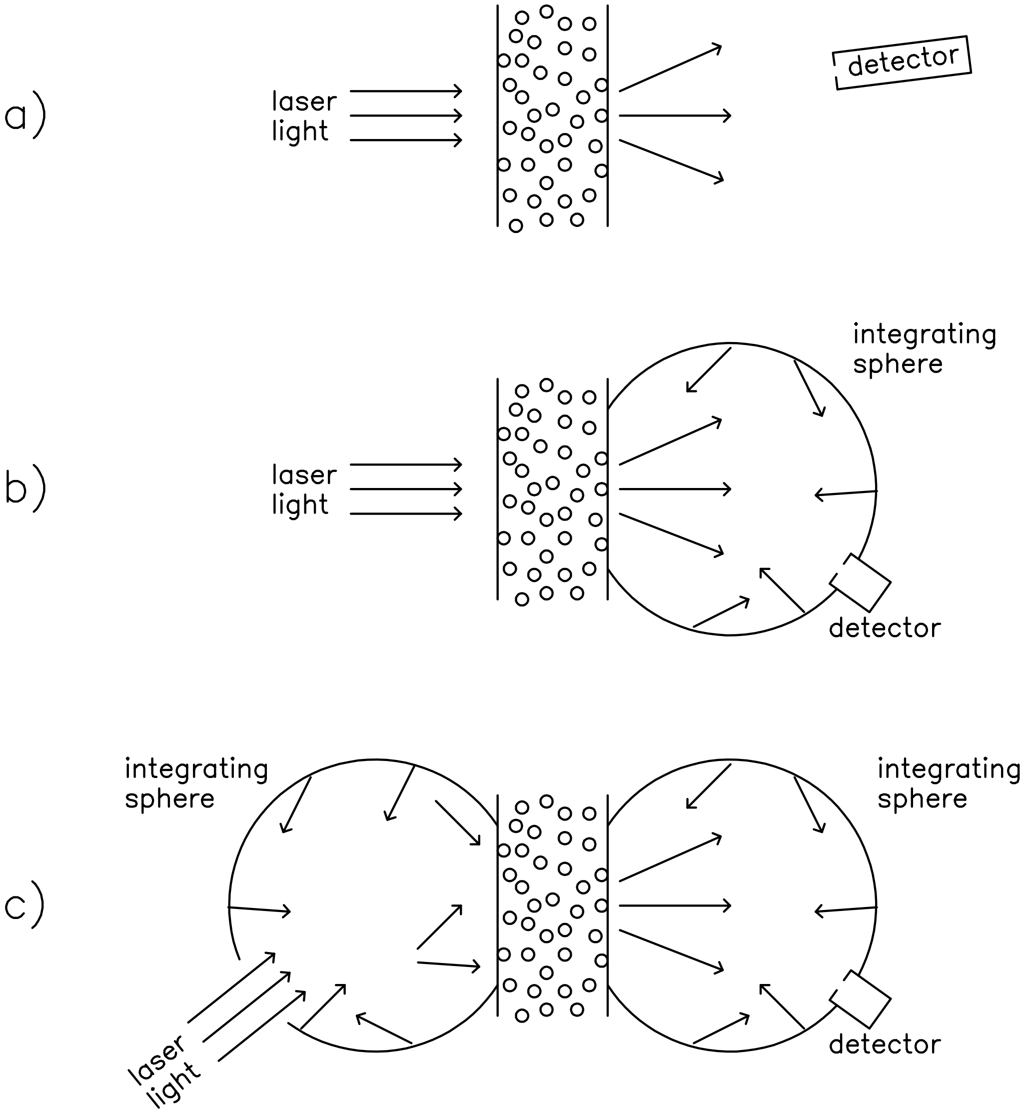

Figure 3.5: *The tree types of measurements of the correlation* $C_{aba'b'}$.

measured as a function of the angle of rotation of the sample. In this configuration the requirement $\delta_{\Delta\mathbf{p}_{\perp a},\Delta\mathbf{p}_{\perp b}}$ is met. A typical fluctuating intensity pattern recorded in this experimental set-up is shown in Fig. (3.1).

The long-range correlation C_2 is measured in a one-mode-in-all-modes-out or all-modes-in-one-mode-out configuration. We will concentrate on the first configuration. The integrating sphere in Fig. (3.5 b) collects all the transmitted light. A detector in a porthole of the integrating sphere detects the intensity inside the integrating sphere, which is proportional to the total transmitted intensity. The fluctuating pattern is measured as a function of the angle of rotation of the sample. Since the total transmission is the sum of many independent speckle spots, the fluctuations are much smaller than in the first experimental set-up, as can be seen in Fig. (4.2), and will be shown to have long-range correlation.

The last type of correlation, C_3, or the optical analog of the universal conductance correlation is measured in an all-modes-in-all-modes-out configuration. An integrating sphere scrambles the incoming direction of the laser light completely. In transmission the light is collected in an integrating sphere. The fluctuations should be recorded as a function of different sample-realizations (which is extremely impractical).

The same types of correlation: short-range, long-range, and ‘infinite-range’ (UCF) respectively, will show in the corresponding three components of the two-frequency correlator $\langle \delta T_{ab}(\omega)\delta T_{ab}(\omega')\rangle$ when not the angle but the frequency of the light is varied. The experimental configurations to measure the fluctuations are the same, but now instead of rotating the sample, the fluctuations are recorded as a function of wavelength (the frequency ω) of the incoming light. From an experimental point of view this is more convenient, since the spot of the laser beam on the sample varies when the sample is rotated. We will now turn to a detailed description of the short-range and the long-range correlation.

3.3.2 The short-range correlation C_1

The property that is calculated is the correlation in the second moment of the transmitted intensity as a function of incoming and outgoing angle of the light and as a function of frequency. A coherent laser beam falling on a disordered sample generates a speckle pattern in transmission. When the angle of incidence or the wavelength (the frequency) of the light is changed, the speckle pattern will change. We are interested in how much correlation exists in the speckle patterns as a function of the change in the angle of incidence or the wavelength (the frequency) of the light. The correlation is defined as,

$$C_{aba'b'}(\omega,\omega') \equiv \frac{\langle T_{ab}(\omega)T_{a'b'}(\omega')\rangle - \langle T_{ab}(\omega)\rangle^2}{\langle T_{ab}(\omega)\rangle^2}. \tag{3.33}$$

The average transmission from mode a to mode b, $\langle T_{ab}\rangle$, is given by,

$$\begin{aligned}\langle T_{ab}\rangle = \frac{\ell^2}{16\pi}\int\cdot\cdot\int \mathrm{d}\mathbf{r}_{\perp 1}\cdot\cdot\mathrm{d}\mathbf{r}_{\perp 4}\mathrm{d}t\, e^{-i\mathbf{p}_{\perp b}\mathbf{r}_{\perp 1}}e^{i\mathbf{p}_{\perp b}\mathbf{r}_{\perp 2}}\\ L(\mathbf{r}_{\perp 1},\mathbf{r}_{\perp 2},z_{1e},z_{2e};\mathbf{r}_{\perp 3},\mathbf{r}_{\perp 4},z_{3i},z_{4i},t)\rangle e^{i\mathbf{p}_{\perp a}\mathbf{r}_{\perp 3}}e^{-i\mathbf{p}_{\perp a}\mathbf{r}_{\perp 4}},\end{aligned} \tag{3.34}$$

with $L(\mathbf{r}_1,\mathbf{r}_2;\mathbf{r}_3,\mathbf{r}_4,t) = \delta(\mathbf{r}_1-\mathbf{r}_2)\delta(\mathbf{r}_3-\mathbf{r}_4)L(\mathbf{r}_1,\mathbf{r}_3,t)$ the bare intensity propagator, and where the injection depth in Eq. (2.144) and the ejection depth in Eq. (2.161) were used. In this calculation we take an incident plane wave. As can be shown the short-range correlation function does not depend on the beam profile[57].The relative phases of the incoming and outgoing plane waves is explained in Fig. (3.6).

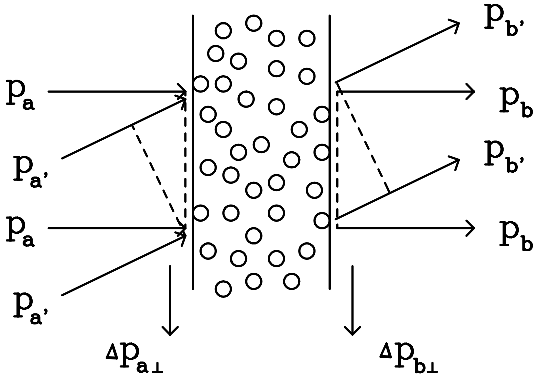

Figure 3.6: *Incoming and outgoing directions of the waves scattered by the disordered slab. The dashed lines denote the equal phase front of the waves. The incoming field in the direction* $\mathbf{p}_a$ *has a relative phase of* $e^{\mathbf{p}_{\perp a}\mathbf{r}_{\perp i}}$ *at the injection depth* z_i*. The outgoing field in the direction* $\mathbf{p}_b$ *has a relative phase of* $e^{-\mathbf{p}_{\perp b}\mathbf{r}_{\perp e}}$ *when observed far away from the slab.*

The intensity correlator $\langle T_{ab}(\omega)T_{a'b'}(\omega')\rangle$ is given by,

$$\begin{aligned}\langle T_{ab}(\omega)T_{a'b'}(\omega')\rangle = \frac{\ell^4}{(16\pi)^2}\int\cdots\int \mathrm{d}\mathbf{r}_{\perp 1}\cdots \mathrm{d}\mathbf{r}_{\perp 8}\times \\ \exp[-i\mathbf{p}_{\perp b}\mathbf{r}_{\perp 1} + i\mathbf{p}_{\perp b}\mathbf{r}_{\perp 2} - i\mathbf{p}_{\perp b}'\mathbf{r}_{\perp 3} + i\mathbf{p}_{\perp b}'\mathbf{r}_{\perp 4}]\times \\ \langle K(\omega,\omega',\mathbf{r}_{\perp 1},\cdots,\mathbf{r}_{\perp 4},z_{1e},\cdots,z_{4e};\mathbf{r}_{\perp 5},\cdots,\mathbf{r}_{\perp 8},z_{5i},\cdots,z_{8i})\rangle\times \\ \exp[i\mathbf{p}_{\perp a}\mathbf{r}_{\perp 5} - i\mathbf{p}_{\perp a}\mathbf{r}_{\perp 6} + i\mathbf{p}_{\perp a}'\mathbf{r}_{\perp 7} - i\mathbf{p}_{\perp a}'\mathbf{r}_{\perp 8}].\end{aligned} \tag{3.35}$$

The eight-point vertex $\langle K\rangle$ contains all possible four amplitude diagrams. Feng *et al.*[8] showed that the intensity correlations of interest can be classified by writing the eight-point vertex $\langle K\rangle$ in an expansion of g^{-1}, where $g \propto N\ell/L$. In the lowest order expansion the eight point vertex $\langle K\rangle$ factorizes as a product of two ladder vertices $\langle L\rangle\times\langle L\rangle$. Higher order terms of the expansion in g^{-1} contain Hikami boxes [58], (irreducible) eight-point vertices connecting two ladder vertices, which describe the long-range correlations in volume speckle. In this section we are interested in the short-range correlation only, which follows from the lowest order expansion of $\langle K\rangle$.

$$\begin{aligned}\langle K(\omega,\omega',\mathbf{r}_1,\cdots,\mathbf{r}_4;\mathbf{r}_5,\cdots,\mathbf{r}_8)\rangle = \\ \langle L(\omega,\omega,\mathbf{r}_1,\mathbf{r}_2;\mathbf{r}_5,\mathbf{r}_6)\rangle\times\langle L(\omega',\omega',\mathbf{r}_3,\mathbf{r}_4;\mathbf{r}_7,\mathbf{r}_8)\rangle \\ +\langle L(\omega,\omega',\mathbf{r}_1,\mathbf{r}_2;\mathbf{r}_5,\mathbf{r}_8)\rangle\times\langle L(\omega,\omega',\mathbf{r}_3,\mathbf{r}_4;\mathbf{r}_6,\mathbf{r}_7)\rangle.\end{aligned} \tag{3.36}$$

Only paired amplitudes survive the averaging process. Fig. (3.7) shows the lowest order expansion of $\langle K\rangle$. The vertex $\langle L(\omega,\omega)\rangle$ in Eq. (3.36) denotes the ladder diagrams in which two amplitudes with the same frequency travel along the same

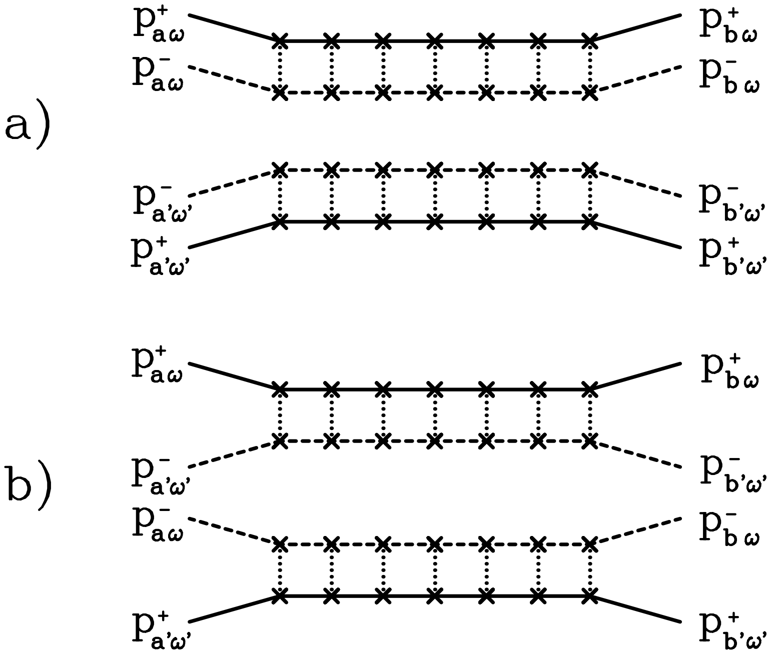

Figure 3.7: *Four amplitudes travelling through the slab, which can be combined in two ways in intensity propagators.*
Diagram (a) shows the first term of the factorization in Eq. (3.39), the trivial part. Diagram (b) shows the second term of the factorization in Eq. (3.39), the part that gives the correlation.

path,

$$\langle L(\omega,\omega,\mathbf{r}_1,\mathbf{r}_2;\mathbf{r}_5,\mathbf{r}_6)\rangle = \delta(\mathbf{r}_1-\mathbf{r}_2)\delta(\mathbf{r}_5-\mathbf{r}_6)\int L(\mathbf{r}_1,\mathbf{r}_5,t)\mathrm{d}t. \tag{3.37}$$

The vertex $\langle L(\omega,\omega')\rangle$ in Eq. (3.36) denotes the ladder diagrams in which two amplitudes with different frequency travel along the same path,

$$\langle L(\omega,\omega',\mathbf{r}_1,\mathbf{r}_2;\mathbf{r}_5,\mathbf{r}_8)\rangle = \delta(\mathbf{r}_1-\mathbf{r}_2)\delta(\mathbf{r}_5-\mathbf{r}_8)\int e^{i\Delta\omega t}L(\mathbf{r}_1,\mathbf{r}_5,t)\mathrm{d}t, \tag{3.38}$$

with $\Delta\omega = \omega - \omega'$. The effect of the different wavelengths of the two amplitudes is taken into account by observing that the phase difference between the two amplitudes that builds up during the propagation through the medium is given by $e^{i\Delta\omega t}$. Thus the intensity correlator $\langle T_{ab}(\omega)T_{a'b'}(\omega')\rangle$ in Eq. (3.33) consists of four amplitudes, which can be combined in two ways in intensity propagators as is shown in Fig. (3.7). The second moment $\langle T_{ab}(\omega)T_{a'b'}(\omega')\rangle$ factorizes in two parts,

$$\begin{aligned}\langle T_{ab}(\omega)T_{a'b'}(\omega')\rangle &= \langle T_{ab}(\omega)\rangle\langle T_{a'b'}(\omega')\rangle + \\ &\langle T_{ab}(\Delta\mathbf{p}_a,\Delta\mathbf{p}_b,\omega,\Delta\omega)\rangle\langle T_{a'b'}(\Delta\mathbf{p}_{a'},\Delta\mathbf{p}_{b'},\omega',\Delta\omega')\rangle.\end{aligned} \tag{3.39}$$

The last term in the right hand side of Eq. (3.39) is the product of two intensity propagators, where each one consists of an incoming amplitude and a complex conjugate with different incoming and outgoing angle and wavelength. The complex conjugate of $\langle T_{a'b'}(\Delta\mathbf{p}_{a'}, \Delta\mathbf{p}_{b'}, \omega', \Delta\omega')\rangle$ is exactly $\langle T_{ab}(\Delta\mathbf{p}_a, \Delta\mathbf{p}_b, \omega, \Delta\omega)\rangle$. The correlation is determined by the last term in the r.h.s. of Eq. (3.39),

$$C_{aba'b'}(\omega, \omega') = \frac{|\langle T_{ab}(\Delta\mathbf{p}_a, \Delta\mathbf{p}_b, \omega, \Delta\omega)\rangle|^2}{\langle T_{ab}(\omega)\rangle^2}. \tag{3.40}$$

As is seen in Fig. (3.7) two incoming plane waves with transversal wave vector $\mathbf{p}_{a\perp}$ and $\mathbf{p}_{a'\perp} = \mathbf{p}_{a\perp} - \Delta\mathbf{p}_{a\perp}$ and internal frequency $\omega$and $\omega' = \omega + \Delta\omega$ and two outgoing plane waves with transversal wave vector $\mathbf{p}_{b\perp}$ and $\mathbf{p}_{b'\perp} = \mathbf{p}_{b\perp} - \Delta\mathbf{p}_{b\perp}$ are attached to the propagator $L(z_i, z_e, \mathbf{r}_{\perp i}, \mathbf{r}_{\perp e}, t)$,

$$\begin{aligned} &\langle T_{ab}(\Delta\mathbf{p}_a, \Delta\mathbf{p}_b, \omega, \Delta\omega)\rangle = \\ &\frac{\ell^2}{16\pi}\int e^{i\Delta\mathbf{p}_{\perp a}\mathbf{r}_{\perp i}} e^{-i\Delta\mathbf{p}_{\perp b}\mathbf{r}_{\perp e}} e^{i\Delta\omega t} L(z_i, z_e, \mathbf{r}_{i\perp}, \mathbf{r}_{\perp e}, t)\mathrm{d}t\mathrm{d}\mathbf{r}_{\perp i}\mathrm{d}\mathbf{r}_{\perp e} = \\ &\frac{\ell^2}{16\pi}(2\pi)^2\delta(\Delta\mathbf{p}_{\perp a} - \Delta\mathbf{p}_{\perp b})L(z_i, z_e, \Delta\mathbf{p}_{\perp a}, \Delta\omega). \end{aligned} \tag{3.41}$$

Notice the resulting delta function in Eq. (3.41), which gives the condition that the change in the incoming angle has to be equal to the change in the outgoing angle of the light, $\Delta\mathbf{p}_{\perp a} = \Delta\mathbf{p}_{\perp b}$. In experiments, as described in chapter 4 and 6, where a finite spot size is used, this condition can be relaxed to the condition that $\Delta\mathbf{p}_{\perp a} - \Delta\mathbf{p}_{\perp b}$ is (much) smaller than the angular width of a speckle. Using the injection depth $z_i = \ell$ (Eq. (2.144)), the ejection depth $z_e = L - \frac{2}{3}\ell - 2\tau_0$ (Eq. (2.161)), the approximate form of the bare Ladder vertex in Eq. (2.162) and the approximation $\sinh(x) \approx x$ we obtain for the correlation function in Eq. (3.40),

$$C_{aba'b'}(\omega, \omega') = \left| \frac{L(\Delta\mathbf{p}_{\perp a}^2 + \frac{1}{D\tau_a} - \frac{i\Delta\omega}{D})^{1/2}}{\sinh\left[L(\Delta\mathbf{p}_{\perp a}^2 + \frac{1}{D\tau_a} - \frac{i\Delta\omega}{D})^{1/2}\right]} \right|^2; \quad \text{with } \Delta\mathbf{p}_{\perp a} = \Delta\mathbf{p}_{\perp b}. \tag{3.42}$$

The correlation in Eq. (3.42) is called the short-range correlation, because it shows an exponential decay, in contrast to the long-range correlation that will be derived later. The short-range correlation functions that depend only on angle or frequency are given by respectively,

$$\begin{aligned} C_{aba'b'}(\omega, \omega) &= \frac{L^2(\Delta\mathbf{p}_{\perp a}^2 + \frac{1}{D\tau_a})}{\sinh^2[L(\Delta\mathbf{p}_{\perp a}^2 + \frac{1}{D\tau_a})^{1/2}]} \quad \text{with } \Delta\mathbf{p}_{\perp a} = \Delta\mathbf{p}_{\perp b} & (3.43) \\ C_{abab}(\omega, \omega') &= \frac{2L^2\Delta\omega/D}{\cosh[L(2\Delta\omega/D)^{1/2}] - \cos[L(2\Delta\omega/D)^{1/2}]}. & (3.44) \end{aligned}$$

When measuring the angular part of the short-range correlation in an experimental set-up the requirement $\Delta\mathbf{p}_{\perp a} = \Delta\mathbf{p}_{\perp b}$ is fulfilled by keeping the laser and the

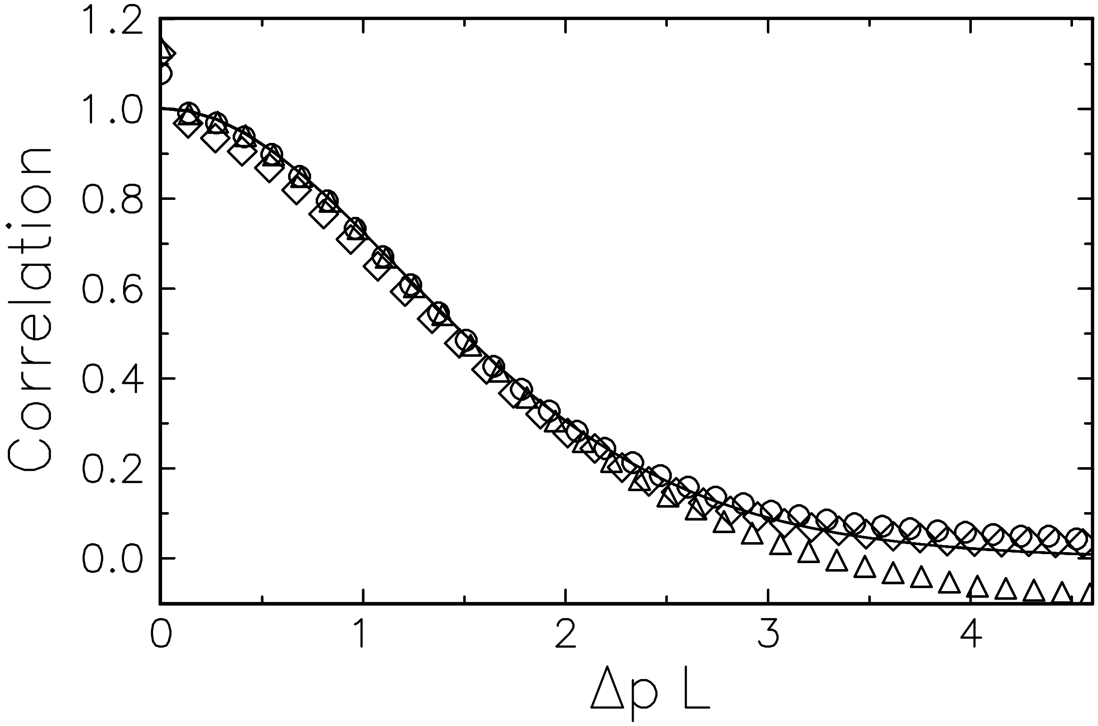

Figure 3.8: *A result from the experiments to be described in chapter 6, the measured short-range correlation as a function of the angle of rotation of the sample,* $p_\perp = \frac{2\pi}{\lambda}\sin\theta$*. The x-axis is scaled to* $\Delta p_\perp L$ *to make the curves for different sample thickness coincide. Symbols: experimental data for* $\triangle$: $L = 27\mu m$, $\circ$: $L = 38\mu m$, $\diamond$: $L = 65\mu m$*. Solid line: Theoretical curve of Eq. (3.43). The correlations were measured in the infra-red region.*

detector at fixed positions and rotating the sample. The angular short-range correlation, a result from the experiments to be described in chapter 6, is shown here in Fig. (3.8). The frequency dependence is measured by keeping the laser and the detector at fixed positions and varying the wavelength of the laser. The measurements of the frequency short-range correlation will be presented in chapter 4. Two different parameters can be determined from the measurement of the short-range correlation functions. From the angular correlation function the thickness of the sample can be determined. From the frequency correlation the diffusion constant in the medium can be determined (if the thickness is known). The diffusion constant is an important parameter, since the mean free path can be derived from it.

3.4 Long-range correlation

We turn to the long-range correlation, the correlation on the total transmission. The theory derived here will be used to describe the experimental results in the next chapter of the measurements of the long-range correlation in the fluctuations of the total transmission. Because of interference, the intensity *inside* the static random dielectric slab will fluctuate strongly in space ("volume speckle"). Correlation in the total transmitted intensity may be calculated using a Langevin approach. In this approach, which was first used in the present context by Spivak *et al.*[56], volume speckle acts as a source for a fluctuating flux component $\mathbf{j}_{ext}(\mathbf{r})$, which leads to the long-range intensity correlations. The fluctuating flux component $\mathbf{j}_{ext}(\mathbf{r})$ is generated by the large fluctuations in the intensity (volume speckle). The decay of the volume speckle with frequency or incoming angle of the light leads to a decay in the fluctuating flux correlation, which determines the long-range correlation. Pnini *et al.*[54] used the method to calculate a.o. the intensity-intensity correlation in the total transmission as a function of frequency shift for an incident plane wave. We shall extend Pnini's method to include an incident beam with Gaussian intensity profile in the theory, which we will need to be able to describe the experimental results of our experimental set-up. We will first calculate the correlation in the volume speckle that incorporates the influence of the beam profile. The correlation in the volume speckle will be used to determine the local flux-flux correlator. Using the Langevin approach we will then calculate the long-range correlation on the total transmission.

3.4.1 Short-range correlation in "volume"-speckle

The average correlation in the intensity in a correlation volume (speckle-spot) at depth z is calculated as a function of incoming angle and wavelength. The correlation function *inside* the medium is defined as,

$$C_{aa'}(\omega, \triangle\omega, \mathbf{r}) \equiv \frac{\langle I_a(\omega,\mathbf{r})\, I_{a'}(\omega',\mathbf{r})\rangle - \langle I_a(\omega,\mathbf{r})\rangle\langle I_{a'}(\omega',\mathbf{r})\rangle}{\langle I_a(\omega,\mathbf{r})\rangle\langle I_{a'}(\omega',\mathbf{r})\rangle}, \tag{3.45}$$

with $\langle I_a(\omega,\mathbf{r})\rangle$ the isotropic (diffuse) intensity at $\mathbf{r}$ due to incoming light with transverse wave vector $\mathbf{p}_{\perp a}$ and frequency ω inside the medium. From now on we drop the ω dependence in $C(\omega, \Delta\omega, \mathbf{r})$. Writing the diffuse part $\langle I_a(\omega,\mathbf{r})\rangle$ in its field components we get

$$\begin{aligned}\langle I_a(\omega,\mathbf{r})\rangle &= \int\cdot\cdot\int \mathrm{d}\mathbf{r}_1\cdot\cdot\mathrm{d}\mathbf{r}_4\,\langle G(\omega,\mathbf{r},\mathbf{r}_3)\rangle\langle G^*(\omega,\mathbf{r},\mathbf{r}_4)\rangle\times\\ &\quad\langle L(\omega,\mathbf{r}_3,\mathbf{r}_4;\mathbf{r}_1,\mathbf{r}_2)\rangle\langle\Psi_a(\omega,\mathbf{r}_1)\rangle\langle\Psi_a^*(\omega,\mathbf{r}_2)\rangle\\ &= 4\pi\int H(\mathbf{r}_1,\mathbf{r})\delta(\mathbf{r}_1-\mathbf{r}_2)\langle\Psi_a(\omega,\mathbf{r}_1)\rangle\langle\Psi_a^*(\omega,\mathbf{r}_2)\rangle\mathrm{d}\mathbf{r}_1\mathrm{d}\mathbf{r}_2,\end{aligned} \tag{3.46}$$

with $\langle G(\omega,\mathbf{r},\mathbf{r}_3)\rangle$ the average amplitude Green's function for propagation from $\mathbf{r}_3$ to $\mathbf{r}$ in a disordered medium, and $\langle\Psi_a(\omega,\mathbf{r}_1)\rangle$ the incoming amplitude with transversal wave vector $\mathbf{p}_{\perp a}$. Writing the correlator $\langle I_a(\omega,\mathbf{r})\, I_{a'}(\omega',\mathbf{r})\rangle$ in its field components we get

$$\begin{aligned}\langle I_a(\omega,\mathbf{r})\, I_{a'}(\omega',\mathbf{r})\rangle = \int\cdots\int \mathrm{d}\mathbf{r}_1\cdots\mathrm{d}\mathbf{r}_8\, \langle G(\omega,\mathbf{r},\mathbf{r}_5)\rangle\langle G^*(\omega,\mathbf{r},\mathbf{r}_6)\rangle \times \\ \langle G(\omega',\mathbf{r},\mathbf{r}_7)\rangle\langle G^*(\omega',\mathbf{r},\mathbf{r}_8)\rangle\langle K(\omega,\omega',\mathbf{r}_5,\cdots,\mathbf{r}_8;\mathbf{r}_1,\cdots,\mathbf{r}_4)\rangle \times \\ \langle\Psi_a(\omega,\mathbf{r}_1)\rangle\langle\Psi_a^*(\omega,\mathbf{r}_2)\rangle\langle\Psi_{a'}(\omega',\mathbf{r}_3)\rangle\langle\Psi_{a'}^*(\omega',\mathbf{r}_4)\rangle. \qquad (3.47)\end{aligned}$$

The eight-point vertex $\langle K\rangle$ factorizes in the same way as in section 3.3.2 (See also Fig. (A.1)). Using Eqs. (3.46), (3.47) and (3.36) the numerator of Eq. (3.45) is written as

$$\begin{aligned}\langle I(\omega,\mathbf{r})\rangle^2\, C_{aa'}(\Delta\omega,\mathbf{r}) = \int \langle G(\omega,\mathbf{r},\mathbf{r}_5)\rangle\langle G^*(\omega',\mathbf{r},\mathbf{r}_6)\rangle \times \\ \langle L(\omega,\omega',\mathbf{r}_5,\mathbf{r}_6;\mathbf{r}_1,\mathbf{r}_4)\rangle\langle\Psi_a(\omega,\mathbf{r}_1)\rangle\langle\Psi_{a'}^*(\omega',\mathbf{r}_4)\rangle \mathrm{d}\mathbf{r}_1\mathrm{d}\mathbf{r}_4\mathrm{d}\mathbf{r}_5\mathrm{d}\mathbf{r}_6 \times \\ \int \langle G(\omega',\mathbf{r},\mathbf{r}_7)\rangle\langle G^*(\omega,\mathbf{r},\mathbf{r}_8)\rangle \times \\ \langle L(\omega,\omega',\mathbf{r}_7,\mathbf{r}_8;\mathbf{r}_2,\mathbf{r}_3)\rangle\langle\Psi_{a'}(\omega',\mathbf{r}_3)\rangle\langle\Psi_a^*(\omega,\mathbf{r}_2)\rangle \mathrm{d}\mathbf{r}_2\mathrm{d}\mathbf{r}_3\mathrm{d}\mathbf{r}_7\mathrm{d}\mathbf{r}_8. \qquad (3.48)\end{aligned}$$

To ease the calculation the incoming amplitudes are decomposed into their plane wave components at the injection depth z_i,

$$\Psi_{a\omega}(\mathbf{q}_\perp) = \int \mathrm{d}\mathbf{r}_\perp \Psi_a(\mathbf{r}_\perp,\omega) e^{i\mathbf{r}_\perp\mathbf{q}_\perp}; \quad \Psi_a(\mathbf{r}_\perp,\omega) = \frac{1}{(2\pi)^2}\int \mathrm{d}\mathbf{q}_\perp \Psi_{a\omega}(\mathbf{q}_\perp) e^{-i\mathbf{r}_\perp\mathbf{q}_\perp}. \qquad (3.49)$$

Using the plane wave decomposition of the incoming waves and the injection source in Eq. (2.144) the average intensity in Eq. (3.46) becomes,

$$\begin{aligned}\langle I_a(\omega,\mathbf{r})\rangle = \frac{\ell}{(2\pi)^4}\int \langle\Psi_{a\omega}(\mathbf{q}_{1\perp})\rangle\langle\Psi_{a'\omega}^*(\mathbf{q}_{2\perp})\rangle \times \\ \exp[-i\mathbf{r}_{1\perp}\Delta\mathbf{q}_{1\perp}] H(t,z_i,z,\mathbf{r}_{1\perp}-\mathbf{r}_\perp)\mathrm{d}\mathbf{q}_{1\perp}\mathrm{d}\mathbf{q}_{2\perp}\mathrm{d}\mathbf{r}_{1\perp}\mathrm{d}t, \qquad (3.50)\end{aligned}$$

with $\Delta\mathbf{q}_{1\perp} \equiv \mathbf{q}_{2\perp} - \mathbf{q}_{1\perp}$. In the same way using the two frequency Ladder in Eq. (3.38) Eq. (3.48) becomes,

$$\begin{aligned}\langle I(\mathbf{r}_\perp,z)\rangle^2\, C_{aa'}(\Delta\omega,\mathbf{r}_\perp,z) = \frac{\ell^2}{(2\pi)^8} \times \\ \int \langle\Psi_{a\omega}(\mathbf{q}_{1\perp})\rangle\langle\Psi_{a'\omega'}^*(\mathbf{q}_{4\perp})\rangle\, e^{-i\mathbf{r}_{1\perp}\Delta\mathbf{q}_{1\perp}} H(t,z_i,z,\mathbf{r}_\perp-\mathbf{r}_{1\perp})\, e^{i\Delta\omega t}\mathrm{d}\mathbf{q}_{1\perp}\mathrm{d}\mathbf{q}_{4\perp}\mathrm{d}\mathbf{r}_{1\perp}\mathrm{d}t \times \\ \int \langle\Psi_{a'\omega'}(\mathbf{q}_{3\perp})\rangle\langle\Psi_{a\omega}^*(\mathbf{q}_{2\perp})\rangle\, e^{i\mathbf{r}_{2\perp}\Delta\mathbf{q}_{2\perp}} H(t,z_i,z,\mathbf{r}_\perp-\mathbf{r}_{2\perp})\, e^{-i\Delta\omega t}\mathrm{d}\mathbf{q}_{2\perp}\mathrm{d}\mathbf{q}_{3\perp}\mathrm{d}\mathbf{r}_{2\perp}\mathrm{d}t, \qquad (3.51)\end{aligned}$$

with $\Delta\mathbf{q}_{1\perp} \equiv \mathbf{q}_{4\perp} - \mathbf{q}_{1\perp}$ and $\Delta\mathbf{q}_{2\perp} \equiv \mathbf{q}_{3\perp} - \mathbf{q}_{2\perp}$. We now integrate over t, $\mathbf{r}_{1\perp}$ and $\mathbf{r}_{2\perp}$ respectively, which gives the Fourier transform of H_L in Eq. (2.140). Since we are only interested in the average correlation at depth z, Eq. (3.51) is integrated over $\mathbf{r}_\perp$. Subsequent integration over $\Delta\mathbf{q}_{2\perp}$ gives $\Delta\mathbf{q}_{1\perp} = \Delta\mathbf{q}_{2\perp}$. The short-range correlation in volume speckle as a function of depth in the slab, beam profile, incoming angle and frequency-shift is then given by

$$\langle I(z)\rangle^2\, C_{aa'}(\Delta\omega, z) = \frac{v_{_E}^2(\ell+\tau_0)^2}{4(2\pi)^8 D^2}\times$$
$$\int \langle\Psi_a(\mathbf{q}_{1\perp})\rangle\langle\Psi^*_{a'}(\mathbf{q}_{1\perp}+\Delta\mathbf{q}_{1\perp})\rangle\langle\Psi_{a'}(\mathbf{q}_{2\perp}+\Delta\mathbf{q}_{1\perp})\rangle\langle\Psi^*_a(\mathbf{q}_{2\perp})\rangle\times$$
$$\frac{\cosh[2(L-z)\gamma_1]-\cos[2(L-z)\gamma_2]}{\cosh[2L\gamma_1]-\cos[2L\gamma_2]}\mathrm{d}\mathbf{q}_{1\perp}\mathrm{d}\mathbf{q}_{2\perp}\mathrm{d}\Delta\mathbf{q}_{1\perp}, \qquad (3.52)$$

with $\gamma_1 \equiv (a^2+b^2)^{1/4}\cos(\phi/2)$, $\gamma_2 \equiv (a^2+b^2)^{1/4}\sin(\phi/2)$, $a \equiv \Delta\omega/D$, $b \equiv \Delta\mathbf{q}^2_{1\perp}+k_a^2$, $k_a \equiv \sqrt{1/D\tau_a}$ and $\tan\phi \equiv a/b$. Eq. (3.52) holds independently for 3 orthogonal directions of polarization. To summarize, Eq. (3.52) gives the correlation function of the fluctuations (bulk speckle)*inside* the sample. In the Langevin approach that we are going to use, the local strong fluctuations in the intensity (they are of order unity) will generate local random fluxes, which act as sources for the fluctuations on the total transmission. The local random flux is a consequence of the local spatial intensity fluctuations. When the local spatial intensity changes (as described by Eq. (3.52)) the local fluxes change, and consequently the total transmission changes. The importance of Eq. (3.52) is that the correlation in the local intensity fluctuations will describe the correlation in the local current fluctuations as a function of the angle of incidence of the light or the frequency change. An important second observation is that the correlation function of the bulk speckle depends not only on the angle of incidence of the light or the frequency change, but also on the incoming beam profile.

3.4.2 Long-range correlation in the Langevin approach

The local random fluctuating flux is determined by the fluctuations on the local intensity $\delta I(\mathbf{r}) \equiv I(\mathbf{r}) - \langle I(\mathbf{r})\rangle$ according to the following constitutive equation,

$$D\nabla^2\delta I(\omega,\mathbf{r}) = \nabla\cdot\mathbf{j}_{ext}(\omega,\mathbf{r}). \qquad (3.53)$$

As is shown in Pnini's paper[54], from Eq. (3.53) an expression for the long-range intensity correlation function $\langle\delta I(\omega,\mathbf{p}_{\perp 1},z_1)\,\delta I^*(\omega',\mathbf{p}_{\perp 2},z_2)\rangle_{aa'}$ is obtained (the Fourier transform in the (x,y) plane is taken) that in our notation reads

$$\langle\delta I(\omega,\mathbf{p}_{\perp 1},z_1)\,\delta I^*(\omega',\mathbf{p}_{\perp 2},z_2)\rangle_{aa'} =$$
$$D^{-2}\int_0^L\int_0^L \mathrm{d}\,z'\,\mathrm{d}\,z''\ \langle j^i_{ext}(\omega,\mathbf{p}_{\perp 1},z')\,j^{i\,*}_{ext}(\omega',\mathbf{p}_{\perp 2},z'')\rangle_{aa'}\times$$
$$[\,H_D(\mathbf{p}_{\perp 1};z_1,z')\,H_D(\mathbf{p}_{\perp 2};z_2,z'')\,(\mathbf{p}_{\perp 1}\cdot\mathbf{p}_{\perp 2}) + H'_D(\mathbf{p}_{\perp 1};z_1,z')\,H'_D(\mathbf{p}_{\perp 2};z_2,z'')\,], \qquad (3.54)$$

where

$$H_D(\mathbf{p}_\perp;z,z') = \frac{\sinh[p_\perp z_<]\ \sinh[p_\perp(L-z_>)]}{p_\perp\ \sinh[p_\perp L]}, \qquad (3.55)$$

is the propagator of the diffusion equation in Eq. (3.53), $z_< \equiv min[z,z']$, $z_> \equiv max[z,z']$ and $H'_D(\mathbf{p}_\perp; z, z')$ is the derivative of H_D with respect to its second argument z'. The flux correlator $\langle j_{ext}(\omega,\mathbf{r})\; j^*_{ext}(\omega',\mathbf{r}')\rangle_{aa'}$ in Eq. (3.54) is obtained from the correlation function (Eq. (3.52)) for volume speckle and the velocity of energy transport v_E between neighbouring correlation volumes.

Originally the Langevin approach was used to describe the brownian motion of a particle[59]. A random external force F_{ext} on the particle was proposed, with $\langle F_{ext}(t)\rangle = 0$ and $\langle F_{ext}(t)F_{ext}(t')\rangle = \Gamma\delta(t-t')$. Here we apply the Langevin approach not to a random force in time, but to a random flux j_{ext} in space, static in time, $\langle j_{ext}(\mathbf{r})\rangle = 0$, $\langle j_{ext}(\mathbf{r})j_{ext}(\mathbf{r}')\rangle = \Gamma\delta(\mathbf{r}-\mathbf{r}')$. With heuristic arguments we will derive the magnitude Γ of the random flux correlator. The large fluctuations in the intensity (volume speckle) lead to local random fluxes $\mathbf{j}_{ext}(\mathbf{r})$. The correlation in $\mathbf{r}$-space between these random fluxes is determined by the size in $\mathbf{r}$-space of one volume speckle. Since on the length scale of one volume speckle spot (the volume of one speckle is approximately $\ell\lambda^2$) the diffusion propagator varies slowly, the dependence of $\langle j_{ext}(\omega,\mathbf{r})\; j^*_{ext}(\omega',\mathbf{r}')\rangle_{aa'}$ on $|\mathbf{r}-\mathbf{r}'|$ is replaced by a δ-function. The 'strength' of this δ-function is found by integrating the *spatial* short-range correlation function [51] over space to obtain the correlation volume of one speckle spot (this yields $2\pi\ell/k^2$ with k the wave vector in the medium). The magnitude of the random flux and the flux correlator are determined by the energy transport velocity and the fluctuations of the volume speckle, respectively,

$$j_{ext} = v_E(I-\langle I\rangle); \qquad \langle j^i_{ext} j^j_{ext}\rangle = \delta_{ij}\frac{v_E^2\langle (I-\langle I\rangle)^2\rangle}{3}, \tag{3.56}$$

where averaging over angles gave a factor of 1/3. The correlation between the random fluxes as a function of angle of incidence or the frequency change of the incoming light is given by the correlation function of volume speckle. For the flux correlator it results in,

$$\langle j^i_{ext}(\omega,\mathbf{r})\; j^{j\,*}_{ext}(\omega',\mathbf{r}')\rangle_{aa'} = \delta_{ij}\;\frac{v_E^2\pi\ell}{3k^2}\;\langle I(\mathbf{r})\rangle^2\; C_{aa'}(\Delta\omega,\mathbf{r}_\perp,z)\;\delta(\mathbf{r}_\perp-\mathbf{r}'_\perp)\;\delta(z-z'). \tag{3.57}$$

The prefactor that we obtain in the right-hand side of Eq. (3.57) is a factor of 2 lower than the corresponding factor in Pnini's paper, to make up for the fact that $\mathbf{j}_{ext}(\omega, r)$ consists of two independent polarization components. An other important difference is the appearance of the energy transport velocity in Eq. (3.57).

In order to obtain a description that goes beyond the plane-wave solution for the correlation in the total transmission in Pnini's paper we have to retain the information of the beam profile in the flux correlator. We proceed as follows. We transform Eq. (3.54) to real space, and integrate over $\mathbf{r}_{1\perp}$ and $\mathbf{r}_{2\perp} \equiv \mathbf{r}_{1\perp} + \Delta\mathbf{r}_\perp$ at $z_1, z_2 = z_e$, with z_e the ejection depth, to obtain the fluctuations on the total transmission $\delta T = \pi\delta I(z_e)$, in analogy with Eq. (2.147),

$$\langle \delta T^2(\Delta\omega)\,\rangle_{aa'} \equiv \frac{\pi^2}{(2\pi)^4}\int \langle \delta I(\omega,\mathbf{p}_{\perp 1},z_e)\;\delta I^*(\omega',\mathbf{p}_{\perp 2},z_e)\rangle_{aa'}$$

$$
e^{i\mathbf{r}_{1\perp}(\mathbf{p}_{\perp 1}-\mathbf{p}_{\perp 2})}\, e^{-i\mathbf{p}_{\perp 2}\Delta\mathbf{r}_\perp}\mathrm{d}\mathbf{r}_{1\perp}\mathrm{d}\Delta\mathbf{r}_\perp\mathrm{d}\mathbf{p}_{\perp 1}\mathrm{d}\mathbf{p}_{\perp 2}
$$
$$
= \pi^2\langle\delta I(\omega,\mathbf{p}_{\perp 1}=0,z_e)\,\delta I^*(\omega',\mathbf{p}_{\perp 2}=0,z_e)\rangle_{aa'}. \tag{3.58}
$$

Since after the integration over $\mathbf{r}_{1\perp}$ in Eq. (3.58) it holds $\mathbf{p}_{\perp 1}=\mathbf{p}_{\perp 2}$, Eq. (3.54) depends on the length of the vector $\mathbf{p}_\perp$ only, and the effect of absorption may be introduced by substituting $\mid\mathbf{p}_\perp\mid\to\sqrt{\mid\mathbf{p}_\perp\mid^2+k_a^2}$ with $k_a=\sqrt{1/D\tau_a}$, where τ_a is the inelastic mean-free time. Moreover, because $\mathbf{p}_{\perp 1}=\mathbf{p}_{\perp 2}$, the Fourier transform in the (x,y) plane of the flux correlator (Eq. (3.57)) that depends on $\mathbf{p}_{\perp 1}-\mathbf{p}_{\perp 2}$, turns out to be independent of $\mathbf{p}_\perp$ and will read

$$
\langle j_{ext}(\omega,\mathbf{p}_{\perp 1},z)\,j^*_{ext}(\omega',\mathbf{p}_{\perp 1},z)\rangle_{aa'}=\frac{v_E^2\pi\ell}{3k^2}\,\langle I(z)\rangle^2\,C_{aa'}(\Delta\omega,z). \tag{3.59}
$$

Though independent of $\mathbf{p}_{\perp 1}$, the flux correlator still depends on the beam profile through the correlation function for volume speckle (see Eq. (3.52)). Assuming the perpendicular incident beam to be Gaussian, we have

$$
\langle\Psi_{inc}(\mathbf{r}_\perp)\rangle=\frac{\sqrt{2}}{\rho_0\sqrt{\pi}}e^{-\mathbf{r}_\perp^2/\rho_0^2}, \tag{3.60}
$$

and its Fourier transform

$$
\langle\Psi_{inc}(\mathbf{q}_\perp)\rangle=\rho_0\sqrt{2\pi}e^{-\mathbf{q}_\perp^2\rho_0^2/4}. \tag{3.61}
$$

The plane wave decomposition around the incoming direction $\mathbf{q}_{a\perp}$ of the cylindrical symmetric beam is then given by the above plane wave decomposition, with the argument $\mathbf{q}_\perp$ shifted by $\mathbf{q}_{a\perp}$,

$$
\Psi_a(\mathbf{q}_\perp)=\Psi_{inc}(\mathbf{q}_\perp-\mathbf{q}_{a\perp}). \tag{3.62}
$$

The incoming fields in Eqs. (3.51) and (3.52) are respectively,

$$
\langle\Psi_a(\mathbf{q}_{1\perp})\rangle=\rho_0\sqrt{2\pi}e^{-(\mathbf{q}_{1\perp}-\mathbf{q}_{a\perp})^2\rho_0^2/4}\qquad\langle\Psi_{a'}(\mathbf{q}_{3\perp})\rangle=\rho_0\sqrt{2\pi}e^{-(\mathbf{q}_{3\perp}-\mathbf{q}_{a'\perp})^2\rho_0^2/4}\quad. \tag{3.63}
$$

Integrating over $\mathbf{q}_{1\perp}$ and $\mathbf{q}_{2\perp}$ in Eq. (3.52) we get

$$
\int\mathrm{d}\mathbf{q}_{1\perp}\,\mathrm{d}\mathbf{q}_{2\perp}\langle\Psi_a(\mathbf{q}_{1\perp})\rangle\,\langle\Psi^*_{a'}(\mathbf{q}_{1\perp}+\Delta\mathbf{q}_{1\perp})\rangle\,\langle\Psi_{a'}(\mathbf{q}_{2\perp}+\Delta\mathbf{q}_{1\perp})\rangle\,\langle\Psi^*_a(\mathbf{q}_{2\perp})\rangle=
$$
$$
(2\pi)^4e^{-\rho_0^2(\Delta\mathbf{q}_{1\perp}-\Delta\mathbf{q}_{a\perp})^2/4}, \tag{3.64}
$$

with $\Delta\mathbf{q}_{a\perp}\equiv\mathbf{q}_{a\perp}-\mathbf{q}_{a'\perp}$. We may now combine all intermediate results to calculate $\langle\delta T^2(\Delta\omega)\rangle$. Using Eqs. (3.52), (3.54), (3.55), (3.58), (3.59) and (3.64) and taking $\mathbf{p}_{\perp 1}=\mathbf{p}_{\perp 2}=k_a\hat{\mathbf{p}}_\perp 1$ we get

$$
\langle\delta T^2(\Delta\omega)\rangle_{aa'}=\frac{\ell v_E^4(\ell+\tau_0)^2(\frac{2}{3}\ell+\tau_0)^2k_a^2}{192\pi k^2D^4}\int\mathrm{d}\Delta\mathbf{q}_{1\perp}\int_0^L\mathrm{d}z'\,e^{-\rho_0^2(\Delta\mathbf{q}_{1\perp}-\Delta\mathbf{q}_{a\perp})^2/4}\times
$$
$$
\frac{\cosh[2(L-z')\gamma_1]-\cos[2(L-z')\gamma_2]}{\cosh[2L\gamma_1]-\cos[2L\gamma_2]}\times\frac{\cosh[2k_az']}{\sinh^2[k_aL]}, \tag{3.65}
$$

where $\Delta\mathbf{q}_{\perp 1}$ represents the effect of the angular spread in a focussed beam and $\Delta\mathbf{q}_{\perp a}$ represents the change in the incoming angle of the beam. The total transmission $\langle T_a\rangle$ is obtained by integrating Eq. (3.50) over $\mathbf{r}_{1\perp}$ at $z = z_e$ and yields $(T = \pi I(z_e))$

$$\langle T_a\rangle = \frac{v_E(\ell+\tau_0)(\frac{2}{3}\ell+\tau_0)k_a}{4D\sinh[k_a L]}. \tag{3.66}$$

Integrating over z' in Eq. (3.65), dividing by $\langle T_a\rangle^2$, and putting for later convenience the energy- and phase velocities v_E and v_ϕ (that are not rigorously known) into one parameter $\alpha = v_E \times v_\phi^2/c^3$ (using $k = 2\pi c/(v_\phi\lambda_{vac})$), we obtain the final result in which the mean free path is eliminated in favour of the diffusion constant.

$$C_2(\Delta\mathbf{q}_{\perp a},\Delta\omega) = \frac{\langle\delta T^2(\Delta\omega)\rangle_{aa'}}{\langle T_a\rangle^2} = \alpha\times\frac{c\lambda_{vac}^2 L}{8\pi^2\rho_0^2 D}\, F_2(\Delta\mathbf{q}_{\perp a},\Delta\omega), \tag{3.67}$$

with

$$F_2(\Delta\mathbf{q}_{\perp a},\Delta\omega) \equiv \int\frac{\mathrm{d}\Delta\mathbf{q}_{1\perp}}{4\pi}\,\frac{\rho_0^2\, e^{-\rho_0^2(\Delta\mathbf{q}_{1\perp}-\Delta\mathbf{q}_{a\perp})^2/4}}{L(\cosh[2L\gamma_1]-\cos[2L\gamma_2])}\times$$
$$\left\{\frac{\gamma_1\sinh[2L\gamma_1]}{\gamma_1^2-k_a^2}-\frac{\gamma_2\sin[2L\gamma_2]}{\gamma_2^2+k_a^2}-\frac{k_a\sinh[2Lk_a]}{\gamma_1^2-k_a^2}-\frac{k_a\sinh[2Lk_a]}{\gamma_2^2+k_a^2}\right\}. \tag{3.68}$$

Eqs. (3.67) and (3.68) give the desired result with which we will be able to describe the measurements in the next chapter, the long-range correlation as a function of angle of incidence and frequency, incorporating the influence of the beam profile. In the plane wave limit $\rho_0 \gg L$ and in the absence of absorption the long range correlation function as a function of frequency only reduces to

$$C_2(\Delta\omega) = \frac{3v_\phi^2\lambda_{vac}^2\,(\sinh[L\sqrt{2a}]-\sin[L\sqrt{2a}])}{4\pi^2c^2\ell\rho_0^2\,\sqrt{2a}\,(\cosh[L\sqrt{2a}]-\cos[L\sqrt{2a}])}, \tag{3.69}$$

which differs from Pnini's result in the prefactor only. Apart from the already mentioned factor of two that results from the effect of the transversal nature of the waves, this is due to different definitions of the beam profile.

3.4.3 Conclusion

Let us discuss some properties of the correlation function in Eq. (3.67). In the limit $\rho_0 \to \infty$, $F_2(0,0) \to 2/3$. This makes the relative variance on the total transmission,

$$\frac{\langle\delta T_a^2\rangle}{\langle T_a\rangle^2} = \frac{2L}{2k^2\rho_0^2\ell} \approx \frac{L}{2N\ell}, \tag{3.70}$$

where Eq. (3.18) was used. In the heuristic derivation of the variance of the total transmission in section 3.2, where we assumed that transmission modes were independent, we found the relative variance to be proportional to $1/N$ (Eq. (3.29)).

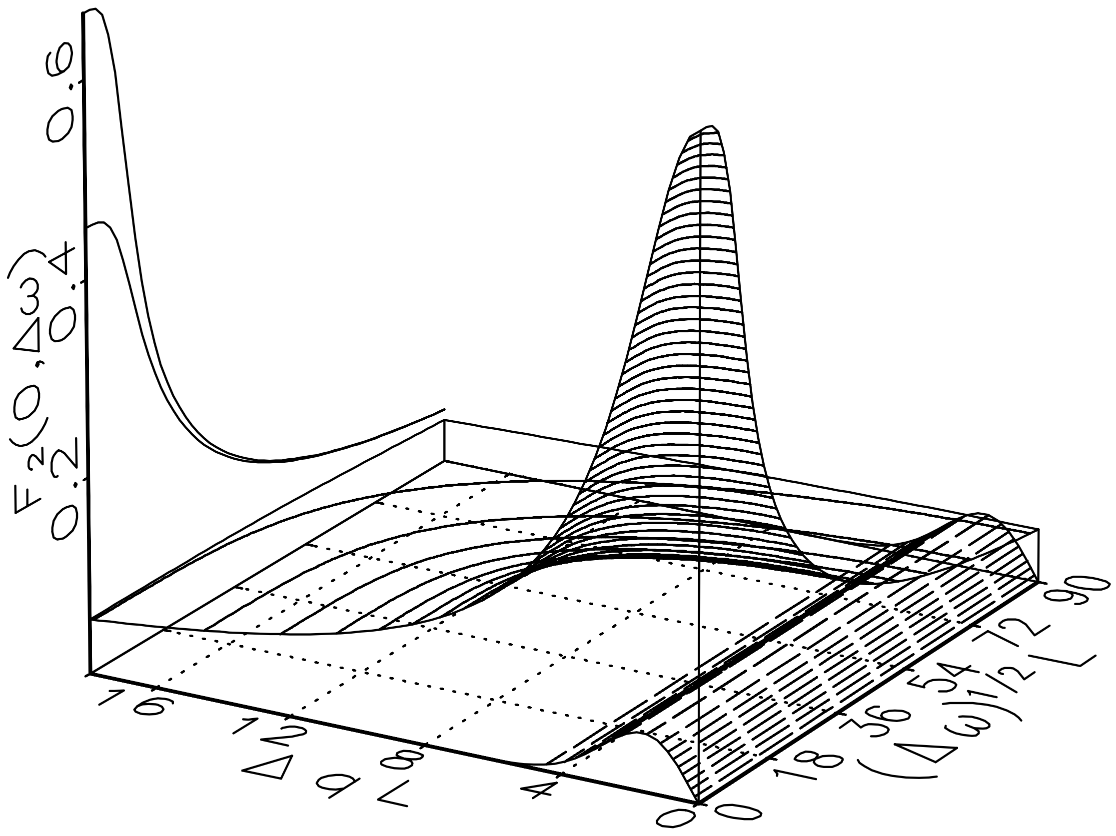

Figure 3.9: *A three dimensional plot of the integrand,*

$$\frac{1}{L(\cosh[2L\gamma_1]-\cos[2L\gamma_2])}\left\{\frac{\gamma_1\sinh[2L\gamma_1]}{\gamma_1^2}-\frac{\gamma_2\sin[2L\gamma_2]}{\gamma_2^2}\right\},$$

in Eq. (3.68) for $k_a \to 0$, $\Delta\mathbf{q}_{\perp a}=0$*(i.e. no change in the incoming angle of the beam). The upper surface shows the value of the integrand as a function of* Δq *and* $\Delta\omega$*, for a sample thickness of* $L = 30\mu m$*. Contour lines connect points of equal height. The lower surface shows the weight function* $\frac{\Delta q\rho_0^2}{4\pi L}\exp(-\rho_0^2\Delta q^2/4)$ *determined by the spot size of* $\rho_0 = 26\mu m$ *on the sample. To obtain the correct prediction of the long range correlation function as a function of frequency only, the upper surface is multiplied by the weight function and summed over* Δq*-space. In the back plane of the graph the upper curve shows the correlation as a function of* $\Delta\omega$ *for the plane wave limit:* $\lim \rho_0 \to \infty F_2(0,\Delta\omega)$ *(Eq. (3.68)), and the result of the correlation function convolved over* Δq*-space for* $\rho_0 = 26\mu m$*(lower curve). The lower curve shows the prediction of a measurement for a sample with* $L = 30\mu m$ *and a finite spot size determined by* $\rho_0 = 26\mu m$*. Clearly is seen that the top of the correlation function is flattened by the convolution over* Δq*-space.*

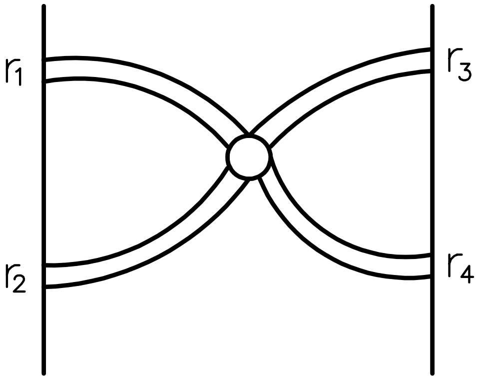

Figure 3.10: *Simple physical picture of the enhancement of the variance on the total transmission by interference inside the sample. Two intensities propagate through the sample and interfere. Suppose the interference is constructive. The intensity at the point of interference is higher than the average intensity, and this higher intensity diffuses to* $\mathbf{r}_{\perp 3}$ *and* $\mathbf{r}_{\perp 4}$ *at the transmission side of the slab. Since both higher intensities come from the same bulk speckle, the intensities at* $\mathbf{r}_{\perp 3}$ *and* $\mathbf{r}_{\perp 4}$ *are correlated. The correlation over large (i.e. diffusion) length scales of the fluctuating intensity enhances the fluctuations on the total transmission.*

Clearly transmission modes become correlated, and the relative variance is enhanced proportional to L/ℓ. In Fig. (3.10) a simple physical picture is drawn to explain the correlation in the transmission. The relative variance also can be explained in the following way. The probability that two intensities will interfere is inverse proportional to the illuminated area (the number of modes), since intensities that start to propagate far apart have a low probability to interfere. The thicker the slab, the larger the probability that two intensities will diffuse towards each other. Thus the variance is proportional to $L/N\ell$. In an experiment, to be able to observe the fluctuations, one wants the fluctuations to be as large as possible. This means a small mean free path, and a small illuminated area (spot size). However, as can be seen in Fig. (3.9), a small spot size influences the general shape of the correlation function and its magnitude. Even so, coming in with a point source (an infinite small spot size) gives a diffuse broadened intensity profile at the exit interface of the order of the sample thickness (i.e. a large number of modes). The only way to prevent this is to confine the sample by perfectly reflecting walls (a waveguide with disorder). This is difficult in the optical regime. We chose to use non-confined samples to be able to probe different parts of the same sample to improve the statistics of the measurement. We turn to the explanation of the shape of the correlation function. For large $\Delta\omega$ or large $\Delta\mathbf{q}_\perp$ the correlation decays as respectively $1/(\Delta\omega^{1/2}L)$ or $1/(\Delta\mathbf{q}_\perp L)$, an algebraic decay. This can be explained as follows. The fluctuations are caused by the interference inside the sample. As the place of interference is close to the entrance interface, the correlation in the bulk speckle decays slower with $\Delta\omega$ or $\Delta\mathbf{q}_\perp$ than deep in the sample. The sum of all exponential decaying bulk speckles with their decay parameter depending on the depth in the medium results in an algebraic decay. The influence of the finite spot size on the correlation function for small $\Delta\omega$ is most clearly seen in Fig. (3.9). The integrand of Eq. (3.68) is shown as a function of both $\Delta\omega^{1/2}L$ and $\Delta\mathbf{q}_\perp L$ in a three dimensional graph. The back plane shows the plane wave limit of $F_2(\Delta\mathbf{q}_{\perp a} = 0, \Delta\omega)$ and the result for $F_2(\Delta\mathbf{q}_{\perp a} = 0, \Delta\omega)$ after the convolution over $\Delta\mathbf{q}_{\perp 1}$ because of the finite beam diameter with $\rho_0 = 26\mu m$, which clearly demonstrates the flattening of the top.

Chapter 4

Experiments on the transmission

4.1 Introduction

In this chapter we discuss the experiments that were performed to measure the short-range and long-range correlation functions in the frequency domain. We measured the fluctuations on the transmission as a function of the wave length (frequency) of the light. The samples consisted of slabs of titanium dioxide particles in a static random structure. Titanium dioxide was used because of its high refractive index ($n \sim 2.7$) in the visible wavelength range combined with an extremely low absorption. It is the most effective readily available scatterer in optical experiments. The theory of the short- and long-range correlation was discussed in the previous chapter. It was shown that the relative fluctuations in a one channel in-one channel out experiment (C_1) are of order unity, and that the relative fluctuations in a one-channel-in-all-channel-out experiment (C_2) are of order one over the conductance, g^{-1}. To make the fluctuations on the total transmission experimentally accessible the conductance should be small. In the optical experiments to be described in this chapter and the next, the achieved conductance was typically of the order of 10000. The expected fluctuations on the total transmission are therefore still extremely small, and great care had to be taken to ensure that the measured fluctuations were indeed caused by interference processes in the disordered sample, and not by experimental artefacts. The experimental set-up is discussed in section 4.2, and the techniques used to eliminate trivial sources of fluctuations are explained. Section 4.3 discusses the data analysis. A fundamental problem results from the finiteness of the frequency range over which the transmission can be measured. This finiteness impedes the resolution of very slowly oscillating components in the fluctuations, i.e. it impedes the detection of very long-range correlations. Section 4.3 explains how the data were analysed to deal with the above mentioned fundamental problem in the interpretation of the results. In section 4.4 the results of the measurements of the short- and long-range correlations are presented. Indications for a long-range correlation have been found earlier in the form of a long-range tail in the short-range correlation function by Genack *et al.*[60], in microwave experiments on samples of

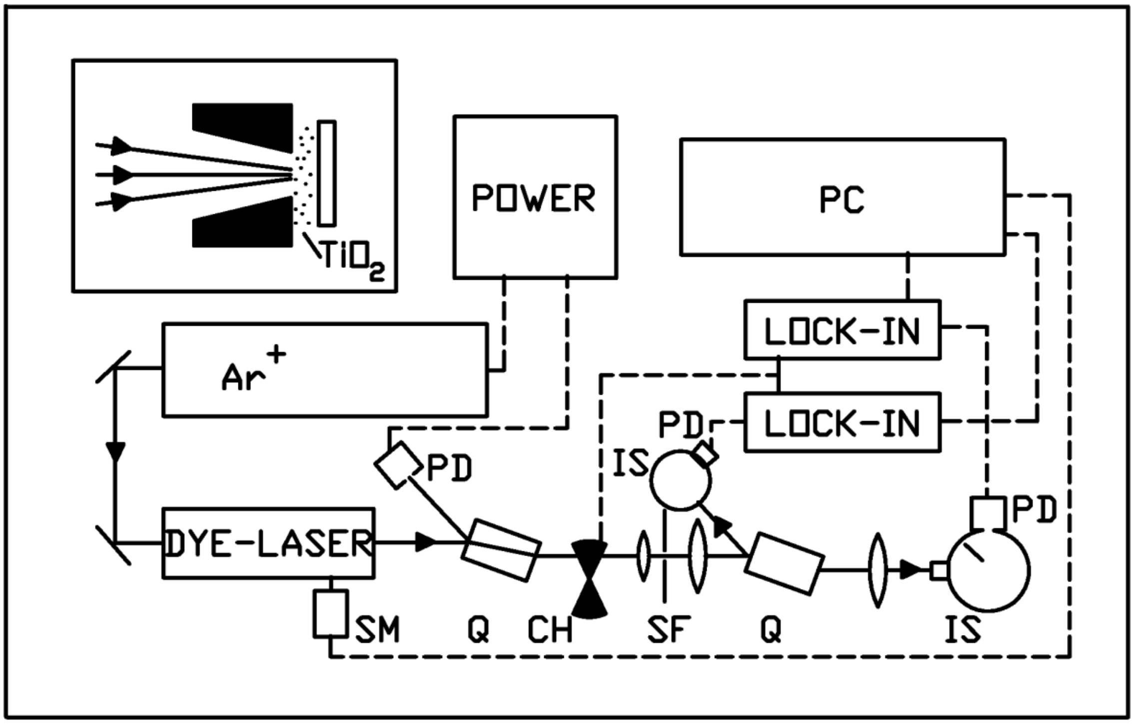

Figure 4.1: *Experimental set up for the recording of fluctuations in the total transmission. SM: steppermotor; Q: quartz beam splitter; CH: chopper; SF: spatial filter; L: focussing lens; IS: integrating sphere. Inset: Insert as fitted in port of integrating sphere, carrying a sample on transparent supporting material.*

a confined geometry. The long-range correlation functions that we measured for different sample thickness and different spot size on the sample are shown to be in excellent agreement with the theory of chapter 3, thus establishing for the first time the full long-range correlation function on the total transmission[61, 57]. Finally, the experiments gave the second independent confirmation of the reduction of transport velocity of light in disordered media, as was first shown by van Albada *et al.*[9].

4.2 Measurements

4.2.1 Experimental set-up

The experimental set up for the total transmission experiments is shown in outline in Fig. (4.1). A Coherent Radiation 590 dye laser operating in broadband mode was used as a light source, and its frequency was varied by driving the birefringent filter under computer control. The beam was chopped, spatially filtered, slightly expanded, and then focussed onto the sample, which was mounted on an insert, fit-

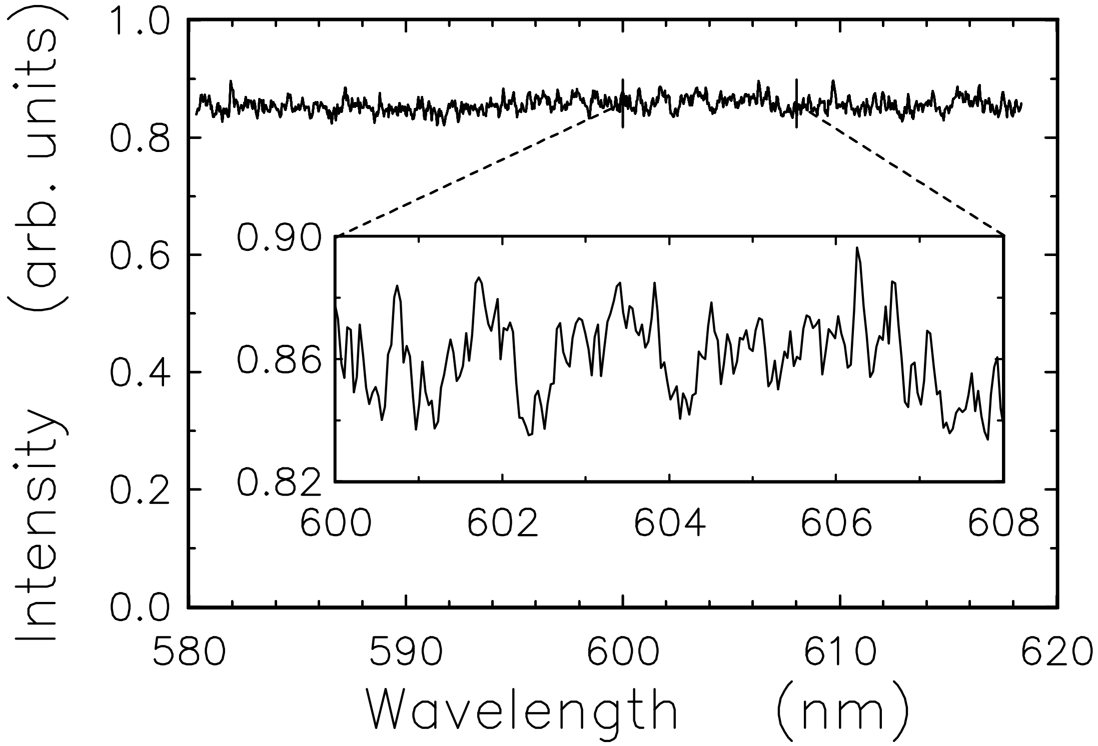

Figure 4.2: *Total transmission as a function of wavelength for a sample of* $30\mu m$ *thickness at* $\rho_0 = 26\mu m$. *The relative fluctuation in the transmission is about 1 %.*

ting in the porthole of an integrating sphere. Fluctuations in the total transmission were measured by recording the diffuse intensity in the sphere as a function of wavelength. The beam diameter could be varied by changing the position of the focussing lens L with respect to the sample, and was determined by measuring the distance across the beam between the $1/e$-points with a $10\mu m$ pinhole. The sample-detector assembly was mounted on a translation stage driven by stepper motors under computer control. In each scan, 1024 data points were taken over a wavelength interval between 622 nm and 583 nm. In between scans, the lateral position of the sample was changed by at least 4 times the beam diameter. A set of scans consisted of 16 consecutive scans probing different parts of a same sample. In the case of C_1-type scans, the integrating detector was replaced by a photomultiplier fitted with a polarizer and a pinhole, positioned at some distance from the sample. Extreme care was taken to eliminate any fluctuations that are not due to interference effects within the sample: The output of the dye laser was stabilized through a feedback circuit coupled to the pump laser (this also minimizes the influence of non-linearities of the signal- and reference detectors and permits the dynamic range of the lock-in amplifiers and A/D-converters to be fully exploited over the entire wavelength range). A ratio-technique was used to filter out the remaining source fluctuations.

The reference photo-diode was installed within another integrating sphere because with an unscrambled incident beam its protective coating was found to produce interference fringes. The recorded (total) transmitted intensity showed a drift as a function of wavelength, resulting from different wavelength dependent transmission characteristics of optical components in the signal- and reference beams, the wavelength-dependence of the average transmission through the sample (the total transmission is proportional to ℓ/L, and ℓ is wavelength dependent), and from different response curves of the detectors. This drift was corrected for by recording a response curve before a set of scans was started, using an unfocussed beam. The fluctuations on the total transmission are proportional to $L/\ell N$, i.e. proportional to the optical thickness L/ℓ and inverse proportional to the number of modes (see Eq. (3.70)). The number of modes is proportional to the area of the beam. The fluctuations on a scan with an unfocussed beam are extremely small, and this gives a smooth response curve of the experimental set-up. The recorded curves were divided by this response curve. We found that even so, some wavelength dependent drift remained. Experiments at different power levels showed this remaining drift to be of thermal origin: the focussed beam raises the temperature of the probed part of the sample more than does an unfocussed beam, and the resulting expansion slightly changes the wavelength-dependence of ℓ. Before processing the data, we therefore calculated the average remaining linear drift in the scans belonging to a set, and corrected each individual scan for this linear drift. Part of a genuine linear drift component of the fluctuating intensity is lost in this way. A typical individual scan is shown in Fig. (4.2). It is seen that the fluctuating part of the signal appears on top of a large background. Depending on the sample-thickness and spot-size, relative fluctuations were found ranging from $0.6 - 2.8$ %. At constant wavelength of the incoming light the relative fluctuation was less than 0.05 %.

Samples were prepared by suspending rutile TiO_2 pigment in a solution of 3 volume % of PMMA relative to TiO_2 in chloroform. The diameter of the (potato shaped) TiO_2 particles was $220\ nm \pm 70\ nm$. A droplet of the suspension was put on a transparent substrate, and spread out with a razor blade mounted on a translation stage to produce an uniform thickness of the sample. After evaporation of the chloroform, the thickness of the sample was determined microscopically. The PMMA was added to act as a glue between the TiO_2 particles. The volume fraction of TiO_2 in the resulting samples was calculated from density determinations to be 36%, the absorption length ℓ_a was determined to be $\simeq 70\mu m$.

4.3 Data analysis

In this section we discuss experimental constraints on the measurement of the correlation functions, and describe methods that we used to get past their effect in the interpretation of the results.

4.3.1 Ensemble average versus the average over the frequency range

The correlation functions sought are defined as

$$C(\Delta\omega) \equiv \frac{\langle \delta T(\omega)\delta T(\omega\prime)\rangle}{\langle T(\omega)\rangle^2}, \tag{4.1}$$

with $T(\omega)$ the (total) transmitted intensity at frequency ω, and $\delta T(\omega) \equiv T(\omega) - \langle T(\omega)\rangle$. Under the experimental conditions (rigid samples) the average over the *disorder* $\langle T(\omega)\rangle$ cannot be obtained, and the best approximation at hand for its value is the average over the *frequency range* $\overline{T(\omega)}$. Since e.g. the sample thickness may slightly vary with the position of the beam on the sample (and thus the average total transmission may slightly vary), $\overline{T(\omega)}$-values can only be calculated per individual scan and not for a whole set of scans. The consequence of using the average over the frequency-range instead of that over the disorder is that in a Fourier decomposition of $\delta T(\omega)$ the zeroth component will be missing (the zeroth component of $\delta T(\omega)$ is $\overline{T(\omega)} - \langle T(\omega)\rangle$). Similarly, the linear drift correction discussed in the former section will reduce the first Fourier component and cause some redistribution among a few low-order components. The combined effect of the reduction of the measured slow oscillating fluctuations with respect to the 'true' oscillations will be a negative offset of the experimental $C(\Delta\omega)$ with respect to the 'true' function, since fluctuations are missing and since the slow oscillating fluctuations determine the decay of the correlation function for large $\Delta\omega$ outside our plotrange. In the measurement of $C_1(\Delta\omega)$ this effect is not important, but for $C_2(\Delta\omega)$ it is. In section 4.4 we will therefore compare theoretical $C_2(\Delta\omega)$ curves to both 'raw' measured ones, and measured ones that were recalculated on the basis of a comparison with theory of all but their lowest Fourier components.

4.3.2 The correlation function in the Fourier domain

We will make use of the fact that there exist a simple relation between the Fourier decomposition of the correlation function and the Fourier decomposition of the measured fluctuations (cf. Eq. (4.4) and [62]). By comparing the Fourier decomposed theoretical correlation function with the Fourier decomposed measurements, a good agreement is shown between measurements and theory. The measured correlation functions are recalculated by adding the (unavailable) zeroth component and substituting the first component by its theoretical value. The recalculated correlation functions were obtained as follows: The discrete Fourier transform of $\delta T(\omega_m)$ is defined as,

$$\delta T(k_n) \equiv \frac{1}{\sqrt{\Omega}} \sum_{m=0}^{\Omega-1} [T(\omega_m) - \overline{T(\omega)}] e^{ik_n\Delta\omega_m}, \tag{4.2}$$

with $k_n \equiv 2\pi n/(\omega_{\Omega-1} - \omega_0)$; $n = 0, \cdots, \Omega{-}1$; Ω is the total number of data points in a scan; $\Delta\omega_m$ is m times the frequency step in the measurement. If we define the

Fourier transform of $C(\Delta\omega)$ as,

$$C(k_n) \equiv \frac{1}{\sqrt{\Omega}} \left[\sum_{m=0}^{\Omega/2-1} C(\Delta\omega_m) e^{ik_n \Delta\omega_m} + \sum_{m=\Omega/2}^{\Omega-1} C(\Delta\omega_{\Omega-m}) e^{ik_n \Delta\omega_m} \right], \tag{4.3}$$

the following simple expression for the Fourier decomposition of $C(\Delta\omega)$ can be proven, if we assume $T(\omega_m)$ to be periodic (with periodicity Ω),

$$C(k_n) = \frac{1}{\sqrt{\Omega}} \left[\delta T(k_n) \delta T^*(k_n) / \overline{T(\omega)}^2 \right]. \tag{4.4}$$

This is a very useful equation. It relates the Fourier decomposition of the correlation function directly to the Fourier decomposition of the fluctuations. The Fourier decomposition of the theoretical correlation function is done numerically.

To perform the numerical Fourier decomposition in Eq. (4.3) of the long-range correlation function all parameters in the theoretical correlation function need to be known. The largest problem poses the constant $\alpha = v_E v_\phi^2/c^3$ in Eq. (3.67). The experimentally determined values for ρ_0 and L used in the calculation of the theoretical $C(k_n)$ may differ somewhat from the actual values. Relatively small errors in ρ_0 and L mainly affect the magnitude of the correlation function that is proportional to L/ρ_0^2, but hardly affect its general shape. We therefore express the Fourier decomposition of the long-range correlation function as $C(\alpha_{fit}, k_n)$, with α_{fit} an adjustable parameter instead of the constant α ($\equiv v_E v_\phi^2/c^3$). The value of the adjustable parameter α_{fit} may vary from sample to sample and from beam diameter to beam diameter in the measurements due to inaccuracies in the experimental determination of ρ_0 and L. Later we will compare the experimentally found value of α_{fit} with a value of α based on a reasonable estimate of v_E and v_ϕ. We proceeded the following way. For every individual combination of sample thickness and spot size, the calculated curve was fitted to the 4^{th} through 300^{th} experimental Fourier component using the value for the diffusion constant D found from the C_1 measurements, and α_{fit} as only adjustable parameter. We 'improved' the set of experimental Fourier components by replacing the first one by its calculated counterpart, and adding the calculated zeroth component. The improved set was then transformed back.

4.4 Results

4.4.1 The short-range correlation C_1

In Fig. (4.3) we present the results of the short-range $C_1(\Delta\omega)$ measurements for samples of 13, 22, 30 and 45 micron thickness. The scans were made over frequency intervals of 19113 GHz for the 13 and 22 μm-samples, and 6371 GHz for the 30 and 45 μm-samples respectively. Using the diffusion coefficient D as only adjustable parameter, the theoretical curve Eq. (3.44), convolved with the (Gaussian) laser line width of 10 GHz, was fitted to the data points. The smooth curves correspond to a

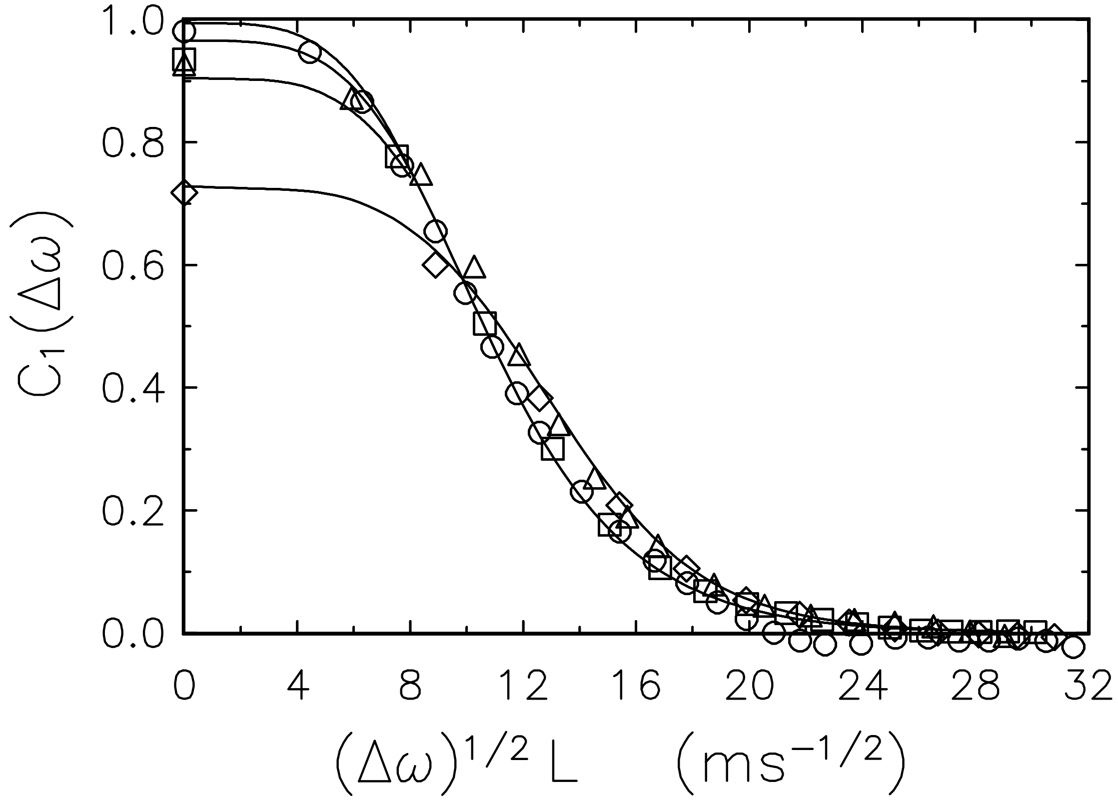

Figure 4.3: *Comparison of measured $C_1(\Delta\omega)$-correlation functions with theory. Symbols: experimental data for ○: $L = 13\mu m$, □ : $L = 22\mu m$, △ : $L = 30\mu m$, ◇ : $L = 45\mu m$. Smooth lines: theoretical curves as calculated for $D = 12 m^2 s^{-1}$, convolved with the laser linewidth of $10GHz$.*

value of $D = 12\ m^2 s^{-1}$. The horizontal scale was chosen such as to scale out the L-dependence of the theoretical curves. Deviations from the resulting 'universal' curve are due to the convolution with the laser linewidth. We conclude that Eq. (3.44) provides a good description of the experimental results.

In Fig. (4.4) we compare theory and experiment for the C_1 correlation function in the Fourier domain. The data correspond to 30 and 45 μm-samples respectively. The measured curves represent $C(k_n)$ averaged over 32 scans, plotted as a function of the Fourier component number. The smooth curves are the calculated $C(k_n)$, obtained by numerically Fourier transforming Eq. (3.44) after convolving with the laser line width of 10 GHz. Up to a cut-off that results from the finite slab-thickness, the Fourier components of the C_1-correlation function are of equal strength, and this explains why the absence of the zeroth component (*c.f.* section 4.3) is of little importance here.

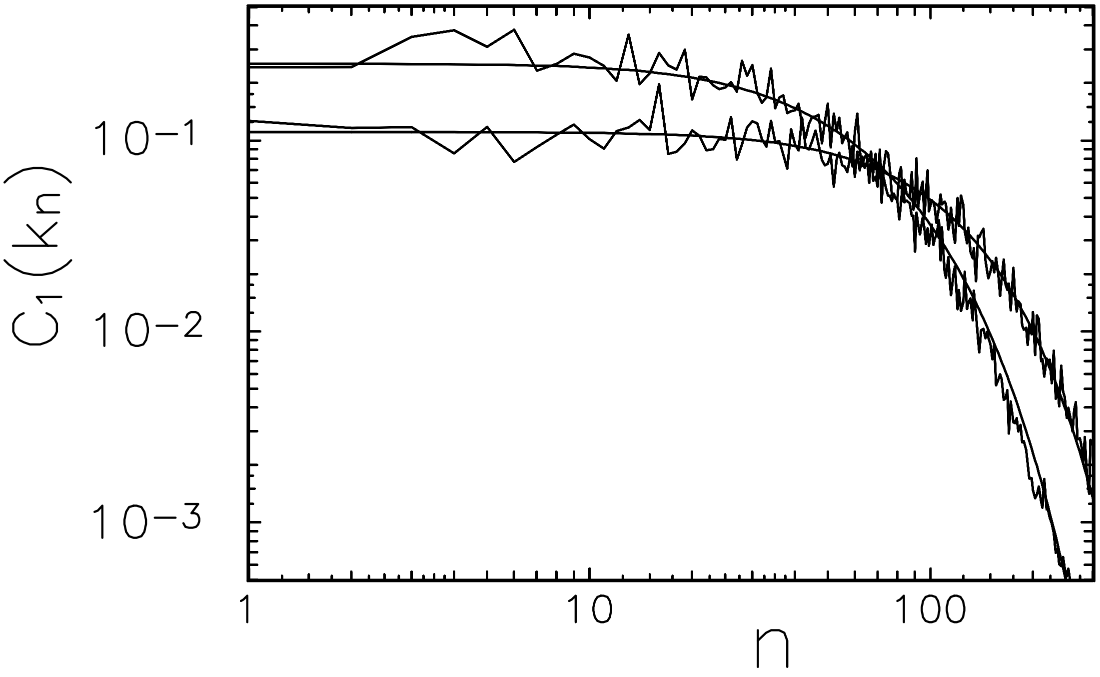

Figure 4.4: *Comparison of measured $C_1(\Delta\omega)$-correlation functions with theory in the Fourier domain. Upper curve: $L = 30\mu m$; lower curve: $L = 45\mu m$. Smooth lines: theoretical curves convolved with the laser line width of 10 GHz.*

4.4.2 The long-range correlation C_2

Fig. (4.5) shows experimental $C_2(\Delta\omega)$ curves as measured for 13, 30, 45 and 78 μm-samples using a beam diameter defined by $\rho_0 = 26\mu m$. All scans were made over a frequency range of 31856 GHz. The choice of the horizontal and vertical scales is such that the theoretical curves (only the plane-wave limit is shown) should exhibit an uniform tail. The presented results for each thickness are averages over 32 scans. All experimental curves indeed show a slowly decaying tail that, as expected from the absence of the zeroth Fourier component, lies below the theoretical curve. The discrepancy is smaller for the thicker samples because there the relative scan length (the absolute scan length times the square of the thickness) is larger, and consequently the value of $\overline{\delta T(\omega)}$ is expected to be closer to $\langle \delta T(\omega) \rangle$. The predicted decrease in correlation for small $\Delta\omega$ with increasing slab-thickness that is due to the finite beam diameter, is indeed found.

Fig. (4.6) shows how theory and experiment compare for the C_2-function in the Fourier domain. The curves correspond to 13 and 53 μm-samples respectively. The measured curves represent the real Fourier components $C_2(k_n)$ averaged over 32 scans, and plotted as a function of the Fourier component number. The smooth curves are least squares fits of the calculated $C_2(k_n)$, with α in Eq. (3.67) replaced

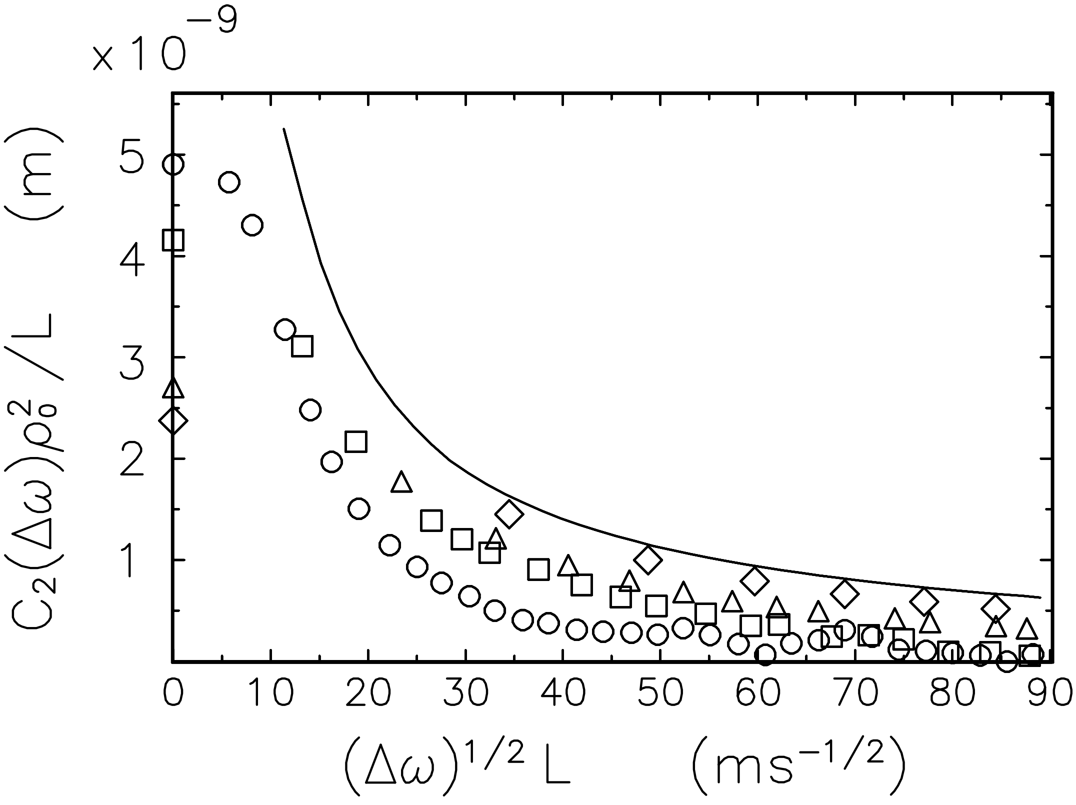

Figure 4.5: *Raw experimental $C_2(\Delta\omega)$ data as a function of sample thickness at constant beam diameter given by $\rho_0 = 26\mu m$. ○ : $L = 13\mu m$, □ : $L = 30\mu m$, △ : $L = 53\mu m$, ◇ : $L = 78\mu m$; Solid line: 'plane-wave limit' ($\rho_0 \gg L$).*

by an adjustable parameter α_{fit}, to these data points over the fourth up to the three-hundredth Fourier component. The calculated $C_2(\alpha_{fit}, k_n)$ were obtained by numerically integrating Eq. (3.68) over $\Delta\mathbf{q}_{1\perp}$ for each frequency-shift $\Delta\omega_m$, and numerically Fourier-transforming the $C_2(\Delta\omega_m)$ according to Eq. (4.3).

The presence of a long-range tail in the measured $C_2(\Delta\omega)$ correlation function and its absence in the $C_1(\Delta\omega)$ function is very clearly seen by comparing Figs. (4.4) and (4.6). In the C_2 correlation function the magnitude of the Fourier components increases with decreasing component number, whereas in the C_1-function their magnitude is constant.

In Figs. (4.7) and (4.8), experimental C_2 correlation functions as obtained by back transformation after correction (*c.f.* section 4.3) of $C(k_n)$ are presented. Fig. (4.7) shows the shape of $C_2(\Delta\omega)$ as a function of the slab thickness at constant beam diameter, and Fig. (4.8) shows the effect of the beam diameter at constant slab-thickness. In both figures the tails of the correlation functions have an uniform algebraic decay. The different shapes for small $\Delta\omega$ reflects the effect of the beam

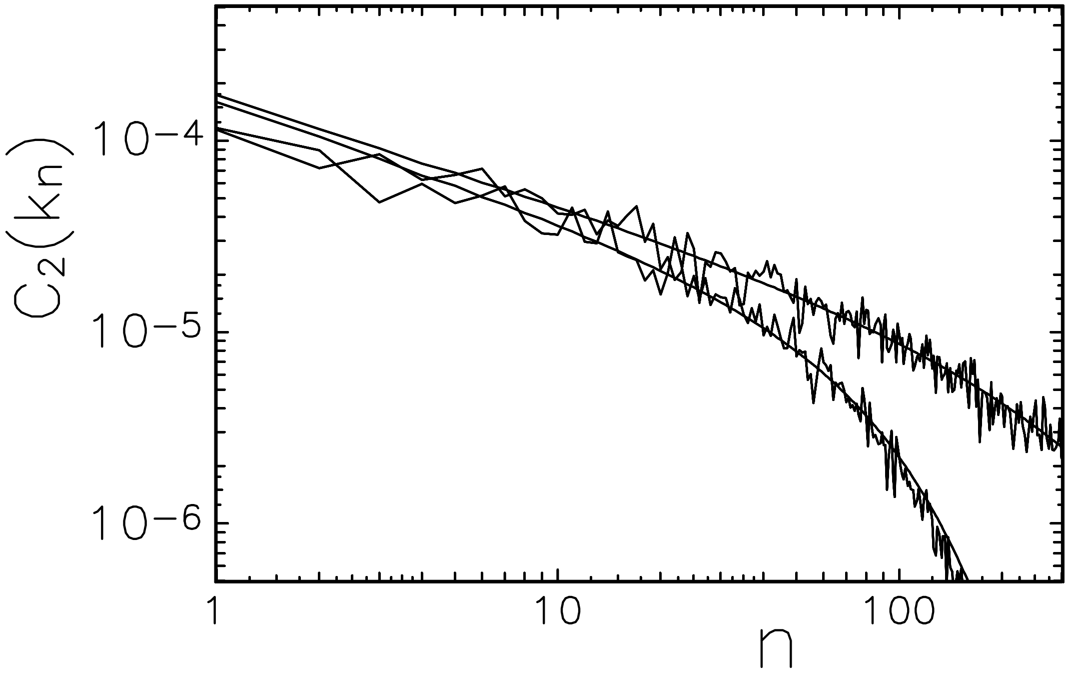

Figure 4.6: *Comparison of $C_2(\Delta\omega)$-data with theory in the Fourier domain. Upper curve: $L = 53\mu m$, lower curve: $L = 13\mu m$, both curves $\rho_0 = 26\mu m$. Smooth lines: least squares fits of theory to the data over the 4^{th} through 300^{th} Fourier component with α_{fit} as the only adjustable parameter.*

diameter on the shape of the correlation function that is explained in Fig. (3.9). As mentioned in section 4.3, the fits were made using an adjustable parameter α_{fit} instead of the proportionality constant α in calculating the theoretical curves. The α_{fit}-values found for the various curves are listed in Table (4.1). For clarity, the theoretical curves in the figures were all calculated using the average value $\overline{\alpha}_{fit} = 0.10$ (with the chosen x- and y-scales, this makes the tails coincide). The y-values of the data points corresponding to each curve were multiplied by the respective values of $\overline{\alpha}_{fit}/\alpha_{fit}$. From the Figs. (4.7) and (4.8) it is seen that the theory in chapter 3 (Eqs. (3.67) and (3.68)) correctly describe the shape of the $C_2(\Delta\omega)$-correlation function, including the influence of L and ρ_0.

4.4.3 The variance of the long-range fluctuations

We now turn to the magnitude of the correlation functions. The slight variation in the values of α_{fit} listed in Table (4.1) is easily explained in terms of inaccuracies in the values of ρ_0 and L, and in view of the wide range over which these parameters were varied, we conclude that α_{fit} is indeed a constant. In earlier theoretical work, different values were found for the magnitude of the C_2 correlation function[54, 56].

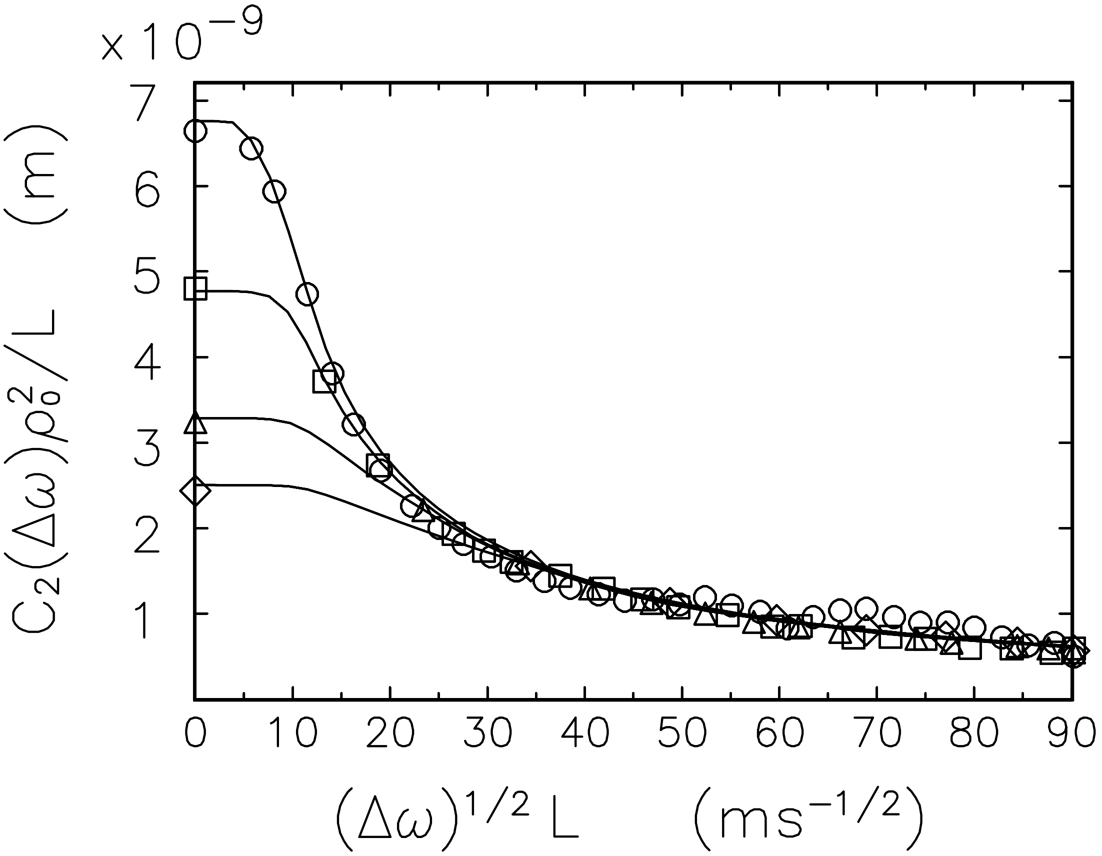

Figure 4.7: *Recalculated (see the end of section 4.3.2 and 4.4.2) $C_2(\Delta\omega)$-correlation as a function of sample thickness at constant beam diameter, given by $\rho_0 = 26\mu m$. Symbols: ○ : $L = 13\mu m$; □ : $L = 30\mu m$; △ : $L = 53\mu m$; ◇ : $L = 78\mu m$. Solid lines: calculated from Eqs. (3.67) and (3.68), using $\overline{\alpha}_{fit} = 0.10$.*

The present results permit the evaluation of the magnitude.

In the previous chapter the shape and magnitude of the C_2 correlation function were calculated (Eq. (3.67)), and the data show that this expression is directly proportional to the experimental $C_2(\Delta\omega)$-function. We will compare the average value $\overline{\alpha}_{fit}$ as found from the fit of theory to the data to the predicted value of α, $\alpha = v_E v_\phi^2/c^3$. We therefore calculate α: The velocity of energy transport between neighbouring correlation volumes in our medium by light waves of $\lambda \simeq 600nm$ is low, due to resonances in the scattering particles. From independent measurements of ℓ and the mean-free time τ_{mf} a value of $v_E \simeq 5 \pm 1 \times 10^7$ ms^{-1} was found[9]. A reliable experimental value for the phase velocity in the medium v_ϕ is not available. From Brewster angle measurements it was found $v_\phi = 2.3 \pm 0.2 \times 10^8$ ms^{-1}[63]. This technique however probes sample properties very near the surface, that may be different from the bulk properties. Values, estimated on the basis of Mie theory[64] and the

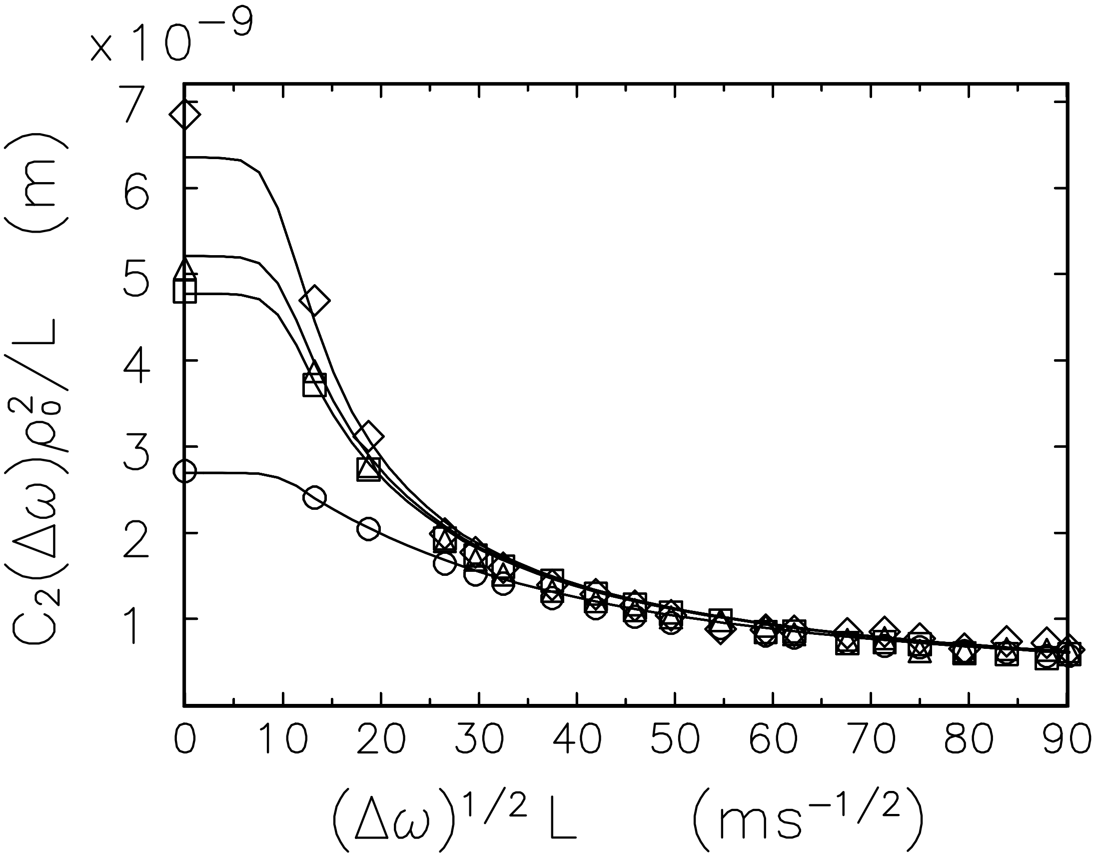

Figure 4.8: *Recalculated (see the end of section 4.3.2 and 4.4.2) $C_2(\Delta\omega)$ correlation as a function of beam diameter at constant sample thickness L of 30μm. Symbols: ○ : $\rho_0 = 10\mu m$; □ : $\rho_0 = 26\mu m$; △ : $\rho_0 = 32\mu m$; ◇ : $\rho_0 = 74\mu m$. Solid lines: calculated from Eqs. (3.67) and(3.68), using $\overline{\alpha}_{fit} = 0.10$.*

Bruggeman effective medium approximation[65] fall in the range $2.3 \pm 0.3 \times 10^8$ ms^{-1}. Substitution of these values into the definition of α yields $\alpha \simeq 0.1$, in complete agreement with the value found for $\overline{\alpha}_{fit}$ in Table (4.1). We conclude that the description by Eq. (3.67) is quantitative, and that the energy transport velocity is approximately six times lower than the vacuum velocity.

4.5 Conclusions

We have performed a detailed experimental study of correlations in wavelength-dependent intensity fluctuations in light after transmission through random dielectric slabs. The theory in chapter 3 fully describes the measured short-range and long-range correlations in the transmitted intensity. The model incorporates the in-

Sample thickness L (in μm)	Beam profile ρ_0 (in μm)	Number of scans	α_{fit}
13	26	32	0.087
30	26	32	0.098
53	26	32	0.091
78	26	32	0.106
30	10	32	0.113
30	26	32	0.098
30	32	16	0.117
30	74	16	0.102

Table 4.1: *Values of the only adjustable parameter* α_{fit}*, obtained by fitting Eq (3.67) to the experimental data, for the specified sample thickness, spot diameter and number of scans over which was averaged. Average value* $\overline{\alpha}_{fit}$ *of* α_{fit} *is* 0.10

tensity profile of the incident beam, and its predictions for both the short-range and the long-range correlation functions are in quantitative agreement with the experimental results, thus establishing the full long-range correlation function for the first time [61, 57] In addition, the experiments give the second independent confirmation of the reduction of the transport velocity of light in disordered media, as was first shown by van Albada *et al.*[9].

Chapter 5

The distribution of the total transmission

5.1 Introduction

In this chapter we discuss the distribution of the fluctuations on the total transmission. In the previous chapters it was shown theoretically and proven experimentally that the second cumulant (i.e. the variance) of the total transmission is larger than expected for independent transmission coefficients T_{ab}. Recently the full distribution has received much attention. For electrons it was theoretically shown that the distribution of the Universal Conductance Fluctuations (UCF) is Gaussian, but crosses over to a log-normal distribution as one approaches the Anderson transition[12]. For light Genack and Garcia[11] showed experimentally that in the multiple scattering regime the intensity statistics of the speckle changes from Rayleigh for small intensity speckles to a stretched exponential for large intensity speckles. This was confirmed theoretically by Kogan*et al.* [10], who also predicted a Gaussian distribution for the fluctuations on the total transmission of light. In computer simulations Edrei *et al.* [66] found a Gaussian distribution of the total transmission in two dimensions in the diffusive regime, which changed to a log-normal distribution for increasing disorder.

In this chapter we present the experimental distribution function of the fluctuating light intensity in total transmission through a disordered slab. The data show a distribution that is almost Gaussian, but contains a small but significant non-Gaussian contribution due to the presence of a third cumulant. It expresses a correlation in the cubed total transmission, which is different from the optical short-range and long-range correlations in the previous chapter. The scattering diagrams responsible for this new correlation are calculated in appendix B without free parameters and a good agreement is found between experiment and theory.

5.2 Distributions

5.2.1 Cumulants

The full distribution of a quantity is completely determined by all the moments or cumulants of the quantity and vice versa[67]. Take a probability distribution $P(x)$. The characteristic function $\phi(k)$ associated with this distribution is the Fourier transform of the distribution. A Taylor expansion of the characteristic function gives,

$$\phi(k) = \int P(x) e^{ikx} \mathrm{d}x = \sum_{n=0}^{\infty} \frac{(ik)^n \langle x^n \rangle}{n!}. \tag{5.1}$$

The cumulants $K_n$are implicitly defined as,

$$\phi(k) \equiv \exp\left[\sum_{n=0}^{\infty} \frac{(ik)^n K_n}{n!}\right]. \tag{5.2}$$

Expansion with respect to k yields the relation between cumulants and moments,

$$K_{n+1} = \langle x^{n+1} \rangle - \sum_{j=1}^{n} \left(\begin{array}{c} n \\ j \end{array} \right) \langle x^j \rangle K_{n+1-j}. \tag{5.3}$$

The normalized cumulants we use are defined as the n'th cumulant divided by the n'th moment. The first three normalized cumulants are given by,

$$\begin{aligned} \langle\langle T \rangle\rangle &= \frac{\langle T \rangle}{\langle T \rangle} = 1 \\ \langle\langle T^2 \rangle\rangle &= \frac{\langle T^2 \rangle - \langle T \rangle^2}{\langle T \rangle^2} \\ \langle\langle T^3 \rangle\rangle &= \frac{\langle T^3 \rangle - 3\langle T \rangle \langle T^2 \rangle + 2\langle T \rangle^3}{\langle T \rangle^3}, \end{aligned} \tag{5.4}$$

where double angular brackets denote the normalized cumulants. The n'th cumulant expresses a correlation in the n'th moment that is irreducible, i.e. that cannot be expressed in products of lower order moments. For instance, *all* the moments of a Gaussian distributed quantity about a mean unequal zero are unequal zero, while *only* the first and second cumulant are unequal zero.

5.2.2 Overview

Let us first give an overview of the present experimental and theoretical results on the distribution of transmission coefficients. The theoretical transmission coefficient T_{ab} follows initially an exponential (Rayleigh) distribution[51] (see also section 3.1 and Eq. (3.5)), while for large transmission coefficients a stretched exponential has been found experimentally[11] and theoretically[10]. The distribution has a relative variance $\langle \delta T_{ab}^2 \rangle / \langle T_{ab} \rangle^2 \approx 1$, with $\delta T_{ab} = T_{ab} - \langle T_{ab} \rangle$.

The total transmission is obtained by summing over all outgoing modes N, $T_a = \sum_b T_{ab} \sim \ell/L$. Naively one would expect for the distribution function $P(T_a)$ a convolution of N independent Rayleigh distributions that for large N becomes a Gaussian distribution with relative variance $1/N$ (see section 3.2). However, the interference between two light paths inside the sample correlates outgoing modes[52], which was the subject of the previous two chapters. This results in an increase of the relative variance by a factor L/ℓ. The distribution of the total transmission, based on the first and second cumulant (i.e. the average and the variance) only, is by definition Gaussian[10, 66],

$$P(T_a) \sim \exp\left[-\frac{1}{2}\frac{(T_a - \langle T_a\rangle)^2}{\langle \delta T_a^2\rangle}\right], \tag{5.5}$$

with relative variance $\langle \delta T_a^2\rangle/\langle T_a\rangle^2 \sim L/N\ell$.

The conductance is given by summing over all incoming and outgoing modes, $g \equiv \sum_{a,b} T_{ab} \sim N\ell/L$ with relative variance $\langle \delta g^2\rangle/\langle g\rangle^2 \sim \langle g\rangle^{-2}$[52, 8]. In electronic systems Altshuler *et al.* [12] predicted a distribution of the conductance $P(g)$, with the n'*th* normalized cumulant $\langle\langle g^n\rangle\rangle$ (i.e. the n'*th* cumulant over $\langle g\rangle^n$) proportional to $\langle g\rangle^{2-2n}$. In the metallic regime (i.e. for large values of the average conductance) the distribution is predominantly Gaussian. To our knowledge, neither the measurement of the conductance distribution in the metallic regime, nor of the total transmission distribution of optical systems has been reported.

5.2.3 Experimental distribution

We measured the fluctuations in the total transmission using the set-up described in detail in the previous chapter. The samples consisted of TiO_2 particles in air, with an absorption length $\ell_a \simeq 70\ \mu m$. The mean free path ℓ for all samples was $\simeq 0.8\ \mu m$. In the experiment the thickness of the samples and the width of the incident Gaussian beam were varied to measure the fluctuations for different values of g. Table 5.1 lists the thickness of the samples, the width of the beam, and the number of scans over which was averaged to obtain the probability distribution and the second and third cumulant.

Fig. (5.1) shows the measured distribution function summed over all samples and beam widths to improve the statistics. Before summing the probability distributions of the scans the second cumulant of each scan was scaled to unity (FWHM is $2\sqrt{2\ln 2}$). The upper part of Fig. (5.1) shows the full distribution function, the solid line is the Gaussian of Eq. (5.5). The lower half of the graph shows the difference between the measured distribution and the Gaussian distribution, smoothed over half a unit of the x-axis. The predicted effect of a third cumulant is shown by the solid line. Scaling the second cumulant to unity fixes its zero crossings, its vertical scale relates to the magnitude of the third cumulant. The shape of the $\delta P(T_a)$ curve clearly demonstrates the presence of a third cumulant in the measured distribution.

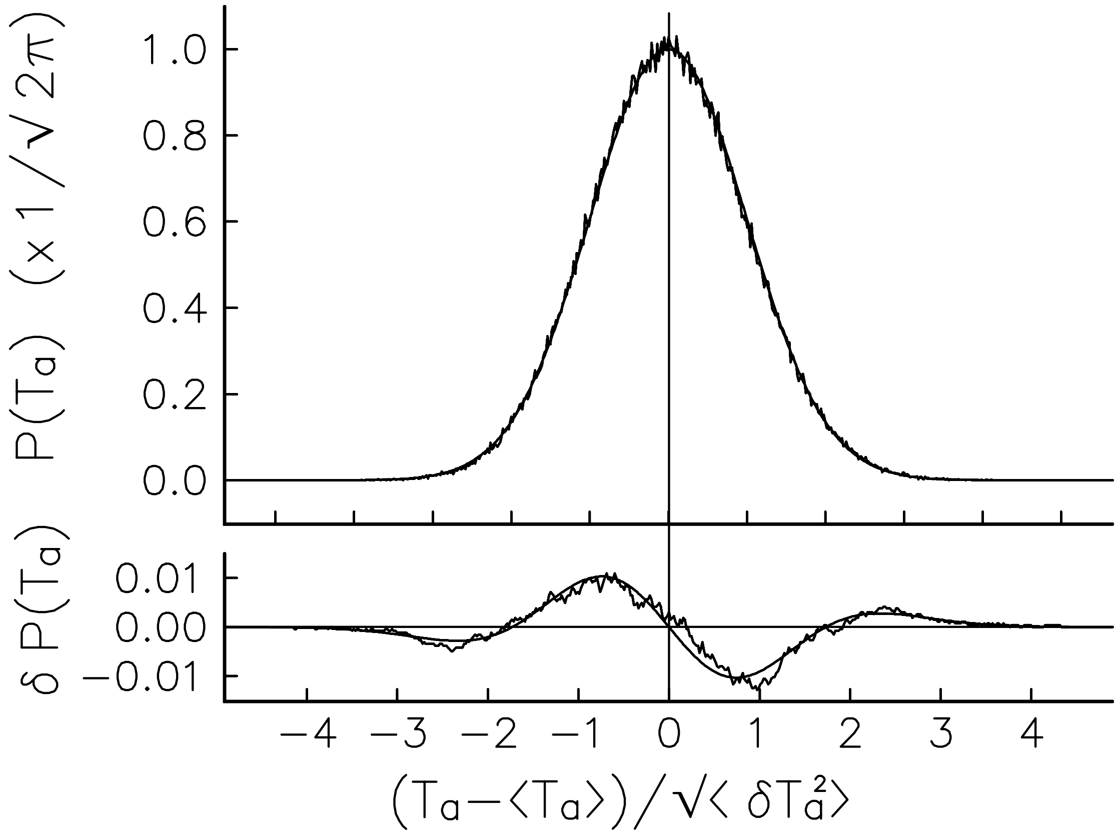

Figure 5.1: *Probability distribution of the fluctuations in total transmission, summed over all samples after scaling the normalized second cumulant to unity. Upper graph: Full distribution. Solid line is a Gaussian, completely determined by the normalized second cumulant that was scaled to unity. Lower graph presents the difference between the measured distribution and the Gaussian. The solid line shows a fit of the contribution expected from a third cumulant to the difference with the magnitude on the* y*-scale as only adjustable parameter.*

5.2.4 The second and third cumulant

The distribution is characterised by a second cumulant and a small but significant third cumulant, that both need to be calculated. The normalized second cumulant is

$$\langle\langle T_a^2\rangle\rangle \equiv \frac{\langle T_a^2\rangle - \langle T_a\rangle^2}{\langle T_a\rangle^2} \sim \frac{L}{N\ell}. \tag{5.6}$$

Double brackets define normalized cumulants. The second moment of the intensity distribution contains a disconnected (Fig. (5.2a)) and a connected part (Fig. (5.2b)). The connected part (Fig. (5.2b)) contains the interference between two diffusons (at

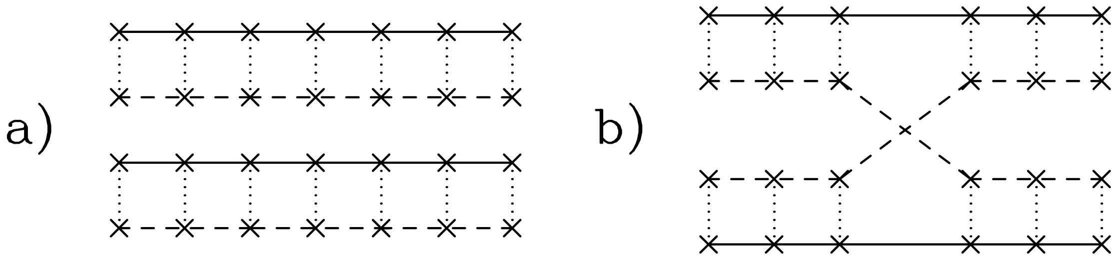

Figure 5.2: *Diagrams contributing to the second moment of the fluctuations on the total transmission. Diffusons (diffuse propagating intensities) are depicted by close parallel lines. Incoming and outgoing fields are not drawn. (a) Two disconnected diffusons. (b) Two diffusons interfering inside the sample. This is the leading contribution to the second cumulant.*

a Hikami vertex[58]) and is proportional to $L/N\ell$[52], which is the leading contribution to the second cumulant. The contribution to the second cumulant of the disconnected part is proportional to $1/N$, the naively predicted variance on the total transmission.

The diagrams contributing to the third moment are given in Fig. (5.3). From their structure the contribution to the third cumulant of the diagrams in Figs. (5.3a), (5.3b), and (5.3c) are seen to be of the order of respectively $1/N^2$, $L/N^2\ell$, and $L^2/N^2\ell^2$. The leading contribution to the third cumulant of the intensity distribution comes from the connected diagrams (Fig. (5.3c)). The factor $L^2/N^2\ell^2$ can be interpreted as the probability that three light paths will interfere twice, just as $L/N\ell$ gives the probability that two light paths will interfere once. As important result a quadratic relation between the second and the third normalized cumulant is found,

$$\langle\langle T_a^3\rangle\rangle \propto \langle\langle T_a^2\rangle\rangle^2. \tag{5.7}$$

Later the prefactor of this quadratic relation will be determined. To verify the predicted quadratic relation between the second and third cumulant, we plot in Fig. (5.4) the third cumulant versus the second cumulant for each value of the conductance, i.e. for each value of the sample thickness and beam diameter (the mean free path was the same for all samples). The error bars were obtained from the variance in the second and third cumulant within a set of scans with the same sample thickness and beam width. The second and third cumulant are averaged over sets of 16, 32, 48 or 64 scans. The resulting values and their standard errors are given in Table 5.1. The expected standard error of a third cumulant due to finite sampling can be estimated to be $(15/N_p)^{1/2}\langle\langle T_a^2\rangle\rangle^{3/2}$ [68], with N_p the number of points in a scan (1024) times the number of scans. The experimental error bars on the third cumulant are in good agreement with the expected magnitude of the standard error.

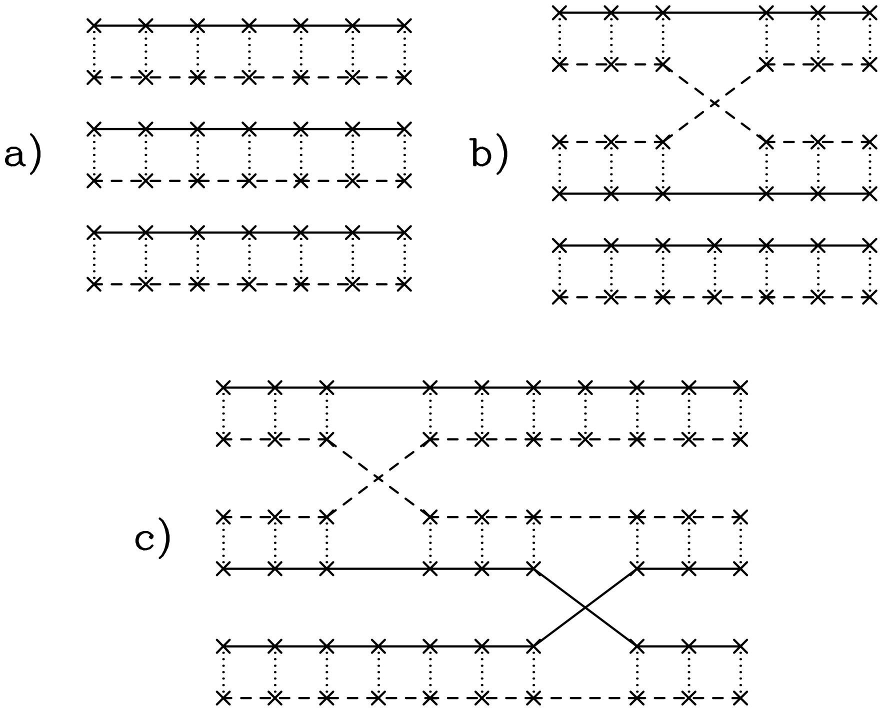

Figure 5.3: *The diagrams contributing to the third moment of the fluctuations on the total transmission. Incoming and outgoing fields are not drawn. (a) Three disconnected diffusons. (b) Two interfering diffusons and a disconnected diffuson. (c+d) Three interfering diffusons, in diagram (c) through two Hikami vertices, in diagram (d) through a six-point vertex. The diagrams in (c) and (d) are the leading contributions to the third cumulant.*

5.2.5 The non-linear least squares fit

The solid line in Fig. (5.4) is a weighted non-linear least squares fit to the data of,

$$\langle\langle T_a^3 \rangle\rangle = \alpha \langle\langle T_a^2 \rangle\rangle^{\beta}. \tag{5.8}$$

The optimum value of the fit parameters α and β is found by minimising the χ^2 merit function,

$$\chi^2 = \sum_i \frac{(y_i - \alpha x_i^{\beta})^2}{\sigma_i^2}, \tag{5.9}$$

with y_i the third cumulant, x_i the second cumulant, and σ_i the variance of the third cumulant. This results in $\chi^2_{minimum} = 9.0$, $\alpha = 0.7$ and $\beta = 1.83$.

The statistical tools to determine the error on the fit parameters and to test a linear, a quadratic, and a cubic relation between the second and third cumulant are found in Bevington[69]. A fit is considered "good" when the minimum value of χ^2 is approximately equal to the degrees of freedom. The degrees of freedom

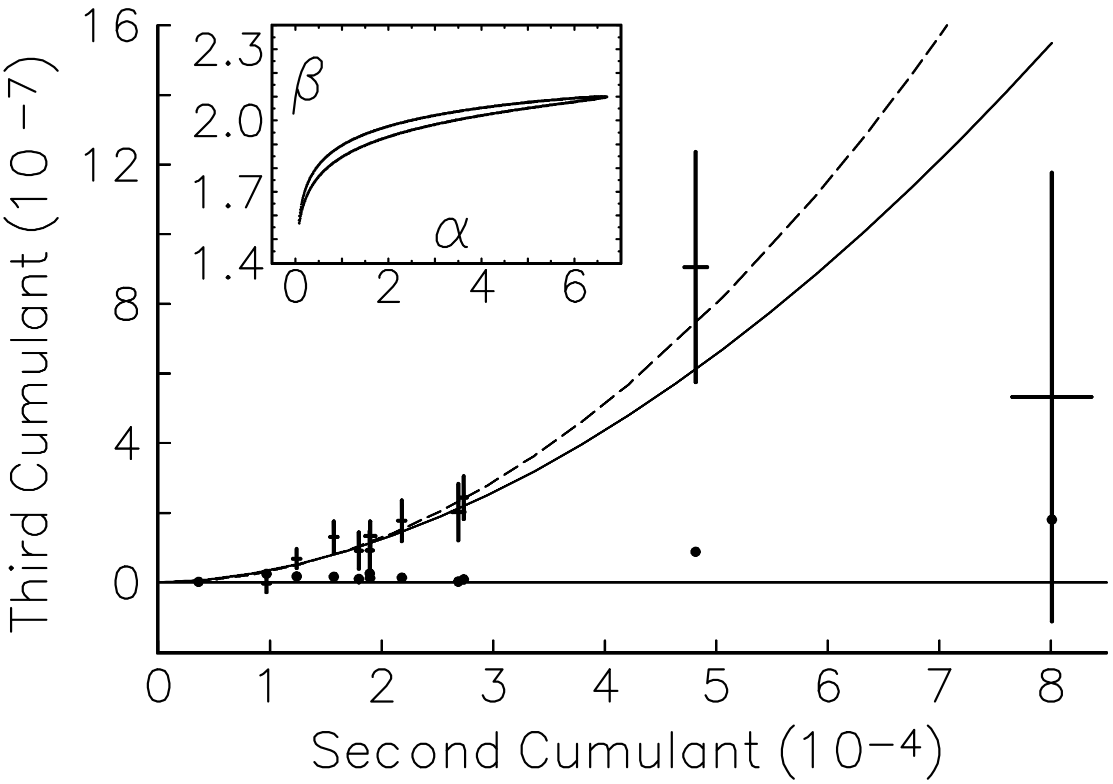

Figure 5.4: *The third cumulant as a function of the second cumulant of the intensity distribution. Solid line is weighted least squares fit to the data of* $\langle\langle T_a^3\rangle\rangle = \alpha\langle\langle T_a^2\rangle\rangle^\beta$. *The insert shows the 68% confidence region of the fit parameters* α *and* β, *yielding* $\alpha = 0.7\ {+6.0}/{-0.7}$, $\beta = 1.83 \pm 0.26$. *Dashed line is theoretical prediction* $\langle\langle T_a^3\rangle\rangle = 3.2\langle\langle T_a^2\rangle\rangle^2$. *Dots show the upper bound of the contribution of the mundane diagram in Fig. (5.3b) to the third cumulant.*

ν is the number of data points (12) minus the number of fit parameters (2), $\nu = 10$. Important for determining the confidence region of the fit parameters is the Probability Integral of the χ^2-distribution $P_\chi(\chi^2, \nu)$. It describes the probability that a random set of N data points would yield a value of χ^2 as large or larger when compared with the parent function. So given the parent function (determined by fixed values of α and β) and its resulting value for χ^2 the probability integral of the χ^2-distribution gives the probability to measure this data set or one that would fit the parent function worse.

First we calculate the probability that we would have measured our data set provided the parent function is linear,

$$\langle\langle T_a^3\rangle\rangle = \alpha\langle\langle T_a^2\rangle\rangle. \tag{5.10}$$

The minimum value of χ^2 is 34.1 with $\alpha = 3.7 \times 10^{-4}$. The Probability Integral of

Sample thickness L (in μm)	Beam width ρ_0 (in μm)	Number of scans	Second cumulant ($\times 10^{-4}$)	Third cumulant ($\times 10^{-7}$)	Number of modes N	Number of modes N^*
30	77	16	0.36 $\pm$0.01	0.014 $\pm$0.035	388000	193000
12	26	32	0.97 $\pm$0.03	$-$0.03 $\pm$0.25	46900	23300
22	32	48	1.24 $\pm$0.04	0.68 $\pm$0.28	88700	43500
30	33	16	1.57 $\pm$0.04	1.30 $\pm$0.46	119000	57300
53	35	32	1.80 $\pm$0.03	0.91 $\pm$0.53	241000	112000
30	26	32	1.90 $\pm$0.03	0.92 $\pm$0.56	95000	45000
45	33	32	1.90 $\pm$0.05	1.33 $\pm$0.43	187000	87600
53	26	32	2.18 $\pm$0.03	1.77 $\pm$0.59	208000	94500
170	27	32	2.69 $\pm$0.06	2.02 $\pm$0.82	1415000	632000
78	28	64	2.74 $\pm$0.03	2.43 $\pm$0.62	396000	177000
30	17	16	4.82 $\pm$0.10	9.1 $\pm$3.3	72000	33000
30	10	32	8.01 $\pm$0.36	5.3 $\pm$6.4	60300	26700

Table 5.1: *Sample parameters in the experiment. The number of modes N and N^* are defined in respectively Eq. (5.13) or Eq. (B.32) and Eq. (5.18) or Eq. (B.38).*

the χ^2-distribution $P_\chi(34.1, 11) = 3.5 \times 10^{-4}$, which means that provided the parent function is linear, the probability to have measured our data set is 0.035 %.

If the parent function is quadratic,

$$\langle\langle T_a^3 \rangle\rangle = \alpha \langle\langle T_a^2 \rangle\rangle^2, \tag{5.11}$$

the minimum value of χ^2 is 10.0 with $\alpha = 2.94$. The Probability Integral of the χ^2-distribution $P_\chi(10.0, 11) = 0.53$, which means that provided the parent function is quadratic, the probability to have measured our data set is 53 %.

If the parent function is cubic, the probability to have measured our data set is 0.003%. From this analysis we concluded that the quadratic relation is clearly the most likely, which is in good agreement with the predicted quadratic relation.

For the parent function of a fractional power (Eq. (5.8)),

$$\langle\langle T_a^3 \rangle\rangle = \alpha \langle\langle T_a^2 \rangle\rangle^\beta, \tag{5.12}$$

the 68% confidence region of the simultaneous fit parameters α and β is found by searching the value of χ^2 for which the Probability integral $P_\chi(\chi^2, \nu)$ is 0.32, in our case $P_\chi(\chi^2 = 11.5, \nu = 10) = 0.32$. The contour of constant $\chi^2 = 11.5$ gives the 68% confidence region for the parameters α and β, and is shown in the insert of Fig. (5.4). The errors on α and β as given by the contour are respectively $\alpha = 0.7$ $+6.0/-0.7$, $\beta = 1.83 \pm 0.26$, and the predicted quadratic relation lies well within the confidence region of the experimentally determined power.

5.3 The prefactor of the second versus the third cumulant

Assuming a quadratic relation between the second and third cumulant we try to find the prefactor in Eq. (5.7). A fit of the quadratic behaviour ($\beta = 2$) yields a prefactor $\alpha = 2.9$. The 68% confidence region of the fit parameter α is found by searching the value of χ^2 for which the Probability integral $P_\chi(\chi^2, \nu)$ is 0.32, in this case $P_\chi(\chi^2 = 12.6, \nu = 11) = 0.32$ (the minimum value for χ^2 is 10.0, for $\alpha = 2.93$). This results in $\alpha = 2.9 \pm 0.6$.

To calculate the prefactor of the quadratic relation between the second and third cumulant an explicit calculation of the diagrams in Figs. (5.2b) and (5.3c) has to be done that includes the incident Gaussian profile of the beam, $I_{inc}(\mathbf{r}_\perp) \sim \exp(-2\mathbf{r}_\perp^2/\rho_0^2)$. The details of the calculation are presented in Appendix B. We need the number of modes (independent speckle spots) in transmission. In chapter 3 it was shown to be given by Eq. (3.16) and Eq. (3.20) for an incident Gaussian beam profile,

$$N \equiv \mathit{2} \times \frac{k_0^2 I^2(q=0)}{\displaystyle\int_0^\infty 2qI(q)I(-q)dq}, \tag{5.13}$$

with k_0 the wave vector of the light and $I(q)$ the Fourier transform of the intensity profile at the exit interface of the sample. In Appendix B it is proven that with this definition of the number of modes the contribution of the diagram in Fig. (5.2a) to the second cumulant is exactly $1/N$. The factor $\mathit{2}$ distinguishes the vector wave ($\mathit{2} = 2$) from the scalar wave ($\mathit{2} = 1$) results[57]. In the limit $\rho_0 \gg L$ the number of modes N is not influenced by the diffuse broadening of the incident profile, $N = \mathit{2} k_0^2\rho_0^2/4$. In this limit the conductance $g = 4N\ell/3L$ is given by

$$g = \frac{\mathit{2} k_0^2 \rho_0^2 \ell}{3L}. \qquad (\rho_0 \gg L) \tag{5.14}$$

The results for the second cumulant (Fig. (5.2b)) are well known[52, 8, 70] and give (see also Eq. (3.70)),

$$\langle\langle T_a^2 \rangle\rangle = \frac{2L}{\mathit{2} k_0^2 \rho_0^2 \ell} = \frac{2}{3} g^{-1}. \qquad (\rho_0 \gg L) \tag{5.15}$$

In Fig. (5.3c) we present the third cumulant, the first diagram contains two Hikami four-point vertices, the second a six-point vertex. In the calculation the six-point vertex is found to cancel against the extra contribution of the first diagram that arises when the distance between the two Hikami vertices is of the order of one mean free path. The third cumulant depends in a non-trivial manner on the beam profile. For the incident Gaussian profile we find (see Appendix B)

$$\langle\langle T_a^3 \rangle\rangle = \frac{64L^2}{\mathit{2}^2\, 5k_0^4 \rho_0^4 \ell^2} = \frac{64}{45} g^{-2}. \qquad (\rho_0 \gg L) \tag{5.16}$$

(For a square profile the result would be $16/15g^2$). This gives the following simple relation between the second and third cumulant,

$$\langle\langle T_a^3\rangle\rangle = \frac{16}{5}\langle\langle T_a^2\rangle\rangle^2. \tag{5.17}$$

The experimentally observed prefactor of 2.9 ± 0.6 is in good agreement with the theoretical value of 16/5.

5.3.1 Contributions of experimental artefacts

Let us now estimate corrections to the leading contributions of the second and third cumulant and the influence of the experimental beam width $\rho_0 \sim L$. The correction to the leading contribution of the second cumulant is given by the diagram in Fig. (5.2a), yields $1/N$ (see Appendix B) and can be neglected. The correction to the leading contribution of the third cumulant comes from the diagram in Fig. (5.3b), that gives an extra contribution to the measured third cumulant of $\Delta\langle\langle T_a^3\rangle\rangle \leq 6 \times \langle\langle T_a^2\rangle\rangle/N^*$. The factor of six is of combinatorial origin and the effective number of modes N^* is given by

$$N^* \simeq \mathit{2} \times \frac{k_0^2 I(q=0)}{\displaystyle\int_0^\infty 2qI(q)dq}. \tag{5.18}$$

The proof of the estimate on the upper bound of $\Delta\langle\langle T_a^3\rangle\rangle$ is given in Appendix B. Table 5.1 gives the number of modes N^* for each sample and each incident beam width ($\mathit{2} = 2$). The resulting upper bound of the contribution of the diagram in Fig. (5.3b) to the measured third cumulant is shown in Fig. (5.4) by the dots. Since the upper bound of the correction is small, the measured third cumulant is nearly completely the effect of the interference process in Fig. (5.3c).

The magnitudes of the second cumulant as calculated with the experimental parameters as input are larger than the measured values by maximally 25 %. This difference was addressed in chapter 4, where it was shown to be caused by the finite range over which the wavelength was varied in the experiment. For the same reason the experimental values of the third cumulant are also lower than predicted. By plotting the second versus the third cumulant (Fig. (5.4)) the effects of the finite scan length largely cancel, as do effects of inaccuracies in the exact beam width, mean free path, and sample thickness.

The influence of the beam width was numerically evaluated for the diagrams of Figs. (5.2b) and (5.3c). The resulting relation between the second and third cumulant remained quadratic, only the prefactor of 16/5 was reduced by at most 14% for the smallest value of ρ_0/L. If this reduction were included in the theory it would make the agreement with the observed prefactor even better.

In conclusion, we showed experimentally that the probability distribution of the fluctuations in total transmission is predominantly Gaussian. The data clearly demonstrate a skewness of the probability distribution, caused by correlation in the cubed intensity. These correlations were calculated within a diagrammatic approach, and a good agreement is found between the experiment and the theory. Recently the full distribution function of the total transmission has been calculated[71] that confirms the theoretical result for the second and third cumulant presented here.

Chapter 6

Non-linear disordered media

6.1 Correlation in transmission and reflection

6.1.1 Introduction

In this chapter we present theoretical and experimental results of the leading order angular correlations of second harmonic light generated *inside* a random medium, for both the transmission and reflection geometries.

Many of the interesting linear multiple scattering effects have their non-linear equivalent. We will investigate the interference effects of second harmonic light, generated by a non-linear susceptibility of the scattering particles. The samples consist of slabs of small $LiNbO_3$ particles, which have a very high non-linear susceptibility. The fundamental light is multiply scattered by these particles, but a small part of the fundamental light is converted to second harmonic light. The second harmonic (SH) light is also multiply scattered by the particles. The multiply scattered SH light generated at different particles does interfere, and a speckle pattern is observed in transmission and reflection. The interest in interference effects of SH light was first raised by theoreticians. For instance, Agranovich and Kravtsov calculated the enhanced backscattering peak for second harmonic light, and found its magnitude to be much smaller than in the linear optics case[14, 15].

In this chapter we present both theoretical and experimental results for the leading angular correlations ($C^{(1)}$) of the second harmonic light generated inside random media, for both the transmission and reflection geometries. In contrast to the enhanced backscattering peak which is much reduced for second harmonic light, the $C^{(1)}$ correlation function remains a quantity of order unity. We find generally good agreement between theory and experiment. As we shall see, the correlation properties in the nonlinear optics regime exhibit richer and more complex features, as they result from the multiple scattering of both the second harmonic and the fundamental light, as well as the randomness in the second harmonic light generation process inside a powder-like random medium containing nonlinear crystallites. The above mentioned non-linear effects in multiple scattering are unique to optics and do not have an easily accessible counterpart in electronic wave transport systems. The phase coherent nature in the second harmonic light generation is also distinct from that in the generation and propagation of light in random media with luminescent centres. In the latter case the pump light excites radiating transitions that do not in general have a well defined relative phase relation as long as stimulated radiation effects can be ignored. As a consequence, speckle patterns do not form, in contrast to the second harmonic generation that we study here.

6.2 Theory

We will first describe the theoretical results briefly. In a poly-crystalline powder sample, the small crystallites are responsible for generation of second harmonic light, as well as for multiple scattering of both the fundamental and generated second harmonic light. For convenience in theoretical treatment, we assume the sample has a waveguide geometry, with a crosssectional area $\mathcal{A}$ corresponding to the area of illumination in the experiment. $N = 2\pi\mathcal{A}/\lambda^2$ (Eq. (3.21)) corresponds to the number of propagating modes (which we label by α), and equals the number of independent speckle spots in the far field that can be observed. The intensity transmission and reflection coefficients $T_{\alpha\beta}$ and $R_{\alpha\beta}$ respectively, give the fraction of the power in the incoming mode α that is coupled to the outgoing mode β.

6.2.1 Correlation in the fundamental light

The lowest order correlation function ($C^{(1)}$) in transmission in linear optics, defined as the leading contribution to $C_{\alpha\beta\alpha'\beta'} = \langle \delta T_{\alpha\beta} \delta T_{\alpha'\beta'} \rangle / \langle T_{\alpha\beta} \rangle^2$, with $\delta T_{\alpha\beta} = T_{\alpha\beta} - \langle T_{\alpha\beta} \rangle$, has been calculated previously, giving the result (neglecting surface reflection effects and absorption) [8] and Eq. (3.43),

$$C^{T\,(1)}_{\alpha\beta\alpha'\beta'}(\Delta\mathbf{q}_{\perp\alpha}L) = \left[\frac{\Delta\mathbf{q}_{\perp\alpha}L}{\sinh(\Delta\mathbf{q}_{\perp\alpha}L)}\right]^2 \times \delta_{\Delta\mathbf{q}_{\perp\alpha},\Delta\mathbf{q}_{\perp\beta}}. \tag{6.1}$$

The triangular brackets denote an ensemble average over the disorder, L is the length of the sample (thickness of the slab in the experiment), $\mathbf{q}_{\perp}$ is the transverse wave vector for a given waveguide mode (incoming or outgoing direction in the experiment), and the condition $\Delta\mathbf{q}_{\perp\alpha} = \mathbf{q}_{\perp\alpha} - \mathbf{q}_{\perp\alpha'}$ represents the "memory effect".

It can be shown that for reflection the $C^{(1)}$ correlation function in the one-mode-in-one-mode-out geometry is given by the square of the enhanced backscattering intensity function [3, 4, 72], which takes the form

$$C^{R(1)}_{\alpha\beta\alpha'\beta'}(\Delta\mathbf{q}_{\perp\alpha}, \ell, L) = \left[\frac{(L+2\tau_0)\mathrm{cosech}(\Delta\mathbf{q}(L+2\tau_0))}{\Delta\mathbf{q}(\ell L + \tau_0 L - 2\tau_0\ell + 2\tau_0^2 - 2\ell^2)}\right] \times$$
$$\left\{ \frac{\cosh(\Delta\mathbf{q}(L+2\tau_0)) - \Delta\mathbf{q}\ell\sinh(\Delta\mathbf{q}(L+2\tau_0))}{1-(\Delta\mathbf{q}\ell)^2} - \right.$$

$$\left.\left.\frac{(1+(\Delta\mathbf{q}\ell)^2)\cosh(\Delta\mathbf{q}L)-2\Delta\mathbf{q}\ell\sinh(\Delta\mathbf{q}L)}{(1-(\Delta\mathbf{q}\ell)^2)^2}\right\}\right]^2\times\delta_{\Delta\mathbf{q}_{\perp\alpha},\Delta\mathbf{q}_{\perp\beta}}. \qquad (6.2)$$

This expression is taken from Ref. [73]. Corrections due to internal reflection are accounted for by τ_0, $\tau_0=\ell(2+6C_2)/(3-6C_1)$, as described by Zhu, Pine and Weitz[39], where C_1 and C_2 are constants determined by the average refractive index of the medium. It is crucial to include the surface effects for the reflection geometry, as the main contribution to the $C^{R(1)}$ correlation function comes from scattering paths that are only a few transport mean free paths ℓ long. This is reflected by the scaling variable $\Delta\mathbf{q}_{\perp\alpha}\ell$ for this function. For the transmission geometry, the average path length $s\sim L^2/\ell$, which gives rise to the scaling variable $\Delta\mathbf{q}_{\perp\alpha}L$, so that surface effects are not so important. Thus we may use the simplest boundary condition to calculate the $C^{T(1)}$ correlation function, as we have done in Eq. (6.1).

6.2.2 Correlation in the second harmonic light

We turn now to the calculation of the leading ($C^{(1)}$) correlation function for the second harmonic light. The physical picture for this correlation function is the following [14, 15]: The fundamental light, which is impinging on the surface of the sample at $z=0$ from a direction characterized by $\mathbf{q}_{\perp\alpha}$, propagates inside the sample while suffering multiple scattering, thus setting up a sample specific speckle-like random amplitude (electrical field function) $E_\omega(\mathbf{r})$. Second harmonic light is generated on the randomly placed (and oriented) micro-crystallites, described by a source function,

$$S_{2\omega}(\mathbf{r},t)=\int_V\chi_2(\mathbf{r}-\mathbf{r}_1,t-t_1;\mathbf{r}-\mathbf{r}_2,t-t_2):[E_\omega(\mathbf{r}_1,t_1)\times E(\mathbf{r}_2,t_2)]\mathrm{d}\mathbf{r}_1\mathrm{d}t_1\mathrm{d}\mathbf{r}_2\mathrm{d}t_2, \qquad (6.3)$$

where the tensor field $\chi_2(\mathbf{r})$ describes the random nonlinear susceptibility of the crystalline powder and the integral is taken over the volume of one particle. This randomly generated second harmonic light then propagates throughout the sample, also being multiply scattered by the disordered powder sample. The reflected and transmitted 2ω light in the far field then exhibits a speckle pattern whose correlations we must calculate.

The diagram for calculating the average SH intensity is given in Fig. (6.1a). The corresponding diagram for the $C^{(1)}$ correlation function is given in Fig. (6.1b). Upon evaluating these diagrams, we obtain for the correlation functions for both the transmission geometry as well as the reflection geometry, defined as $C^{T,SH\,(1)}_{\alpha\beta\alpha'\beta'}=\langle\delta T^{SH}_{\alpha\beta}\delta T^{SH}_{\alpha'\beta'}\rangle/\langle T^{SH}_{\alpha\beta}\rangle^2$ and $C^{R,SH\,(1)}_{\alpha\beta\alpha'\beta'}=\langle\delta R^{SH}_{\alpha\beta}\delta R^{SH}_{\alpha'\beta'}\rangle/\langle R^{SH}_{\alpha\beta}\rangle^2$, the following simple analytical form:

$$C^{T,SH\,(1)}_{\alpha\beta\alpha'\beta'}(\Delta\mathbf{q}_{\perp\alpha}L)=\left[\frac{3}{\sinh^2(\Delta\mathbf{q}_{\perp\alpha}L)}-\frac{6}{\Delta\mathbf{q}_{\perp\alpha}L\sinh(2\Delta\mathbf{q}_{\perp\alpha}L)}\right]^2\times\delta_{2\Delta\mathbf{q}_{\perp\alpha},\Delta\mathbf{q}_{\perp\beta}}. \qquad (6.4)$$

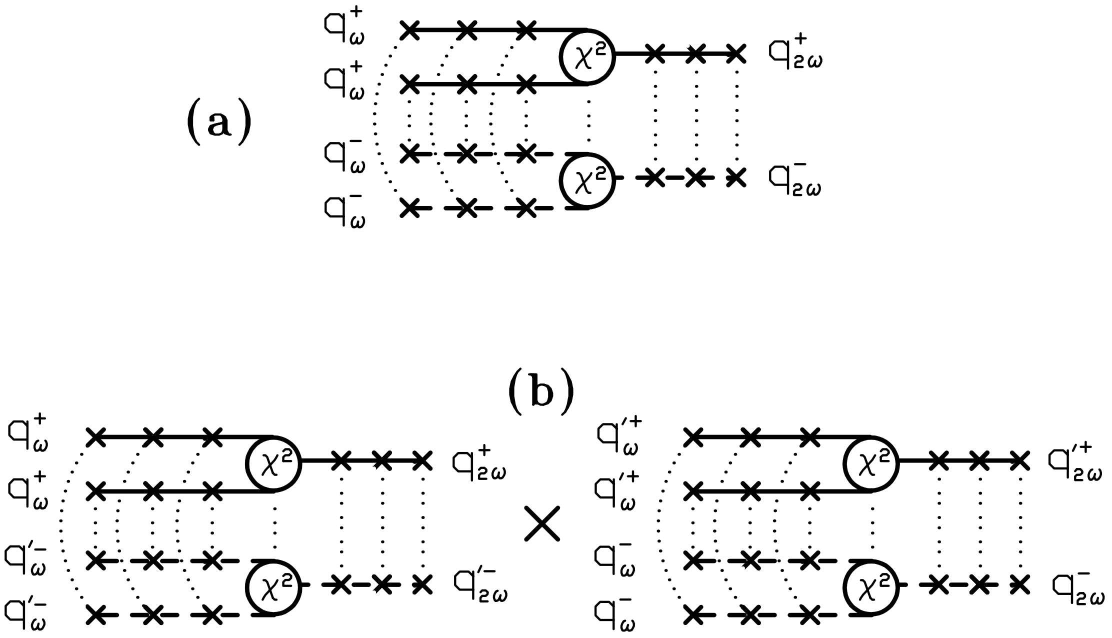

Figure 6.1: *(a) Feynman diagram for the ensemble average second harmonic intensity transmission and reflection coefficients* $\langle T^{SH}_{\alpha\beta}\rangle$ *and* $\langle R^{SH}_{\alpha\beta}\rangle$. *(b) Diagram for the leading order* ($C^{(1)}$) *correlation function for the second harmonic light,* $\langle \delta T^{SH}_{\alpha\beta}\delta T^{SH}_{\alpha'\beta'}\rangle$ *or* $\langle \delta R^{SH}_{\alpha\beta}\delta R^{SH}_{\alpha'\beta'}\rangle$. *Dashed lines connect a series of identical scatterers.*

$$C^{R,SH\,(1)}_{\alpha\beta\alpha'\beta'}(\Delta\mathbf{q}_{\perp\alpha}L) = \left[\frac{\tanh(\Delta\mathbf{q}_{\perp\alpha}L)}{\Delta\mathbf{q}_{\perp\alpha}L}\right]^2 \times \delta_{2\Delta\mathbf{q}_{\perp\alpha},\Delta\mathbf{q}_{\perp\beta}}. \tag{6.5}$$

In calculations leading to the above results an integration over the position of the SH sources $S_{2\omega}$ is performed. In transmission the simplest boundary conditions can be used for the same reason as in the transmission case for the fundamental light. In deriving Eq. (6.5) we have put $\tau_0 = 0$, which amounts to the neglect of surface effects. As Berkovits showed recently[74], a non-zero τ_0 should be included for finite size samples, leading to the expression,

$$C^{R,SH\,(1)}_{\alpha\beta\alpha'\beta'}(\Delta\mathbf{q}_{\perp\alpha},\ell,L) = \delta_{2\Delta\mathbf{q}_{\perp\alpha},\Delta\mathbf{q}_{\perp\beta}} \times$$
$$\left[\frac{L^3\sinh[\Delta\mathbf{q}_{\perp\alpha}(L-2\tau_0)](\sinh^2[\Delta\mathbf{q}_{\perp\alpha}\tau_0]+\sinh^2[\Delta\mathbf{q}_{\perp\alpha}(L-\tau_0)])}{\Delta\mathbf{q}_{\perp\alpha}\sinh^2[\Delta\mathbf{q}_{\perp\alpha}L]\cosh[\Delta\mathbf{q}_{\perp\alpha}L]((L-\tau_0)^4-\tau_0^4)}\right]^2. \tag{6.6}$$

As the ratio L/τ_0 increases, the surface corrections become less important, and Eq. (6.6) converges to Eq. (6.5). In this limit the correlation in reflection is a pure bulk effect. This leads to a striking difference between the SH and the fundamental (linear) correlations in the reflection geometry: The SH correlation in reflection (Eq. (6.5)) depends, to first approximation, only on the product of the thickness L and the transverse wave vector change $\Delta\mathbf{q}_{\perp\alpha}$; whereas the fundamental correlation

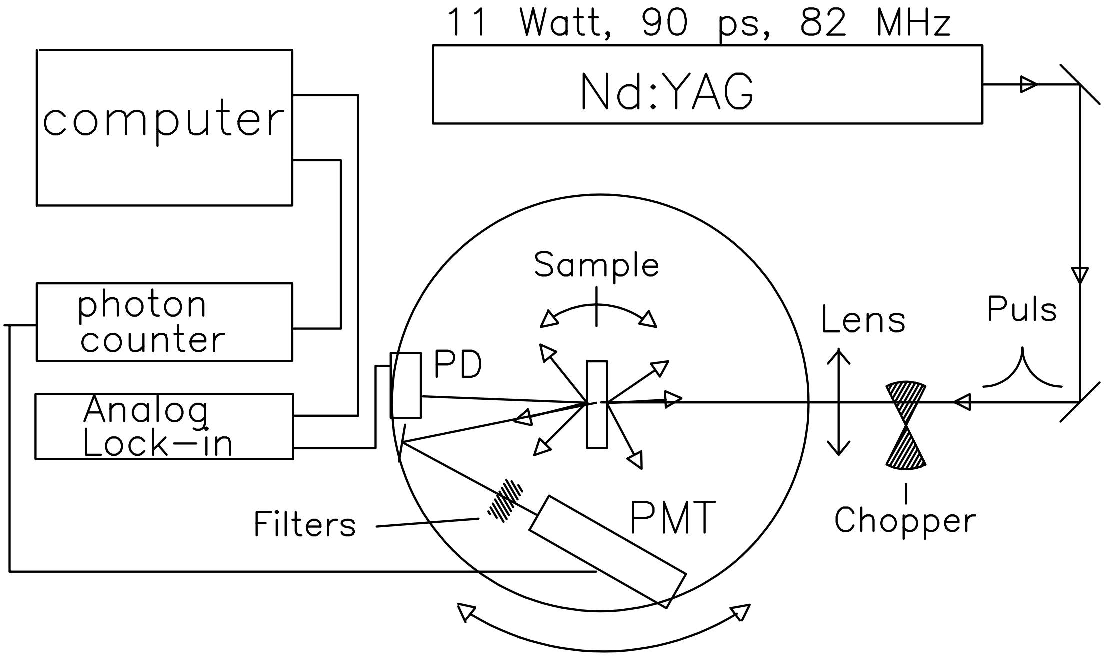

Figure 6.2: *Experimental set up for recording the angular speckle fluctuations in transmission and reflection. The sample and the detectors can rotate independently over 360 degrees. PMT: Photo multiplier (for detecting SH speckles); PD: Photo diode (for detecting fundamental light speckles).*

in reflection (Eq. (6.2)) is dominated by $\Delta \mathbf{q}_{\perp\alpha}\ell$. In transmission the halfwidth of the SH correlation is half the halfwidth of the fundamental (linear) correlation, while both show an exponential decay with $\Delta \mathbf{q}_{\perp} L$. Although it is hard to predict the absolute yield of SH light in a random sample, one can easily predict the ratio of the SH intensity in transmission over the SH intensity in reflection because the unknown prefactor is divided out. The ratio $\langle T^{SH}_{\alpha\beta}\rangle / \langle R^{SH}_{\alpha\beta}\rangle$ is approximately 1/3 for large L/τ_0, upon evaluating the diagram in Fig. (6.1a) for both the transmission and reflection geometries (corresponding to the $\Delta \mathbf{q}_{\perp} \to 0$ limit in the calculation of the correlation functions). This is an interesting theoretical result which was however not experimentally investigated.

6.3 Experiment

6.3.1 Experimental set-up

The experimental set-up is shown schematically in Fig. (6.2). A Spectra Physics 3800 Nd:YAG laser was used, giving 90 ps pulses at 1064 nm with a repetition rate of 82 Mhz and an average power of 11 Watt. A pulsed laser system was used because

Sample Thickness L (in μm)	$\ell(\omega)$ 1064 nm (in μm)	$\ell(2\omega)$ 532 nm (in μm)
27	1.9	1.1
38	3.7	3.2
65	3.4	2.5

Table 6.1: *Values of the mean free paths for the wavelength of 1064 nm (fundamental) and 532 nm (second harmonic) for each sample used in our measurement.*

Second Harmonic Generation is a non-linear process and SH yield is proportional to the average of the laser power squared. The beam was chopped and focused to 560 μm on the sample. The sample was prepared by suspending $LiNbO_3$ powder, obtained through milling a single crystal, in chloroform. Particle sizes range between 0.1 and 5 μm. The suspension was then spread on a 2 mm thick quartz window, and after evaporation of the chloroform, its thickness was determined microscopically. Sample thicknesses were 27, 38 and 65 μm. The infrared contribution was separated from the detected SH signal by absorption filters placed in front of the photo multiplier tube, that suppressed the fundamental light by more than a factor of 10^{16}. The transmission of the filters for the SH light was more than 40%. The second harmonic light was detected by a Hamamatsu R585 photo multiplier tube, with a dark count of approximately 0.4 cps. The photo multiplier tube was operated in photon counting mode. The count signal was sent to a digital (i.e. pulse count) lock-in detector to eliminate any contributions of ambient light to the signal. The average SH intensity was about 15 counts per second. The signal was accumulated for 5 sec. at each point in an angular scan. The intensity at the fundamental frequency was measured simultaneously by a photodiode. The detectors can be rotated independently from the sample, with an accuracy of 18 μrad and 43 μrad respectively for the detectors and the sample. The sample-holder was placed on two translation stages, one to position the sample surface exactly over the rotation axis, and the other to translate the sample perpendicular to the incoming beam to probe different areas of the sample when making multiple scans of the same sample. To ensure detection of only one outgoing mode, polarisers were placed in front of the detectors, and the solid angles seen by the photo detectors for the fundamental and the SH light were chosen to be smaller than the solid angle of a single speckle spot. The fluctuating intensity in transmission was recorded as a function of the angle of rotation of the sample. In the reflection measurements the detectors were also rotated to satisfy $\Delta \mathbf{q}_{\perp\alpha} = \Delta \mathbf{q}_{\perp\beta}$ (linear) or $2 \times \Delta \mathbf{q}_{\perp\alpha} = \Delta \mathbf{q}_{\perp\beta}$ (SH). Fig. (6.3) shows a typical Second Harmonic speckle pattern as observed in transmission by rotating the sample. From these scans the (experimental) short-range ($C^{(1)}$) correlation functions were computed.

The mean free path of each sample was determined by measuring the total

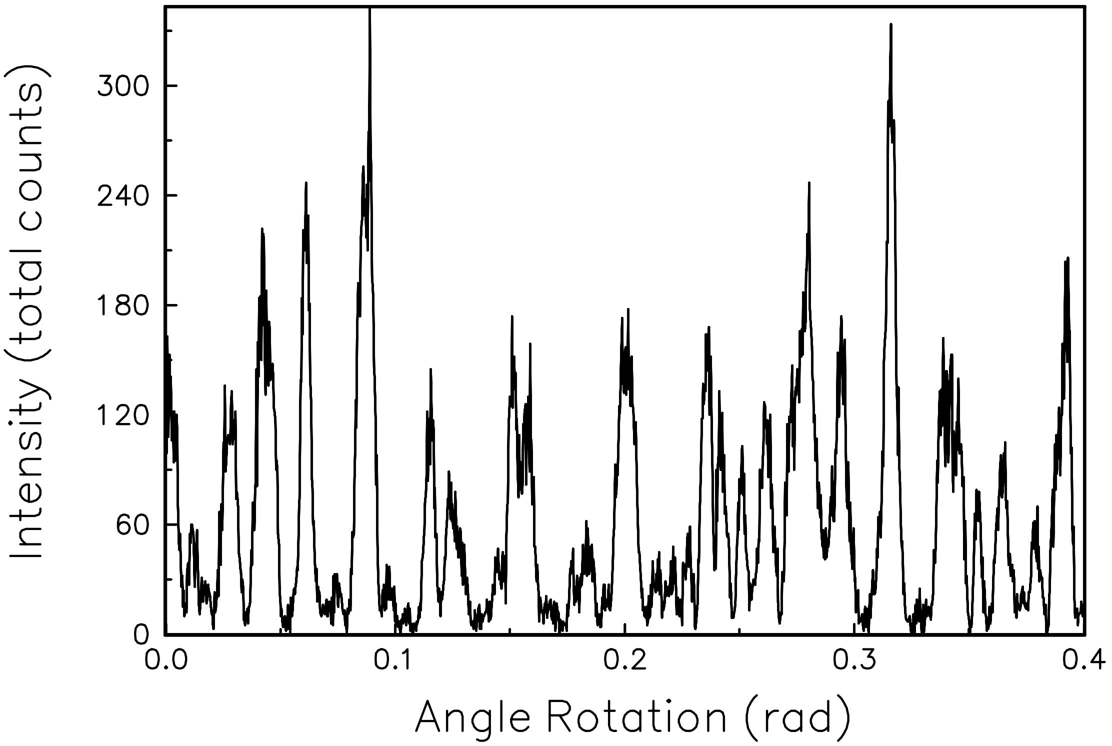

Figure 6.3: *Typical second harmonic speckle pattern in transmission, observed as a function of sample rotation. Sample thickness is* $38\mu m$.

(linear) transmission coefficient between 1100 *nm* and 500 *nm* wavelength, with a Fourier transform infrared spectrometer, using the formula $\langle T\rangle = 2\ell/(L_{slab}+2\ell)$ [9] or equivalently Eq. (2.165) with $\tau_0 = \ell$. The value $\tau_0 = \ell$ in Eq. (2.165) results from internal reflections because of the mismatch in refractive index of the disordered medium and the surrounding medium (air) [38, 75, 39]. The mean free paths for the different samples that are used for the computation of the correlation in the reflection geometry are given in Table (6.1).

6.3.2 Results

Both in transmission and reflection we were able to observe a clear speckle pattern in the SH light. Fig. (6.4) shows the measured correlation function in transmission for the SH and the fundamental light, together with their respective theoretical curves (from Eqs. (6.1) and (6.4)). The experimental correlation functions were averaged over six to eight scans. The thickness of each sample was determined by fitting the theory to the experimental curves (the only adjustable parameter). The values found agreed within the experimental accuracy of the microscopic thickness determination. We observe that the agreement between theory and experiment is excellent.

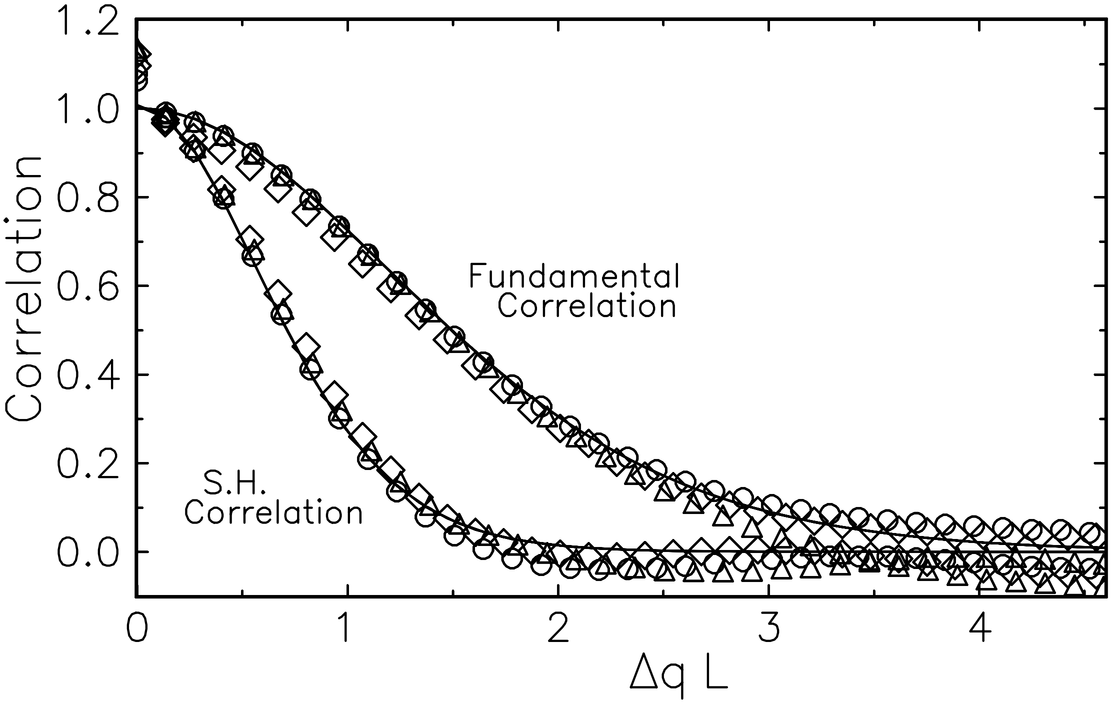

Figure 6.4: *Fundamental and second harmonic correlation in transmission as a function of sample rotation. Symbols: experimental data for* △ : $L = 27\mu m$, ○: $L = 38\mu m$, ◇ : $L = 65\mu m$, *with* L *the thickness of the sample. Smooth lines: theoretical curves.*

Fig. (6.5) shows the measured correlation function in reflection for the SH and the fundamental light, together with their respective theoretical curves (from Eq. (6.2) and Eq. (6.6)). The experimental data were averaged over eight to ten scans. The thicknesses of the samples used in the theory are obtained from the transmission experiment. The different theoretical curves for the fundamental correlation reflect their strong dependence on the mean free path, obtained from the total transmission and given in Table (6.1). A fit of the only free parameter τ_0 in Eq. (6.2) to the fundamental reflection data gave $\tau_0 \approx 2.4\ell$, which was used as input for Eq. (6.6). The value of τ_0 results in $n \approx 1.5$ [39], a surprisingly high value in view of the average refractive index of the TiO_2 samples in chapter 4. The different theoretical curves for the SH correlation are close together, reflecting their scaling behaviour with $\Delta\mathbf{q}L$.

In Fig. (6.4) and Fig. (6.5), the second data point of all experimental curves was normalized to one, rather than the first point, because all the high frequency auto-correlation noise is accumulated in the first point $C(\Delta\mathbf{q}_\perp = 0)$. The experimental data for reflection are in good agreement with the theory. The relative RMS fluctuations, defined as the square root of $C(\Delta\mathbf{q}_\perp = 0)$ were between 0.7 and 0.9 for all measurements. The small deviation from the theoretically expected value of

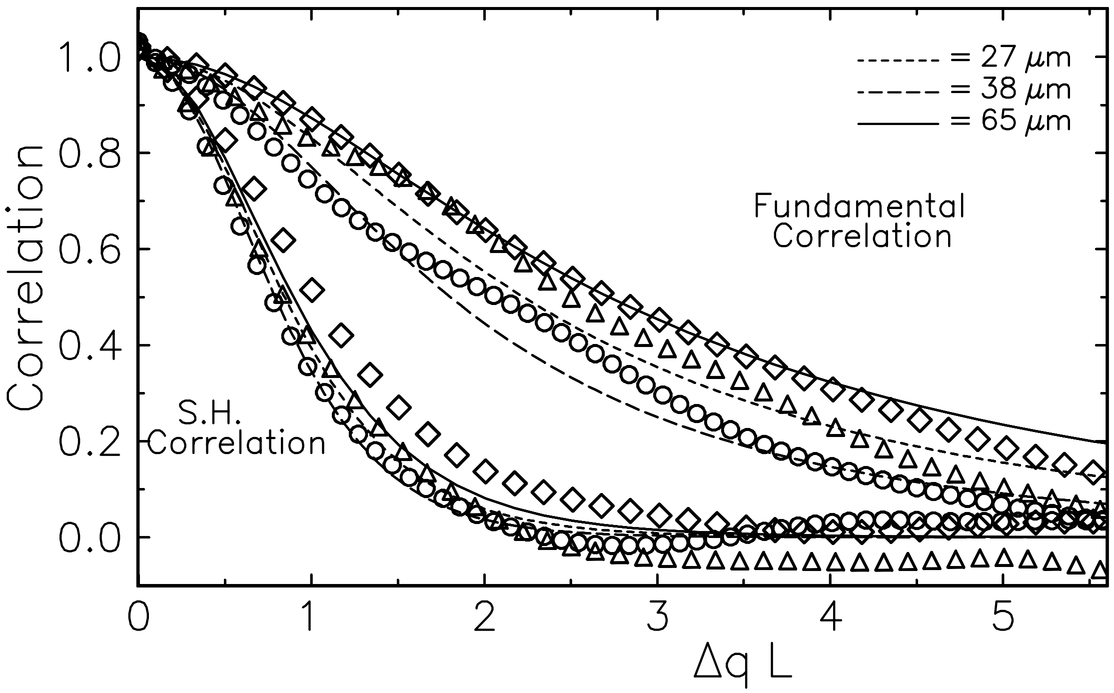

Figure 6.5: *Fundamental and second harmonic correlation in reflection as a function of sample rotation. The detectors are rotated at twice the angle of the sample rotation. Symbols: experimental data for* $\triangle : L = 27\mu m$, $\circ : L = 38\mu m$, $\diamond : L = 65\mu m$, *with L the thickness of the sample. Lines: theoretical curves for the respective sample thicknesses.*

unity for this quantity may be attributed to the heating of the sample by the intense fundamental beam, which made the static disorder slightly unstable.

6.4 Conclusion

In conclusion, we have studied both theoretically and experimentally for the first time the leading contribution ($C^{(1)}$) to the correlation properties in SH light generated inside a random sample, and shown that the measurements are in good agreement with our theoretical results. The measurements clearly demonstrate the different scale dependence of the SH and fundamental correlation in reflection. The correlations in reflection of the second harmonic light scales with the sample thickness L, in contrast to the corresponding short-range correlation function in reflection of the fundamental light in the linear scattering regime, which scales with mean free path ℓ.

Appendix A

A diagrammatic approach

A.1 Long-range correlation

In this appendix the long-range correlation in transmission is calculated in a diagrammatic approach. The appendix is based on lectures given by Th. M. Nieuwenhuizen[76] and worked out by the participants[77]. The core of the long-range correlation is the Hikami vertex, first calculated by Gor'kov[78] and Hikami[58]. The calculation of the Hikami-vertex here is in the second order Born approximation. For results beyond the second order Born approximation, see [55]. The calculations are presented here to show that the Langevin approach gives the same result as the diagrammatic approach, and because the results obtained here are needed in Appendix B to calculate the cumulants of the total transmission.

The correlation in transmission is given in Eq. (3.35) or Eq. (3.47), with the lowest order expansion of the vertex K given in Eq. (3.36). The expansion of the vertex K is discussed in more detail. The vertex K contains all diagrams in which two amplitudes and their complex conjugate interact. Only paired amplitudes (intensity propagators) survive the averaging process. Correlation between intensity propagators occurs when two paired amplitudes interact. In Fig. (A.1) the three basic diagrams of which K consists are drawn. In the first diagram the two paired amplitudes travel through the medium without interaction, leading to the short-range correlation. The second diagram shows the exchange of one amplitude between the two paired amplitudes, giving the long-range correlation, and in the last diagram the two paired amplitudes exchange an amplitude that later is exchanged again, giving back the original two pairs of amplitudes. The last diagram is responsible for the Universal Conductance Fluctuations on the conductance of disordered samples, the optical analog of the conductance fluctuations observed in mesoscopic electronic systems. The core of the diagrams leading to the long-range correlation and the UCF is the part where the amplitudes are exchanged (in physical terms: where amplitudes interfere). This exchange part, the Hikami-vertex, is calculated in the second order born approximation ,Eq. (2.33). The leading part of the Hikami-vertex in the second order Born approximation is given by the diagrams in Fig. (A.2). The diagrams are

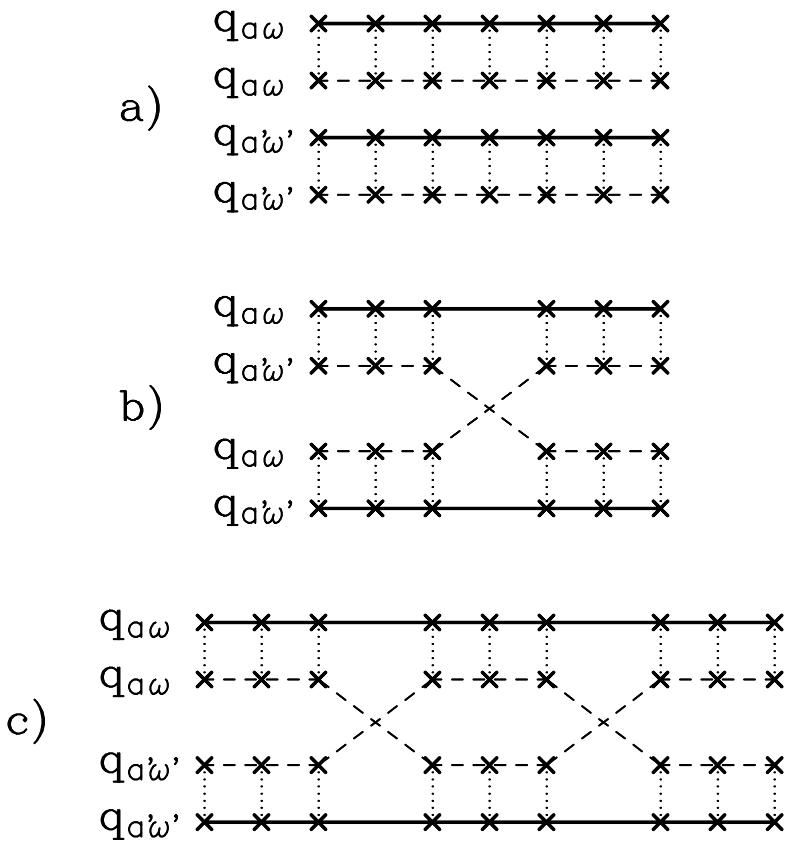

Figure A.1: *The decomposition of the vertex K into the most important diagrams. In the first diagram two intensities propagate through the medium without interaction. In the second diagram the two intensities exchange an amplitude. The last diagram shows the exchange of an amplitude and the subsequent exchange back. The diagrams are responsible for respectively the short-range and long-range correlation on the transmission and the optical analog of the Universal Conductance Fluctuations (UCF). In the text diagram b is denoted by* $\mathcal{H}_4(\mathbf{r}_{a1}, \mathbf{r}_{a3}; \mathbf{r}_b, \mathbf{r}_{b'})$

calculated for an infinite medium. In real space the diagram of Fig. (A.2) with the Ladder vertices connected is given by,

$$\begin{aligned}\mathcal{H}_4(\mathbf{r}_{a1}, \mathbf{r}_{a3}; \mathbf{r}_b, \mathbf{r}_{b'}) = \int_{-\infty}^{\infty} \mathrm{d}\mathbf{r}_1 \cdots \mathrm{d}\mathbf{r}_4\, L(\mathbf{r}_{a1}, \mathbf{r}_1) L(\mathbf{r}_2, \mathbf{r}_b) L(\mathbf{r}_{a3}, \mathbf{r}_3) L(\mathbf{r}_4, \mathbf{r}_{b'}) \\ G(\mathbf{r}_1 - \mathbf{r}_2) G^*(\mathbf{r}_3 - \mathbf{r}_2) G(\mathbf{r}_3 - \mathbf{r}_4) G^*(\mathbf{r}_1 - \mathbf{r}_4),\end{aligned} \tag{A.1}$$

where $\mathcal{H}_4(\mathbf{r}_{a1}, \mathbf{r}_{a3}; \mathbf{r}_b, \mathbf{r}_{b'})$ denotes the diagram in Fig. (A.1b) where the incoming and outgoing propagators in a slab geometry have to be connected to. In the above integral $L(\mathbf{r}_{a1}, \mathbf{r}_1)$ and $L(\mathbf{r}_{a3}, \mathbf{r}_3)$ are the Ladders that propagate intensity *to* $\mathbf{r}_{1,3}$, and

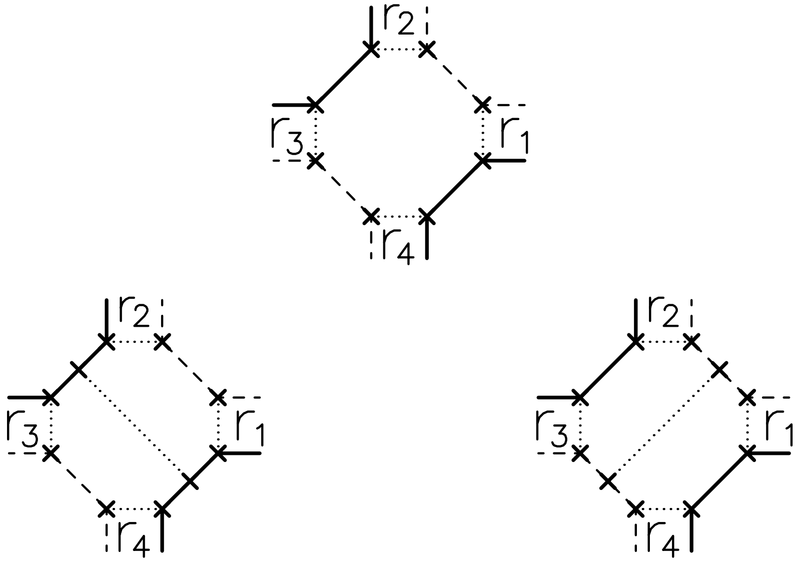

Figure A.2: *The exchange process of an amplitude in Fig. (A.1) in more detail. To get the correct expression for the Hikami vertex in the second order Born approximation three diagrams need to be calculated. The first is a product of four Green's functions. In the second and the third diagram the diagram is dressed with an extra scatterer. It turns out that the first diagram completely cancels against part of the second and third diagram.*

$L(\mathbf{r}_2, \mathbf{r}_b)$ and $L(\mathbf{r}_4, \mathbf{r}_{b'})$ are the Ladders that propagate intensity *from* $\mathbf{r}_{2,4}$. The product of the four amplitude propagators (GGG^*G^*) is the bare Hikami-vertex, the top diagram in Fig. (A.2). The diagrams are most easily calculated in $\mathbf{p}$-space. To that end the Ladders and the Green's functions in the following Fourier representation are substituted in Eq. (A.1),

$$L(\mathbf{p}_a, \mathbf{p}_1) = \int L(\mathbf{r}_a - \mathbf{r}_1) e^{i\mathbf{p}_a\mathbf{r}_a} e^{i\mathbf{p}_1\mathbf{r}_1} \mathrm{d}\mathbf{r}_a \mathrm{d}\mathbf{r}_1 = L(-\mathbf{p}_1)(2\pi)^3 \delta(\mathbf{p}_a + \mathbf{p}_1), \tag{A.2}$$

$$L(\mathbf{r}_a, \mathbf{p}_1) = L(-\mathbf{p}_1) e^{i\mathbf{p}_1\mathbf{r}_a}; \qquad L(\mathbf{p}_2, \mathbf{r}_b) = L(\mathbf{p}_2) e^{i\mathbf{p}_2\mathbf{r}_b}. \tag{A.3}$$

Substituting the Fourier representation into Eq. (A.1) leads to,

$$\begin{gathered}\mathcal{H}_4(\mathbf{r}_{a1}, \mathbf{r}_{a3}; \mathbf{r}_b, \mathbf{r}_{b'}) = \\ \int_{-\infty}^{\infty} L(\mathbf{r}_{a1}, \mathbf{p}_1) L(\mathbf{p}_2, \mathbf{r}_b) L(\mathbf{r}_{a3}, \mathbf{p}_3) L(\mathbf{p}_4, \mathbf{r}_{b'}) e^{-i\mathbf{p}_1\mathbf{r}_1 - i\mathbf{p}_2\mathbf{r}_2 - i\mathbf{p}_3\mathbf{r}_3 - i\mathbf{p}_4\mathbf{r}_4} \\ G(\mathbf{q}_1) G^*(\mathbf{q}_2) G(\mathbf{q}_3) G^*(\mathbf{q}_4) e^{-i\mathbf{q}_1(\mathbf{r}_1 - \mathbf{r}_2) - i\mathbf{q}_2(\mathbf{r}_2 - \mathbf{r}_3) - i\mathbf{q}_3(\mathbf{r}_3 - \mathbf{r}_4) - i\mathbf{q}_4(\mathbf{r}_4 - \mathbf{r}_1)} \\ \frac{\mathrm{d}\mathbf{p}_1 \cdots \mathrm{d}\mathbf{p}_4 \mathrm{d}\mathbf{r}_1 \cdots \mathrm{d}\mathbf{r}_4 \mathrm{d}\mathbf{q}_1 \cdots \mathrm{d}\mathbf{q}_4}{(2\pi)^{3\times 8}}.\end{gathered} \tag{A.4}$$

In Eq. (A.4) we separate out the Hikami vertex in the Fourier representation,

$$\mathcal{H}_4(\mathbf{r}_{a1},\mathbf{r}_{a3};\mathbf{r}_b,\mathbf{r}_{b'}) = \int_{-\infty}^{\infty} L(\mathbf{r}_{a1},\mathbf{p}_1)L(\mathbf{p}_2,\mathbf{r}_b)L(\mathbf{r}_{a3},\mathbf{p}_3)L(\mathbf{p}_4,\mathbf{r}_{b'})H(\mathbf{p}_1,\mathbf{p}_3;\mathbf{p}_2,\mathbf{p}_4)\frac{\mathrm{d}\mathbf{p}_1\cdots\mathrm{d}\mathbf{p}_4}{(2\pi)^{12}}, \tag{A.5}$$

with the Hikami vertex in the Fourier representation,

$$H(\mathbf{p}_1,\mathbf{p}_3;\mathbf{p}_2,\mathbf{p}_4) = \int_{-\infty}^{\infty} e^{-i\mathbf{p}_1\mathbf{r}_1-i\mathbf{p}_2\mathbf{r}_2-i\mathbf{p}_3\mathbf{r}_3-i\mathbf{p}_4\mathbf{r}_4}\, G(\mathbf{q}_1)G^*(\mathbf{q}_2)G(\mathbf{q}_3)G^*(\mathbf{q}_4)$$
$$e^{-i\mathbf{q}_1\,(\mathbf{r}_1-\mathbf{r}_2)-i\mathbf{q}_2\,(\mathbf{r}_2-\mathbf{r}_3)-i\mathbf{q}_3\,(\mathbf{r}_3-\mathbf{r}_4)-i\mathbf{q}_4\,(\mathbf{r}_4-\mathbf{r}_1)}\,\frac{\mathrm{d}\mathbf{r}_1\cdots\mathrm{d}\mathbf{r}_4\mathrm{d}\mathbf{q}_1\cdots\mathrm{d}\mathbf{q}_4}{(2\pi)^{12}}. \tag{A.6}$$

A.1.1 The Hikami-vertex

We will calculate the Hikami-vertex $H(\mathbf{p}_1,\mathbf{p}_3;\mathbf{p}_2,\mathbf{p}_4)$ in momentum space. Integration over $\mathbf{r}_{1,2,3,4}$ gives the following delta functions,

$$\begin{array}{lll}
\int \mathrm{d}\mathbf{r}_1 \to \delta(\mathbf{p}_1+\mathbf{q}_1-\mathbf{q}_4)(2\pi)^3 & \mathbf{q}_4\to\mathbf{q} & \mathbf{q}_1=\mathbf{q}-\mathbf{p}_1 \\
\int \mathrm{d}\mathbf{r}_2 \to \delta(\mathbf{p}_2+\mathbf{q}_2-\mathbf{q}_1)(2\pi)^3 & & \mathbf{q}_2=\mathbf{q}-\mathbf{p}_1-\mathbf{p}_2 \\
\int \mathrm{d}\mathbf{r}_3 \to \delta(\mathbf{p}_3+\mathbf{q}_3-\mathbf{q}_2)(2\pi)^3 & & \mathbf{q}_3=\mathbf{q}-\mathbf{p}_1-\mathbf{p}_2-\mathbf{p}_3 \\
\int \mathrm{d}\mathbf{r}_4 \to \delta(\mathbf{p}_4+\mathbf{q}_4-\mathbf{q}_3)(2\pi)^3 & & \mathbf{q}_4=\mathbf{q}-\mathbf{p}_1-\mathbf{p}_2-\mathbf{p}_3-\mathbf{p}_4 \\
 & & \Rightarrow \mathbf{p}_1+\mathbf{p}_2+\mathbf{p}_3+\mathbf{p}_4=0,
\end{array}$$

where $\mathbf{q}_4$ was renamed $\mathbf{q}$. Note that $\mathbf{q}$ is a free momentum now, and that the other momenta ($\mathbf{q}_{1,2,3}$) are fixed. The integration over the momenta $\mathbf{q}$ in Eq. (A.6) gives,

$$H(\mathbf{p}_1,\mathbf{p}_3;\mathbf{p}_2,\mathbf{p}_4) = (2\pi)^3\delta(\mathbf{p}_1+\mathbf{p}_2+\mathbf{p}_3+\mathbf{p}_4)\times$$
$$\int\frac{\mathrm{d}\mathbf{q}}{(2\pi)^3}G(\mathbf{q}-\mathbf{p}_1)G^*(\mathbf{q}+\mathbf{p}_3+\mathbf{p}_4)G(\mathbf{q}+\mathbf{p}_4)G^*(\mathbf{q}). \tag{A.7}$$

The above term is the top of the three diagrams in Fig. (A.2), which we label as H_1, H_2 and H_3, with $H(\mathbf{p}_1,\mathbf{p}_3;\mathbf{p}_2,\mathbf{p}_4) = (2\pi)^3\delta(\mathbf{p}_1+\mathbf{p}_2+\mathbf{p}_3+\mathbf{p}_4)(H_1+H_2+H_3)$. H_1 is given by,

$$H_1 = \int\frac{\mathrm{d}\mathbf{q}}{(2\pi)^3}G(\mathbf{q}-\mathbf{p}_1)G^*(\mathbf{q}+\mathbf{p}_3+\mathbf{p}_4)G(\mathbf{q}+\mathbf{p}_4)G^*(\mathbf{q}). \tag{A.8}$$

First H_1, H_2 and H_3 are calculated in the limit $\mathbf{p}_i\to 0$. With the help of the useful integrals $I_{k,l}$, which are given in Appendix A.2, we find,

$$H_1(\mathbf{p}_i\to 0) = I_{2,2} + O(\mathbf{p}_i^2) = \frac{\ell^3}{8\pi k^2} + O(\mathbf{p}_i^2), \tag{A.9}$$

where k is the length of the wave vector in the medium. Next the diagrams with one extra scatterer are given, H_2 en H_3.

$$H_2 = nt^2 \int \frac{\mathrm{d}\mathbf{q}}{(2\pi)^3} G(\mathbf{q}-\mathbf{p}_1)G^*(\mathbf{q})G(\mathbf{q}+\mathbf{p}_4) \int \frac{\mathrm{d}\mathbf{q}'}{(2\pi)^3} G(\mathbf{q}'-\mathbf{p}_3)G^*(\mathbf{q}')G(\mathbf{q}'+\mathbf{p}_2), \tag{A.10}$$

$$H_3 = nt^{*2} \int \frac{\mathrm{d}\mathbf{q}}{(2\pi)^3} G^*(\mathbf{q}-\mathbf{p}_4)G(\mathbf{q})G^*(\mathbf{q}+\mathbf{p}_3) \int \frac{\mathrm{d}\mathbf{q}'}{(2\pi)^3} G^*(\mathbf{q}'-\mathbf{p}_2)G(\mathbf{q}')G^*(\mathbf{q}'+\mathbf{p}_1). \tag{A.11}$$

Both diagrams are split in two products, with in each part a free momentum. The calculation of H_2 and H_3 in the limit $\mathbf{p}_i \to 0$ yields,

$$H_2(\mathbf{p}_i = 0) = nt^2 I_{2,1}^2 \approx nt^2 \frac{-\ell^4}{64\pi^2 k^2} \approx \frac{t}{t^*}\frac{-\ell^3}{16\pi k^2}, \tag{A.12}$$

$$H_3(\mathbf{p}_i = 0) = nt^{*2} I_{1,2}^2 \approx nt^{*2} \frac{-\ell^4}{64\pi^2 k^2} \approx \frac{t^*}{t}\frac{-\ell^3}{16\pi k^2}. \tag{A.13}$$

In the second order Born approximation one has:

$$t = V + iV^2 \frac{E}{4\pi c}, \qquad \ell = \frac{4\pi}{nV^2}, \qquad \mathrm{Re}\frac{t}{t^*} = 1. \tag{A.14}$$

With this one finds,

$$H_2(0) + H_3(0) = \frac{-\ell^3}{8\pi k^2}, \tag{A.15}$$

and thus,

$$H_1(0) + H_2(0) + H_3(0) = 0 + O(\mathbf{p}^2). \tag{A.16}$$

The leading term in the first diagram (H_1) cancels completely against the leading term of the second and third diagram! The diagrams have to be calculated up to order $\mathbf{p}^2$. To this end $G(\mathbf{q}-\mathbf{p})$ is approximated up to order $\mathbf{p}^2$ by a Taylor expansion around $\mathbf{p} = 0$.

$$\begin{aligned} G(\mathbf{q}-\mathbf{p}) &= \frac{1}{(\mathbf{q}-\mathbf{p})^2 + \mu^2} = \frac{1}{\mathbf{q}^2 + \mu^2 - 2\mathbf{q}\cdot\mathbf{p} + \mathbf{p}^2} \approx \\ & G(\mathbf{q}) + (2\mathbf{q}\cdot\mathbf{p} - \mathbf{p}^2)G^2(\mathbf{q}) + 4(\mathbf{q}\cdot\mathbf{p})^2 G^3(\mathbf{q}) + O(\mathbf{p}^3), \end{aligned} \tag{A.17}$$

where μ is defined in Appendix A.2. Use the following approximation for the third term in the right hand side of Eq. (A.17),

$$\int \mathrm{d}\mathbf{q}(\mathbf{q}\cdot\mathbf{p})^2\, G^n(\mathbf{q})G^{*\,m}(\mathbf{q}) \approx \frac{1}{3}\mathbf{p}^2 k^2 \int \mathrm{d}\mathbf{q} G^n(\mathbf{q})G^{*\,m}(\mathbf{q}). \tag{A.18}$$

The factor 1/3 originates from the averaging over the angle in the inner product, $\mathbf{q}^2 \to k^2$ because that is the pole in the integral that gives the most important contribution. A second approximation is made, that is not immediately obvious. The second factor $-\mathbf{p}^2 G^2(\mathbf{q})$ in the second term of the r.h.s. of Eq. (A.17) is neglected because it gives a contribution in lower order of the mean free path than the other terms. The first factor $2(\mathbf{q}\cdot\mathbf{p})G^2(\mathbf{q})$ of the second term is 0 after integration over $\mathbf{q}$ because the integrand is asymmetric in $\mathbf{q}$. Terms that do not cancel are products of the second term: $(2\mathbf{q}\cdot\mathbf{p}_i)(2\mathbf{q}\cdot\mathbf{p}_j)$. These contributions are approximated in the same way as is done in Eq. (A.18), where terms asymmetric in $\mathbf{q}_i$ give 0. What remains is,

$$\int \mathrm{d}\mathbf{q}\,(\mathbf{q}\cdot\mathbf{p}_i)(\mathbf{q}\cdot\mathbf{p}_j)\,G^n(\mathbf{q})G^{*\,m}(\mathbf{q}) \approx \frac{1}{3}k^2\,(\mathbf{p}_i\cdot\mathbf{p}_j)\int \mathrm{d}\mathbf{q}G^n(\mathbf{q})G^{*\,m}(\mathbf{q}). \tag{A.19}$$

With the help of the $I_{k,l}$ integrals in Appendix A.2 the diagrams $H_1(\mathbf{p}_i)\cdots H_3(\mathbf{p}_i)$ are calculated up to order $\mathbf{p}^2$,

$$\begin{aligned}
H_1(\mathbf{p}_i) &= \frac{\ell^3}{8\pi k^2} - \frac{\ell^5}{24\pi k^2}(\mathbf{p}_1^2+\mathbf{p}_2^2+\mathbf{p}_3^2+\mathbf{p}_4^2+\mathbf{p}_1\mathbf{p}_3+\mathbf{p}_2\mathbf{p}_4),\\
H_2(\mathbf{p}_i) &= \frac{t}{t^*}\Big(\frac{-\ell^3}{16\pi k^2} + \frac{\ell^5}{48\pi k^2}(\mathbf{p}_1^2+\mathbf{p}_2^2+\mathbf{p}_3^2+\mathbf{p}_4^2-\mathbf{p}_1\mathbf{p}_4-\mathbf{p}_2\mathbf{p}_3)\Big),\\
H_3(\mathbf{p}_i) &= \frac{t^*}{t}\Big(\frac{-\ell^3}{16\pi k^2} + \frac{\ell^5}{48\pi k^2}(\mathbf{p}_1^2+\mathbf{p}_2^2+\mathbf{p}_3^2+\mathbf{p}_4^2-\mathbf{p}_1\mathbf{p}_2-\mathbf{p}_3\mathbf{p}_4)\Big).
\end{aligned} \tag{A.20}$$

Adding up the contributions of the first, second and third diagram and using Eq. (A.14) we find the Hikami vertex in the symmetric form,

$$\begin{aligned}
&H(\mathbf{p}_1,\mathbf{p}_3;\mathbf{p}_2,\mathbf{p}_4) = (2\pi)^3\delta(\mathbf{p}_1+\mathbf{p}_2+\mathbf{p}_3+\mathbf{p}_4)\sum_{j=1}^{3} H_j(\mathbf{p}_i) =\\
&(2\pi)^3\delta(\mathbf{p}_1+\mathbf{p}_2+\mathbf{p}_3+\mathbf{p}_4)\frac{-\ell^5}{96\pi k^2}(2\mathbf{p}_1\mathbf{p}_3+2\mathbf{p}_2\mathbf{p}_4-\mathbf{p}_1^2-\mathbf{p}_2^2-\mathbf{p}_3^2-\mathbf{p}_4^2).
\end{aligned} \tag{A.21}$$

Using the momentum conservation $\delta(\mathbf{p}_1+\mathbf{p}_2+\mathbf{p}_3+\mathbf{p}_4)$ Eq. (A.21) may be simplified into the equivalent asymmetric forms,

$$\sum_{j=1}^{3} H_j(\mathbf{p}_i) = \frac{-\ell^5}{48\pi k^2}(2\mathbf{p}_1\mathbf{p}_3-\mathbf{p}_2^2-\mathbf{p}_4^2) = \frac{-\ell^5}{48\pi k^2}(2\mathbf{p}_2\mathbf{p}_4-\mathbf{p}_1^2-\mathbf{p}_3^2). \tag{A.22}$$

The $\mathbf{p}^2$ terms in the Hikami vertex lead to double derivatives in a real space representation of the Hikami vertex. The double derivative with respect to $\mathbf{r}$ of the Ladder in Eq. (2.162) leads essentially to a δ-function. This means that the $\mathbf{p}^2$ terms only give a contribution near the slab boundaries, were the incoming intensity is coupled to the Ladders. The main contribution of the Hikami vertex is in the bulk of the medium, and for the moment the boundary contributions (i.e. the $\mathbf{p}^2$ terms) are neglected. The Hikami vertex becomes,

$$\sum_{j=1}^{3} H_j(\mathbf{p}_i) = \frac{-\ell^5}{24\pi k^2}(\mathbf{p}_1\cdot\mathbf{p}_3) = \frac{-\ell^5}{24\pi k^2}(\mathbf{p}_2\cdot\mathbf{p}_4). \tag{A.23}$$

A.1.2 The long-range correlation function

We will use the expression for the Hikami vertex in Eq. (A.23) to calculate the long range correlation. Substituting Eq. (A.23) in the expression for the ladders attached to the Hikami vertex in Eq. (A.4) gives,

$$\begin{aligned}\mathcal{H}_4(\mathbf{r}_{a1},\mathbf{r}_{a3};\mathbf{r}_b,\mathbf{r}_{b'}) = \int_{-\infty}^{\infty} L(\mathbf{r}_{a1},\mathbf{p}_1)L(\mathbf{p}_2,\mathbf{r}_b)L(\mathbf{r}_{a3},\mathbf{p}_3)L(\mathbf{p}_4,\mathbf{r}_{b'})\\ \delta(\mathbf{p}_1+\mathbf{p}_2+\mathbf{p}_3+\mathbf{p}_4)\frac{-\ell^5}{24\pi k^2}(\mathbf{p}_1\cdot\mathbf{p}_3)\frac{\mathrm{d}\mathbf{p}_1\cdots\mathrm{d}\mathbf{p}_4}{(2\pi)^{3\times 3}}.\end{aligned} \tag{A.24}$$

For the slab geometry the most convenient form of the above equation is in $(z,\mathbf{p}_\perp)$ coordinates. Substituting the following forms of the Ladder into Eq. (A.24),

$$\begin{aligned}L(\mathbf{r}_a,\mathbf{p}_1) &= \int L(z_a,z_1,-\mathbf{p}_{\perp 1})e^{i\mathbf{p}_{\perp 1}\mathbf{r}_{\perp a}}e^{i\mathbf{p}_{z_1}z_1}\mathrm{d}z_1;\\ L(\mathbf{p}_2,\mathbf{r}_b) &= \int L(z_2,z_b,\mathbf{p}_{\perp 2})e^{i\mathbf{p}_{\perp 2}\mathbf{r}_{\perp b}}e^{i\mathbf{p}_{z_2}z_2}\mathrm{d}z_2,\end{aligned} \tag{A.25}$$

leads to,

$$\begin{aligned}&\mathcal{H}_4(\mathbf{r}_{a1},\mathbf{r}_{a3};\mathbf{r}_b,\mathbf{r}_{b'}) =\\ &\int L(z_{a1},z_1,-\mathbf{p}_{\perp 1})L(z_2,z_b,\mathbf{p}_{\perp 2})L(z_{a3},z_3,-\mathbf{p}_{\perp 3})L(z_4,z_{b'},\mathbf{p}_{\perp 4})\\ &e^{i\mathbf{p}_{\perp 1}\mathbf{r}_{\perp a1}}e^{i\mathbf{p}_{z_1}z_1}e^{i\mathbf{p}_{\perp 2}\mathbf{r}_{\perp b}}e^{i\mathbf{p}_{z_2}z_2}e^{i\mathbf{p}_{\perp 3}\mathbf{r}_{\perp a3}}e^{i\mathbf{p}_{z_3}z_3}e^{i\mathbf{p}_{\perp 4}\mathbf{r}_{\perp b'}}e^{i\mathbf{p}_{z_4}z_4}\\ &\delta(\mathbf{p}_1+\mathbf{p}_2+\mathbf{p}_3+\mathbf{p}_4)\frac{-\ell^5}{24\pi k^2}(\mathbf{p}_1\cdot\mathbf{p}_3)\frac{\mathrm{d}\mathbf{p}_1\cdots\mathrm{d}\mathbf{p}_4,\mathrm{d}z_1\cdots\mathrm{d}z_4}{(2\pi)^{3\times 3}}.\end{aligned} \tag{A.26}$$

By partial integration and neglecting the stok terms (that give a small contribution at the boundaries) the Hikami vertex is rewritten as,

$$\frac{-\ell^5}{24\pi k^2}(\mathbf{p}_1\cdot\mathbf{p}_3) \to \frac{\ell^5}{24\pi k^2}\left[\frac{\partial}{\partial z_1}\frac{\partial}{\partial z_3} - \mathbf{p}_{\perp 1}\cdot\mathbf{p}_{\perp 3}\right], \tag{A.27}$$

where the derivatives work only on the Ladders. Integration over $\mathbf{p}_{z_1}$ and subsequent integration over $\mathbf{p}_{z_2}$, $\mathbf{p}_{z_3}$ and $\mathbf{p}_{z_4}$ gives three δ-functions on the z coordinates. We integrate over the z_1, z_2 and z_3 coordinates and substitute $z_1 \to z$. Since the total transmission is sought we integrate over the transversal coordinates $\mathbf{r}_{\perp b}$ and $\mathbf{r}_{\perp b'}$, which gives two δ-functions of $\mathbf{p}_{\perp 2}$ and $\mathbf{p}_{\perp 4}$. Integration over $\mathbf{p}_{\perp 2}$, $\mathbf{p}_{\perp 3}$ and $\mathbf{p}_{\perp 4}$ gives the intermediate result,

$$\begin{aligned}&\int \mathcal{H}_4(\mathbf{r}_{a1},\mathbf{r}_{a3};\mathbf{r}_b,\mathbf{r}_{b'})\mathrm{d}\mathbf{r}_{\perp b}\mathrm{d}\mathbf{r}_{\perp b'} =\\ &\frac{\ell^5}{24\pi k^2}\int\Big[L'(z_{a1},z,-\mathbf{p}_{\perp 1})L(z,z_b)L'(z_{a3},z,\mathbf{p}_{\perp 1})L(z,z_{b'}) +\\ &\mathbf{p}_{\perp 1}^2 L(z_{a1},z,-\mathbf{p}_{\perp 1})L(z,z_b)L(z_{a3},z,\mathbf{p}_{\perp 1})L(z,z_{b'})\Big]\\ &e^{i\mathbf{r}_{\perp a1}\mathbf{p}_{\perp 1}-i\mathbf{r}_{\perp a3}\mathbf{p}_{\perp 1}}\frac{\mathrm{d}\mathbf{p}_{\perp 1}\mathrm{d}z}{(2\pi)^2},\end{aligned} \tag{A.28}$$

where L' denotes the derivative of L with respect to z. The sources that are connected to $\mathcal{H}_4(\mathbf{r}_{a1}, \mathbf{r}_{a3}; \mathbf{r}_b, \mathbf{r}_{b'})$ to give the interference term of the correlation are,

$$\begin{aligned}
S_{aa'\omega\omega'}(\mathbf{r}_{a1}) &= \int \Psi_a(\mathbf{r}_{a1}, \omega)\Psi^*_{a'}(\mathbf{r}_{a1'}, \omega')\delta(\mathbf{r}_{a1}-\mathbf{r}_{a1'})\mathrm{d}\mathbf{r}_{a1'} = \\
&\frac{\ell}{(2\pi)^4}\int \Psi_{a\omega}(\mathbf{q}_{\perp 1})\Psi^*_{a'\omega'}(\mathbf{q}_{\perp 1} + \Delta\mathbf{q}_{\perp 1})e^{i\mathbf{r}_{\perp a1}\Delta\mathbf{q}_{\perp 1}}\delta(z_i - z_{a1})\mathrm{d}\mathbf{q}_{\perp 1}\mathrm{d}\Delta\mathbf{q}_{\perp 1}; \\
S_{aa'\omega\omega'}(\mathbf{r}_{a3}) &= \int \Psi^*_a(\mathbf{r}_{a3}, \omega)\Psi_{a'}(\mathbf{r}_{a3'}, \omega')\delta(\mathbf{r}_{a3}-\mathbf{r}_{a3'})\mathrm{d}\mathbf{r}_{a3'} = \\
&\frac{\ell}{(2\pi)^4}\int \Psi^*_{a\omega}(\mathbf{q}_{\perp 2})\Psi_{a'\omega'}(\mathbf{q}_{\perp 2} + \Delta\mathbf{q}_{\perp 2})e^{-i\mathbf{r}_{\perp a3}\Delta\mathbf{q}_{\perp 2}}\delta(z_i - z_{a3})\mathrm{d}\mathbf{q}_{\perp 2}\mathrm{d}\Delta\mathbf{q}_{\perp 2},
\end{aligned} \tag{A.29}$$

where the injection source Eq. (2.144) and the plane wave decomposition of the incoming amplitudes Eq. (3.49) was used with the injection depth $z_i = \ell$. Attaching the sources to the Ladders in Eq. (A.28), integrating over $\mathbf{r}_{a1}$ and $\mathbf{r}_{a3}$, using Eq. (3.64) and employing the emission drain Eq. (2.161) by substituting for z_b and $z_{b'}$ the emission depth z_e gives the fluctuations on the total transmission,

$$\begin{aligned}
\langle \delta T^2(\Delta\omega)\rangle_{aa'} &= \int S_{aa'\omega\omega'}(\mathbf{r}_{a1})S_{aa'\omega\omega'}(\mathbf{r}_{a3})\mathcal{H}_4(\mathbf{r}_{a1}, \mathbf{r}_{a3}; \mathbf{r}_b, \mathbf{r}_{b'}) \times \\
&\qquad \frac{\ell^2\delta(z_b - z_e)\delta(z_{b'} - z_e)}{(16\pi)^2}\mathrm{d}\mathbf{r}_{a1}\mathrm{d}\mathbf{r}_{a3}\mathrm{d}\mathbf{r}_b\mathrm{d}\mathbf{r}_{b'} = \\
&\frac{\ell^9}{24\pi k^2(16\pi)^2}\int\Big[L'(z_i, z, \Delta\mathbf{q}_{\perp 1})L(z, z_e)L'(z_i, z, -\Delta\mathbf{q}_{\perp 1})L(z, z_e) + \\
&\qquad \Delta\mathbf{q}_{\perp 1}^2 L(z_i, z, \Delta\mathbf{q}_{\perp 1})L(z, z_e)L(z_i, z, -\Delta\mathbf{q}_{\perp 1})L(z, z_e)\Big] \\
&\qquad\qquad e^{-\rho_0^2(\Delta\mathbf{q}_{1\perp} - \Delta\mathbf{q}_{a\perp})^2/4}\,\frac{\mathrm{d}\Delta\mathbf{q}_{\perp 1}\mathrm{d}z}{(2\pi)^2}.
\end{aligned} \tag{A.30}$$

Before performing the integration over z the explicit form of the Ladders is given. As can be seen from the sources in Eq. (A.29) the amplitudes travelling along the two incoming Ladders develop a phase difference because of their frequency difference with opposite sign, i.e. they are each others complex conjugate. The approximate form of the Ladders in the slab geometry chosen in the calculation is given in Eq. (2.162),

$$\begin{aligned}
L(z_i, z, \mathbf{p}_\perp) &= \frac{4\pi v_E}{\ell^2 D\,\mathsf{Q}}\frac{\sinh\left[(z_i + \tau_0)\,\mathsf{Q}\right]\sinh\left[(L - z - \tau_0)\,\mathsf{Q}\right]}{\sinh\left[L\,\mathsf{Q}\right]}, \\
L(z_i, z, -\mathbf{p}_\perp) &= \frac{4\pi v_E}{\ell^2 D\,\mathsf{Q}^*}\frac{\sinh\left[(z_i + \tau_0)\,\mathsf{Q}^*\right]\sinh\left[(L - z - \tau_0)\,\mathsf{Q}^*\right]}{\sinh\left[L\,\mathsf{Q}^*\right]}, \\
\text{with } \mathsf{Q} &= \left(\mathbf{p}_\perp{}^2 + \frac{1}{D\tau_a} - \frac{i\Delta\omega}{D}\right)^{1/2}, \quad \mathsf{Q}^* = \left(\mathbf{p}_\perp{}^2 + \frac{1}{D\tau_a} + \frac{i\Delta\omega}{D}\right)^{1/2}.
\end{aligned} \tag{A.31}$$

In the Hikami vertex two amplitudes are exchanged between the Ladders, and the frequency difference between the amplitudes in the outgoing Ladders vanishes. The outgoing Ladders are given by,

$$L(z, z_e) = \frac{4\pi v_E}{\ell^2 D\,\mathsf{Q}} \frac{\sinh\left[(z+\tau_0)\,\mathsf{Q}\right]\sinh\left[(L-z_e-\tau_0)\,\mathsf{Q}\right]}{\sinh\left[L\,\mathsf{Q}\right]},$$
$$\text{with } \mathsf{Q} = \left(\frac{1}{D\tau_a}\right)^{1/2}. \tag{A.32}$$

The derivation of the Hikami vertex was for scalar waves. The vector character of the light is taken into account by dividing the final expression for the correlation on the total transmission by a factor of two since the two independent directions of polarization effectively doubles the number of independent modes in transmission. After the integration over z and some elaborate but straightforward manipulations the correlation on the total transmission is found,

$$C_2(\Delta\mathbf{q}_{\perp a}, \Delta\omega) = \frac{\langle \delta T^2(\Delta\omega)\rangle_{aa'}}{\langle T_a\rangle^2} = \frac{3L}{2k^2\rho_0^2\ell}\,F_2(\Delta\omega), \tag{A.33}$$

with

$$F_2(\Delta\omega) \equiv \int \frac{\mathrm{d}\Delta\mathbf{q}_{1\perp}}{4\pi}\, \frac{\rho_0^2\, e^{-\rho_0^2(\Delta\mathbf{q}_{1\perp}-\Delta\mathbf{q}_{a\perp})^2/4}}{L(\cosh[2L\gamma_1]-\cos[2L\gamma_2])} \times$$
$$\left(\frac{\gamma_1\sinh[2L\gamma_1]}{\gamma_1^2-k_a^2} - \frac{\gamma_2\sin[2L\gamma_2]}{\gamma_2^2+k_a^2} - \frac{k_a\sinh[2Lk_a]}{\gamma_1^2-k_a^2} - \frac{k_a\sinh[2Lk_a]}{\gamma_2^2+k_a^2}\right), \tag{A.34}$$

with $\gamma_1 \equiv (a^2+b^2)^{1/4}\cos(\phi/2)$, $\gamma_2 \equiv (a^2+b^2)^{1/4}\sin(\phi/2)$, $a \equiv \Delta\omega/D$, $b \equiv \Delta\mathbf{q}_{1\perp}^2 + k_a^2$, $k_a \equiv \sqrt{1/D\tau_a}$ and $\tan\phi \equiv a/b$. The result is completely equal to the result obtained through the Langevin approach in section 3.4.2. The total transmission $\langle T_a\rangle$ in Eqs. (A.33,A.34) is given by,

$$\langle T_a\rangle = \frac{\ell^2}{16\pi}L(z_i, z_e) = \frac{3}{4\ell L}(z_i+\tau_0)(L-z_e-\tau_0). \tag{A.35}$$

The attentive reader might suggest that there exists another diagram that contributes to the fluctuations on the total transmission. The sources in Eq. (A.29) could be chosen such that the incoming Ladders have no frequency difference, and the outgoing Ladders have a frequency difference after the exchange of an amplitude in the Hikami vertex. However outgoing Ladders with a frequency difference do not contribute to the total transmission. The outgoing propagator that transports the intensity outside the slab in Eq. (2.155) has an extra oscillating term $e^{\pm i\Delta\omega|\mathbf{r}'|/c}$, with $\mathbf{r}'$ outside the medium, that makes the net contribution to the total transmission zero.

A.2 Useful integrals

We introduce a few integrals and definitions that simplify the calculation of the Hikami vertex.

$$I_{k,l} = \int \frac{\mathrm{d}\mathbf{q}}{(2\pi)^3} G^k(\mathbf{q}) G^{*\,l}(\mathbf{q}), \quad \text{with}$$

$$G(\mathbf{q}) = \frac{1}{\mathbf{q}^2 - k_0^2 - nt} = \frac{1}{\mathbf{q}^2 + \mu^2}\ ; \qquad G^*(\mathbf{q}) = \frac{1}{\mathbf{q}^2 + \bar{\mu}^2}, \tag{A.36}$$

and $\mu^2 = -k_0^2 - nt(E)$, $\mu = -ik + 1/(2\ell)$ (see Eq. (2.59)). $\bar{\mu}$ is the complex conjugate of μ. The choice of the sign is arbitrary, the sign of $\bar{\mu}$ is fixed by the choice of the sign of μ. Thus $\bar{\mu} = ik + 1/(2\ell)$. The choice of the sign determines the position of the poles in the complex plane, but does not influence the result of the contour integration. The simplification is that once you know $I_{1,1}$, $I_{k,l}$ is calculated with the help of,

$$I_{k+1,l} = \frac{-1}{2k\mu}\frac{\mathrm{d}}{\mathrm{d}\mu} I_{k,l}\ ; \qquad I_{k,l+1} = \frac{-1}{2l\mu}\frac{\mathrm{d}}{\mathrm{d}\mu} I_{k,l}. \tag{A.37}$$

We need $I_{1,1}$.

$$I_{1,1} = \int \frac{\mathrm{d}\mathbf{q}}{(2\pi)^3} G(\mathbf{q}) G^*(\mathbf{q}) = \int_{\infty}^{\infty} \frac{\mathrm{d}q}{(2\pi)^2} \frac{q^2}{(q^2 + \mu^2)(q^2 + \bar{\mu}^2)}. \tag{A.38}$$

This integral is performed by contour integration. Assume Im $t(E) > 0$. The sum of the residues gives $1/4\pi(\mu + \bar{\mu})$. We need the following equation,

$$\mu + \bar{\mu} = \frac{1}{\ell}. \tag{A.39}$$

At the last equal signs the optical theorem Eq. (2.44) and Eq. (2.61) without absorption were used. Using Eq. (A.39) the expressions for the following integrals are found,

$$\begin{gathered}
I_{1,1} = \frac{1}{4\pi(\mu + \bar{\mu})} = \frac{\ell}{4\pi}; \qquad I_{2,2} = \frac{1}{8\pi\mu\bar{\mu}(\mu + \bar{\mu})^3} \approx \frac{\ell^3}{8\pi k^2} \\
I_{1,2} = \frac{1}{8\pi\bar{\mu}(\mu + \bar{\mu})^2} \approx \frac{-i\ell^2}{8\pi k}; \qquad I_{2,1} = \frac{1}{8\pi\mu(\mu + \bar{\mu})^2} \approx \frac{i\ell^2}{8\pi k} \\
I_{1,3} = \frac{1}{16\pi\bar{\mu}^2(\mu + \bar{\mu})^3} \approx \frac{-\ell^3}{16\pi k^2}; \qquad I_{3,1} = \frac{1}{16\pi\mu^2(\mu + \bar{\mu})^3} \approx \frac{-\ell^3}{16\pi k^2} \\
I_{2,3} = \frac{3}{32\pi\mu^1\bar{\mu}^2(\mu + \bar{\mu})^4} \approx \frac{-3i\ell^4}{32\pi k^3}; \qquad I_{3,2} = \frac{3}{32\pi\mu^2\bar{\mu}^1(\mu + \bar{\mu})^4} \approx \frac{3i\ell^4}{32\pi k^3} \\
I_{1,4} = \frac{1}{32\pi\bar{\mu}^3(\mu + \bar{\mu})^4} \approx \frac{i\ell^4}{32\pi k^3}; \qquad I_{4,1} = \frac{1}{32\pi\mu^3(\mu + \bar{\mu})^4} \approx \frac{-i\ell^4}{32\pi k^3} \\
I_{2,4} = \frac{1}{16\pi\mu\bar{\mu}^3(\mu + \bar{\mu})^5} \approx \frac{-\ell^5}{16\pi k^4}; \qquad I_{4,2} = \frac{1}{16\pi\mu^3\bar{\mu}(\mu + \bar{\mu})^5} \approx \frac{-\ell^5}{16\pi k^4} \\
I_{3,3} = \frac{3}{32\pi\mu^2\bar{\mu}^2(\mu + \bar{\mu})^5} \approx \frac{3\ell^5}{32\pi k^4}.
\end{gathered} \tag{A.40}$$

Appendix B

The second and third cumulant of the total transmission

In this appendix the second and third cumulant of the total transmission will be calculated. The calculations are done for scalar waves. The effect of the vector character of light is implemented heuristicly and indicated by $\mathcal{Q}$, $\mathcal{Q} = 1$ gives the scalar waves result, $\mathcal{Q} = 2$ gives the heuristic vector waves result. All calculations are done in the plane wave limit, which means that the incoming beams have a Gaussian intensity profile, with the diameter of the beam much larger than the sample thickness, $\rho_0 \gg L$.

B.1 The conductance

First we will derive an expression for the conductance. The conductance is defined as the sum over all incoming and outgoing modes (see Eq. (3.23)),

$$g \equiv \sum_{a,b} \langle T_{ab} \rangle. \tag{B.1}$$

The sum over all outgoing modes b gives the total transmission (Eq. (A.35)),

$$\langle T_a \rangle = \frac{\ell^2}{16\pi} L(z_i, z_e) = \frac{v_E}{4DL}(z_i + \tau_0)(L - z_e - \tau_0). \tag{B.2}$$

The conductance is the number of incoming modes N times the average total transmission,

$$g = N \langle T_a \rangle. \tag{B.3}$$

Since all incoming modes are excited (the light falls on the sample from all directions) the injection depth z_i is not equal to ℓ as in Eq. (2.144), but equal to $\frac{2\ell}{3}$, as derived for the ejection depth z_e in Eq. (2.160). The ejection depth z_e is given in Eq. (2.161). The position of the trapping plane is taken to be $\tau_0 = \frac{2\ell}{3}$. The number of incoming modes is given in Eq. (3.18),

$$N = \frac{\mathcal{Q} k_0^2 \rho_0^2}{4}. \tag{B.4}$$

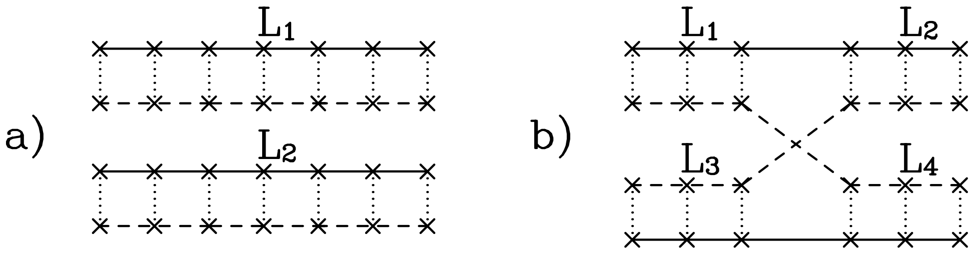

Figure B.1: *The two diagrams contributing to the second moment. Diagram b) is the leading contributions to the second cumulant.*

For the conductance we derive,

$$g = \frac{4N\ell}{3L} = \frac{2k_0^2\rho_0^2\ell}{3L}; \qquad (\rho_0 \gg L) \tag{B.5}$$

B.2 The second cumulant

The calculation of the second cumulant was done in Appendix A and is given by Eq. (A.33) and Eq. (A.34) in the limit $\Delta \mathbf{q}_\perp \to 0$, $\Delta\omega \to 0$ and $\rho_0 \gg L$ or directly by Eq. (3.70). In Eq. (A.33) and Eq. (3.70) the vector character of light was taken into account,

$$\langle\langle T_a^2 \rangle\rangle = \frac{2L}{2k^2\rho_0^2\ell} = \frac{2}{3}g^{-1}. \tag{B.6}$$

B.3 The third cumulant

The third cumulant is given by the sum of diagram *c*) and *d*) in Fig. (B.2), respectively $\mathcal{H}_{6c}$ and $\mathcal{H}_{6d}$. Only diagram *c*) is explicitly calculated.

$$\begin{aligned} &\mathcal{H}_{6c}(\mathbf{r}_{a1}, \mathbf{r}_{a3}, \mathbf{r}_{a5}; \mathbf{r}_{b2}, \mathbf{r}_{b4}, \mathbf{r}_{b6}) = \\ &\int_{-\infty}^{\infty} L_1(\mathbf{r}_{a1}, \mathbf{p}_1) L_3(\mathbf{r}_{a3}, \mathbf{p}_3) H(\mathbf{p}_1, \mathbf{p}_3; \mathbf{p}_2, \mathbf{p}_7) L_2(\mathbf{p}_2, \mathbf{r}_{b2}) L_{int}(\mathbf{p}_7, \mathbf{p}_8) L_5(\mathbf{r}_{a5}, \mathbf{p}_5) \\ &\quad H(\mathbf{p}_5, \mathbf{p}_8; \mathbf{p}_4, \mathbf{p}_6) L_4(\mathbf{p}_4, \mathbf{r}_{b4}) L_6(\mathbf{p}_6, \mathbf{r}_{b6}) \frac{\mathrm{d}\mathbf{p}_1 \cdots \mathbf{p}_8}{(2\pi)^{3\times 8}}, \end{aligned} \tag{B.7}$$

The incoming and outgoing intensity propagators have to be connected to $\mathcal{H}_{6c}$ in a slab geometry. The ladders are given in Eq. (A.3). L_{int} denotes the intensity that propagates from the first to the second Hikami-vertex. The calculation is similar to what is done in Appendix A after Eq. (A.24) and the details will be skipped. The asymmetric form of the Hikami vertex (Eq. (A.22)),

$$H(\mathbf{p}_1, \mathbf{p}_3; \mathbf{p}_2, \mathbf{p}_4) = (2\pi)^3 \delta(\mathbf{p}_1 + \mathbf{p}_2 + \mathbf{p}_3 + \mathbf{p}_4) \frac{-\ell^5}{48\pi k_0^2} (2\mathbf{p}_2\mathbf{p}_4 - \mathbf{p}_1^2 - \mathbf{p}_3^2). \tag{B.8}$$

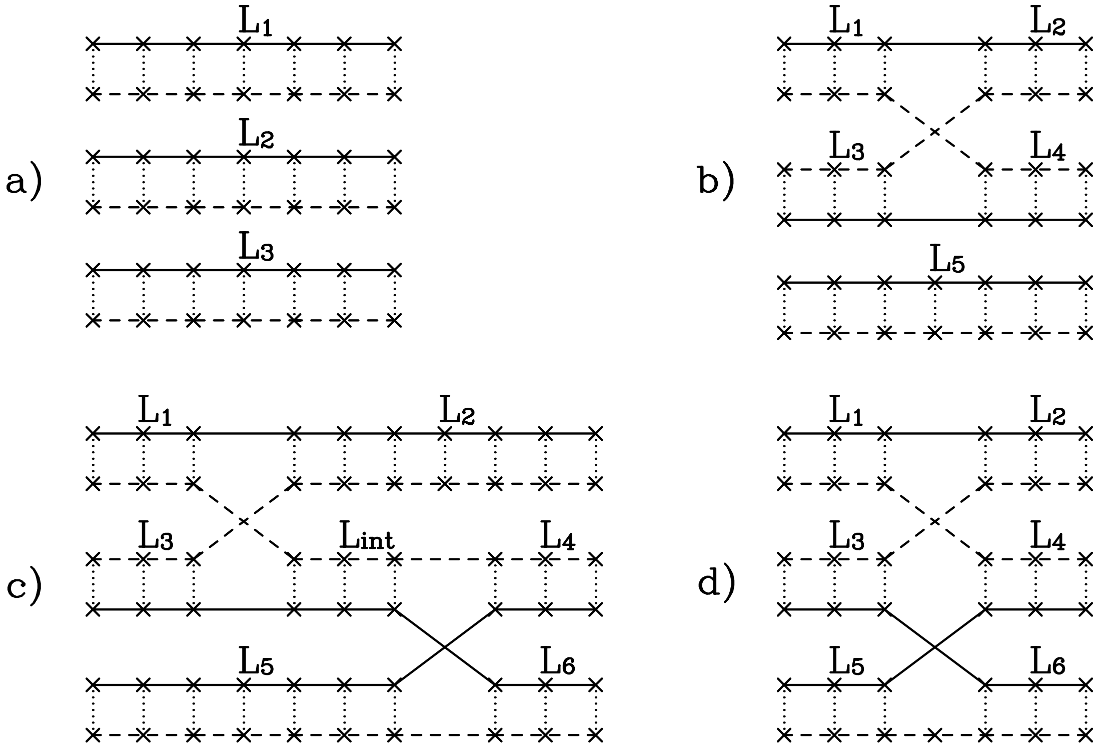

Figure B.2: *The four diagrams contributing to the third moment. Diagrams c) and d) are the leading contributions to the third cumulant. Diagram d) cancels completely against the contribution of diagram c) when the two Hikami-vertices approach one other within one mean free path. In the text diagram c) is denoted by $\mathcal{H}_{6c}$ and diagram d) by $\mathcal{H}_{6d}$.*

and Eq. (A.2) are used,

$$L_{int}(\mathbf{p}_7, \mathbf{p}_8) = L_{int}(\mathbf{p}_7)(2\pi)^3\delta(\mathbf{p}_7 + \mathbf{p}_8). \tag{B.9}$$

The δ-functions give conditions on the momenta $\mathbf{p}$. As shown in Appendix A the integration over all outgoing modes makes the transverse momenta of the outgoing Ladders L_2, L_4 and L_6 zero. Together with the conditions on the momenta by the δ-functions this leads to a condition on the incoming transverse momenta,

$$\begin{aligned} \mathbf{p}_{\perp 2} = \mathbf{p}_{\perp 4} = \mathbf{p}_{\perp 6} = 0 & \\ \delta(\mathbf{p}_5 + \mathbf{p}_8 + \mathbf{p}_4 + \mathbf{p}_6) &\Rightarrow \mathbf{p}_{\perp 5} = -\mathbf{p}_{\perp 8} \\ \delta(\mathbf{p}_7 + \mathbf{p}_8) &\Rightarrow \mathbf{p}_{\perp 7} = -\mathbf{p}_{\perp 8} \\ \delta(\mathbf{p}_1 + \mathbf{p}_3 + \mathbf{p}_2 + \mathbf{p}_7) &\Rightarrow \mathbf{p}_{\perp 1} + \mathbf{p}_{\perp 3} + \mathbf{p}_{\perp 5} = 0 \end{aligned} \tag{B.10}$$

Connecting the sources (Eq. (A.29)) to $\mathcal{H}_{6c}(\mathbf{r}_{a1}, \mathbf{r}_{a3}, \mathbf{r}_{a5}; \mathbf{r}_{b2}, \mathbf{r}_{b4}, \mathbf{r}_{b6})$ leads to a product of ladder vertices that depend on the incoming transverse momenta times a weight function of the incoming transverse momenta that comes from the sources. This is seen in Eq. (A.30), the part of the integrand in square brackets is the product of ladder vertices that depend on the incoming transverse momenta, the exponential function is the weight function of the incoming transverse momenta that come from the sources. Here we simplify the calculation by separating the weight function from the product of Ladder vertices. This is justified in the plane wave limit $\rho_0 \gg L$. Then the weight function decays much faster than the Ladder vertices as a function of the transverse momenta and the Ladder vertices are evaluated at zero transverse momentum. The fluctuating part of the third moment from the diagram in Fig. (B.2c) is,

$$\langle \delta T_a^3 \rangle_c = \left(\frac{\ell}{16\pi} \right)^3 \int S_a(\mathbf{r}_{a1}) S_a(\mathbf{r}_{a3}) S_a(\mathbf{r}_{a5}) \mathcal{H}_c(\mathbf{r}_{a1}, \mathbf{r}_{a3}, \mathbf{r}_{a5}; \mathbf{r}_{b2}, \mathbf{r}_{b4}, \mathbf{r}_{b6})$$
$$\delta(z_{b2} - z_e)\delta(z_{b4} - z_e)\delta(z_{b6} - z_e) \mathrm{d}\mathbf{r}_{a1} \mathrm{d}\mathbf{r}_{a3} \mathrm{d}\mathbf{r}_{a5} \mathrm{d}\mathbf{r}_{b2} \mathrm{d}\mathbf{r}_{b4} \mathrm{d}\mathbf{r}_{b6}. \tag{B.11}$$

where the sources S_a are given in Eq. (A.29), and the factors $\frac{\ell\delta(z_b - z_e)}{16\pi}$ come from the ejection drain (Eq. (2.161)). Writing symbolically the separation of the weight function and the Ladders with zero transverse momentum we get (all the $\mathbf{r}_\perp$ dependence has been swept into the sources),

$$\langle \delta T_a^3 \rangle_c = \mathcal{H}_{6c}(z_i, z_i, z_i; z_e, z_e, z_e) \times$$
$$\left(\frac{\ell}{16\pi} \right)^3 \int \mathcal{S}(\mathbf{r}_{a1}) \mathcal{S}(\mathbf{r}_{a3}) \mathcal{S}(\mathbf{r}_{a5}) \mathrm{d}\mathbf{r}_{a1} \mathrm{d}\mathbf{r}_{a3} \mathrm{d}\mathbf{r}_{a5} \mathrm{d}\mathbf{r}_{b2} \mathrm{d}\mathbf{r}_{b4} \mathrm{d}\mathbf{r}_{b6} \tag{B.12}$$

The integration over the weight function gives,

$$\left(\frac{\ell}{16\pi} \right)^3 \int \mathcal{S}(\mathbf{r}_{a1}) \mathcal{S}(\mathbf{r}_{a3}) \mathcal{S}(\mathbf{r}_{a5}) \mathrm{d}\mathbf{r}_{a1} \mathrm{d}\mathbf{r}_{a3} \mathrm{d}\mathbf{r}_{a5} \mathrm{d}\mathbf{r}_{b2} \mathrm{d}\mathbf{r}_{b4} \mathrm{d}\mathbf{r}_{b6} =$$
$$\left(\frac{\ell^2}{16\pi} \right)^3 \int \Psi(\mathbf{q}_{\perp 1}) \Psi^*(\mathbf{q}_{\perp 1} + \mathbf{p}_{\perp 1}) \Psi(\mathbf{q}_{\perp 3}) \Psi^*(\mathbf{q}_{\perp 3} + \mathbf{p}_{\perp 3}) \Psi(\mathbf{q}_{\perp 5}) \Psi^*(\mathbf{q}_{\perp 5} + \mathbf{p}_{\perp 5})$$
$$(2\pi)^2 \delta(\mathbf{p}_{\perp 1} + \mathbf{p}_{\perp 3} + \mathbf{p}_{\perp 5}) \frac{\mathrm{d}\mathbf{q}_{\perp 1} \mathrm{d}\mathbf{q}_{\perp 3} \mathrm{d}\mathbf{q}_{\perp 5} \mathrm{d}\mathbf{p}_{\perp 1} \mathrm{d}\mathbf{p}_{\perp 3} \mathrm{d}\mathbf{p}_{\perp 5}}{(2\pi)^{2\times 6}} =$$
$$\left(\frac{\ell^2}{16\pi} \right)^3 \frac{4}{3\rho_0^4 \pi^2} \tag{B.13}$$

$\mathcal{H}_{6c}(z_i, z_i, z_i; z_e, z_e, z_e)$ is given by,

$$\mathcal{H}_{6c}(z_i, z_i, z_i; z_e, z_e, z_e) =$$
$$\int L_1(z_i, z_1) L_3(z_i, z_3) H(z_1, z_3; z_2, z_7) L_2(z_2, z_e) L_{int}(z_7, z_8)$$
$$L_5(z_i, z_5) H(z_5, z_8; z_4, z_6) L_4(z_4, z_e) L_6(z_6, z_e) \mathrm{d}z_1 \cdots \mathrm{d}z_8 \tag{B.14}$$

where the following choice for the asymmetric Hikami vertex with zero transverse momenta in the real space representation was made,

$$H(\mathbf{p}_1, \mathbf{p}_3; \mathbf{p}_2, \mathbf{p}_4) \to H(z_1, z_3; z_2, z_4) =$$

$$\delta(z_1-z_2)\delta(z_1-z_3)\delta(z_1-z_4)\frac{\ell^5}{48\pi k^2}\left[2\frac{\partial^2}{\partial z_2 \partial z_4}-\frac{\partial^2}{\partial z_1^2}-\frac{\partial^2}{\partial z_3^2}\right] \tag{B.15}$$

The derivatives do only work on the ladder vertices and not on the δ-functions We make the same approximation as in Appendix A. The double derivatives on incoming and outgoing Ladder vertices give a δ-function on the slab boundary and these terms are neglected (this the same as the neglect of the $\mathbf{q}^2$ terms as argued after Eq. (A.22)). The only double derivative retained is the one working on the internal Ladder L_{int} that connects the two Hikami vertices. $\mathcal{H}_{6c}(z_i, z_i, z_i; z_e, z_e, z_e)$ consists of two parts,

$$\begin{aligned}\mathcal{H}_{6c} = \left(\frac{\ell^5}{48\pi k^2}\right)^2 \int \Bigg\{ & 4L_1(z_i,z_1)L_3(z_i,z_1)L_2'(z_1,z_e)L_{int}'(z_1,z_2) \times \\ & L_5(z_i,z_2)L_4'(z_2,z_e)L_6'(z_2,z_e) + \\ & 2L_1(z_i,z_1)L_3(z_i,z_1)\left[\frac{12\pi}{\ell^3}\frac{\partial}{\partial z_1}\delta(z_1-z_2)\right]L_2'(z_1,z_e) \times \\ & L_5(z_i,z_2)L_4(z_2,z_e)L_6(z_2,z_e)\Bigg\} \mathrm{d}z_1 \mathrm{d}z_2.\end{aligned} \tag{B.16}$$

The L' denote the derivative of L. The δ-function in the second term of the integrand comes from the double derivative of the internal Ladder,

$$\frac{\partial^2}{\partial z_8^2}L_{int}(z_7,z_8) = -\frac{12\pi}{\ell^3}\delta(z_7-z_8) \tag{B.17}$$

Performing the integration of terms gives,

$$\mathcal{H}_{6c} = \left(\frac{\ell^5}{48\pi k^2}\right)^2\left(\frac{12\pi}{\ell^3}\right)^7\left(\frac{4\ell}{3}\right)^6\left(\frac{8}{45L}+\frac{2}{15L}\right). \tag{B.18}$$

Three permutations of the diagram in Fig. (B.2c) exists, plus their complex conjugate, giving six possible diagrams. Multiplying $\mathcal{H}_{6c}$ by six gives the contribution to the normalized third cumulant,

$$\langle\langle T_a^3\rangle\rangle_c = \frac{12L^2}{\ell^2k^4\rho_0^4}\left(\frac{16}{15}+\frac{4}{5}\right). \tag{B.19}$$

As was shown in van Rossum, de Boer and Nieuwenhuizen [79] the contribution of the six point vertex $\mathcal{H}_{6d}$ (diagram d in Fig. (B.2)) cancels exactly against the second term of the integrand in Eq. (B.16).

$$\langle\langle T_a^3\rangle\rangle_d = -\frac{12L^2}{\ell^2k^4\rho_0^4}\frac{4}{5} \tag{B.20}$$

In words, the contribution of the six point vertex $\mathcal{H}_{6d}$ cancels against the diagram with the two Hikami vertices when the two Hikami vertices overlap (or approach one another within a mean free path). The vector character of the light is taken into account by dividing the third cumulant calculated for scalar waves by a factor of 2 for each Hikami vertex (note that the second cumulant was reduced by a factor of 2 for a single Hikami vertex). Thus the third cumulant is given by,

$$\langle\langle T_a^3 \rangle\rangle = \langle\langle T_a^3 \rangle\rangle_c + \langle\langle T_a^3 \rangle\rangle_d = \frac{12L^2}{2^2 \ell^2 k^4 \rho_0^4} \frac{16}{15} = \frac{64}{45} g^{-2} \tag{B.21}$$

Finally this gives us the relation between the second and third cumulant that was experimentally observed in chapter 5,

$$\langle\langle T_a^3 \rangle\rangle = \frac{16}{5} \langle\langle T_a^2 \rangle\rangle^2 \tag{B.22}$$

B.4 Disconnected contribution to the cumulants

So far the leading contributions to the second and third cumulant have been calculated. There are also non-leading contributions to the second and third cumulant. The diagrams of Fig. (B.1) and Fig. (B.2) give all contributions to respectively the second and third moment. The leading contributions to the second and third cumulant are given by the connected diagrams in Fig. (B.1b) and Figs. (B.2c and B.2d) respectively. However, the diagram in Fig. (B.1a) gives an additional contribution to the second cumulant, just as the diagrams of Figs. (B.2a and B.2b) give an additional contribution to the third cumulant. We will first explain the contribution of Fig. (B.1a) to the second cumulant and the contribution of Figs. (B.2a and B.2b) to the third cumulant in the waveguide model of section 3.2. The second cumulant is given by

$$\langle\langle T_a^2 \rangle\rangle = \frac{\langle T_a^2 \rangle - \langle T_a \rangle^2}{\langle T_a \rangle^2}. \tag{B.23}$$

The second moment $\langle T_a^2 \rangle$ is split into a connected part ($\langle T_a^2 \rangle_{con}$, Fig. (B.1b)) and a disconnected part ($\langle T_a^2 \rangle_{dis}$, Fig. (B.1a)). As was shown in Eq. (3.29) of section 3.2 the disconnected part $\langle T_a^2 \rangle_{dis}$ is not equal to the averaged transmission squared $\langle T_a \rangle^2$ (disconnected means in the context of section 3.2 independent outgoing modes). Using Eq. (B.6) (the contribution of the connected part to the second cumulant) and Eq. (3.29) we find,

$$\langle\langle T_a^2 \rangle\rangle = \langle\langle T_a^2 \rangle\rangle_{con} + \langle\langle T_a^2 \rangle\rangle_{dis} \propto \frac{L}{N\ell} + \frac{1}{N} \tag{B.24}$$

where the last term comes from the disconnected part of Fig (B.2a). Extending the argument in section 3.2 to three transmission coefficients, and taking into account that two transmission coefficients can be correlated and their contribution to the fluctuations is enhanced by L/ℓ, we can estimate the contribution to the third cumulant of the diagrams of Figs. (B.2d + B.2c, B.2b and B.2a), yielding respectively

$$\langle\langle T_a^3 \rangle\rangle \propto \frac{L^2}{N^2\ell^2} + \frac{L}{N^2\ell} + \frac{1}{N^2}, \tag{B.25}$$

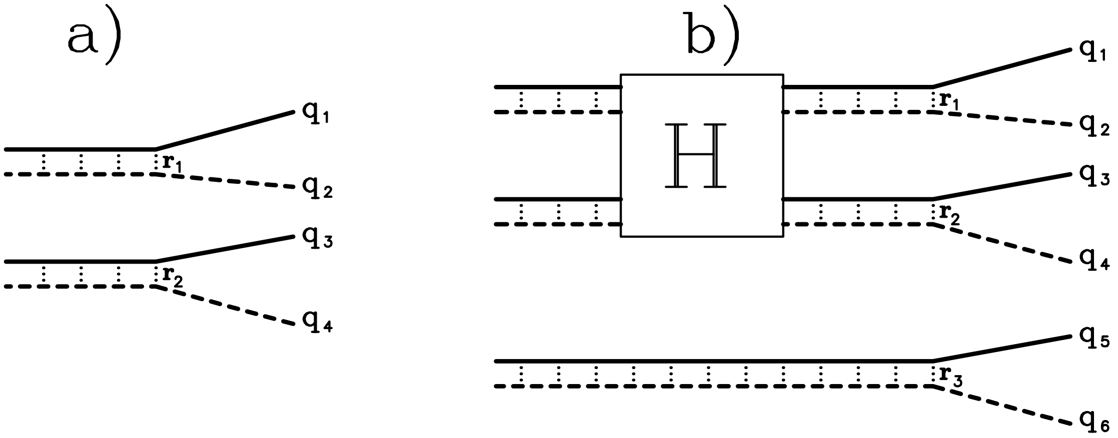

Figure B.3: *a) The disconnected contribution to the second moment, the amplitudes making up the intensity at* $\mathbf{r}_{\perp 1}$ *and* $\mathbf{r}_{\perp 2}$ *propagate out in different directions.*
b) The mundane (disconnected) contribution to the third cumulant, the box symbolises the Hikami vertex. The amplitudes making up the intensities at $\mathbf{r}_{\perp 1}$, $\mathbf{r}_{\perp 2}$ *and* $\mathbf{r}_{\perp 3}$ *propagate out in different directions.*

Especially the second term from Fig. (B.2b) needs to be evaluated under the experimental conditions to prove that the experimentally measured third cumulant is dominated by the contribution of Figs. (B.2c and B.2d), and not the mundane contribution of Fig. (B.2b).

B.4.1 The disconnected contribution to the second cumulant

To calculate the disconnected contribution to the second cumulant, only the intensity distribution at the exit interface at transversal coordinates $\mathbf{r}_{\perp 1}$ and $\mathbf{r}_{\perp 2}$ is needed. The amplitudes, making up the intensity at $\mathbf{r}_{\perp 1}$ and $\mathbf{r}_{\perp 2}$, can propagate in different directions, respectively $\mathbf{p}_{\perp 1}$, $\mathbf{p}_{\perp 2}$, $\mathbf{p}_{\perp 3}$ and $\mathbf{p}_{\perp 4}$ (see Fig. (B.3a)).

$$\begin{aligned} & I(z_e, \mathbf{r}_{\perp 1}; \mathbf{p}_{\perp 1}, \mathbf{p}_{\perp 2}) I(z_e, \mathbf{r}_{\perp 2}; \mathbf{p}_{\perp 3}, \mathbf{p}_{\perp 4}) \equiv \\ & \Psi(\mathbf{r}_{\perp 1}) e^{i\mathbf{p}_{\perp 1}\mathbf{r}_{\perp 1}} \Psi^*(\mathbf{r}_{\perp 1}) e^{-i\mathbf{p}_{\perp 2}\mathbf{r}_{\perp 1}} \Psi(\mathbf{r}_{\perp 2}) e^{i\mathbf{p}_{\perp 3}\mathbf{r}_{\perp 2}} \Psi^*(\mathbf{r}_{\perp 2}) e^{-i\mathbf{p}_{\perp 4}\mathbf{r}_{\perp 2}}. \end{aligned} \tag{B.26}$$

To obtain intensities the amplitudes need to be paired giving the following possibilities

$$a) \quad \mathbf{p}_{\perp 1} = \mathbf{p}_{\perp 2}, \mathbf{p}_{\perp 3} = \mathbf{p}_{\perp 4}; \qquad b) \quad \mathbf{p}_{\perp 1} = \mathbf{p}_{\perp 4}, \mathbf{p}_{\perp 2} = \mathbf{p}_{\perp 3}. \tag{B.27}$$

To get the contribution to the second moment of the total transmission, first one integrates over the transversal coordinates $\mathbf{r}_{\perp 1}$ and $\mathbf{r}_{\perp 2}$ to get the contribution of the whole exit interface to the intensity in a certain direction, then one integrates over all directions to get the total transmission. The first possible pairing of the amplitudes *a*) gives

$$\langle I(z_e;\mathbf{p}_{\perp 1})I(z_e;\mathbf{p}_{\perp 3})\rangle = \int \mathrm{d}\mathbf{r}_{\perp 1}\mathrm{d}\mathbf{r}_{\perp 2}\langle\Psi(\mathbf{r}_{\perp 1})\Psi^*(\mathbf{r}_{\perp 1})\rangle\langle\Psi(\mathbf{r}_{\perp 2})\Psi^*(\mathbf{r}_{\perp 2})\rangle = \langle I(z_e;\mathbf{q}_\perp=0)\rangle^2, \quad \text{(B.28)}$$

where $I(z_e;\mathbf{p}_{\perp 1},\mathbf{p}_{\perp 2})$ is equivalent to $J_A(\mathbf{p}_{\perp 1},\mathbf{p}_{\perp 2})$ in Eq. (3.7). Here $I(z_e;\mathbf{p}_{\perp 1},\mathbf{p}_{\perp 2})$ is defined on the exit interface of the sample. Subsequent integration over all outgoing directions results in

$$a) \quad \langle T_a^2\rangle = \pi^2 k_0^4\langle I(z_e;\mathbf{q}_\perp=0)\rangle = \langle T_a\rangle^2. \quad \text{(B.29)}$$

The second possible pairing of the amplitudes *b*) gives

$$\langle I(z_e;\mathbf{p}_{\perp 1})I(z_e;\mathbf{p}_{\perp 2})\rangle = \int \mathrm{d}\mathbf{r}_{\perp 1}\mathrm{d}\mathbf{r}_{\perp 2}\langle\Psi(\mathbf{r}_{\perp 1})\Psi^*(\mathbf{r}_{\perp 1})\rangle\langle\Psi(\mathbf{r}_{\perp 2})\Psi^*(\mathbf{r}_{\perp 2})\rangle e^{i\mathbf{r}_{\perp 1}(\mathbf{p}_{\perp 1}-\mathbf{p}_{\perp 2})}e^{-i\mathbf{r}_{\perp 2}(\mathbf{p}_{\perp 1}-\mathbf{p}_{\perp 2})} = \langle I(z_e;\mathbf{q}_\perp)\rangle\langle I(z_e;-\mathbf{q}_\perp)\rangle \text{ with } \mathbf{q}_\perp = \mathbf{p}_{\perp 1}-\mathbf{p}_{\perp 2} \quad \text{(B.30)}$$

Subsequent integration over the outgoing directions $\mathbf{p}_{\perp 1}$ and $\mathbf{p}_{\perp 3}$ yields,

$$b) \quad \langle T_a^2\rangle = \pi k_0^2\int_0^{k_0}\mathrm{d}\mathbf{q}_\perp 2\pi\mathbf{q}_\perp\langle I(z_e;\mathbf{q}_\perp)\rangle^2. \quad \text{(B.31)}$$

The integration boundary can be extended to infinity since $I(z_e;\mathbf{q}_\perp)$ is an exponentially decaying function. The contribution of the disconnected diagram (Fig. (B.1b)) to the second cumulant comes only from part *b*),

$$\langle\langle T_a^2\rangle\rangle_{dis} = \frac{\pi k_0^2\int_0^\infty 2\pi\mathbf{q}_\perp\langle I(z_e;\mathbf{q}_\perp)\rangle^2\mathrm{d}\mathbf{q}_\perp}{2\pi^2 k_0^4\langle I(z_e;\mathbf{q}_\perp=0)\rangle} \equiv \frac{1}{N} \quad \text{(B.32)}$$

The factor *2* in the denominator has been added to make the result apply to vector waves as well. This is the proof of Eq. (5.13). For a Gaussian incoming beam Eq. (B.32) is exactly equal to the result in Eq. (3.16) with Eq. (3.20). This number of modes is the number of independent speckle spots in transmission, derived from the intensity distribution at the exit interface. For the experimental beam diameters and sample thicknesses the number of modes are tabulated in Table (5.1).

B.4.2 The disconnected contribution to the third cumulant

We will apply the same method to estimate the contribution of the diagram in Fig. (B.2b) to the third cumulant. As can be seen in Fig. (B.3b) there are three possibilities to combine three intensities into two connected intensities (through a

Hikami vertex) and an independent intensity. Connecting outgoing directions to the amplitudes at the exit interface gives (see Fig. (B.3b),

$$\begin{gathered} I(z_e, \mathbf{r}_{\perp 1}; \mathbf{p}_{\perp 1}, \mathbf{p}_{\perp 2}) I(z_e, \mathbf{r}_{\perp 2}; \mathbf{p}_{\perp 3}, \mathbf{p}_{\perp 4}) I(z_e, \mathbf{r}_{\perp 3}; \mathbf{p}_{\perp 5}, \mathbf{p}_{\perp 6}) \equiv \\ \Psi(\mathbf{r}_{\perp 1}) e^{i\mathbf{p}_{\perp 1}\mathbf{r}_{\perp 1}} \Psi^*(\mathbf{r}_{\perp 1}) e^{-i\mathbf{p}_{\perp 2}\mathbf{r}_{\perp 1}} \Psi(\mathbf{r}_{\perp 2}) e^{i\mathbf{p}_{\perp 3}\mathbf{r}_{\perp 2}} \Psi^*(\mathbf{r}_{\perp 2}) e^{-i\mathbf{p}_{\perp 4}\mathbf{r}_{\perp 2}} \times \\ \Psi(\mathbf{r}_{\perp 3}) e^{i\mathbf{p}_{\perp 5}\mathbf{r}_{\perp 3}} \Psi(\mathbf{r}_{\perp 3}) e^{-i\mathbf{p}_{\perp 6}\mathbf{r}_{\perp 3}} \end{gathered} \tag{B.33}$$

There are six possibilities to combine the outgoing directions into intensities,

$$\begin{array}{llll} 1) & \mathbf{p}_{\perp 1} = \mathbf{p}_{\perp 2}, \mathbf{p}_{\perp 3} = \mathbf{p}_{\perp 4}, \mathbf{p}_{\perp 5} = \mathbf{p}_{\perp 6} & 2) & \mathbf{p}_{\perp 1} = \mathbf{p}_{\perp 4}, \mathbf{p}_{\perp 3} = \mathbf{p}_{\perp 2}, \mathbf{p}_{\perp 5} = \mathbf{p}_{\perp 6} \\ 3) & \mathbf{p}_{\perp 1} = \mathbf{p}_{\perp 2}, \mathbf{p}_{\perp 3} = \mathbf{p}_{\perp 6}, \mathbf{p}_{\perp 5} = \mathbf{p}_{\perp 4} & 4) & \mathbf{p}_{\perp 1} = \mathbf{p}_{\perp 6}, \mathbf{p}_{\perp 3} = \mathbf{p}_{\perp 4}, \mathbf{p}_{\perp 5} = \mathbf{p}_{\perp 2} \\ 5) & \mathbf{p}_{\perp 1} = \mathbf{p}_{\perp 4}, \mathbf{p}_{\perp 3} = \mathbf{p}_{\perp 6}, \mathbf{p}_{\perp 5} = \mathbf{p}_{\perp 2} & 6) & \mathbf{p}_{\perp 1} = \mathbf{p}_{\perp 6}, \mathbf{p}_{\perp 3} = \mathbf{p}_{\perp 2}, \mathbf{p}_{\perp 5} = \mathbf{p}_{\perp 4} \end{array}$$

Integrating over the transversal coordinates $\mathbf{r}_{\perp 1}, \mathbf{r}_{\perp 2}$ and $\mathbf{r}_{\perp 3}$ gives the following six contributions of the diagram in Fig. (B.2b) to the third moment,

$$\begin{array}{lcl} 1) & I_c(z_e; 0) I_c(z_e; 0) I(z_e; 0) & \\ 2) & I_c(z_e; \mathbf{q}_\perp) I_c(z_e; -\mathbf{q}_\perp) I(z_e; 0) & \text{with } \mathbf{q}_\perp = \mathbf{p}_{\perp 1} - \mathbf{p}_{\perp 3} \\ 3) & I_c(z_e; 0) I_c(z_e; \mathbf{q}_\perp) I(z_e; -\mathbf{q}_\perp) & \text{with } \mathbf{q}_\perp = \mathbf{p}_{\perp 3} - \mathbf{p}_{\perp 5} \\ 4) & I_c(z_e; \mathbf{q}_\perp) I_c(z_e; 0) I(z_e; -\mathbf{q}_\perp) & \text{with } \mathbf{q}_\perp = \mathbf{p}_{\perp 1} - \mathbf{p}_{\perp 5} \\ 5) & I_c(z_e; \mathbf{q}_{\perp 1}) I_c(z_e; \mathbf{q}_{\perp 2}) I(z_e; \mathbf{q}_{\perp 3}) & \text{with } \mathbf{q}_{\perp 1} = \mathbf{p}_{\perp 1} - \mathbf{p}_{\perp 5}, \mathbf{q}_{\perp 2} = \mathbf{p}_{\perp 3} - \mathbf{p}_{\perp 1}, \\ & & \mathbf{q}_{\perp 3} = \mathbf{p}_{\perp 5} - \mathbf{p}_{\perp 3} \\ 6) & I_c(z_e; \mathbf{q}_{\perp 1}) I_c(z_e; \mathbf{q}_{\perp 2}) I(z_e; \mathbf{q}_{\perp 3}) & \text{with } \mathbf{q}_{\perp 1} = \mathbf{p}_{\perp 1} - \mathbf{p}_{\perp 3}, \mathbf{q}_{\perp 2} = \mathbf{p}_{\perp 3} - \mathbf{p}_{\perp 5}, \\ & & \mathbf{q}_{\perp 3} = \mathbf{p}_{\perp 5} - \mathbf{p}_{\perp 1}, \end{array} \tag{B.34}$$

where $I_c(z_e, \mathbf{q}_\perp)$ denotes the connected intensity. The contribution of three disconnected intensities in Fig. (B.2a) to the third moment can be written down immediately by making the substitution $I_c(z_e, \mathbf{q}_\perp) \to I(z_e, \mathbf{q}_\perp)$ in Eq. (B.34),

$$\begin{array}{lc} 1) & I(z_e; 0) I(z_e; 0) I(z_e; 0) \\ 2) & 3 \times I(z_e; 0) I(z_e; \mathbf{q}_\perp) I(z_e; -\mathbf{q}_\perp) \\ 3) & 2 \times I(z_e; \mathbf{q}_{\perp 1}) I(z_e; \mathbf{q}_{\perp 2}) I(z_e; \mathbf{q}_{\perp 3}) \end{array}$$

The third cumulant is defined as,

$$\langle\langle T_a^3 \rangle\rangle = \frac{\langle T_a^3 \rangle - 3\langle T_a \rangle \langle T_a^2 \rangle + 2\langle T_a \rangle^3}{\langle T_a \rangle^3}. \tag{B.35}$$

If we add up all contributions to the third cumulant the result is,

$$\begin{aligned} \langle\langle T_a^3 \rangle\rangle = \langle\langle T_a^3 \rangle\rangle_{con} + \frac{1}{\langle T_a \rangle^3} \int \mathrm{d}\mathbf{q}_{\perp 1} \mathrm{d}\mathbf{q}_{\perp 2} \mathrm{d}\mathbf{q}_{\perp 3} \Big[& 6 I_c(z_e; 0) I_c(z_e; \mathbf{q}_{\perp 1}) I(z_e; -\mathbf{q}_{\perp 1}) \\ & + 6 I_c(z_e; \mathbf{q}_{\perp 1}) I_c(z_e; \mathbf{q}_{\perp 2}) I(z_e; \mathbf{q}_{\perp 3}) + 2 I(z_e; \mathbf{q}_{\perp 1}) I(z_e; \mathbf{q}_{\perp 2}) I(z_e; \mathbf{q}_{\perp 3}) \Big], \end{aligned} \tag{B.36}$$

where $\langle\langle T_a^3\rangle\rangle_{con}$ is the contribution of the diagrams in Fig. (B.2c) and Fig. (B.2d), and the integral contains the contribution of the disconnected diagrams in Fig. (B.2b) and Fig. (B.2a) Now we can estimate the contribution of the disconnected diagrams. The last term in the integrand originates from the diagram in Fig. (B.2a), gives a contribution proportional to $2/N^2$ (cf. Eq. (B.25)) and can be neglected. The second term can also be neglected, since the integrand is dominated by the first term. An absolute upper bound on the contributions of the disconnected diagrams is found by approximating the first term: $I_c(z_e;0)I_c(z_e;\mathbf{q}_{\perp 1})I(z_e;-\mathbf{q}_{\perp 1}) \rightarrow I_c(z_e;0)I_c(z_e;0)I(z_e;\mathbf{q}_{\perp 1})$. This is a crude approximation an should give a save upper bound.

$$\langle\langle T_a^3\rangle\rangle_{dis} \leq \frac{\int \mathrm{d}\mathbf{q}_{\perp 1}\mathrm{d}\mathbf{q}_{\perp 2}\mathrm{d}\mathbf{q}_{\perp 3} 6 I_c(z_e;0)I_c(z_e;0)I(z_e;\mathbf{q}_{\perp 1})}{(\pi k_0^2)^3 I^3(z_e;0)} = \frac{6\langle\langle T_a^2\rangle\rangle_{con}(\pi k_0^2)^2 \int I(z_e;\mathbf{q}_\perp)\mathrm{d}\mathbf{q}_\perp}{(\pi k_0^2)^3 I(z_e;0)} \tag{B.37}$$

We define a new number of modes, N^*, with

$$\langle\langle T_a^3\rangle\rangle_{dis} \leq \frac{6\langle\langle T_a^2\rangle\rangle_{con}}{N^*}; \quad N^* \equiv \frac{2\pi k_0^2 I(z_e;0)}{\displaystyle\int_0^\infty 2\pi \mathbf{q}_\perp I(z_e;\mathbf{q}_\perp)\mathrm{d}\mathbf{q}_\perp} \tag{B.38}$$

The factor *2* in the numerator of the second term in Eq. (B.38) has been added to make the result apply to vector waves as well. This is the proof of the estimate above Eq. (5.18) on the contribution of the mundane (disconnected) diagram in Fig. (5.3b) or Fig. (B.2b) to the third cumulant in the experiment. For the experimental beam diameters and sample thicknesses the number of modes N^* are tabulated in Table (5.1).

Units

Symbol	Unit	Unit in this thesis
$V(\mathbf{r})$	$1/m^2$	$1/m^2$
$g(\mathbf{r})$	$1/m$	$1/m$
$g(\mathbf{p})$	m^2	m^2
$g(\mathbf{r}_1, \mathbf{r}_2)$	$1/m$	$1/m$
$g(\mathbf{p}_1, \mathbf{p}_2)$	m^6	m^6
$t_\alpha(\mathbf{r}_1, \mathbf{r}_2, E)$	m^{-5}	m^{-5}
$t_\alpha(\mathbf{p}_1, \mathbf{p}_2, E)$	m	m
$V\delta(\mathbf{r})$	$1/m^2$	$1/m^2$
$L(\mathbf{r})$	$1/m^4$	$1/m^4$
$L(\mathbf{r}, t)$	$1/m^4s$	$1/m^4s$
$H(\mathbf{r}, t)$	$1/m^3s$	$1/m^3s$
$G(\mathbf{r}, t)$	$1/ms$	$1/ms$
$G(E^+, \mathbf{r})$	$1/m$	$1/m$
$G(\mathbf{p}, E)$	m^2	m^2
V	m	m
$\Psi(\mathbf{r})$	Vs/m	$1/m$
ε_0	J/V^2m	J/m
$\eta \equiv \varepsilon_0 c^2/v_\phi$	J/V^2s	J/s
$I(\mathbf{r}, \hat{\mathbf{s}}),\ I(\mathbf{r})$	η/m^2	η/m^2
$S(\mathbf{r}, t)$	V/m^3	$1/m^3$
$S(\mathbf{r}, \omega)$	Vs/m^3	s/m^3
$S(E)$	Vs	s
$[\Psi * \Psi^*](\mathbf{r}, \omega)$	V^2s/m^2	s/m^2

The last collomn gives the units when the units volt second of the scalar waves are omitted, $\Psi = \left[\frac{1}{m}\right]$ (See also section 2.2.1).

Bibliography

[1] A. B. Fowler, A. Hartstein, and R. A. Webb. Conductance in restricted-dimensionality accumulation layers. *Phys. Rev. Lett.*, **48**, 196, (1982).

[2] C. P. Umbach, S. Washburn, R. B. Laibowitz, and R. A. Webb. Magnetoresistance of small, quasi-one-dimensional, normal-metal rings and lines. *Phys. Rev. B*, **30**, 4048, (1984).

[3] M. P. van Albada and A. Lagendijk. Observation of weak localization of light in a random medium. *Phys. Rev. Lett.*, **55**, 2692, (1985).

[4] P. E. Wolf and G. Maret. Weak localization and coherent backscattering of photons in disordered media. *Phys. Rev. Lett.*, **55**, 2696, (1985).

[5] For an overview of mesoscopic electron systems, see: Quantum Transport in Semiconductor Nanostructures, C. W. J. Beenakker, and H. van Houten, *Solid State Physics*, **44**, (1991), editors H. Ehrenreich, and D. Turnbull, Academic Press Inc.

[6] For an overview of mesoscopic light systems, see: P. Sheng, *Introduction to wave scattering, localization, and mesoscopic phenomena*, Academic Press Inc., New York, 1995.

[7] P. W. Anderson. Absence of diffusion in certain random lattices. *Phys. Rev.*, **109**, 1492, (1958).

[8] S. Feng, C. Kane, P. Lee, and A. D. Stone. Correlations and fluctuations of coherent wave transmission through disordered media. *Phys. Rev. Lett.*, **61**, 834, (1988).

[9] M. P. van Albada, B. A. van Tiggelen, A. Lagendijk, and A. Tip. Speed of propagation of classical waves in strongly scattering media. *Phys. Rev. Lett.*, **66**, 3132, (1991).

[10] E. Kogan, M. Kaveh, R. Baumgartner, and R. Berkovits. Statistics of waves propagating in a random medium. *Phys. Rev. B*, **48**, 9404, (1993).

[11] A. Z. Genack and N. Garcia. Intensity statistics and correlation in absorbing random media. *Europhys. Lett.*, **21**, 753, (1993).

[12] B. L. Altshuler, V. E. Kravtsov, and I. V. Lerner. Distribution of mesoscopic fluctuations and relaxation processes in disordered conductors. In B. L. Altshuler, P. A. Lee, and R. A. Webb, editors, *Mesoscopic phenomena in solids*, volume 30, page 449. North-Holland, Amsterdam, 1991.

[13] W. van Haeringen and D. Lenstra. *Analogies in Optics and Micro Electronics.* Kluwer Academic, Haarlem, 1990.

[14] V. M. Agranovich and V. E. Kravtsov. Effects of weak localization of photons in nonlinear optics: second harmonic generation. *Phys. Lett. A*, **131**, 378, (1988).

[15] V. E. Kravtsov, V. M. Agranovich, and K. I. Grigorishin. Theory of second-harmonic generation in strongly scattering media. *Phys. Rev. B*, **44**, 4931, (1991).

[16] A. Ishimaru. *Wave propagation and scattering in random media, Vols. 1 and 2.* Academic, New York, 1978.

[17] U. Frisch. Wave propagation in random media. In A. T. Barucha-Reid, editor, *Probabilistic Methods in Applied Mathematics*, volume 1, page 76. Academic, New York, 1968.

[18] M. B. van der Mark, M. P. van Albada, and Ad Lagendijk. Light scattering in strongly scattering media: Multiple scattering and weak localization. *Phys. Rev. B*, **37**, 3575, (1988).

[19] B. A. van Tiggelen, A. Lagendijk, M. P. van Albada, and A. Tip. Speed of light in random media. *Phys. Rev. B*, **45**, 12233, (1992).

[20] T. R. Kirkpatrick. Localization of acoustic waves. *Phys. Rev. B*, **31**, 5746, (1985).

[21] See e.g. Ishimaru[16], Chapter 7.

[22] P. M. Morse and H. Feshbach. *Methods of Theoretical Physics.* McGraw-Hill, 1953. page 304.

[23] See e.g. E. Merzbacher. *Quantum Mechanics.* J. Wiley & Sons, New York, 1970. page 238. The t-matrix describes only the isotropic part of the scattered intensity, a valid approximation in the regime $maE/c \ll 1$.

[24] s-wave scattering close to the first resonance is a crude approximation, since s-wave scattering is valid only in the regime $maE/c \ll 1$.

[25] Th. M. Nieuwenhuizen, A. Lagendijk, and B. A. van Tiggelen. Resonant point scatterers in multiple scattering of classical waves. *Phys. Lett. A*, **169**, 191, (1992).

[26] H. C. van de Hulst. *Light Scattering by Small Particles.* Dover, New York, 1957.

[27] For a consistent multiple scattering theory that goes beyond the lowest order approximation of Σ and U, see B. A. van Tiggelen and A. Lagendijk. Resonantly induced dipole-dipole interactions in the diffusion of scalar waves. *Phys. Rev. B*, **50**, 16729, (1994).

[28] M. Born and E. Wolf. *Principles of Optics.* Pergamon Press, Oxford, sixth edition, 1986.

[29] D. Vollhardt and P. Wölfe. Anderson localization in $d \leq 2$ dimensions: A self-consistent diagramatic theory. *Phys. Rev. Lett.*, **45**, (1980).

[30] D. Vollhardt and P. Wölfle. Diagrammatic, self-consistent treatment of the anderson localization problem in $d \leq 2$ dimensions. *Phys. Rev. B*, **22**, 4666, (1980).

[31] B. A. van Tiggelen. *Multiple scattering and localization of light.* PhD thesis, University of Amsterdam, 1992.

[32] M. B. van der Mark. *Propagation of Light in Disordered Media: A Search for Anderson Localization.* PhD thesis, University of Amsterdam, 1990.

[33] See Frisch[17], page 169.

[34] For a more thorough treatment of the arctan, see Ishimaru[16], page 222.

[35] See Ishimaru[16], Chapter 7 and Chapter 9.

[36] S. Chandrasekhar. *Radiative Transfer.* Dover, New York, 1960.

[37] H. C. van de Hulst. *Multiple Light Scattering, Vols. 1 and 2.* Academic, New York, 1980.

[38] A. Lagendijk, R. Vreeker, and P. de Vries. Influence of internal reflection on diffuse transport in strongly scattering media. *Phys. Lett. A*, **136**, 81, (1989).

[39] J. X. Zhu, D. J. Pine, and D. A. Weitz. Internal reflection of diffusive light in random media. *Phys. Rev. A*, **44**, 3948, (1991).

[40] It is assumed that the position of the trapping plane is time-independent. As remarked by van der Mark[32] this might not be correct.

[41] I. S. Gradsteyn and I. M. Ryzhik. *Table of Integrals, Series and Products.* Academic, New York, 1980. page 340, [form. 3.471.9].

[42] Gradsteyn and Ryznik[41], page 672, [form. 6.521.2].

[43] E. R. Hansen. *A Table of Series and Products.* Prentice-Hall, London, 1975. page 243.

[44] E. Akkermans, P. E. Wolf, and R. Maynard. Coherent backscattering of light by disordered media: Analysis of the peak line shape. *Phys. Rev. Lett.*, **56**, 1471, (1986).

[45] D. J. Durian. Influence of boundary reflection and refraction on diffusive photon transport. *Phys. Rev. E*, **50**, 857, (1994).

[46] For an overview of laser speckle, see:*Laser speckle and related phenomena*, J. C. Dainty, editor, Springer-Verlag, Berlin, second edition, 1984, and: A. Consortini, J. F. Holmes, and J. C. Dainty, Optical propagation and scattering related to the atmosphere, dense volume media, and rough surfaces. An Introduction by the feature editors. A feature issue of *Applied Optics*, **32**, 2649, (1993).

[47] J. W. Goodman. Statistical properties of laser speckle patterns. In J. C. Dainty, editor, *Laser speckle and related phenomena*, volume 9, page 9. Springer-Verlag, Berlin, second edition, 1984.

[48] J. W. Goodman and E. G. Rawson. Statistics of modal noise in fibers: a case of constrained speckle. *Opt. Lett.*, **6**, 324, (1981).

[49] J. H. Li, A. A. Lisyansky, T. D. Cheung, D. Livdan, and A. Z. Genack. Transmission and surface intensity profiles in random media. *Europhys. Lett.*, **22**, 675, (1993).

[50] P. A. Lee. Universal conductance fluctuations in disordered metals. *Physica*, **140A**, 169, (1986).

[51] B. Shapiro. Large intensity fluctuations for wave propagation in random media. *Phys. Rev. Lett.*, **57**, 2168, (1986).

[52] M. J. Stephen and G. Cwilich. Intensity correlation functions and fluctuations in light scattered from a random medium. *Phys. Rev. Lett.*, **59**, 285, (1987).

[53] P. A. Mello, E. Akkermans, and B. Shapiro. Macroscopic approach to correlations in the electronic transmission and reflection from disordered conductors. *Phys. Rev. Lett.*, **61**, 459, (1988).

[54] R. Pnini and B. Shapiro. Fluctuations in transmission of waves through disordered slabs. *Phys. Rev. B*, **39**, 6986, (1989).

[55] Th. M. Nieuwenhuizen and M. C. W. van Rossum. Role of a single scatterer in a multiple scattering medium. *Phys. Lett. A*, **177**, 102, (1993).

[56] B. Z. Spivak and A. Yu. Zyuzin. Fluctuations of coherent light transmission through disordered media. *Solid State Commun.*, **65**, 311, (1988).

[57] J. F. de Boer, M. P. van Albada, and A. Lagendijk. Transmission and intensity correlations in wave propagation through random media. *Phys. Rev. B*, **45**, 658, (1992).

[58] S. Hikami. Anderson localization in a nonlinear-σ-model representation. *Phys. Rev. B*, **24**, 2671, (1981).

[59] N. G. van Kampen. *Stochastic processes in physics and chemistry.* North-Holland, Amsterdam, 1992.

[60] A. Z. Genack, N. Garcia, and W. Polkosnik. Long-range intensity correlation in random media. *Phys. Rev. Lett.*, **65**, 2129, (1990).

[61] M. P. van Albada, J. F. de Boer, and A. Lagendijk. Observation of long-range intensity correlation in the transport of coherent ligth through a random medium. *Phys. Rev. Lett.*, **64**, 2787, (1990).

[62] R. N. Bracewell. *The Fourier transform and its applications.* McGraw-Hill, Singapore, second edition, 1986.

[63] P. A. Molenaar. Optical time-resolved transmission experiments on strongly scattering media. Master's thesis, University of Amsterdam, 1990.

[64] H. C. van de Hulst. *Light scattering by small particles.* Dover, New York, 1981. page 128, or Fig.(4) in Ref. [9].

[65] W. G. Egan and D. E. Aspnes. Finite-wavelength effects in composite media. *Phys. Rev. B*, **10**, 5313, (1982).

[66] I. Edrei, M. Kaveh, and B. Shapiro. Probabilty distribution functions for transmission of waves through random media: a new numerical method. *Phys. Rev. Lett.*, **62**, 2120, (1989).

[67] L. E. Reichl. *A Modern Course in Statistical Physics.* Edward Arnold, 1980.

[68] W. H. Press, W. T. Vetterling, S. A. Teukolsky, and B. P. Flannery. *Numerical Recipes.* Cambridge University Press, Cambridge, 1992. Sec. Ed.

[69] P. R. Bevington. *Data Reduction and Error Analysis for the Physical Sciences.* McGraw-Hill, New York, 1969.

[70] M. C. W. van Rossum and Th. M. Nieuwenhuizen. Influence of skin layers on speckle correlations of light transmitted through disordered media. *Phys. Lett. A*, **177**, 452, (1993).

[71] Th. M. Nieuwenhuizen and M. C. W. van Rossum. Intensity distribution of waves transmitted through a multiple scattering medium. *Phys. Rev. Lett.*, **74**, 2674, (1995).

[72] I. Freund, M. Rosenbluh, and R. Berkovits. Geometric scaling of the optical memory effect in coherent-wave propagation through random media. *Phys. Rev. B*, **39**, 12403, (1989).

[73] The enhanced backscattering intensity function is given by Eq. (68b) in M. B. van der Mark, M. P. van Albada, and Ad Lagendijk, Phys, Rev. B. **37**, 3575 (1988). The short-range correlation function for reflection $C^{R\,(1)}_{\alpha\beta\alpha'\beta'}$ is the square of this (slightly simplified) expression.

[74] R. Berkovits, Private communication.

[75] I. Freund and R. Berkovits. Surface reflections and optical transport through random media: Coherent backscattering, optical memory effect, frequency, and dynamical correlations. *Phys. Rev. B*, **41**, 496, (1990).

[76] Th. M. Nieuwenhuizen and J. M. Luck. Skin layer of diffusive media. *Phys. Rev. E*, **48**, 560, (1993).

[77] Th. M. Nieuwenhuizen. Veelvoudige verstrooiing van golven, 1993. diktaat UVA.

[78] L. P. Gor'kov, A. I. Larkin, and D. E. Khmel'nitskii. Particle conductivity in a two-dimensional random potential. *JETP Lett.*, **30**, 228, (1979).

[79] M. C. W. van Rossum, J. F. de Boer, and Th. M. Nieuwenhuizen. Third cumulant of the total transmission of diffuse waves. (1995). To be published in Physical Review E.

Nederlandse samenvatting

Dit proefschrift behandelt de voortplanting van licht door een wanordelijke structuur. Bij een wanordelijke structuur moet je je een medium voorstellen met willekeurig geplaatste obstakels. Het licht kan niet eindeloos recht door reizen, maar botst op een gegeven moment op een obstakel. De botsing zorgt er voor dat het licht verder reist in een andere richting, het licht wordt verstrooid. Het licht kan natuurlijk ook geabsorbeerd worden bij de botsing, maar in dit proefschrift worden obstakels gebruikt die het licht alleen maar verstrooien. De gemiddelde afstand die het licht reist voordat het botst met een obstakel wordt de vrije weglengte genoemd. Als het licht door een wanordelijke structuur reist dat vele vrije weglengten dik is, zal het vele malen verstrooien voordat het er doorheen gekomen is. De werkelijk afgelegde afstand is veel groter dan de hemelsbrede afstand. De manier waarop het licht zich verspreidt wordt diffusie genoemd. Het is te vergelijken met een dronkemanswandeling. Zwaar beneveld door de alcohol probeert een man een brede straat over te steken. Na elke stap verliest hij zijn evenwicht, staat weer op, en doet een nieuwe stap in een willekeurige richting. Je kan je voorstellen dat het even duurt voordat hij de overkant bereikt heeft. De kans dat hij überhaupt de overkant bereikt bij elke poging de straat over te steken is slechts zijn stapgrootte gedeeld door de breedte van de straat, afgezien van eventueel verkeer (dat hier voor een vrij gruwelijke vorm van absorptie zorgt).

Diffusie van licht is geen exotisch verschijnsel dat alleen onder moeilijke omstandigheden in een laboratorium optreedt. Een mooi voorbeeld uit het dagelijks leven is een glas melk. Kleine vetbolletjes die in de melk drijven verstrooien het licht, het licht propageert diffusief door de melk. Omdat de vloeistof en de vetbolletjes het licht niet absorberen, ziet de melk er wit uit. Andere voorbeelden van een wanordelijke structuur voor licht zijn (dikke) mist en witte muurverf. Hoofdstuk 2 behandelt voornamelijk de diffuse voortplanting van licht door een laagje witte verf.

Bovenstaande beschrijving van licht is gebaseerd op een deeltjesbeeld en wordt wel klassieke diffusie genoemd. Licht is eigenlijk een golf, een electro-magnetische golf, en golven kunnen met elkaar interfereren. Twee golven kunnen elkaar versterken of uitdoven. Voor watergolven kun je dit waarnemen in een (zwem)bad of afwasteiltje. Het golfkarakter van licht en de daarmee samenhangende interferentie zorgt voor een aantal interessante verschijnselen in de voortplanting van licht door een wanordelijke structuur. Licht is niet het enige dat een golfkarakter heeft. Elektronen hebben ook een golfkarakter, net als geluidsgolven. In de quantum mechanica worden zelfs alle deeltjes (interacties) beschreven met golffuncties. Het mag duidelijk zijn dat interferentie een zeer veel voorkomend verschijnsel is in de natuurkunde. Meestal wordt het optreden van veelvuldige verstrooiïng van golven gezien als de vervuiling van een schoon systeem (in electrontransport worden verstrooiïngscentra onzuiverheden genoemd). Wij zijn juist geïnteresseerd in deze “vuile” systemen. Veelvuldige verstrooiïng van laserlicht in een laagje witte verf is een ideaal modelsysteem om interferentieëffecten in wanordelijke structuren te bestuderen.

In hoofdstuk 3 worden twee interferentieverschijnselen behandelt die wij experimenteel hebben waargenomen. Het eerste verschijnsel beschrijft de interferentie van licht op de detector dat langs verschillende paden door het verfmonster is gereisd. De dronkemanswandeling zorgt er voor dat alle paden door het monster een verschillende lengte hebben. De bijdragen van alle paden kunnen zowel destructief als constructief met elkaar interfereren. De waargenomen intensiteit kan sterk variëren, en hangt af van de realisatie van padlengten. Voor een ingevroren wanorde (de verstrooiers staan op een vaste plaats) is de waargenomen intensiteit constant. Als echter de golflengte van het laserlicht wordt veranderd, verandert ook de waargenomen intensiteit, omdat de fase verandert waarmee de golven, die langs verschillende paden hebben gereisd, aankomen bij de detector. De fase verandert omdat het aantal golflengten dat past in een pad met een bepaalde lengte anders is geworden. Een meting van de fluctuaties in de intensiteit als functie van de verandering van de golflengte van het laserlicht geeft informatie over de padlengtedistributie in het monster. Een belangrijke fysische parameter, de diffusieconstante van het licht, kan hiermee bepaald worden. Omdat de gemeten intensiteit snel verandert met de verandering van de golflengte, wordt de gemeten correlatiefunctie de korte-dracht correlatiefunctie genoemd.

Het tweede verschijnsel beschrijft de interferentie van het licht *in* het verfmonster. Ook in het verfmonster komen golven die langs verschillende paden hebben gereisd elkaar tegen en interfereren met elkaar. Veronderstel dat de golven constructief interfereren. Lokaal is de intensiteit dan hoger dan gemiddeld. Deze lokaal hogere intensiteit reist langs verschillende paden verder door het verfmonster (verspreidt zich door het monster). Het bijzondere is dat er nu samenhang (correlatie) is ontstaan in de intensiteit in het verfmonster. De invloed van dit interferentieëffect is meetbaar op de totale hoeveelheid licht die door een laagje witte verf heen komt. Deze totale transmissie fluctueert veel langzamer met het veranderen van de golflengte van het licht, en daarom wordt de correlatie op de totale transmissie de lange-dracht correlatiefunctie genoemd. In hoofdstuk 3 wordt uitgerekend hoe groot beide effecten zijn en hoe snel de gemeten intensiteit verandert met het veranderen van de golflengte van het inkomende licht. Vooral het laatste effect vereist enig rekenwerk omdat de precieze omstandigheden waaronder het experiment werd uitgevoerd meegenomen moesten worden.

Een effect dat niet beschreven wordt in dit proefschrift is de interferentie tussen twee golven in het monster die even verder weer met elkaar interfereren. Dit effect is waargenomen voor elektronen in 1984, en wordt de universele geleidingsfluctuatie genoemd. De analogie tussen elektronen en licht (hun golfkarakter) was een belangrijke aanleiding voor de experimenten met licht.

In hoofdstuk 4 wordt de experimentele opstelling beschreven om de fluctuaties in de intensiteit als functie van de golflengte te meten. Vooral het meten van de lange-dracht correlatie vereiste zorgvuldigheid, omdat de fluctuaties niet groot zijn. De resultaten van de metingen worden uitstekend beschreven door de berekeningen in het vorige hoofdstuk. De meting van fluctuaties op de totale transmissie was de eerste experimentele bevestiging van de volledige lange-dracht correlatiefunctie.

Voor hoofdstuk 5 is opnieuw inspiratie geput uit de analogie tussen elektronen en licht. Behalve naar de correlatie in de fluctuaties van de intensiteit kan je ook kijken naar de distributie van de fluctuaties. De distributie van de fluctuaties beschrijft hoe groot de kans is dat je een bepaalde waarde voor de intensiteit meet. De interferentieprocessen die leiden tot de lange-dracht correlatie geven een Gaussische distributie van de fluctuaties. De theorie voor de universele geleidingsfluctuaties voor elektronen voorspelt in de simpelste benadering ook een Gaussische distributie van de geleidingsfluctuaties, die verandert in een log-normale distributie als ingewikkeldere interferentieprocessen worden meegenomen. De distributie van de universele geleidingsfluctuaties voor elektronen is echter tot op heden niet experimenteel gemeten. De vraag was of in onze metingen van de fluctuaties op de totale transmissie voor licht misschien een afwijking van de Gaussische distributie aangetoond kon worden. Dat zou betekenen dat nieuwe interferentieprocessen een rol spelen die anders zijn dan diegene die leiden tot de lange-dracht correlatie. Een zorgvuldige analyse van de metingen toont inderdaad een afwijking aan van de Gaussische distributie. Niet alleen kwalitatieve, maar zelfs quantitatieve overeenstemming wordt aangetoond tussen de metingen en berekeningen van de nieuwe interferentieprocessen. Dat deze nieuwe interferentieprocessen voor het eerst experimenteel aangetoond konden worden geeft aan dat de metingen in hoofdstuk 4 van zeer hoge kwaliteit waren.

In de appendices worden diagrammatische berekeningen uitgevoerd van de interferentieprocessen die eerder op een andere manier (in de Langevin aanpak of op een heuristische wijze) zijn berekend in hoofdstuk 3 en hoofdstuk 5.

In hoofdstuk 6 wordt naar de interferentie gekeken van frequentie verdubbeld licht in een wanordelijke structuur. De interferentie van frequentie verdubbeld licht wordt vergeleken met interferentie in het fundamentele licht in een wanordelijke structuur. Frequentie verdubbeling van licht is het proces waarbij een (klein) gedeelte van het inkomende licht wordt omgezet in licht met een verdubbelde frequentie (de kleur van het licht wordt omgezet van infrarood naar groen). De omzetting van infrarood naar groen licht is geen lineair proces, de hoeveelheid gegenereerd groen licht is evenredig met het kwadraat van de hoeveelheid infrarood licht. De efficiëntie van dit proces wordt bepaald door de niet-lineaire susceptibiliteit. Een monster werd gemaakt van witte verfdeeltjes met een grote niet lineaire susceptibiliteit. Als dit monster wordt beschoten met zeer intense infrarode laserpulsen, wordt een klein beetje groen licht gegenereerd. Zowel in reflectie als in transmissie is de korte-dracht correlatiefunctie gemeten in zowel het infrarode als het groene laserlicht. Het belangrijkste resultaat is een totaal verschillend gedrag van de korte-dracht correlatiefunctie voor het infrarode en het groene licht in reflectie.